Streaming motions of abell clusters: new evidence for a high-amplitude bulk flow on very large scales

Russell Julian Smith

Streaming Motions of Abell Clusters : New evidence for a high-amplitude bulk flow on very large scales

Russell Julian Smith

Department of Physics & St Chad's College

A thesis submitted to the University of Durham in accordance with the regulations for admission to the Degree of Doctor of Philosophy.

University of Durham
1998

Abstract

Streaming motions of galaxies and clusters provide the only method for probing the distribution of mass, as opposed to light, on scales of $20-100\,h^{-1}$Mpc. This thesis presents a new survey of the local peculiar velocity field, based upon Fundamental Plane (FP) distances for an all-sky sample of 56 clusters to $cz = 12000\,\mathrm{km\ s^{-1}}$.

Central velocity dispersions have been determined from new spectroscopic data for 429 galaxies. From new R-band imaging data the FP photometric parameters (effective diameter and effective surface brightness) have been measured for 324 galaxies. The new spectroscopic and photometric data have been carefully combined with an extensive body of measurements compiled from the literature, to yield a closely homogeneous catalogue of FP data for 725 early type galaxies. Fitting the inverse FP relation to the merged catalogue yields distance estimates with a scatter of 22% per galaxy, resulting in cluster distance errors of 2–13%. The distances are consistent, on a cluster-by-cluster basis, with those determined from Tully–Fisher studies and from earlier FP determinations. The distances are marginally inconsistent with distance estimates based on brightest cluster galaxies, but this disagreement can be traced to a few highly discrepant clusters.

The resulting peculiar velocity field is dominated by a bulk streaming component, with amplitude of $810 \pm 180\,\mathrm{km\ s^{-1}}$ (directed towards $l = 260°, b = -5°$), a result which is robust against a range of potential systematic effects. The flow direction is $\sim$35° from the CMB dipole and $\sim$15° from the X-ray cluster dipole direction. Two prominent superclusters (the Shapley Concentration and the Horologium–Reticulum Supercluster) may contribute significantly to the generation of this flow. More locally, there is no far-side infall into the 'Great Attractor' (GA), apparently due to the opposing pull of the Shapley Concentration. A simple model of the flow in this direction suggests that the GA region generates no more than $\sim$60% of the Local Group's motion in this direction. Contrary to some previous studies, the Perseus–Pisces supercluster is found to exhibit no net streaming motion. On small scales the velocity field is extremely quiet, with an rms cluster peculiar velocity of $< 270\,\mathrm{km\ s^{-1}}$ in the frame defined by the bulk-flow.

The results of this survey suggest that very distant mass concentrations contribute significantly to the local peculiar velocity field. This result is difficult to accommodate within currently popular cosmological models, which have too little large-scale power to generate the observed flow. The results may instead favour models with excess fluctuation power on 60–150 h^{-1}Mpc scales.

Preface

The work described in this thesis was undertaken between 1994 and 1998, whilst the author was a research student in the Department of Physics, at the University of Durham, under the supervision of Dr. J. R. Lucey and Prof. R. L. Davies. This work has not been submitted for any other degree, either at the University of Durham or at any other University.

The work presented here was undertaken in collaboration with Dr. J. R. Lucey, Dr. M. J. Hudson, Dr. D. J. Schlegel, Prof. R. L. Davies and Dr. G. Baggley. In particular, the observations reported in Chapters 3 were obtained through work with Drs. Lucey and Hudson; and those of Chapter 4 were obtained in collaboration with Drs. Lucey, Hudson, Schlegel & Baggley. The construction of a standardized catalogue of Fundamental Plane data (Chapter 5) was the result of collaboration with Dr. Hudson. The charts of Appendix B were supplied by Dr. Hudson. However, the majority of the material presented here is the author's own work.

Acknowledgements

My first acknowledgement must be to my supervisor, John Lucey, for his guidance and encouragement, over the past four years. The production of this thesis testifies to his support, his patience and his extraordinary passion for data.

I must express my gratitude to my other principal colleague in the SMAC team, Mike Hudson. Many parts of this work are results of stimulating late-night email exchanges with Mike over the past few years. I thank, too, the other team members, Roger Davies, David Schlegel and Glenn Baggley, for their input into the project.

I acknowledge financial support from the PPARC and the University of Durham during the (rather extended) course of this work.

This work has benefitted directly and indirectly from the stimulating atmosphere of the Durham astronomy community. I thank in particular those who have shared offices with me: sorry for being a nuisance, guys!

St Chad's College has been my home since 1994. I must thank the college for providing a supportive and lively environment in which to work and to relax. My housemates in Ramsey House especially deserve thanks for their excellent company in recent years.

Finally, my sincerest gratitude must be extended to my parents, for their love and support over these years, and to Jane, to whom above all others, I owe my sanity.

"We measure things because they need measuring — that's all there is to it."

(John Lucey)

Contents

Chapter 1

Introduction

1.1 Hubble flow and peculiar velocities

The discovery, by Hubble (1927), that the line shifts observed in galactic spectra are proportional to the distance of the galaxies, marks the birth of, and remains a cornerstone of twentieth century cosmology. If the kinematic origin of galactic redshifts is accepted (Hubble himself referred only to the 'apparent velocity'), then Hubble's law implies that the universe is *expanding*, and provides the most fundamental empirical evidence for the Big Bang cosmological model.

The Hubble law may be written as

$$cz = H_0 d\,, \tag{1.1}$$

where z is the fractional frequency shift of features in the galaxy's spectrum, d the distance of the galaxy, and c the velocity of light. The constant of proportionality, H_0, known as the Hubble constant, sets the current rate of expansion of the universe, and consequently defines the cosmological distance scale.

Whilst the measurement of H_0, and hence of *absolute* distances, is a notoriously difficult exercise, the existence of 1.1 permits estimation of *relative* galactic distances, through measurement of the redshift, z. Distances are then expressed in terms of the dimensionless parameter $h^{-1} = H_0/100\,\mathrm{km\,s^{-1}\,Mpc^{-1}}$, or in velocity units, such that $H_0 = 1$ by definition.

The measurement of redshifts in large numbers became possible in the mid-1980's, with the development of efficient photon-counting detectors and CCDs. The resulting three-dimensional maps of the galaxy distribution revealed the first clear evidence for departures from homogeneity on large ($\sim 100h^{-1}\,\mathrm{Mpc}$) scales. The walls, filaments and voids evidenced by the CfA 'slice' (de Lapparent et al. 1986) and later surveys show clearly that galaxies are not distributed at random at the present epoch. In

contrast, the smoothness of the cosmic microwave background (CMB) radiation, argues that the density of matter at early times ($z \sim 1000$) was smooth to about one part in 10^5. The current clustered distribution of is matter is thought most likely to have occurred through the process of gravitational instability (GI), that is amplification of initially small density fluctuations, through the infall of material from underdense into overdense regions.

This picture of the growth of cosmic structure requires that 1.1 cannot be exactly true, since galaxies must possess gravitationally-induced motions in addition to their Hubble expansion velocities. Thus the expression for the observed radial velocity of a galaxy should be revised to

$$v_r = H_0 d + \hat{\mathbf{r}} \cdot \mathbf{v}_\mathrm{p} \,. \tag{1.2}$$

Here, the first term represents the Hubble expansion velocity as above, and the second takes account of the 'extra' velocity component, which will hereafter be referred to as the *peculiar velocity* of the galaxy, with respect to a given reference frame. Of course, only the radial component of velocity, defined by the galaxy's unit direction vector $\hat{\mathbf{r}}$ can be measured from the redshift.

It is clear from the above discussion, that the peculiar velocity field $\mathrm{v_p}$ contains significant information concerning the growth of structure in the universe, and that its radial component is, in principle, measurable when a redshift-independent estimate of the distance d is available. The remainder of this chapter considers the theoretical information-content of the peculiar velocity field, and presents a discussion of the observational methods available for its study. Finally, an account is given of the current state of velocity field research, from an observational perspective. In particular, attention is drawn to three outstanding problems, which provide motivation for the work described in the remainder of this thesis. For further details of the background to large-scale structure and motions, of the history of the field, and of current areas of research, the reader is directed to the excellent review of Strauss & Willick (1995).

1.2 The velocity field as a probe of cosmological parameters

The mass density fluctuation field, δ can be defined by

$$\delta(\mathbf{r}) = (\rho(\mathbf{r}) - \overline{\rho})/\overline{\rho} \,, \tag{1.3}$$

where $\rho(\mathbf{r})$ is the mass density field, and $\overline{\rho}$ the mean mass density of the universe. In the late-time, linear régime, where $|\delta| \ll 1$, the equations of GI reduce to direct proportionality between the velocity divergence and the density fluctuation field (Peebles

1980, 1993), *viz*

$$\nabla \cdot \mathbf{v}(\mathbf{r}) = -f(\Omega, \Lambda)\delta(\mathbf{r}) . \tag{1.4}$$

The function f, which sets the rate of growth for cosmic structures, depends in general on both the mean mass density parameter, Ω, and the cosmological constant Λ. However, the Λ-dependance of f is weak, and to a good approximation we may write (Peebles 1980):

$$\nabla \cdot \mathbf{v}(\mathbf{r}) = -\Omega^{0.6}\delta(\mathbf{r}) . \tag{1.5}$$

Equation 1.5 immediately reveals the principal motivation for peculiar velocity studies: the velocity field is sensitive to fluctuations not in the number density of *galaxies*, but in the *mass* density of matter. This allows us, for instance, to constrain the matter power spectrum independent of any assumptions concerning the distribution of galaxies relative to that of mass. Transforming 1.5 into Fourier space, and defining a velocity power spectrum

$$P_v(k) \propto \langle \tilde{\mathbf{v}}^2(\mathbf{k}) \rangle , \tag{1.6}$$

it can easily be shown that the velocity power spectrum is related to the matter power spectrum $P(k)$ through

$$P_v(k) = \Omega^{1.2} k^{-2} P(k) , \tag{1.7}$$

which demonstrates that on large scales, the observed velocity field is a more sensitive probe of structure than the density field, due to the two extra powers of k.

In addition to its sensitivity to large-scale power, the velocity field can be used also to *test* the scenario of structure formation by GI, through Equation 1.5. In particular we may assume a simple relation for the biasing of the galaxy-density fluctuation field, $\delta_{\rm g}$, relative to that of mass, eg

$$\delta_{\rm g} = b\delta . \tag{1.8}$$

Under this assumption, we have

$$\nabla \cdot \mathbf{v}(\mathbf{r}) = -\frac{\Omega^{0.6}}{b}\delta_{\rm g}(\mathbf{r}) = -\beta\delta_{\rm g}(\mathbf{r}) , \tag{1.9}$$

allowing the measurement of $\beta = \Omega^{0.6}/b$, through the comparison of the measured peculiar velocities with the density field of galaxies. In general, the recovered value β will depend on the population of galaxies chosen to define the density field, since the distribution of optically-selected galaxies, for instance, is biased relative to that of IRAS-selected galaxies.

1.3 Peculiar velocity surveys

Many observational surveys of galaxy peculiar velocities, with typical samples of a few hundred galaxies, have been conducted over the past twenty years. Several methods have been employed for the determination of redshift-independent distances, and the surveys have utilised a wide variety of sample strategies. The following sections provide a brief summary of these and other characteristics of peculiar velocity surveys.

1.3.1 Distance indicator relations

Observational studies of the peculiar velocity field require a method for redshift-independent estimation of galaxy distances. In general, distance indicators take the form of empirically-determined relationships between observable quantities, one of which is distance-independent and one of which is a magnitude-like quantity. The measured distance-independent variable is used to predict the absolute magnitude of the galaxy, the distance being then given by the measured apparent magnitude. (The predicted quantity is, in some analyses, the distance-independent variable, but this does not alter the data requirements.)

For the purposes of the following summary of peculiar motion measurements, it will be sufficient to describe here the three distance indicators most significantly employed in the field.

1. The TF relation (Tully & Fisher, 1977) relates rotational velocity to absolute magnitude for spiral galaxies. The relation may be written

$$m = a \log w + b \,, \tag{1.10}$$

where m is the apparent magnitude, and w an appropriately defined rotational velocity. The scatter in the TF relation permits distance estimates with uncertainties of 15–20% per galaxy, depending on the choice of photometric bandpass.

2. For early-type galaxies, the distance indicator most closely analogous to the TF relation is that of Faber & Jackson (1976), which relates central velocity dispersion to intrinsic luminosity. When surface brightness is introduced as a third parameter, the precision of distance estimates is improved by approximately a factor of two, to ~20% per galaxy. This improved distance indicator is the Fundamental Plane (FP) (Dressler et al. 1987b, Djorgovski & Davis 1987). For galaxies with well-behaved luminosity profiles, the $D_n - \sigma$ relation of Dressler et al. is in principle equivalent to the FP.

The FP relation,

$$\log R_e - \beta\langle\mu\rangle_e = \alpha \log \sigma + \gamma\,, \tag{1.11}$$

defines a plane in a three-dimensional parameter space of central velocity dispersion (σ), effective (half-light) radius R_e and mean surface brightness $\langle\mu\rangle_e$ within effective radius. The diameter D_n defined operationally as that which encloses a chosen mean surface brightness, combines size and surface brightness parameters in approximately the correct combination to represent an edge-on projection of the plane. As a result, the $D_n - \sigma$ relation can be written in the TF-like form

$$\log D_n = \alpha \log \sigma + \gamma'\,. \tag{1.12}$$

3. The $L_m - \alpha$ relation (Hoessel 1980, Postman & Lauer 1995) for brightest cluster galaxies (BCGs) relates absolute metric luminosity L_m to a 'structure parameter' α, defined as the logarithmic gradient of the surface brightness profile

$$\alpha \equiv \left.\frac{d \log L_m}{d \log r}\right|_{r_m}\,. \tag{1.13}$$

A quadratic relation between L_m and α is adopted by Postman & Lauer. Involving only parameters derived from photometric data, the method is observationally 'cheap' in contrast to the TF and FP methods. However, although the scatter is small (~16%), the relation is by definition applicable to only one galaxy per cluster.

1.3.2 Survey strategies

The choice of distance indicator for a given study depends upon a number of parameters dictated by the ultimate objective of the project: the depth and angular extent of the volume studied, the desired sampling density, the accuracy required at each sampling point. These and other 'strategic issues' of peculiar velocity surveys are discussed in this section.

Survey geometry

The bulk-motion, ie dipole component of the velocity field is in principle, the simplest statistic measurable from peculiar velocity surveys. The bulk motion is, however, highly sensitive to systematic errors. In particular, for a self-calibrating sample (one in which the velocity zero-point is determined from the average velocity of the sample itself) the bulk-flow component is degenerate with the zero-point (monopole), unless the sample has near-uniform sky coverage.

For the comparison of observed peculiar motions with models (either simple 'toy attractor models' or more realistic models based on the density field of galaxies) however,

the requirement of full-sky coverage can be relaxed, with the zero-point uncertainty allowed for by a 'residual bulk flow' component included in the model.

Sampling density

Although only the radial component of the peculiar velocity field is directly measurable, the POTENT algorithm (Bertschinger & Dekel, 1989) permits the recovery of the full three-dimensional velocity field under the assumption of potential flow. Whilst this approach provides a valuable picture of the local dynamics, and allows the quantitative comparison with redshift survey data at the density-density level, a crucial requirement of the method is a high density of velocity sampling points. The successful extension of the POTENT method into the mildly non-linear régime could break the degeneracy between Ω and b, but this requires still better sampling of the velocity field on scales of $\sim 1000\,\mathrm{km\,s^{-1}}$ (Dekel et al. 1993)

Cluster vs field samples

Since most current distance indicators have errors greater than 15% per galaxy, the peculiar velocity error becomes larger than the typical size of the velocities themselves for galaxies more distant than $4000\,\mathrm{km\,s^{-1}}$. When, as occurs in some analysis methods, these random distance errors couple with varying *a priori* probability distributions for a galaxy to lie at a given distance, the result is a systematic 'Malmquist' bias (Hudson 1994, Strauss & Willick 1995).

By selecting rich clusters as tracers of the velocity field, the distance estimates for many galaxies can be averaged, reducing random errors by $\sqrt{N}$. In consequence, Malmquist effects are also mitigated. With cluster samples, however, one must pay the price of poorly sampling the peculiar velocity field, since rich clusters are rare objects. Cluster samples are therefore quite unsuitable for POTENT-like analyses.

Spirals vs ellipticals

Finally, the choice of distance indicator will depend upon the type of galaxies present in the structures probed. Naturally, the TF relation will remain the most appropriate distance indicator for use with field samples, where 'isolated ellipticals' are rare, and sometimes disturbed systems. In cluster cores, on the other hand, early-type galaxies are numerous, and E/S0 samples will not be severely contaminated by foreground and background objects, except in the case of superposed clusters or groups. Consequently, the FP and BCG relations are the methods of choice in clusters, unless a careful

treatment of cluster membership criteria is employed (as, for example, by Giovanelli et al. 1997).

1.4 Reconstruction of velocity fields from redshift surveys

Under the approximations of linear biasing and linear or quasi-linear gravitational instability, the redshift-space distribution of galaxies measured from redshift surveys can be used to 'reconstruct' self consistent density and velocity fields in real-space (eg Yahil et al. 1991, Nusser & Davis 1994, Fisher et al. 1995a). The resulting velocity fields can be compared point-by-point with measurements from peculiar velocity surveys, to test the assumptions underlying the reconstruction, and to determine the β parameter of Section 1.2.

Redshift surveys of IRAS galaxies selected at 60 microns have provided the most important catalogues for use in velocity field reconstructions. The principal advantage of the IRAS surveys is their excellent sky coverage, reaching to $|b| > 5°$, reducing the uncertainties associated with unsurveyed structures behind the galactic plane. The largest IRAS redshift surveys currently available are the one-in-one 1.2 Jy survey of Fisher et al. (1995b), and the deeper but sparse-sampled (one-in-six) QDOT 0.6 Jy survey of Rowan-Robinson et al. (1990). The new PSCz survey of ~14000 IRAS galaxies to 0.6 Jy will provide a much improved sample for reconstructions (Branchini et al. 1998).

A disadvantage of IRAS galaxies as density-field tracers is that, as dusty late-type spirals, they are effectively absent from the cores of rich clusters, whose contribution to the large-scale dynamics may consequently be underestimated by the IRAS reconstructions. While the use of optically-selected galaxy samples in velocity field reconstructions (Hudson 1993, Baker et al. 1998) can improve the sampling of galaxy-rich environments, this gain comes at the expense of much poorer coverage at low galactic latitude.

An alternative approach uses clusters instead of galaxies as the redshift sample, allowing low-resolution reconstruction to much larger depths (Branchini & Plionis 1996). However, the use of optically-selected cluster samples, subject to complicated selection inhomogeneities and projection effects, compromises the cluster-based reconstructions at present.

1.5 The peculiar velocity field within 3000 km s^{-1}

In discussing the history of streaming motion measurements, it is convenient to divide the subject into the very local ($cz < 3000\,\mathrm{km\ s^{-1}}$) velocity field (on which a broad consensus holds), and more distant flows (often the subject of greater controversy).

The first determination of the Local Group motion with respect to a distant galaxy sample was that of Rubin et al. (1976). The misalignment between the Rubin et al. direction and the subsequently discovered CMB dipole (Smoot et al. 1977), argued for a local bulk-flow of large amplitude and unexpected coherence. In fact, although the Rubin et al. results were essentially dismissed (amongst concerns regarding statistical biases in the sample and method), the implied bulk motion ($730 \pm 250\,\mathrm{km\ s^{-1}}$, towards $l \sim 330, b \sim 30°$) was roughly comparable to results obtained a decade later.

More systematic studies of the velocity field aimed at detecting the infall velocity of the Local Group towards the Virgo cluster (see Davis & Peebles 1983, for a full review). Whilst Virgo apparently represents the centre of the Local Supercluster, it nonetheless became clear that a substantial component of the LG motion (with respect to the CMB frame) was directed orthogonally to the Virgo direction. Tammann & Sandage (1985) and Shaya (1984) were among the first to recognise explicitly that the Hydra–Centaurus (HC) supercluster, at $cz\sim 3000\,\mathrm{km\ s^{-1}}$ (Chincarini & Rood 1979) might contribute significantly to the LG acceleration. From consideration of the residuals in the Virgocentric flow, Lilje, Yahil & Jones (1986) inferred that the local velocity field exhibits a shear, indicating the presence of an external attractor in the direction of HC. While the distance of the inferred attractor was compatible with that of HC, Lilje et al. stressed that the observed tidal field could not be generated by a single nearby supercluster.

In the late 1980's, this picture of the peculiar velocity field was overthrown by the dramatic conclusions of a collaboration who became known as the Seven Samurai (7S). Using the $D_\mathrm{n} - \sigma$ relation for $\sim$ 400 early-type galaxies, the 7S showed that the HC complex itself, far from being the *source* of the local flow, actually *participated in* that motion. In particular, the Centaurus clusters showed positive peculiar velocities of $\sim 1000\,\mathrm{km\,s^{-1}}$ (but see Lucey & Carter 1988; Aaronson et al. 1989). The initial interpretation of the 7S results (Dressler et al., 1987a), suggested that a bulk motion of large (but unconstrained) coherence length was responsible for the observed streaming. Lynden-Bell et al. (1988) later argued from the shear in the velocity field, in the direction of HC, that the flow could be generated by a massive supercluster centred beyond (but perhaps including) HC. The structure so invoked quickly became known as the Great Attractor (GA), but at the proposed GA position (distance $\sim 4500\,\mathrm{km\,s^{-1}}$), no conspicuous central cluster was observed, leading to speculation that the core of the structure was hidden in the Galactic plane.

1.6 Distant flows : Three outstanding questions

In the decade since the 7S announcement of large-scale streaming towards the GA, a general consensus has emerged upon the *existence* of strong outflows in the direction of Centaurus. The coherence length of the local flow, and the nature of its source have, however, remained controversial. Is the GA an isolated structure, dominating the local velocity field? If so, why is it not seen in the galaxy distribution? If a very-large scale bulk flow is the cause of the local motions, then what is its source? And at what scale do coherent perturbations finally damp out to leave pure Hubble expansion?

Motivated by these amongst other questions raised by the Samurai results, a number of projects were initiated which aimed to determine the flow field at distances of $6000\,\mathrm{km\,s^{-1}}$ and beyond. To the present time, these studies have failed to yield unambiguous conclusions. Leaving aside the conflicts surrounding comparison of the observed and IRAS-predicted velocity fields (for which, see Willick & Strauss 1998, and many references therein), three outstanding issues may be identified, which furnish motivation for the work described in this thesis.

1.6.1 The peculiar motion of Perseus–Pisces

The Perseus–Pisces (PP) supercluster, a filamentary complex at $\sim 5000\,\mathrm{km\,s^{-1}}$ on the opposite side of the sky to the GA, was not well sampled by the 7S survey. However, by virtue of its position at the antapex of the local flow pattern, the peculiar motion of PP can discriminate between competing models for the origin of the motions. Since the PP region is $\sim$10000 $\mathrm{km\,s^{-1}}$ distant from the GA, its motion will be small ($< 100\,\mathrm{km\,s^{-1}}$) if the GA dominates the local kinematics. If however the observed velocities are largely due to a bulk motion of very large coherence length, then PP will participate in a streaming with similar amplitude to that of Hydra–Centaurus.

Motivated by such considerations, Willick (1990, 1991) conducted a TF study of field ellipticals in the region, and concluded that PP partakes in a large-amplitude ($\sim 400\,\mathrm{km\,s^{-1}}$) mean motion towards the LG, and therefore towards the GA. A TF study of clusters in PP, by Han & Mould (1992), provided support for Willick's conclusions (but was not fully independent, through a shared calibration scheme). Courteau et al. (1993), extending the TF field sample, similarly found evidence for a PP motion of $\sim 350\,\mathrm{km\,s^{-1}}$, relative to the CMB. These studies, then, argued that local motions were indeed dominated by a bulk streaming component, presumably generated by mass complexes beyond $6000\,\mathrm{km\,s^{-1}}$.

In contrast, the full-sky field TF sample of Giovanelli and collaborators (see da

Costa et al. 1996) found no evidence for a significant net streaming of PP. Further, an FP survey of 6 clusters in the supercluster reported a mean PP velocity of $-60 \pm 220\,\mathrm{km\,s^{-1}}$ (Hudson et al. 1997). These results cast some doubt upon the claims of very-large scale flow, and are consistent with the standard (Lynden-Bell et al.) GA model.

Willick & Strauss (1998) recently reanalysed the 'Mark III' compilation of TF peculiar velocity data (Willick et al. 1997: this catalogue includes the PP data of Willick 1991), using the 'VELMOD' method (Willick et al. 1997). They conclude that distances for Willick's PP sample were initially overestimated, by $\sim 8\%$ (Willick & Strauss 1998). Using the VELMOD calibration, the velocity of PP is reduced to near-zero. However, in this method the TF relations are calibrated simultaneously with a fit for β, using the IRAS-predicted velocity field. The different calibration for the PP data is therefore simply reflects the fact that a coherent streaming in PP is unexpected (given the local density field), rather than offering *a priori* evidence relevant to the peculiar velocity field itself.

The cause of discrepancy between the the above studies has not been fully resolved to date. Individual distance comparisons, even between the cluster samples is not trivial, since the FP and TF studies may probe different physical structures. The question of PP's net motion cannot yet be said to be settled.

1.6.2 The nature of the Great Attractor

If the local peculiar velocity field is dominated by a single structure beyond HC, then we would expect that region to be especially dense in galaxies, as well as in mass. The redshift survey of Dressler (1988), conducted in the GA direction, found a broad overdensity of galaxies at around $4500\,\mathrm{km\,s^{-1}}$. While this structure is *consistent* with a GA candidate at rest, it may instead be that Dressler's structure reflects the foreground HC supercluster itself, with $\sim$1500 $\mathrm{km\,s^{-1}}$ outward streaming velocity. Since peculiar motions of this magnitude are indeed found in HC, it would be premature to interpret Dressler's results as an unambiguous detection of the GA.

Hierarchical clustering scenarios predict the existence of rich clusters embedded within supercluster structures, such as is observed in the Coma and PP superclusters. If such a cluster could be identified within the GA candidate, and if it could be shown that that cluster is essentially at rest with respect to the CMB, then its identification as the source of the local streaming motions could be strengthened. The absence of such a cluster from IRAS maps of the region would not be surprising, since the cores of rich clusters are practically devoid of the dusty spirals detected by IRAS. An early supposition held that much of the GA streaming was due to matter located in the zone

of avoidance, prominent in the Centaurus region. Indeed, the POTENT–reconstructed density-field peaked at $(l, b, cz) \approx (320°, 0°, 4000\,\mathrm{km\,s^{-1}})$ in the analysis of Kolatt, Dekel & Lahav (1995). A visual search for galaxies within the galactic plane (Kraan-Korteweg et al. 1996) revealed a rich cluster very close to this position, at $(325°, -7°, 4700\,\mathrm{km\,s^{-1}})$. It is in fact remarkable that the potential richness of this cluster — A3627, the only Abell/ACO cluster with $|b| < 10°$ (Abell 1958, Abell et al. 1989) — should have been overlooked for so long. Kraan-Korteweg et al. found that the cluster velocity dispersion was $900\,\mathrm{km\,s^{-1}}$, a value typical for rich clusters such as Coma and Perseus. Furthermore, the X-ray data of (Böhringer et al., 1996) reveal that the cluster is the sixth brightest in the ROSAT All Sky Survey. While the identification of this cluster as the 'core cluster' of the supercluster at $cz \sim 4500\,\mathrm{km\,s^{-1}}$ is perhaps appropriate, identifying that supercluster as the cause of local motions requires more care. We expect that the core of an isolated GA should be an 'unmoved mover', ie that its own peculiar velocity should be small. In practice the reliable measurement of peculiar motion for A3627 has proved impossible so far. Lucey et al. (1999) attempted a $D_\mathrm{n} - \sigma$ distance estimate, but abandoned the effort, in the face of extreme stellar contamination in the galaxy images. Mould et al. (1991) reported a peculiar velocity of $+1760 \pm 355\,\mathrm{km\,s^{-1}}$. If confirmed, such a velocity would suggest that A3627 is simply a part of the HC foreground structure, participating in the general flow. However, Mould et al. stress that their result is highly uncertain for this cluster, due to uncertainties in the correction for (probably patchy) extinction, and to stellar contamination effects.

A further test of the source of the local motions is the flow pattern in the background of the proposed GA. If a large-scale bulk flow is responsible, then we expect to observe positive peculiar motions in the Centaurus direction, even far beyond the putative GA. In the case of a well defined attracting structure, however, infall would be expected on the far side, as well as on the near. Detection of this 'back-side' or 'far-side' infall, is however, non-trivial. Firstly, the far-side galaxies and clusters are, of course, distant $(60 - 80\,h^{-1}\,\mathrm{Mpc})$, and consequently subject to large random distance errors. It has been noted, above, however, that such errors give rise to still more damaging systematic effects. In particular, in this context, the coupling of the large distance errors with an intrinsically non-uniform galaxy distribution produces inhomogeneous Malmquist bias (Hudson 1994). The effect is such that a *spurious* infall pattern is observed around any overdensity in galaxies, even if no *physical* infall is present. If the random distance uncertainties are large (as in the case of field samples, especially) then this effect can preclude reliable measurement of the true infall.

Infall on the far-side of the GA was not detected in the 7S survey, as a result

of their shallow sampling. In an extension to the original survey, however, Dressler & Faber (1990) expressly attempted to detect the 'S-wave' expected in the $cz - d$ diagram for infall around a localised structure. Using the $D_n - \sigma$ relation, targeting field galaxies and poor groups, they argued for a return to the Hubble line at $\sim 4500\,\mathrm{km\,s^{-1}}$, and more tentatively for far-side infall. The issue of Malmquist bias, as discussed above, cannot be ignored where individual galaxy or group distance errors are large. Hudson (1994), from a reanalysis of the 7S and Dressler & Faber data, has concluded that when corrected for the bias, there is little evidence for far-side infall.

Matthewson, Ford & Buchhorn (1992) also targeted the GA region in an extensive field TF survey. The study found no evidence for far-side infall into the GA at distances 6000–10000 $\mathrm{km\,s^{-1}}$, nor for a return to the Hubble line. The Mathewson et al. data has been recalibrated and reanalysed as part of the Mark III compilation of peculiar velocity data (Willick et al. 1997). POTENT maps of the Mark III velocity field show some evidence for a return to the Hubble line at $\sim$6000 $\mathrm{km\ s^{-1}}$, but not for the far-side inflow (eg Dekel 1997). Da Costa et al. (1996) applied a POTENT-like algorithm to a merged TF dataset drawn from work of Giovanelli and collaborators, and from the Matthewson et al. catalogue. Again, in the background of the GA, the reconstructed velocity field does not exhibit a strong infall pattern. Da Costa et al. speculate that an external influence may be causing a net flow of the GA, whose influence is correspondingly smaller than that deduced by the 7S.

The rich background supercluster (at $14000\,\mathrm{km\,s^{-1}}$), first noted by Shapley (1930), might indeed exert an additional influence on the velocity field in the HC/GA direction. The Shapley concentration was first identified in this role by Scaramella et al. (1989), who 'rediscovered' the supercluster in the distribution of Abell/ACO clusters. If Shapley were to generate a significant contribution to the velocity field in the immediate background of the GA, then the expected backside infall signal would be much reduced. Furthermore, the influence of the GA at the LG might well be over estimated. Current estimates (Quintana et al. 1995; Raychaudhury et al. 1991) from redshift samples and X-ray mass estimates suggest that Shapley may be responsible for 10–40% of the LG velocity component in that direction. The upper end of this range is consistent with Hudson's (1994) statement that a GA at $4500\,\mathrm{km\,s^{-1}}$ cannot be responsible for more than 60% of the LG motion with respect to the CMB.

1.6.3 The Lauer–Postman bulk flow

Perhaps the most dramatic result to emerge from recent studies of the peculiar velocity field is that of Lauer & Postman (1994, LP). Using the $L_m - \alpha$ relation

for the BCG of 119 Abell clusters with $cz < 15000\,\mathrm{km\,s^{-1}}$, LP find evidence for a coherent bulk flow in the sample, with amplitude $689 \pm 178\,\mathrm{km\,s^{-1}}$ directed towards $(l, b) = (343°, +52°)$. A large-amplitude coherent streaming on such a large scale is quite unexpected in current cosmological models, as shown by N-body simulations (Strauss et al., 1995) and analytic methods (Feldman & Watkins, 1994). At face value, the LP result rules out favoured variants of the Cold Dark Matter cosmology, at the $95 - 97\%$ level. Given the surprising nature of their conclusions, LP performed extensive tests for systematic errors and biases in the data, in the $L_\mathrm{m} - \alpha$ relation, and in the dipole recovery process. No effect was revealed which could give rise to a spurious dipole of the magnitude observed in the data. The dipole solution has proved robust against reanalyses by Colless (1995) and by Graham (1996). A number of authors have speculated upon possible systematic effects in the $L_\mathrm{m} - \alpha$ relation itself, such as correlations of BCG magnitude with environmental parameters. Hudson & Ebeling (1997) investigated the effect of host cluster properties, using available X-ray fluxes as a second parameter. Constructing the $L_\mathrm{X} - L_\mathrm{m} - \alpha$ relation for a subset of 64 LP clusters, the dipole amplitude and its significance are both reduced relative to the $L_\mathrm{m} - \alpha$ solution. Indeed, the bulk motion is consistent with zero, but also with the LP solution.

Independent measurements of the flow on such large scales have been slow to appear, due to the intrinsic scatter of current distance indicators, and the huge volume which must be sampled. An early challenge to the LP conclusions arose from the use of type Ia supernovae as distance indicators. Whilst SN Ia are rare events, and the sample size consequently small, their magnitude at maximum light has a dispersion of only ~ 0.02 magnitudes, when corrected for initial decline rate (Phillips 1993). Riess, Press & Kirshner (1995) applied this distance indicator to sample of 13 SN Ia from the Calán–Tololo survey (Hamuy et al. 1993), with a median depth of $7000\,\mathrm{km\,s^{-1}}$. As a result of the small sample size, the dipole vector is not well determined, but the geometry is such as to pose useful constraints on the velocity component in the direction of the LP bulk-flow. Along this axis, the Riess et al. velocity is consistent with zero, and is inconsistent with LP at the $> 3\sigma$ level.

In a recent study, Müller (1997) applied the FP technique to a field-selected sample of ellipticals in three 'pencil beams', of median depth $\sim 9000\,\mathrm{km\,s^{-1}}$. In the fields directed close to the LP apex and antapex, no significant mean motion is detected, either with respect to the calibrating cluster (Coma), or to the third, orthogonally directed beam. Existing field and cluster TF samples also fail to detect streaming along the LP axis (Giovanelli et al. 1996), but the limited depth of the data precludes a direct comparison with the BCG results. A TF survey of a more distant sample of clusters is

currently underway (Dale et al. 1997, 1998).

In addition to the above programmes, Lauer, Postman and Strauss are currently extending the BCG sample to 24000 km s^{-1} depth, and collecting central velocity dispersions for the ~500 BCG in an attempt to reduce the scatter in the $L_{\rm m} - \alpha$ relation (Strauss 1997).

In conclusion, independent investigations have conflicted with the bulk-flow vector as determined by LP. However, no such test has so far provided a compelling explanation of the *cause* of the BCG dipole, if it is indeed a spurious result. Further, since other studies to date lack the precision, depth or sky-coverage to constrain dipole solutions on these scales, it must be concluded that there there is not yet a reliable measurement of the streaming motion on scales $\sim 200\,h^{-1}$ Mpc.

1.7 Scope of thesis

This thesis reports upon the present status of the 'Streaming Motions of Abell Clusters' (SMAC) project, initiated in 1994. In brief, this is an all-sky, Fundamental Plane survey of streaming motions to a depth of $120\,h^{-1}$ Mpc, with a sample of 56 rich clusters. Substantial new data has been gathered, and combined with literature samples, resulting in a homogeneous catalogue of spectroscopic and photometric data. In the context of the three outstanding problems outlined above, the strengths of the survey are:

1. The cluster sample has excellent sky coverage, as is necessary for unambiguous recovery of a bulk-flow signal. The Fundamental Plane distance indicator is sufficiently precise that bulk-flow errors of < 200 km s^{-1} can be achieved. Since the sample is largely based upon the same Abell clusters studied by Lauer & Postman (1994), SMAC offers a further independent test of their reported bulk motion, based upon a precise, well understood distance indicator.

2. The PP supercluster is well sampled by SMAC, and can be properly zero-pointed with respect to the all-sky sample. The programme can therefore address the problem of the PP bulk motion.

3. The cluster sample contains a number of clusters in the Hydra–Centaurus region and in its background. Moreover, the small random errors, and consequently small Malmquist biases make the SMAC survey able to detect reliably the infall into the GA and other superclusters.

This thesis is organized as follows: The objectives of the project are outlined in Chapter 2, which also presents the survey strategy and sample selection criteria. Chapter 3 describes the collection and reduction of new spectroscopic data for the programme. Chapter 4 treats the new photometric observations and data reduction techniques. The new spectroscopic and photometric measurements are merged with existing datasets in Chapter 5, which closes with presentation of the fully corrected datasets in a form suitable for use in velocity field applications. In Chapter 6, the Fundamental Plane is constructed, and cluster distances estimated and compared with previous results. Analysis of the peculiar velocity field is reserved for Chapter 7, which discusses bulk motions, RMS cluster velocities and other statistics. Finally, in Chapter 8, the conclusions of this work are presented and discussed, with reference to potential extensions to the project.

References

Aaronson M. et al. 1989,, ApJ 258,64

Abell G. O. 1958, ApJS, 3, 211

Abell G. O., Corwin H. G., Olowin R. P. 1989, ApJS, 70, 1

Baker J. E., Davis M. Strauss M. A., Lahav O., Santiago B. X. 1998, ApJ, 508, 6

Bertschinger E., Dekel A. 1989, ApJ, 336, L5

Böhringer H., Neumann D. M., Schindler S., Kraan-Korteweg R. C. 1996, ApJ, 467, 168

Branchini E., Plionis M. 1996, ApJ, 460, 569

Branchini E. et al. 1998 reported at the ESO/MPA Cosmology Conference "Evolution of Large Scale Structure".

Chincarini G., Rood H. J. 1979, ApJ, 230, 648

Colless M. M. 1995, AJ, 109, 1937

Courteau S., Faber S. M., Dressler A., Willick J. A., 1993, ApJ, 412, 51L

Dale D. A., Giovanelli R., Haynes M. P., Scodeggio, M., Hardy E., Campusano, L. E. 1997, AJ, 114, 455

Dale D. A., Giovanelli R. Haynes M. P., Scodeggio M., Hardy E., Campusano L. E. 1998, AJ, 115, 418

Davis M., Peebles P. J. E. 1983, ARA&A, 21, 109

da Costa L. N., Freudling W., Wegner G., Giovanelli R., Haynes M. P., Salzer J. J., 1996, ApJ, 468, L5

de Lapparent V., Geller M. J., Huchra J. P. 1986, ApJ, 302, L1

Dekel A. 1997 in *Galaxy Scaling Relations: Origins, Evolution and Applications*, eds da Costa L.N., Renzini A. p. 245

Dekel A., Bertschinger E., Yahil A., Strauss M. A., Davis M., Huchra J. P. 1993, ApJ, 402, 42

Djorgovski S., Davis M. 1987, ApJ, 313, 59

Dressler A. 1988, ApJ, 329, 519

Dressler A., Faber S. M. 1990, ApJ, 354, 13

Dressler A., Faber S. M., Burstein D., Davies R. L., Lynden-Bell D., Terlevich R. J., Wegner G. 1987a, ApJ, 313, L37

Dressler A., Lynden-Bell D., Burstein D., Davies R. L., Faber S. M., Terlevich R. J., Wegner G. 1987b, ApJ, 313, 42

Faber S. M., Jackson R. E. 1976, ApJ, 204, 668

Fisher K. B., Lahav O., Hoffman Y., Lynden-Bell D., Zaroubi S. 1995a, 272, 885

Fisher K. B., Huchra J. P., Strauss M. A., Yahil A., Schlegel D. J. 1995b, ApJS, 100, 69

Feldman H. A., Watkins R. 1994, ApJ, 430, L17

Giovanelli R., Haynes M. P., Wegner G., da Costa L. N., Freudling W., Salzer J. J. 1996, ApJ, 464, L99

Giovanelli R., Haynes M. P., Herter T., Vogt N. P., Wegner G., Salzer J. J., da Costa L. N., Freudling W., 1997, AJ, 113, 22

Graham A. W. 1996, ApJ, 452, 27

Hamuy M. et al. 1993, AJ, 106, 2392

Han M., Mould J. R., 1992, ApJ, 396, 453

Hoessel J. G. 1980, ApJ, 241, 493

Hubble E. P. 1927, Proc. Nat. Acad. Sci. 15, 168

Hudson M. J. 1993, MNRAS, 265, 43

Hudson M. J. 1994, MNRAS, 266, 468

Hudson M. J., Ebeling H. 1997, ApJ, 479, 621

Hudson, M. J., Lucey J. R., Smith R. J., Steel J. 1997, MNRAS, 291, 488

Kolatt T., Dekel A., Lahav O. 1995, MNRAS, 275, 797

Kraan-Korteweg R. C., Woudt P. A., Cayatte V., Fairall A. P., Balkowski C., Henning P.A. 1996, Nature, 379, 519

Lauer T. R., Postman M. 1994, ApJ, 425, 418 (LP)

Lilje P. B., Yahil A., Jones B. J. T. 1986, ApJ, 307, 91

Lucey J. R., Carter D. 1988, MNRAS, 235, 1177

Lucey J. R., Lahav O., Lynden-Bell D., Terlevich R. J., Infante, L., Melnick J. 1999, in preparation

Lynden-Bell D., Faber S. M., Burstein D., Davies R. L., Dressler A., Terlevich R. J., Wegner G., 1988, ApJ, 326, 19

Nusser A., Davis M. 1994, ApJ, 421, L1

Matthewson D. S., Ford V. L., Buchhorn M. 1992, ApJ, 389, L5

Mould J. R., Staveley-Smith L., Schommer R. A., Bothun G. D., Hall P. J., Han M., Huchra J. P., Roth J., Walsh W., Wright A. E. 1991, ApJ, 383, 467

Müller K. R. 1997, PhD Thesis, Dartmouth College

Peebles P. J. E. 1980 *The Large-Scale Structure of the Universe* (Princeton: Princeton Univ. Press)

Peebles P. J. E. 1993 *Principles of Physical Cosmology* (Princeton: Princeton Univ. Press)

Phillips M. M. 1993, ApJ, 413, L105

Postman M., Lauer T. R. 1995, ApJ, 440, 28

Quintana H., Ramirez A., Melnick J., Raychaudhury S., Slezak E. 1995, AJ, 110, 463

Raychaudhury S., Fabian A. C., Edge A. C., Jones C., Forman W. 1991, MNRAS, 248, 101

Riess A. G., Press W. H., Kirshner R. P. 1995, ApJ, 445, L91

Rowan-Robinson M. et al. 1990, MNRAS, 247, 1

Rubin V. C.., Thonnard N., Ford W. K., Roberts M. S 1976, AJ, 81, 719

Scaramella R., Baiesi-Pillastrini G., Chincarini G., Vettolani G., Zamorani G. 1989, Nature, 338, 562

Shapley H. 1930 Bull. Harvard Obs. 874, 9

Shaya E. J. 1984, ApJ, 280, 470

Smoot G. F., Gorenstein M. V., Muller R. A. 1977, Phys. Rev. Lett., 39, 898

Strauss M. A., 1997, in *Critical Dialogues in Cosmology*, ed. Turok, N.

Strauss M. A., Willick J. A. 1995, Phys. Rep., 261, 271

Strauss M. A., Cen R., Ostriker J. P., Lauer T. R., Postman M. 1995, ApJ, 444, 507

Tammann G. A., Sandage A. 1985, ApJ, 294, 81

Tully R. B., Fisher J. R. 1977, A&A, 54, 661

Willick J. A., 1990, ApJ, 351, L45

Willick J. A., 1991, PhD thesis, University of California, Berkeley

Willick J. A., Strauss M. A. 1998, preprint, astro-ph/9801307

Willick J. A., Courteau S., Faber S. M., Burstein D., Dekel A., Strauss M. A. 1997a, ApJS, 109, 333

Willick J. A., Strauss M. A., Dekel A., Kollat T. 1997, ApJ, 486, 629

Yahil A., Strauss M. A., Davis M., Huchra J. P. 1991, ApJ, 372, 380

Chapter 2

Project description and sample selection

2.1 Introduction

The first part of this short chapter presents a concise statement of the objectives of the SMAC project and provides arguments relevant to the survey strategy adopted. Thereafter, elements of the sample selection are discussed — specifically, the selection of clusters to form the basis of the SMAC sample, and the selection of galaxies for observation in previously unstudied clusters.

2.2 The SMAC project – motivations and strategy

This thesis describes the "Streaming Motions of Abell Clusters" (SMAC) project: a Fundamental Plane (FP) survey of cluster peculiar motions to $\sim 120\,h^{-1}$Mpc, which was conceived in 1994 to provide an extended sampling of the local velocity field to depths comparable to those probed by Lauer & Postman (1994, LP). In the following sections, the aims of the programme are summarized, and referred to in justifying aspects of the survey strategy adopted.

2.2.1 Objectives

The principal objectives of the SMAC project are:

1. To provide a direct and independent measurement of the bulk motion on very large scales ($120h^{-1}$Mpc depth), using a precise, well understood distance indicator.

2. To yield a reliable map of the peculiar velocity field to this depth, sampling a number of prominent supercluster regions.

3. To provide peculiar velocity estimates with sufficient precision for determination of the cosmological density parameter through comparison with predictions from all-sky redshift surveys.

4. To measure statistics related to the large-scale mass power spectrum (eg the rms peculiar velocity) in order to constrain the range of viable cosmological models.

2.2.2 Survey strategy

The objectives stated above guide the choice of strategies for the SMAC survey, in the following manner:

1. All four objectives suggest the use of rich clusters as tracers of the velocity field, rather than field-selected galaxies. Objectives 1 and 2 require us to sample much larger depths than is possible with a dense sample of individual galaxies. Furthermore, the objectives require that distance errors per object should be smaller than 10%, in order to to provide velocity errors no more than twice the typical signal. Small random errors also allow Malmquist biases to be minimised — a requirement essential for meeting objective 3.

2. Objective 1 requires that the cluster sample have good sky coverage, to allow unambiguous recovery of the dipole (bulk-flow) component of the velocity field. Furthermore, the sample should be deep enough to probe the volume from which the LP dipole signal is contributed. Ideally, the sample should be based upon the same clusters as the LP study.

3. The FP distance indicator is the technique of choice for use in clusters, whose cores are dominated by early-type galaxies. The FP provides distance estimates to a precision of $\sim$20% per galaxy observed.

4. The $120h^{-1}$Mpc depth and wide sky-coverage required by Objective 1 requires a study of $\sim$50 clusters (based on the Abell catalogue). The substantial observational demands of such a survey can be reduced by making use of FP data from previously published cluster studies. In combining data from disparate sources, however, extreme care must be taken to ensure the uniformity of the merged catalogue.

5. Published data is currently available for only a fraction of the rich clusters within $100\,h^{-1}$Mpc. Accordingly, new observations are required in order to probe a larger sample of clusters, and also to tie together the various sources sources of data.

2.3 The cluster sample

The LP study targeted Brightest Cluster Galaxies (BCG) in a sample of 119 Abell/ACO clusters with $cz < 15000$ km s^{-1}, this large sample size being rendered practical by relatively modest observational demands of the BCG technique. By contrast, use of the FP method requires complementary imaging data and dispersion-quality spectra, for many galaxies per cluster. Consequently, the SMAC sample has been chosen to be shallower than that of LP, with a nominal limiting depth of 12000 km s^{-1}. Figure 13 of LP demonstrates that the BCG dipole solution is unchanged when their sample is reduced to this limiting redshift. Thus, if the LP dipole is indeed the result of a large-scale bulk flow, then this flow would be detected in the SMAC survey.

To $cz = 12000$ km s^{-1}, there are 65 Abell clusters in the LP sample, and these form the basis of the SMAC cluster sample. Sixteen of these clusters have been the target of previous FP studies by Lucey and collaborators (Lucey & Carter 1988; Lucey et al. 1991, 1993, 1997, 1999; Hudson et al. 1997), by Jørgensen, Franx & Kjærgaard (1996) or by the 7S (Faber et al. 1989). For these 16 clusters, data is drawn principally from the above studies, supplemented by some newly obtained measurements. A further 13 clusters form part of the EFAR sample of Wegner et al. (1996). For these clusters, EFAR data is awaited, although some data was collected during SMAC observing runs. The remaining 36 clusters are those for which new observations have been obtained, as part of the SMAC programme.

While the above discussion represents the sample chosen for the SMAC project in 1994, the final cluster sample employed in the analysis chapters of this thesis is substantially different, for a variety of reasons. While a full description of the final SMAC cluster sample will be presented in Section 5.4, the principal differences with respect to the 'LP within 12000 km s^{-1}' sample are:

1. For 16 of the newly-targeted clusters, data was gathered for fewer than four member galaxies with E/S0 morphologies, and are consequently cut from of the final sample. In some of these cases, many galaxies were observed, but were discovered to be in the foreground or background of the cluster, or to have unsuitable morphologies or other peculiarities. In other cases failed observations or poor weather were to blame. In addition to these 'drop-outs' clusters, nine of the EFAR overlap clusters have insufficient data at present. Section 5.4.2 details the 'drop-out' clusters, case-by-case.

2. A number of clusters which were excluded from the LP sample have previously been the target of FP studies. Since these clusters provide further tracers of the

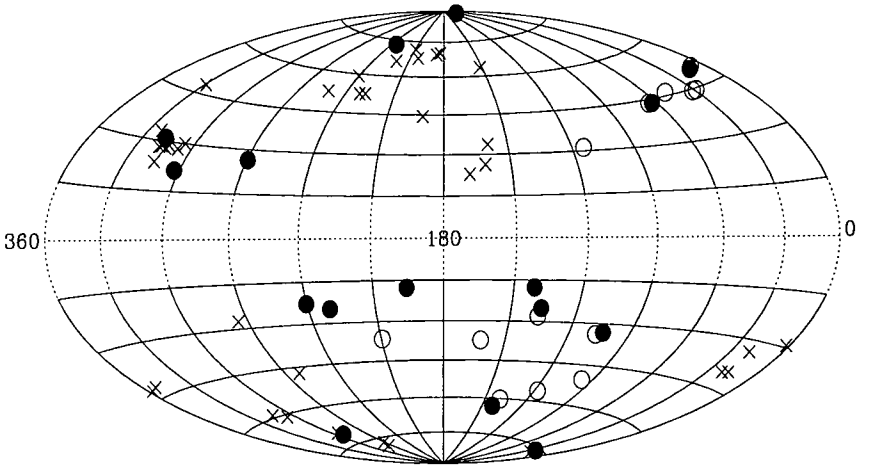

Figure 2.1: Distribution of LP clusters with $cz_{\odot} < 12000\,\mathrm{km\ s^{-1}}$, shown in galactic coordinates. Filled symbols indicate clusters for which data will be drawn primarily from published studies. Crosses mark clusters for which new observations were made for the SMAC project. Clusters marked by open circles are those observed only by EFAR.

peculiar velocity field, they have been included into the SMAC sample where the published data is of high-quality. The sources of these 'extra' clusters are reported case-by-case in Section 5.4.3.

The excellent sky-coverage of the sample is demonstrated by Figure 2.1.

2.4 Selection of target galaxies

As discussed above, the SMAC project aimed, from its inception, to incorporate data from literature sources together with new observations, to form a homogeneous merged catalogue of FP data. Within such a context, it is impossible to aim towards a clearly defined set of galaxy selection criteria, since the various published studies are already subject to widely disparate selection schemes. No attempt has therefore been made to enforce strictly uniform selection criteria for galaxies in newly-targeted clusters.

In the clusters where new observations have been conducted, candidates were generally selected by visual inspection of Schmidt sky-survey plates, guided by position

and magnitude measurements from APM scans (see Irwin & McMahon 1992). Early-type galaxies lying within one Abell radius ($R_A = 1.5h^{-1}$ Mpc) of the nominal cluster center were selected, and those within $0.5R_A$ were prioritised over those at greater projected cluster-centric distance. The APM magnitudes were adjusted for galaxies with companions or other contaminating sources. For clusters with pre-existing redshift information, galaxies were rejected as interlopers if lying outside a conservative $\pm 2000\,\mathrm{km\ s^{-1}}$ velocity range. Cross referencing of candidates with published redshift and morphological data was performed using the NASA/IPAC Extragalactic Database (NED).

Galaxies were ranked and observed by magnitude order within each cluster, from the brightest selected member to the faintest. The total photographic magnitudes of targets fall approximately in the range $b_J = 14.5 - 16.8$. Typically, then, the early-type population of each cluster is sampled in a fairly complete manner by the FP observations. However, the magnitude limits vary from cluster to cluster within the survey, and for several reasons (eg failed observations, preferential observation of galaxy pairs, etc) the limits are not cleanly defined even within a cluster.

The particularly heterogeneous selection criteria employed in the SMAC project necessitate a careful choice of Fundamental Plane analysis technique, as discussed in Chapter 6.

References

Faber S. M., Wegner G., Burstein D., Davies R. L., Dressler A., Lynden-Bell D., Terlevich R. J., 1989, ApJS, 69, 763

Hudson, M. J., Lucey J. R., Smith R. J., Steel J. 1997, MNRAS, 291, 488

Irwin M., McMahon R. 1992, Gemini, 37, 1

Jørgensen I., Franx M., Kjærgaard P. 1996, MNRAS, 280, 167

Lauer T. R., Postman M. 1994, ApJ, 425, 418 (LP)

Lucey J. R., Carter D. 1988, MNRAS, 235, 1177

Lucey J. R., Guzmán R., Carter D., Terlevich R. J. 1991b, MNRAS, 253, 584

Lucey J. R., Lahav O., Lynden-Bell D., Terlevich R. J., Infante, L., Melnick J. 1993, in Large scale structures and peculiar motions in the universe, ASP conference series, vol. 15, Eds. da Costa L. N., Latham D. W., p31.

Lucey J. R., Guzmán R., Steel J., Carter D. 1997, MNRAS, 287, 899

Lucey J. R., Lahav O., Lynden-Bell D., Terlevich R. J., Infante, L., Melnick J. 1999, in preparation

Saglia R. P., Burstein D., Bertschinger E., Baggley G., Colless M. M., Davies R. L., McMahan R. K., Wegner G. 1997, MNRAS, 292, 499

Wegner G., Colless M., Baggley, G. Davies R. L., Bertschinger E., Burstein D., McMahan R. K. Jr., Saglia R. P. 1996, ApJS, 106, 1

Chapter 3

New spectroscopic data

3.1 Introduction

This chapter presents details of the acquisition and reduction of new spectroscopic data for the SMAC project. Section 3.2 describes the procedures employed on five observing runs. Section 3.3 reports upon the basic data-reduction process, and on the techniques adopted for determination of the spectroscopic parameters. The resulting measurements of central velocity dispersion, magnesium index and redshift, for 429 galaxies, are presented in Section 3.4. The scheme adopted for aperture corrections is presented in Section 3.5, and parameter comparisons between the SMAC datasets are performed in Section 3.6. This chapter does not address the combination of spectroscopic datasets, an issue which is treated fully in Chapter 5.

3.2 Observational techniques

3.2.1 Data sources

The data to be presented here were collected during three observing runs at the 3.9m Anglo-Australian Telescope (AAT) and two at the 2.5m Isaac Newton Telescope (INT), as summarized in Table 3.1.

3.2.2 INT observations

For the northern part of the SMAC sample, observations were conducted at the 2.5m Isaac Newton Telescope on La Palma. The resulting datasets are coded I95 and I97A. The Intermediate Dispersion Spectrograph was used in conjunction with the 23.5 cm camera and 900V grating. With a slit width of 3 arcsec, a resolution of $\sim$4Å FWHM was achieved, equivalent to an instrumental dispersion of 98 km s^{-1}. The spectra

Table 3.1: Sources of spectroscopic data. The aperture dimensions are the slit-width followed by the extraction width (ie along the slit), both in arcsec. The listed number of spectra is the number of velocity dispersion measurements contributed by a given system to the data presented in this paper.

Code	Dates	Telescope	Spectral Range	Aperture	N_{sp}
I97A	05–11/01/1997	2.5m INT	4785–5808Å	3.0×3.4	226
I95	20–26/02/1995	2.5m INT	4785–5808Å	3.0×3.4	140
A95B	19–21/09/1995	3.9m AAT	4800–5600Å, 4940–5740Å	3.0×3.8	106
A95A	03–06/05/1995	3.9m AAT	4800–5600Å, 4940–5740Å	3.0×3.8	134
A94	05–07/04/1994	3.9m AAT	4800–5600Å, 4940–5740Å	3.0×3.8	112

cover a wavelength range of ~1000Å, approximately centred on the Mg*b* triplet. A Tektronix CCD was used as a detector in both runs. Typical exposure times for SMAC programme galaxies were 900–1800s. Bright 'standard' galaxies required only 300–450s.

In addition to galaxy observations, several giant stars of spectral type G8–K3 were observed in each run. Stars of these types dominate the spectra of early-type galaxies within the observed wavelength range, and serve as 'templates' for the radial velocity and velocity dispersion measurements. The template stars were trailed across the slit at a shallow angle during the exposure. By this technique, the instrumental dispersion of the spectrograph can be determined, and used to construct a 'mock' template spectrum which includes the extended source effects relevant for the galaxy observations.

The spectrum of a copper-argon arc lamp was observed to provide wavelength calibration. Arc-lamp exposures were taken regularly in the course of the observations, and always after moving the telescope from one cluster or region to another. This allows the calibration to track any mechanical flexure in the telescope and spectrograph system.

In each observing run, spectrophotometric standard stars were observed to provide the flux calibration necessary for the measurement of line-strength indices.

3.2.3 AAT observations

For clusters in the southern hemisphere, spectroscopic observations were obtained at the 3.9m Anglo-Australian Telescope at Siding Spring, NSW. The three AAT observing runs are coded A94, A95A and A95B. The RGO spectrograph was used with a slit width of 3 arcsec, and again a Tektronix CCD detector was employed.

At the AAT, a $900\,\mathrm{lines\,mm^{-1}}$ grating was not available: 1200V grating was instead used, in conjunction with the 25 cm camera. This grating yields spectra of

higher resolution (2.3Å FWHM, equivalent to 56 km s^{-1} instrumental dispersion), but the detector size limits the observable wavelength range to ~800Å. To ensure that the recorded spectra included the Mg*b* triplet, and other strong features, observations were conducted at one of two different grating positions, dependent on the redshift of the target. Standard stars, and galaxies in clusters with nominal recession velocities smaller than 7000 km s^{-1} were observed over the wavelength range 4800–5600Å. For target clusters at larger *cz*, the spectral range was 4940–5740Å. Sufficient signal-to-noise ratios were reached with typical exposure times of 600–1200s for programme galaxies.

Template stars were observed as in the INT runs. Wavelength calibration was achieved by observing arc-lamp spectra over both wavelength ranges. Similarly, flux-standards should have been observed at both grating angles on all runs, to correct for the instrumental response function over the entire spectral range of the observations. In practice, however, flux-standard observations were not obtained for the high-*cz* grating setting, in either the A95A or A95B runs. For these runs, indirect flux-calibration schemes were adopted, as described below.

3.2.4 Overlap and repeat observations

Systematic offsets of ~5% in σ have been detected, between different spectroscopic datasets, by authors attempting to construct merged catalogues of velocity dispersion data (Davies et al. 1987; McElroy 1995; Smith et al. 1997). For clusters at the limiting depth of the SMAC sample, even a 1% systematic offset between northern and southern hemisphere σ measurements would result in a systematic distance error of $\sim 170\,\mathrm{km\,s^{-1}}$. It is clear then, that corrections for these offsets must be obtained, with precision of ~2% or better, if peculiar velocity signals are to be reliably recovered. Accurate corrections can be obtained only by intercomparison of numerous measurements for galaxies in common between datasets.

In order to obtain the required overlap in the SMAC project, approximately one third of all observing time in the five runs was devoted to overlap observations. Bright standard galaxies were observed many times. In addition, galaxies in equatorially located programme clusters were typically observed from both the INT and the AAT. Extensive overlap was secured with external datasets, to facilitate matching of spectroscopic systems as described in Section 5.2. In particular, certain specific datasets were targeted, such as the extensive LICK system of Davies et al. (1987), the high signal-to-noise data of González (1993), and the southern FOCAP data of Lucey & Carter (1988) and Lucey et al. (1999). A combined catalogue incorporating the extensive EFAR database (Wegner et al. 1996) is a long-term objective of the SMAC project. With this in mind,

additional overlap galaxies were selected from EFAR candidate lists, to improve the linkage between the samples.

Repeated observations were obtained for many nearby 'standard' galaxies and also for a subset of programme galaxies. These repeat observations help to suppress random errors, and are used in Section 3.4 to determine internal errors from the observed scatter.

3.3 Data reduction

Data reduction techniques were similar for all five of the new SMAC datasets, which can accordingly be treated here simultaneously. The spectroscopic reduction was performed using standard and customized routines within Starlink's 'Figaro' environment.

3.3.1 Basic reductions

Initial reduction of the CCD frames involved bias and dark current subtraction, the removal of pixel-to-pixel sensitivity variations (using flat field exposures provided by a tungsten calibration lamp) and correction for vignetting along the slit (using twilight sky-line exposures).

Wavelength calibration was performed using the arc–lamp exposures described above. A cubic fit between pixel number and wavelength for ~20 arc lines gave a maximum rms calibration error of ~0.1Å.

The rotation of the CCD with respect to the spectrograph axes was small in most cases and, where necessary, corrected by tracing the spectrum with a low-order polynomial. Spectra were extracted from the frames by simple co-addition of the central five pixels of the galaxy image, resulting in the aperture dimensions given in Table 5.1. Given the pixel-scale of the instrumentation, this choice ensures that the extraction aperture is approximately square, so that its orientation with respect to the galaxy's major axis is unimportant. The darkest rows on the frame were median-filtered to remove cosmic-ray events, and the resulting sky spectrum was subtracted from the extracted spectrum.

Cosmic ray events in the galaxy spectra were removed by a combination of automatic procedures before extraction, and interactive methods applied at the one-dimensional spectrum stage. Features in the spectrum resulting from noise in the subtraction of sky–line features (especially at 5577Å) were similarly removed after extraction.

A few spectra of extremely poor quality were flagged by eye and removed from the datasets prior to any further analysis. In the majority of cases, these were spectra obtained from exposures in poor weather, or spectra of faint companion objects observed on the same slit as a target.

3.3.2 Signal-to-noise ratios

The signal-to-noise ratio per Ångstrom (S/N) has been determined for each of the extracted spectra. Histograms of S/N are presented in Figure 3.1. Before computing statistics of the S/N distribution, spectra of galaxies with $cz < 3000\,\mathrm{km\ s^{-1}}$ are excluded from consideration, thus removing high-S/N standard galaxy observations.

From 561 spectra remaining, the SMAC spectra have a mean S/N of 30, and over 95% of the spectra have $S/N > 14$. Only one spectrum has $S/N < 10$ (this spectrum is for galaxy A1016:SMC-A, for which two further spectra were obtained, with $S/N \sim 20$). The AAT spectra exhibit higher S/N than those from the INT runs.

3.3.3 Velocity dispersion and radial velocity measurements

Central velocity dispersions, σ were measured by use of the well-known Fourier Quotient method of Sargent et al. (1977). In the simplest approximation, the galaxy spectrum $G(n)$ can be considered as the convolution of a representative stellar spectrum $S(n)$, with an appropriate broadening function $B(n)$. Here G, S and B are defined in velocity space, over channels n. The convolution,

$$G(n) = S(n) \star B(n)\,, \tag{3.1}$$

in velocity space becomes, in 'velocity-frequency space', the Fourier transform product

$$\tilde{G}(s) = \tilde{S}(s).\tilde{B}(s)\,, \tag{3.2}$$

where s is the velocity-frequency variable. Assuming a functional form — in practice a Gaussian — for $\tilde{B}$, we fit the observable quotient

$$\tilde{B}(s) = \frac{\tilde{G}(s)}{\tilde{S}(s)} \tag{3.3}$$

and compute its anti-transform to yield the broadening width.

In order for the recovered width to represent only the intrinsic velocity broadening of the galaxy spectrum, it is necessary to ensure that the stellar spectrum has been subject to the same instrumental resolution effects as the galaxy spectrum. In particular, since light from the target galaxy fills the slit, light from the template star should

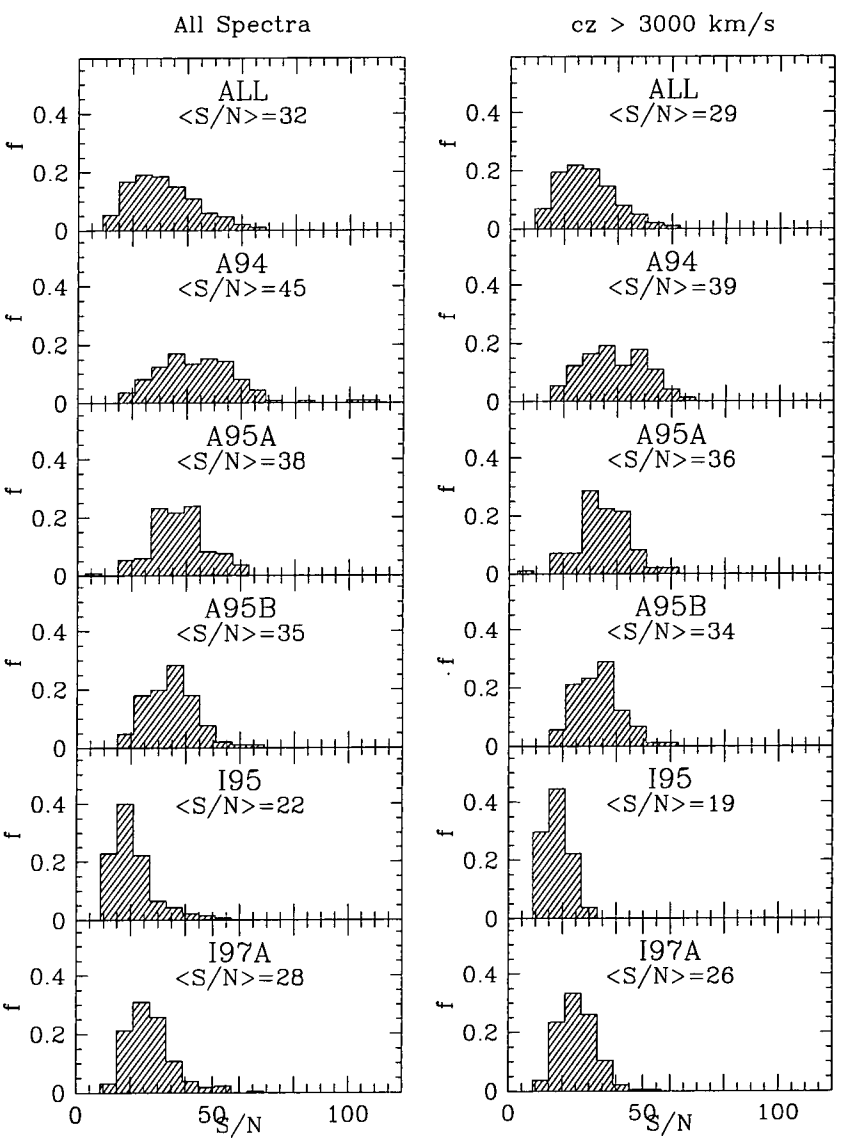

Figure 3.1: Distribution of signal-to-noise ratio per Ångstrom (S/N) for the SMAC spectra. The top-left panel shows S/N for all 718 spectra reported here. Other panels on the left-hand side show individual histograms for the five datasets. In the right-hand panels, S/N for 561 spectra yielding $cz_{\odot} > 3000$ km s^{-1} are similarly displayed. These latter panels are more representative of the typical S/N for observations of programme galaxies.

also do so. By trailing the star at a shallow angle, the form of the instrumental broadening across the slit — the 'instrumental rotation curve' — can be directly observed. Subsequently, the spectrum of a 'galaxy' with zero intrinsic velocity dispersion can be simulated by shifting and co-adding the stellar spectrum, with the shifts determined by the instrumental rotation curve, and the coaddition weights chosen to match the profile, across the slit, of a typical programme galaxy. It is this spectrum, in practice, which is adopted for $S(n)$ above.

Prior to computing $\tilde{G}$ and $\tilde{S}$, continuum fits were subtracted from both the template spectrum and the galaxy spectrum, and modulated by a cosine bell function to fix the ends of the spectrum to zero. The latter step is necessary to avoid unphysical signals appearing at all frequencies in the Fourier transforms.

The spectra require filtering in Fourier-space, to remove signals arising from from noise, inadequate continuum removal and the application of the cosine bell. A cut is made at high (velocity-) frequencies, to suppress channel-to-channel noise. The resulting σ values are fairly insensitive to the exact value, $k_{\rm high}$, chosen for the high frequency cut. $k_{\rm high} = 200 \sim (5\text{Å})^{-1}$ has been used throughout. At low-frequencies, a filter must be applied to remove residual continuum features, and the effects of the cosine-bell modulation function described above. For the case of the low-frequency cut, results are found to exhibit a clear trend : velocity dispersions are measured to be smaller when $k_{\rm low}$ is larger. The cutoff frequency must therefore be chosen with care. It is required that the low-frequency filter should remove the signal arising from the cosine bell modulation, whilst preserving intrinsic features in spectra of velocity dispersion ≤ 500 km s^{-1}. For the INT spectra, these constraints leave a range of $k_{\rm low} = 6 - 9$, while for the AAT spectra, with their smaller wavelength coverage, the range is $k_{\rm low} = 6 - 7$. The portion of the $\sigma - k_{\rm low}$ plot between these limits is flat to $\sim$5% for most galaxies.

After discarding a few stellar template spectra which gave consistently discrepant results, the velocity dispersions obtained from each galaxy spectrum were averaged over all available template spectra from the run (typically $\sim$15 spectra of $\sim$10 different stars), and over the appropriate range of $k_{\rm low}$ for the low frequency filter.

Recession velocities, cz, were obtained simultaneously with velocity dispersions, as a result of the Fourier Quotient fit.

3.3.4 Flux calibration

In order to measure line strength indices from the spectra, it is necessary to calibrate out the variation of instrumental response as a function of wavelength. To this end, spectra of spectrophotometric standard stars ('flux standards') were obtained

in each observing run. The flux calibration process needs only to remove curvature from the spectral response function, since line-indices are defined with reference to two pseudo-continuum bands bracketing the feature of interest.

Ideally, flux standards have fairly smooth spectra over the spectral range, and are densely sampled by the calibration data. In practice, this ideal is not realised, since even white dwarf stars often have a strong $H\beta$ absorption feature in the wavelength range sampled here, and since the calibration data typically sample the spectrum in 50–150Å intervals. The rapidly varying, but sparsely sampled, calibration data introduce uncertainties into the response function, which translate into redshift-dependent systematic errors in line indices. The Mg_2 index is particularly sensitive to this effect, since the continuum bands are widely separated. Comparison between different flux-standards indicates that these uncertainties are of order 0.01 mag for Mg_2.

For the AAT runs, as noted above, two spectral ranges were employed in the galaxy observations. In the A95A and A95B datasets, however, no flux standards were observed over the range used for $cz > 7000$ km s^{-1} targets. For A95A, an indirect calibration scheme was adopted, using a star observed at the longer wavelength range in both A94 and A95A. The relative response was measured and combined with the A94 calibration curve. For A95B, no observation was obtained in common with A94. In this case, by necessity, we adopt the calibration function from an earlier run. In fact the original A94 curve is adopted, since use of the (indirectly obtained) A95A calibration results in a larger scatter.

3.3.5 Mg_2 index measurements

The measurement of Mg line strength indices has become a standard practice in FP applications, where they have been used to limit spurious peculiar motions arising from stellar-population differences, or have been included with the FP in a generalised distance indicator (Guzmán & Lucey 1992, Jørgensen et al. 1996, Hudson et al. 1997). The Lick system Mg_2 index (Burstein et al. 1984) has been the most widely employed line-strength definition for this purpose, although the alternative Mgb index has been favoured by recent studies (Baggley 1996; Müller 1997).

Since a substantial portion of the completed SMAC catalogue will be drawn from literature sources, Mg_2 will remain the most suitable index for these purposes, since Mg_2 measurements exist for nearly all of the external sources. From a flux-calibrated spectrum, Mg_2 can in principle be measured as the quantity of absorbed flux in the line band, with respect to a linear interpolation between the two side bands. The definition of

Table 3.2: Magnesium index definitions. The definitions of Mg_2 and Mgb are those of Burstein et al. (1984). Mgb' represents the Mgb index expressed in magnitudes of absorbed flux, for consistency with Mg_2.

Index	continuum bandpasses	central bandpass	unit
Mg_2	4895.125–4957.625 5301.125–5366.125	5154.125–5196.625	mag
Mgb	5142.625–5161.375 5191.375–5206.375	5160.125–5192.625	Å
Mgb'	5142.625–5161.375 5191.375–5206.375	5160.125–5192.625	mag

the Mg_2 index, from the Lick system of Burstein et al. (1984), is given in Table 3.2[1]. The large separation of the Mg_2 continuum bands allows this index to be measured without correction for velocity broadening effects.

Poisson uncertainties in the Mg_2 index were calculated from the S/N ratio of the input spectrum, together with the noise characteristics of the CCDs employed.

3.3.6 The Mgb index

While many studies (Guzmán & Lucey 1992; Jørgensen et al. 1996; Hudson et al. 1997) have made use of the Mg_2 index described above, more recent works (Baggley 1996; Müller 1997) have suggested that measurements of the Mg_2 index may be compromised as a result of its widely separated continuum bands. Unless a very densely-sampled flux-calibration curve is available, curvature in the instrumental response between the side-bands will introduce redshift-dependent systematic errors into Mg_2 measurements. In addition, the central passband of Mg_2 lies within a broadband molecular feature, MgH. Since the contribution from the molecular absorption exhibits a radial dependance quite different from that of Mg_2, further systematic effects are introduced, again redshift-dependent. The magnitude of these effects is ~ 0.01 mag., comparable to the random errors in Mg_2 but the redshift dependance leads to the danger of coherent shifts in magnesium index, from cluster to cluster, when Mg_2 is used.

By contrast, the Mgb index has narrowly-spaced continuum bands, well inside the MgH feature. This removes much of the sensitivity to the flux calibration (the response function of the system is typically fairly linear with wavelength over the small

[1]Note that while the Lick definitions are adopted for the line-indices, the SMAC spectra *are* flux calibrated, and are *not* broadened to match the instrumental resolution of the Lick/IDS spectrograph.

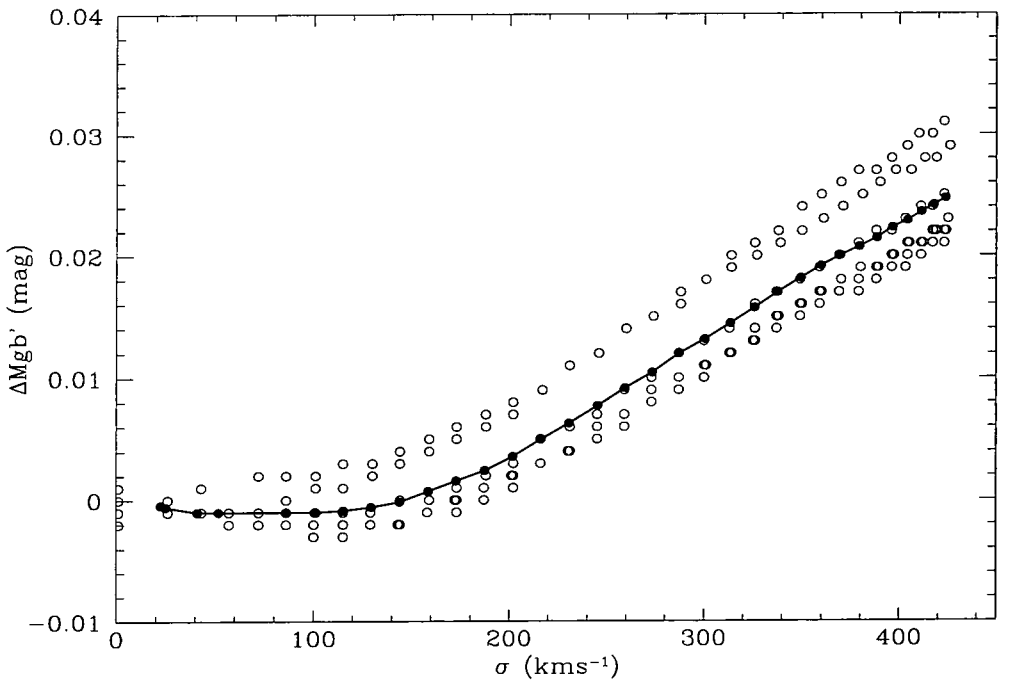

Figure 3.2: Velocity dispersion correction to the Mgb index for the I97A dataset. The corrections are derived from simulations using nine stellar spectra (open points). The mean correction (given by the filled points) is adopted in the derivation of line strengths.

range spanned by the continuum bands), suppressing the redshift-dependent systematic errors to a negligible level.

For the five new datasets discussed here, the Mgb index is, for completeness, measured in addition to Mg_2. Eventually it is possible that Mgb might be measured for earlier datasets, to improve the available sample.

Note that while Mg_2 is a molecular feature, customarily quoted in magnitudes of absorbed flux, the Mgb index, as an atomic feature, is by convention expressed as an equivalent width in angstroms. Since both Mg_2 and Mgb will be referred to in what follows, it is convenient to define the quantity[2]

$$\mathrm{Mg}\, b' = -2.5 \log(1 - \mathrm{Mg}b/32.5)\,. \tag{3.4}$$

As for the Mgb' of Baggley (1996), and the [Mgb] of Müller (1997), the above definition is of the Mgb line-strength expressed in magnitudes of absorbed flux, by analogy with Mg_2.

For the Mgb index, the continuum bands are so close to the index bandpass that velocity-broadening of the Mg lines affects the measured flux in the continuum, causing a σ-dependent underestimate of the line-strength. This effect is circumvented

[2]The factor of 32.5 here is the width, in Angstroms, of the Mgb line band.

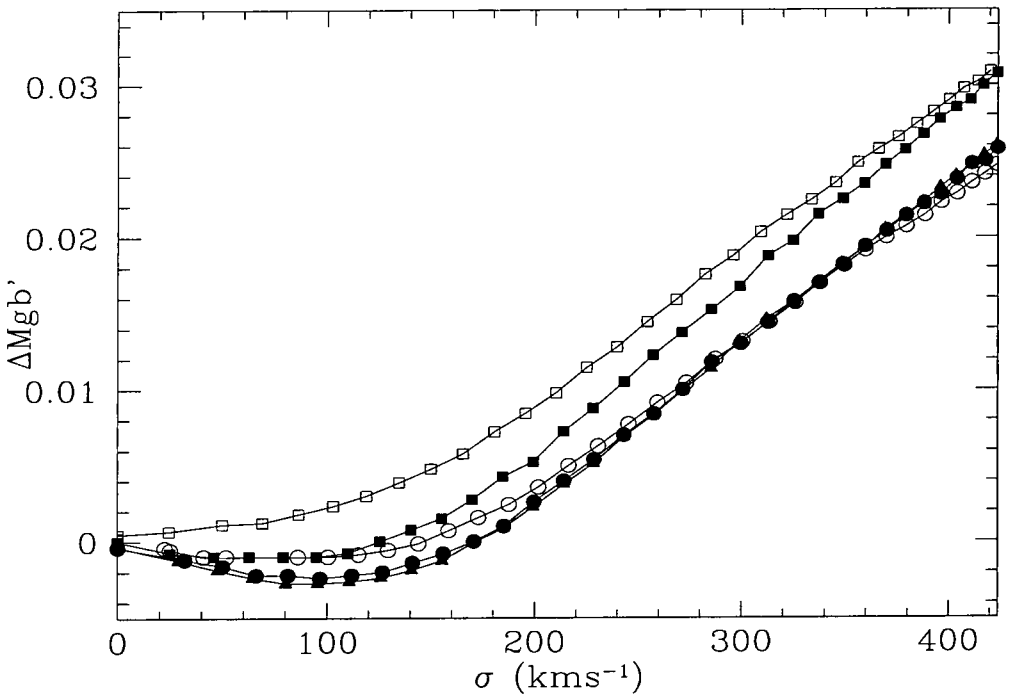

Figure 3.3: Velocity dispersion correction curves for Mg*b* index measurement from the five SMAC datasets. Filled symbols indicate AAT runs (squares – A94; triangles – A95A; circles – A95B) and open symbols INT runs (squares – I95; circles – I97A).

by constructing an empirical correction curve, based upon the Mg*b* values recovered from artificially smoothed stellar spectra. The stars used are the same G8–K3 giants used for the velocity dispersion templates. The use of the Mg*b* index was not anticipated when the observations were made. As a result, the observed template stars do not span so large a range in Mg*b* as do the galaxies – the stars have Mg*b* $\sim$ 0.1, whereas for the galaxies, Mg*b* = 0.1 – 0.2. While there appears to be a weak trend, such that smaller velocity dispersion corrections are derived from some stars which have very low Mg*b*, the effect is small enough to be neglected for present purposes. The form of the correction is shown in Figure 3.3, which reveals also that the corrections are reasonably consistent between runs, with a spread of 0.006 mag. For comparison, the typical random errors on Mg*b* are 0.010 mag.

3.4 Results and internal comparisons

Table A.1 presents spectroscopic parameters derived from the 718 spectra obtained and reduced for the SMAC project.

For a number of galaxies, multiple observations were obtained within each observing run. Such repeat observations were made not only for bright 'standard' galaxies,

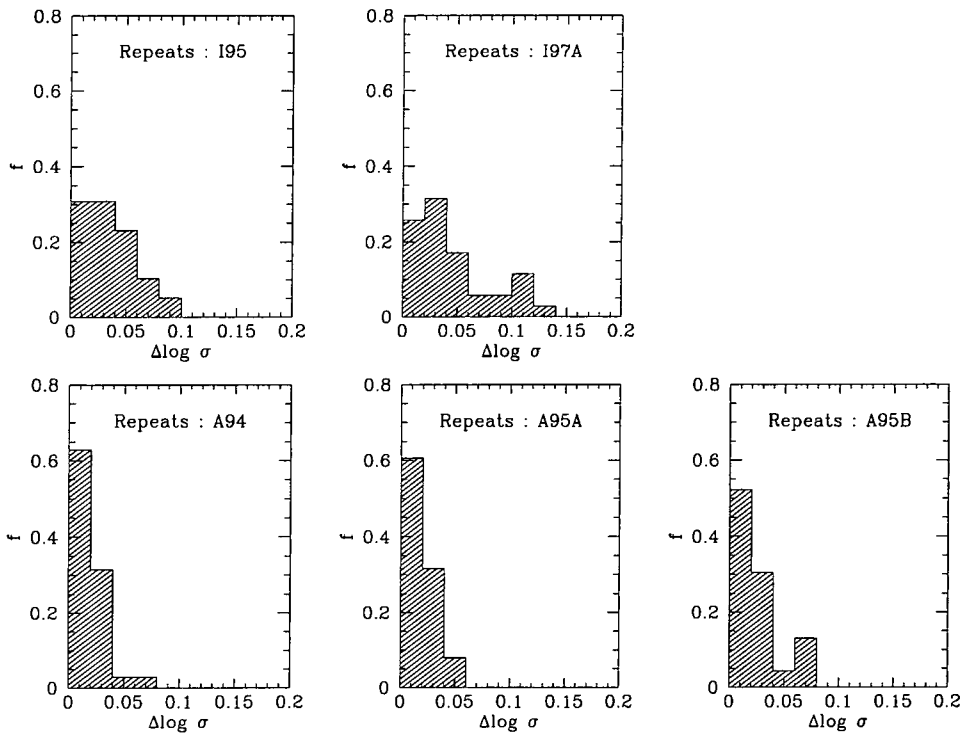

Figure 3.4: Internal comparisons of velocity dispersion measurements. For each system, the plot shows the histogram of $\log\sigma$ differences between all pairs of results.

but also for faint programme galaxies with more representative signal-to-noise ratios. The redundant observations within each dataset have been used to estimate the typical uncertainties of the measured parameters. Such error-estimates include systematic effects such as differences in seeing, telescope tracking etc., and are expected to be more reliable than a formal error calculated for each measurement.

The comparisons of repeat measurements are presented in Figures 3.4–3.7 and quantified in Table 3.3. The difference histograms reveal that the greater resolution and higher signal-to-noise obtained at the AAT result in greater precision in the southern datasets than in those from the INT. Specifically, for the AAT data, the typical errors (per measurement) are 10 km s^{-1} on cz, 0.018 on $\log\sigma$, 0.008 mag on Mg_2 and 0.009 mag on Mgb. Assuming an inverse FP slope of $\alpha = 1.4$ (Hudson et al. 1997), a σ error of 0.018 dex is equivalent to a 6% FP distance error per observation. For the INT data, typical errors are 20 km s^{-1} on cz, 0.035 on $\log\sigma$, 0.011 mag on Mg_2 and 0.012 mag on Mgb. The inverse FP equivalent distance errors are approximately 12% per observation.

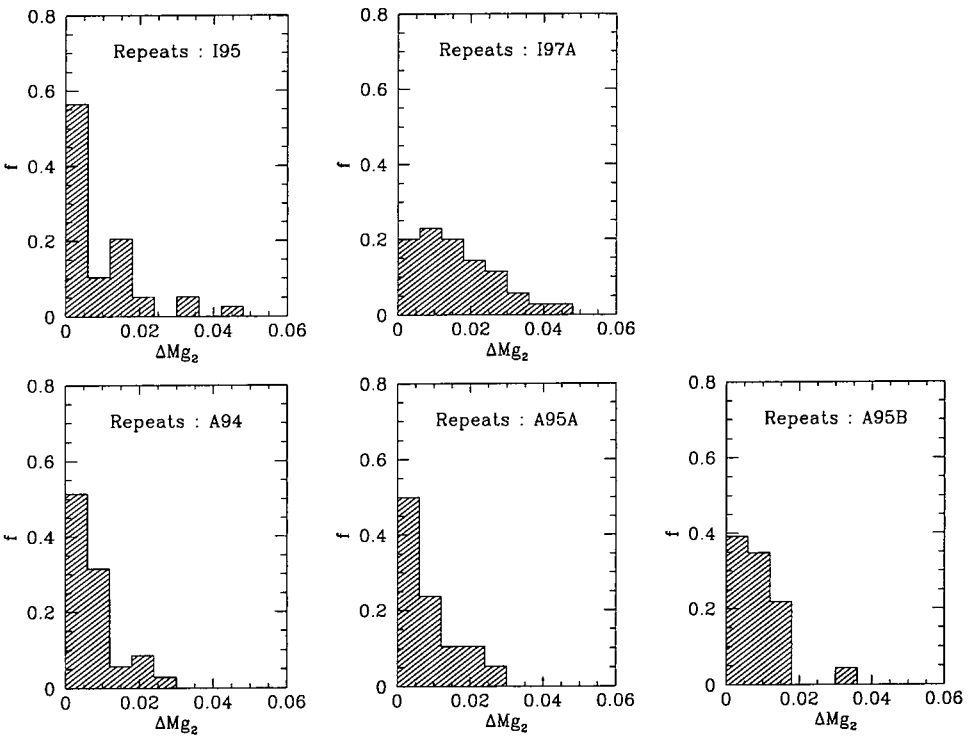

Figure 3.5: Internal comparisons of Mg_2 index measurements. Details as for Figure 3.4.

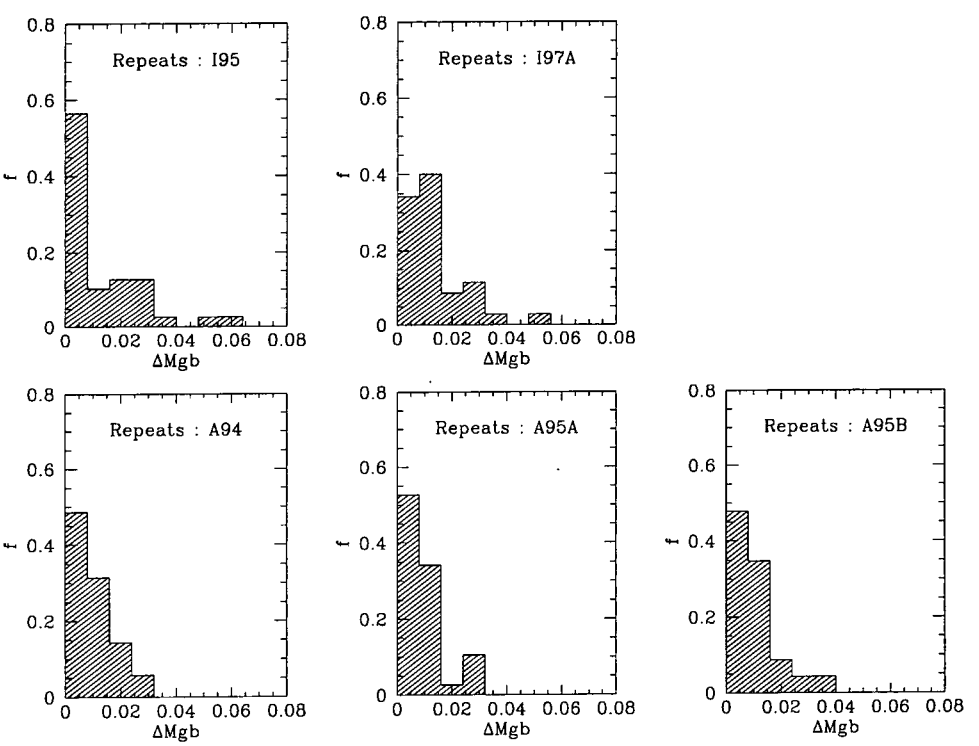

Figure 3.6: Internal comparisons of Mg*b* index measurements. Details as for Figure 3.4.

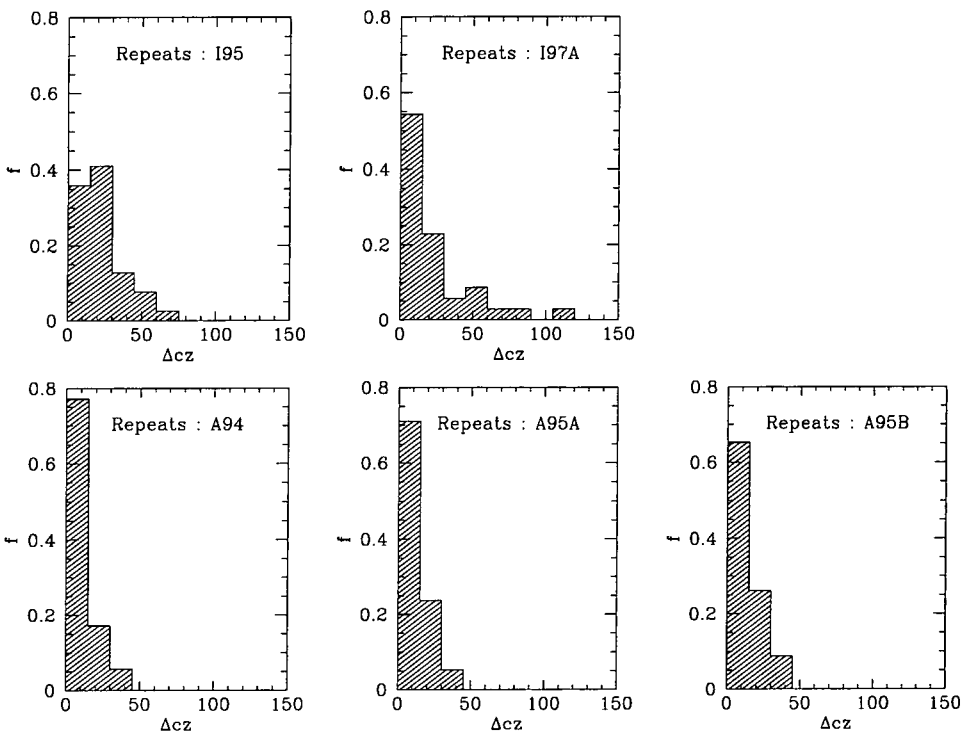

Figure 3.7: Internal comparisons of redshift measurements. Details as for Figure 3.4.

Table 3.3: Internal comparisons for velocity dispersion measurements. For each dataset, the internal scatter is estimated from repeated observations of $N_{\rm gal}$ different galaxies. The scatter in cz, Mg_2, Mgb and $\log\sigma$ are given, and the equivalent distance error *per observation* is computed from the $\log\sigma$ error, adopting an inverse FP slope $\alpha = 1.4$.

Dataset	$N_{\rm gal}$	cz	Mg_2	Mgb	$\log\sigma$	distance
A94	29	10	0.007	0.009	0.016	5.3%
I95	31	19	0.009	0.012	0.029	9.8%
A95A	27	10	0.008	0.009	0.016	5.3%
A95B	19	12	0.008	0.009	0.023	7.7%
I97A	29	24	0.013	0.013	0.042	14.5%

3.5 The aperture correction

The spectrograph aperture samples a larger physical area for distant galaxies than for those nearby. Since galaxies, in the mean, exhibit a negative radial gradient in both $\log\sigma$ and Mg_2, a correction must be applied to the raw data before use. Furthermore, to compare measurements made using different spectrograph apertures (eg between the AAT and INT datasets here), a similar correction is clearly necessary. Jørgensen, Franx & Kjærgaard (1995b) present an analysis based on the observed radial gradients in $\log\sigma$ and Mg_2 for nearby galaxies, while Jørgensen (1997) extends the formalism to Mgb (amongst other indices). They find that a power law provides an adequate description of the required correction:

$$(\log\sigma)_{\rm corr} - (\log\sigma)_{\rm obs} = 0.04 \log \frac{r_{\rm ap}}{r_{\rm norm}} \tag{3.5}$$

$$({\rm Mg}_2)_{\rm corr} - ({\rm Mg}_2)_{\rm obs} = 0.04 \log \frac{r_{\rm ap}}{r_{\rm norm}} \tag{3.6}$$

$$({\rm Mg}b)_{\rm corr} - ({\rm Mg}b)_{\rm obs} = 0.05 \log \frac{r_{\rm ap}}{r_{\rm norm}} \tag{3.7}$$

where $r_{\rm ap}$ is the physical radius sampled by that circular aperture from which one obtains the same $\sigma_{\rm obs}$ as through the actual aperture used. For a rectangular aperture of angular dimensions x and y (in radians), and a galaxy at distance d, the equivalent aperture is

$$r_{\rm ap} \approx 1.025 (\frac{xy}{\pi})^{1/2} d \tag{3.8}$$

where the correction factor 1.025 is included to provide an improved match to more detailed models. An independent analysis (Lucey, priv. comm.), based on measured velocity dispersion profiles, supports the size of this correction.

The normalisation, of Jørgensen et al. is adopted here, such that parameters are referred to a physical diameter $2r_{\rm norm} = 1.19\,h^{-1}$kpc. This is equivalent to an angular diameter of 3.4 arcsec for Coma cluster galaxies.

3.6 External comparisons

Systematic offsets at the $\sim 5\%$ level have been observed between velocity dispersion datasets whenever attempts have been made to combine spectroscopic data from disparate sources (Davies et al. 1987, McElroy 1995, Smith et al. 1997).

In order to investigate the presence of such offsets in the SMAC data, this section presents comparisons between the five new datasets, and comparisons to external data. The problem of matching the SMAC spectroscopic datasets onto a homogeneous system will, however, be fully treated in Chapter 5.

3.6.1 Comparisons between SMAC datasets

Figures 3.8–3.11 display comparisons of (aperture-corrected) spectroscopic parameters ($\log\sigma$, Mg_2, Mgb, cz) between the five SMAC datasets. Numerical results of these comparisons are presented in Table 3.4. Note that there are no galaxies in common between the A95B and I95 systems, and that the A94–A95B and A95A–A95B overlaps are limited to fewer than five galaxies.

Figure 3.8 confirms the existence of significant offsets in $\log\sigma$ between the five systems, especially for comparisons involving I97B, which appears to yield dispersions 7–12% larger than those from the other datasets. Note, however, that the large overlap samples allow these offsets to be constrained with errors of 0.004–0.015 dex, so that appropriate corrections can be determined. In Chapter 5, a simultaneous fit over all overlap galaxies in the merged dataset (including measurements from the literature) will be used to calculate offset corrections with greater precision.

Significant offsets at the level of 0.01–0.02 magnitudes are determined for the Mg_2 index. Again, determination of the most appropriate corrections is deferred to Chapter 5. No substantial systematic offsets are observed between systems of Mgb and cz measurements.

3.6.2 Comparisons with literature datasets

Finally, the newly-obtained spectroscopic parameters can be compared to previous measurements taken from the literature. The comparison data employed for this purpose are taken from the Seven Samurai's extensive 'LICK' dataset (Davies et al. 1987). While the this data is necessarily concentrated in the northern sky, there exists sufficient overlap between LICK and the SMAC datasets reported here (including those from the AAT) to illustrate the offsets.

The comparisons are presented in Figure 3.12 $\log\sigma$ and Mg_2, and the results are quantified by Table 3.5. Prior to the comparison, aperture corrections are applied to data from all sources and mean parameters are calculated for each galaxy on each system.

Again, the comparison reveals systematic offsets of a few per cent in σ (especially for I97A), and of $\sim$0.01 magnitude in Mg_2. The overlap permits determination of these offsets to $\sim$ 2% for all systems, except that for A95B which is not well determined from this comparison alone.

Table 3.4: A summary of the inter-dataset comparisons displayed in Figures 3.8–3.11. In each case, $N_{\rm comp}$ is the number of galaxies available for comparison.

Parameter	Datasets	$N_{\rm comp}$	Offset			rms
$\log\sigma$	I95–I97A	62	-0.026	$\pm$	0.005	0.039
	A94–A95A	31	-0.014	$\pm$	0.004	0.023
	A94–I95	12	$+0.003$	$\pm$	0.010	0.033
	A94–I97A	18	-0.043	$\pm$	0.006	0.026
	A95A–I95	12	-0.001	$\pm$	0.015	0.052
	A95A–I97A	22	-0.036	$\pm$	0.009	0.042
	A95B–I97A	16	-0.048	$\pm$	0.011	0.043
Mg_2	I95–I97A	62	-0.004	$\pm$	0.002	0.014
	A94–A95A	31	$+0.003$	$\pm$	0.002	0.011
	A94–I95	12	$+0.022$	$\pm$	0.003	0.011
	A94–I97A	18	$+0.011$	$\pm$	0.004	0.016
	A95A–I95	12	$+0.007$	$\pm$	0.005	0.017
	A95A–I97A	22	$+0.005$	$\pm$	0.004	0.018
	A95B–I97A	16	$+0.003$	$\pm$	0.004	0.015
Mg*b*	I95–I97A	62	-0.005	$\pm$	0.002	0.015
	A94–A95A	31	$+0.003$	$\pm$	0.002	0.009
	A94–I95	12	$+0.006$	$\pm$	0.003	0.009
	A94–I97A	18	$+0.005$	$\pm$	0.002	0.010
	A95A–I95	12	$+0.004$	$\pm$	0.005	0.016
	A95A–I97A	22	$+0.001$	$\pm$	0.003	0.014
	A95B–I97A	16	-0.004	$\pm$	0.005	0.018
cz	I95–I97A	62	-8	$\pm$	3	27
	A94–A95A	31	$+6$	$\pm$	2	13
	A94–I95	12	$+5$	$\pm$	5	17
	A94–I97A	18	-18	$\pm$	6	24
	A95A–I95	12	-5	$\pm$	4	15
	A95A–I97A	22	-19	$\pm$	4	17
	A95B–I97A	16	$+1$	$\pm$	5	22

Table 3.5: Results of comparisons between SMAC datasets and the 7–Samurai LICK data. The data are corrected for aperture effects, and all offsets are quoted in the sense SMAC–LICK.

Dataset	$N_{\rm comp}$	$\Delta\log\sigma$	rms	ΔMg_2	rms
I97A	53	$+0.015\pm0.007$	0.051	-0.008 ± 0.002	0.011
I95	36	-0.021 ± 0.006	0.037	-0.013 ± 0.002	0.010
A94	18	-0.015 ± 0.009	0.038	$+0.004\pm0.003$	0.012
A95A	14	-0.018 ± 0.010	0.036	$+0.001\pm0.002$	0.009
A95B	14	-0.015 ± 0.019	0.072	-0.010 ± 0.003	0.010

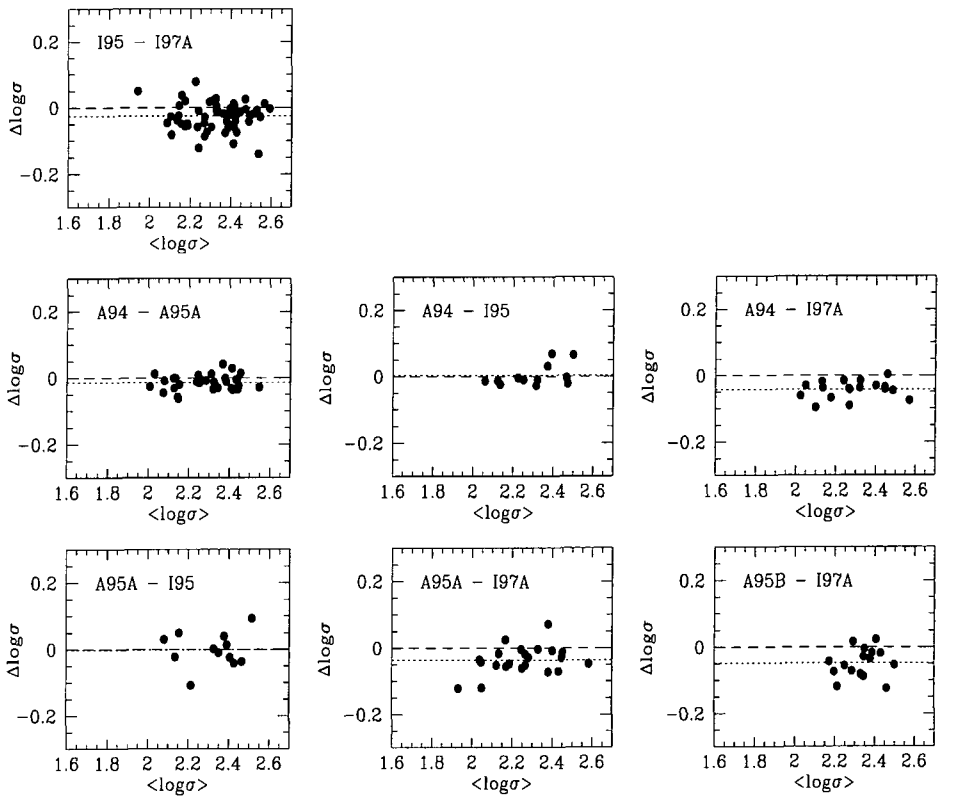

Figure 3.8: Comparison of velocity dispersion measurements between SMAC datasets. In each panel, $\Delta \log \sigma$ is the difference between the mean $\log \sigma$ from the first-named system and the mean $\log \sigma$ from the second-named system. The differences are plotted against the average $\log \sigma$ between the datasets. The dotted line indicates the mean offset between each pair of systems compared. Aperture corrections have been applied prior to this comparison.

3.7 Summary

This chapter has described and presented new measurements of central velocity dispersion, recession velocity and magnesium line-strength indices for 429 early-type galaxies. Errors in the derived parameters have been assessed by a comparison of repeated observations within each dataset. The uncertainties in central velocity dispersion are such as to contribute only 6% FP distance error (per observation), for the high-quality AAT data. For the INT datasets, the distance error is 12% per observation.

References

Baggley G., 1996, DPhil Thesis, Oxford University

Burstein D., Faber S. M., Gaskell C. M., Krumm N. 1984, ApJ, 287, 586

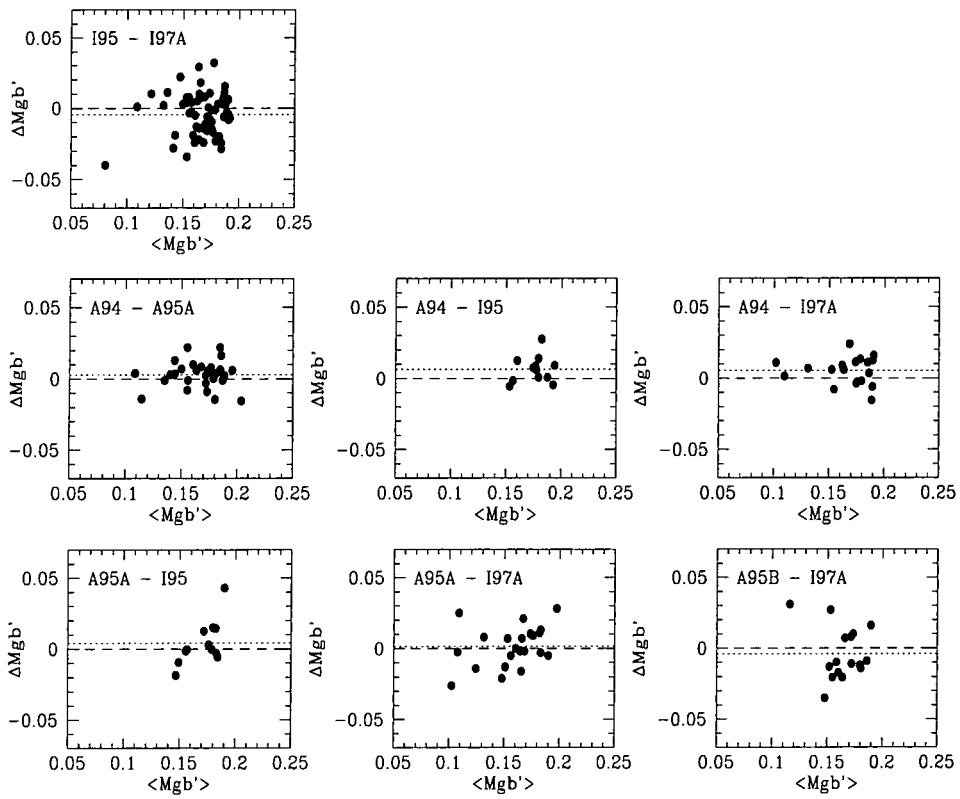

Figure 3.9: As for Figure 3.8, but for Mg*b* measurements.

Davies R. L., Burstein D., Dressler A., Faber S. M., Lynden-Bell D., Terlevich R. J., Wegner G. 1987, ApJS, 64, 581.

González, J. 1993, PhD Thesis, University of California, Santa Cruz

Guzmán R., Lucey J. R. 1992, MNRAS, 263, L47

Hudson, M. J., Lucey J. R., Smith R. J., Steel J. 1997, MNRAS, 291, 488

Jørgensen I. 1997, MNRAS, 288, 161

Jørgensen I., Franx M., Kjærgaard P. 1995b, MNRAS, 276, 1341

Jørgensen I., Franx M., Kjærgaard P. 1996, MNRAS, 280, 167

Lucey J. R., Carter D. 1988, MNRAS, 235, 1177

Lucey J. R., Lahav O., Lynden-Bell D., Terlevich R. J., Infante, L., Melnick J. 1999, in preparation

McElroy, D. B. 1995, ApJS, 100, 105

Müller K. 1997, PhD Thesis, Dartmouth College

Sargent W. L. W., Schechter P. L., Boksenberg A., Shortridge K. 1977, ApJ, 212, 326

Smith R. J., Lucey J. R., Hudson M. J., Steel J. 1997, MNRAS, 291, 461

Wegner G., Colless M., Baggley, G. Davies R. L., Bertschinger E., Burstein D., McMahan R. K. Jr., Saglia R. P. 1996, ApJS, 106, 1

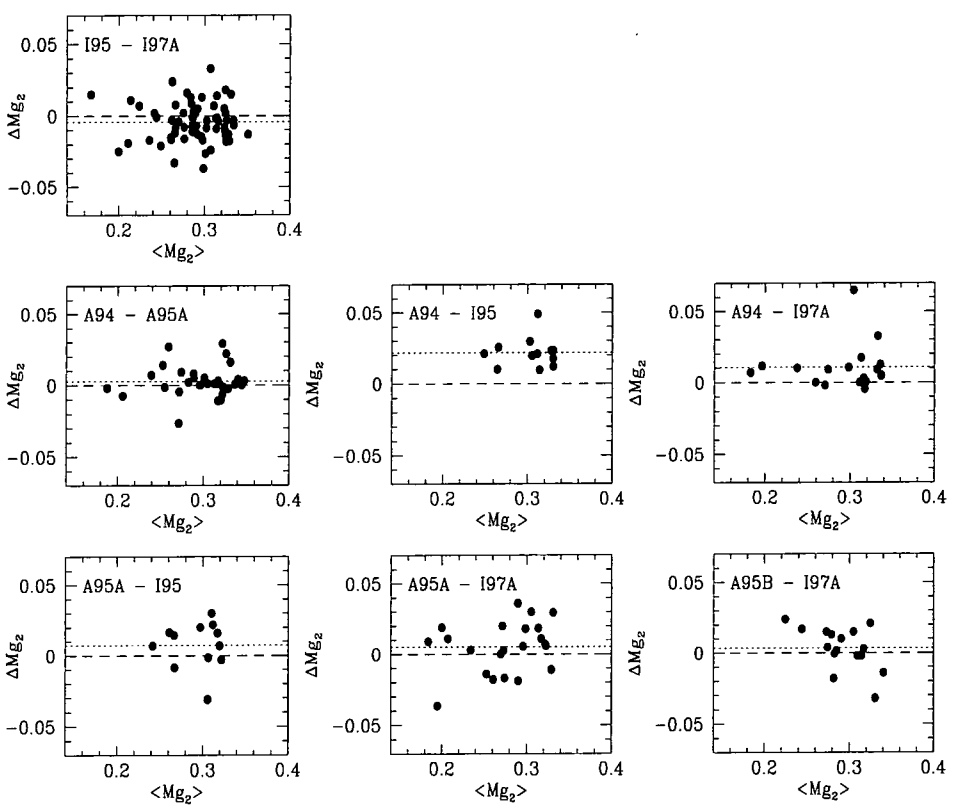

Figure 3.10: As for Figure 3.8, but for Mg_2 measurements.

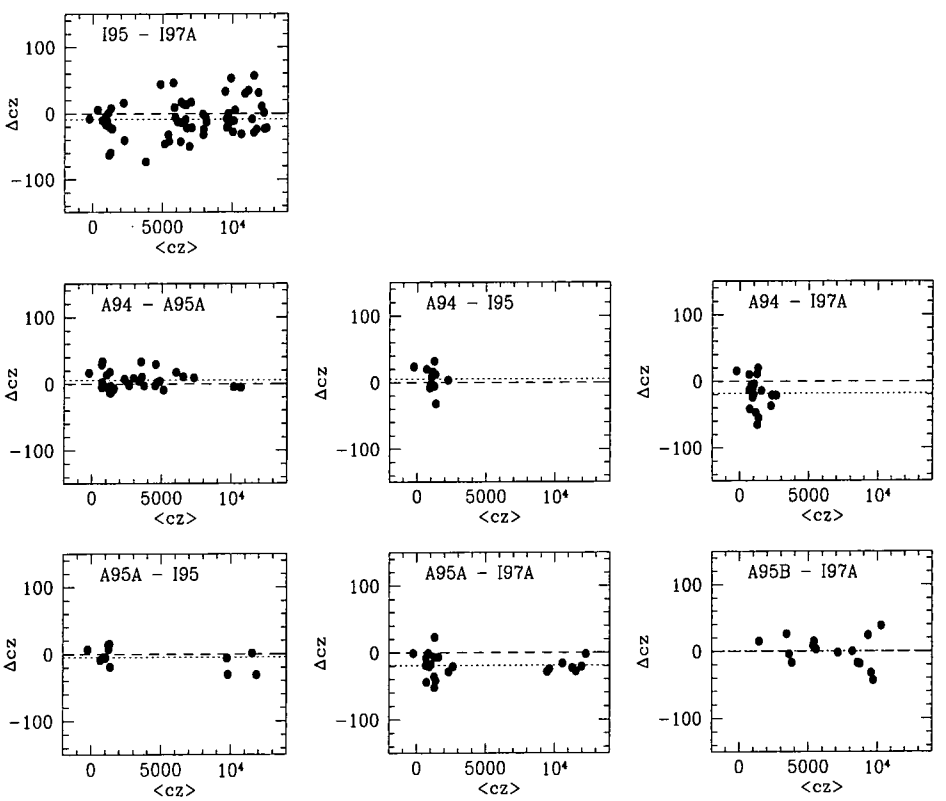

Figure 3.11: As for Figure 3.8, but for cz measurements.

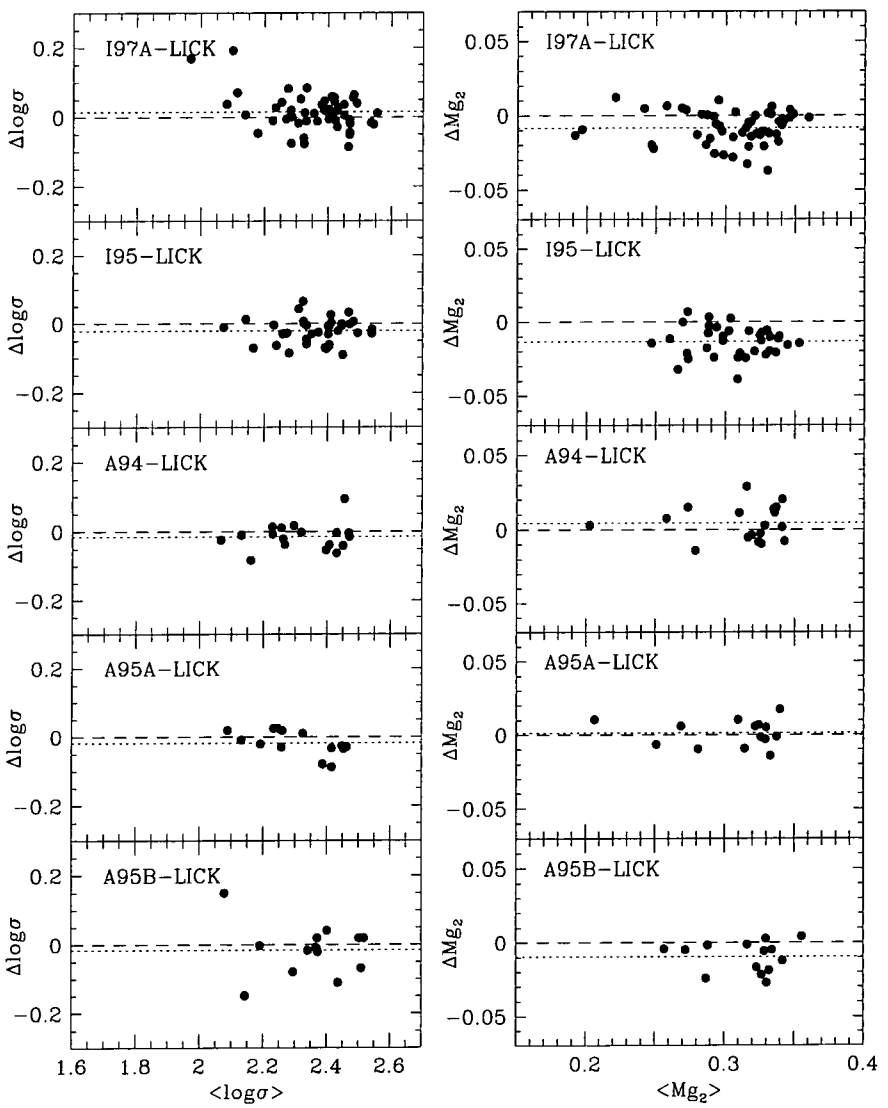

Figure 3.12: Comparison of new spectroscopic measurements with those from the 7-Samurai LICK dataset. The comparisons are made between aperture-corrected mean $\log \sigma$ and aperture-corrected mean Mg_2 from each system. In each panel, the dotted line corresponds to the mean offset.

Chapter 4

New photometric data

4.1 Data sources

This chapter describes the acquisition and reduction of new photometric data for the SMAC programme. Section 4.2 reports the observational procedures adopted for the four imaging runs. Section 4.3 describes the data reduction techniques, and the determination of Fundamental Plane parameters from the galaxy radial profiles. Comparisons within and between the SMAC photometric datasets are provided in Section 4.4, with comparisons to published work discussed in Section 4.5. The issue of combining photometric parameters from the four runs (and from external sources) is deferred until Chapter 5.

4.2 Observational techniques

Photometric observations for the SMAC project were conducted during four observing runs in the period September 1994 – January 1997. For northern clusters, data were obtained at the 1.0m Jacobus Kapteyn Telescope (JKT) on La Palma, while southern observations made use of the 0.9m telescope of the Cerro Tololo Inter-American Observatory (CTIO). The SMAC observations were obtained in the R-band, the choice of bandpass being motivated by the colours of early-type galaxies, the less severe effects of internal and galactic extinction in redder passbands and the reduced sensitivity to stellar population differences from galaxy to galaxy.

Tektronix CCDs detectors, which have high quantum efficiency at red bandpasses, were employed throughout. The 'Harris' R filters employed in the observations provide a close match to the standard Kron–Cousins R bandpass, when convolved with the CCD response.

On each observing run, a number of zero-exposure frames were taken, to deter-

Table 4.1: Sources of new photometric data. The number of photometric nights is given in the penultimate column. The final column gives the number of galaxy profiles from which photometric parameters were finally determined.

Code	Dates	Telescope	CCD	Pixel scale (arcsec)	Field (arcmin)	# of nights	# of images
C94B	Sep. 1994	CTIO 0.9m	2048^2 Tek	0.401	13.7	3	165
J95	Feb. 1995	1.0m JKT	1024^2 Tek	0.330	5.6	1	31
C95	May 1995	CTIO 0.9m	2048^2 Tek	0.401	13.7	2	150
J97	Jan. 1997	1.0m JKT	1024^2 Tek	0.330	5.6	4	88

mine the CCD bias level. Twilight sky frames were obtained each night (typically three to five frames at dusk, and again at dawn) for the purpose of calibrating pixel-to-pixel sensitivity variations. The telescope pointing was adjusted between exposures, so that contaminating stars and cosmic ray events could be removed from the resulting flat-field frames.

Standard star fields from Landolt (1983, 1992) were observed to provide photometric calibration. Standard stars were observed at a range of airmasses and were selected to have colours bracketing those of early-type galaxies. By assessing, in real-time, the photometric stability of each night, observing strategies could be evolved according to the conditions. In particular, the regularity of standard observations varied from around every hour (three or four fields at a time), to alternate observation of galaxies and standards, depending on the estimated stability.

For galaxy observations, exposure times of 300–600 seconds yielded sufficient signal-to-noise for measurement of the photometric FP parameters. Where possible, the efficiency of observations was improved by selecting field centres so as to include several galaxies in each telescope pointing. This technique proved especially valuable at CTIO, where the larger field of view yielded a substantial multiplex gain. A number of 'overlap' galaxies were observed for comparison purposes. These were drawn from the samples of Smith et al. (1997), Jørgensen et al. (1995a), Lucey et al. (1991, 1999), and EFAR (Colless et al. 1993; Saglia et al. 1997b).

4.3 Data reduction

The reduction of the photometric data was performed using a combination of the Starlink and IRAF software packages. This section describes the data processing

from raw CCD frames to individual measurements of photometric parameters for each galaxy.

4.3.1 Basic reduction

All frames were bias-subtracted, using standard IRAF procedures, and bad pixels were identified and corrected by interpolation from neighbouring pixels. A 'master' flatfield was constructed from the several twilight sky exposures from each night. Where evening and morning twilight frames exist, the night was sometimes split into two sections, with the images from each section flattened corrected using the appropriate flatfield. This approach was adopted when the arrival during the night of dust specks in the optical path would otherwise lead to residual flatfield errors of a few per cent.

Cosmic ray events were identified and removed by interpolation, using M. Dickinson's 'qzap' procedure within IRAF. The CCD pixel scale was measured by means of astrometric calibration derived by comparison of observed Landolt fields with star positions from the HST Guide Star Catalogue.

4.3.2 Photometric solutions

Photometric calibration was provided through observations of the standard star fields tabulated by Landolt (1983, 1992). The observed instrumental magnitudes, $R_{\rm inst}$, are fit to the equation

$$R_{\rm Lan} = R_{\rm inst} + ZP - k_R X + C(V-R)\,, \tag{4.1}$$

where $R_{\rm Lan}$ is Landolt's listed R-band magnitude and $V-R$ is the listed colour, ZP is the photometric zero-point, k_R the atmospheric extinction coefficient, and C a colour term. Further analysis is performed only for those nights (or part-nights) with a scatter smaller than 0.025 mag about the photometric solution.

Properties of the photometric periods are presented in Table 4.2. It should be noted that the colour term C is small for all nights, and that for the small range of $V-R$ colours exhibited by elliptical galaxies, it can be safely absorbed into the zero point term. For this purpose, we adopt a mean early-type galaxy colour of $V-R$=0.61 (eg Fukugita et al. 1995).

4.3.3 Profile analysis

With initial reduction thus completed, each galaxy frame was examined by eye. A morphological classification was assigned to each galaxy at this stage, with evident spirals and peculiar galaxies flagged for future rejection. The seeing, defined as the

Table 4.2: Photometric solutions. For each photometric period, the table gives the R-band extinction per unit airmass, k; the $B-V$ colour term, C; and the rms residual of standard star magnitudes from the solution. $N_\star$ is the number of standard stars observed during the period given. The final column gives an approximate range for the seeing over each period.

Run	Night	k	C	$N_\star$	rms	Period (UT)	Seeing
C94B	03/09/94	0.075±0.004	$+0.002 \pm 0.003$	127	0.014	00:40–08:00	1.3–1.8
	04/09/94	0.098±0.003	$+0.005 \pm 0.003$	158	0.019	00:00–09:50	1.2–2.0
	05/09/94	0.094±0.004	-0.006 ± 0.003	201	0.011	01:40–09:50	1.4–2.3
J95	23/02/95	0.059±0.013	-0.017 ± 0.021	9	0.008	20:30–23:10	1.9–2.3
	23/02/95	0.077±0.013	-0.051 ± 0.037	13	0.011	23:15–07:00	1.5–2.1
C95	03/05/95	0.119±0.010	$+0.016 \pm 0.007$	166	0.020	23:10–08:40	1.6–2.5
	04/05/95	0.128±0.013	$+0.007 \pm 0.008$	167	0.021	22:55–08:40	1.2–2.3
J97	03/01/97	0.085±0.013	-0.012 ± 0.014	21	0.015	19:50–01:45	1.0–1.5
	05/01/97	0.088±0.007	-0.020 ± 0.017	15	0.012	03:45–06:05	1.3–1.4
	08/01/97	0.082±0.005	-0.001 ± 0.005	87	0.016	19:50–07:00	0.8–1.2
	09/01/97	0.075±0.007	-0.000 ± 0.006	44	0.013	19:50–03:40	1.2–2.0

FWHM of the point spread function, was measured from the profiles of isolated stars in the field. For all galaxy frames reduced, the seeing was in the range 0.8–2.5 arcsec.

For each galaxy, an Starlink's 'pisafind' procedure was used to identify contaminating stars and companion galaxies, and construct a list of 'masked regions'. This list was afterwards edited if necessary, to exclude additional contaminating objects not identified in the automatic search. Typically, less than 5% of the galaxy area was masked out in this way. The 'galphot' program (written by M. Franx) was then used to construct a model of the galaxy from the unmasked regions, using an elliptical isophote fit including c_4, s_4 harmonic terms. The resulting model was used to 'patch' the masked regions of the original image.

The surface brightness of the night-sky was determined from a number of apertures placed by hand within each field. The rms dispersion between these apertures indicates typical uncertainties of 0.5–1.0% in the sky value.

Radial profiles were produced by summing counts in circular apertures over a diameter range 4–100 arcsec. Aperture magnitudes were corrected for galactic extinction, and for cosmological k-dimming. An R-band extinction of $A_R = 2.35E(B-V)$ was adopted, where $E(B-V)$ are the reddening values of Burstein & Heiles (1984)[1]. The

[1]The extinction corrections of Burstein & Heiles are retained at this stage, for ease of comparison with earlier

k-correction applied was $-1.0z$, appropriate for the spectral energy distribution of early-type galaxies (Oke & Sandage 1968, Frei & Gunn 1994). A correction for the Tolman $(1+z)^4$ surface brightness dimming was also applied, using the spectroscopically determined redshift for each galaxy.

The photometric parameters which enter into the FP distance indicator are the effective diameter (ie the diameter containing half the total flux), A_e, and the effective surface brightness, $\langle\mu\rangle_e$, defined as the mean surface brightness within A_e. Since some extrapolation of the luminosity profile is necessary to determine the total flux, derivation of FP parameters generally assumes a parametric model for the galaxy profile (but see Lucey 1997 for a non-parametric formulation). For the SMAC photometry, the simple de Vaucouleurs $R^{1/4}$ profile was used as the model, and the FP parameters for each galaxy were defined as the A_e and $\langle\mu\rangle_e$ of the best fitting $R^{1/4}$ profile. The typical rms residual from the $R^{1/4}$ law fit is 0.02 mag.

Seeing corrections followed the method of Smith et al. (1997), which is a refinement of the scheme presented by Bower, Lucey & Ellis (1992). Corrections to the aperture photometry were made according to models in which a pure $R^{1/4}$-law galaxy is convolved with a theoretical point spread function. Correction tables, generated for galaxies with a range of A_e, were employed in an iterative scheme, with the appropriate correction table selected according to the measured A_e of the galaxy.

Saglia et al. (1997a) have recently questioned the practice of fitting pure $R^{1/4}$-law profiles to galaxies which potentially have a significant exponential disk component. They show from simulations that such a fit to a galaxy with a disk-to-bulge ratio of just 0.2 can result in A_e measurements which are biased by as much as 30%. Whilst this severely affects the independent determination of A_e and $\langle\mu\rangle_e$, the errors in these two parameters are correlated. Indeed, the same simulations demonstrate that the combination $\log A_e - 0.32\langle\mu\rangle_e$, which enters into the FP relation, is robust against the presence of an exponential disk. Specifically, for a disk-to-bulge ratio smaller than unity, the disk component introduces a scatter of less than 0.03 in $\log A_e - 0.32\langle\mu\rangle_e$, with no systematic bias (Figure 4 of Saglia et al.).

The photometric parameters derived from the SMAC imaging runs are presented in Table A.2.

work. Note, however, that in constructing a final merged catalogue in Chapter 5, these corrections are replaced by those of Schlegel, Finkbeiner & Davis (1998). The latter corrections have been demonstrated to be the more reliable (Hudson 1998), and should now supercede the ageing Burstein & Heiles maps.

Table 4.3: Comparison of R_{20} and $\log A_e - 0.32\langle\mu\rangle_e$ from repeat observations within the SMAC runs. The table gives the error per measurement on these quantities, as determined from the scatter between repeat observations. The final column gives the distance error equivalent to the $\log A_e - 0.32\langle\mu\rangle_e$ scatter. There are no repeat measurements in the J95 dataset.

Run	N_{rpts}	R_{20}	$\log A_e - 0.32\langle\mu\rangle_e$	distance
C94B	51	0.008	0.003	0.8%
C95	53	0.024	0.008	1.8%
J97	7	0.010	0.008	1.9%

4.4 Internal comparisons

The typical uncertainties in our photometric data can be estimated from results for galaxies which were observed more than once in each observing run. Figure 4.1 and Table 4.3 present comparisons of repeat measurements within the C94B, C95 and J97 observing runs. Note that the J95 data, drawn from a single photometric night, contains no repeat observations.

The comparisons are made for magnitudes measured within an aperture of 20 arcsec (R_{20}), and for the FP photometric parameter $\log A_e - 0.32\langle\mu\rangle_e$. The aperture of 20 arcsec diameter is chosen as a standard for the comparisons, since it is relatively insensitive to seeing differences, and to uncertainties in the sky level. It is found that R_{20} agrees to 0.01–0.02 mag between measurements, with the largest discrepancies being due to differences, from one image to another, in the treatment of contaminating objects[2]. The FP parameter shows a scatter of 0.003–0.008, equivalent to 1–2% distance error per observation.

Figure 4.2 shows a comparison of results for galaxies observed in both the C94B and C95 runs. From 11 galaxies in common, the derived mean offset is 0.004 ± 0.009 mag in R_{20}, with C94B the brighter. In the FP parameter, the offset is 0.001 ± 0.004 (C95 brighter). The rms scatter in the FP comparison is 0.011 mag, slightly larger than the quadrature sum of the internal errors. The direct overlap between the JKT runs with each other, and with the CTIO data, is limited to one or two galaxies per comparison. Comparisons with external data sources are therefore required, in order to test more clearly the internal homogeneity of the SMAC data.

[2]Especially for I0664 in C95 (see later).

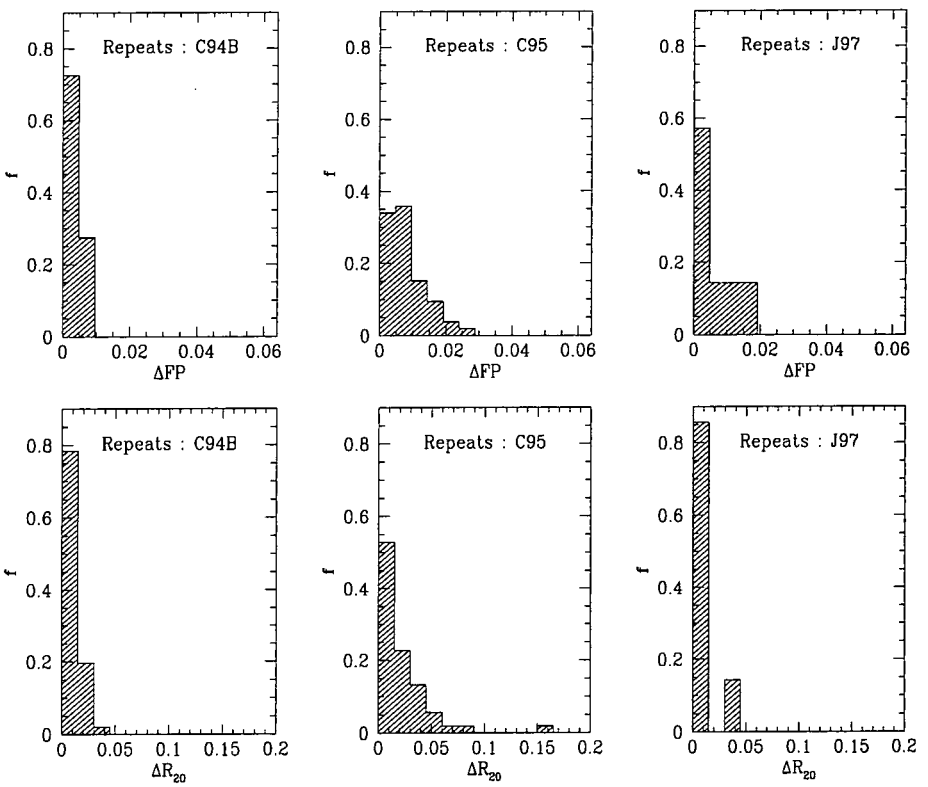

Figure 4.1: Internal photometric comparisons. Comparisons are made for R_{20} (the magnitude within an aperture of 20 arcsec diameter), and the fundamental plane parameter, $FP = \log A_e - 0.32\langle\mu\rangle_e$. Note that the scale of the FP comparison panels is smaller by a factor of 0.32 than that of the R_{20} panels: this ensures that equal distance errors are represented by equal physical intervals on the plot.

4.5 External comparisons

The R-band has been adopted for a number of photometric studies of early-type galaxies in the SMAC distance range. The most important of these works, in the present context, are those which have themselves been directed towards studies of the velocity field. This section presents comparisons of the photometric data from the SMAC project with published data from Jørgensen et al. (1995a), Postman & Lauer (1995, PL), Smith et al. (1997), Steel (1998) and and the EFAR project (Colless et al. 1993, Saglia et al. 1997b).

4.5.1 Aperture photometry comparisons

The most basic comparison which can be made between datasets is that of magnitude measured inside a given aperture. Such comparisons are presented in the left

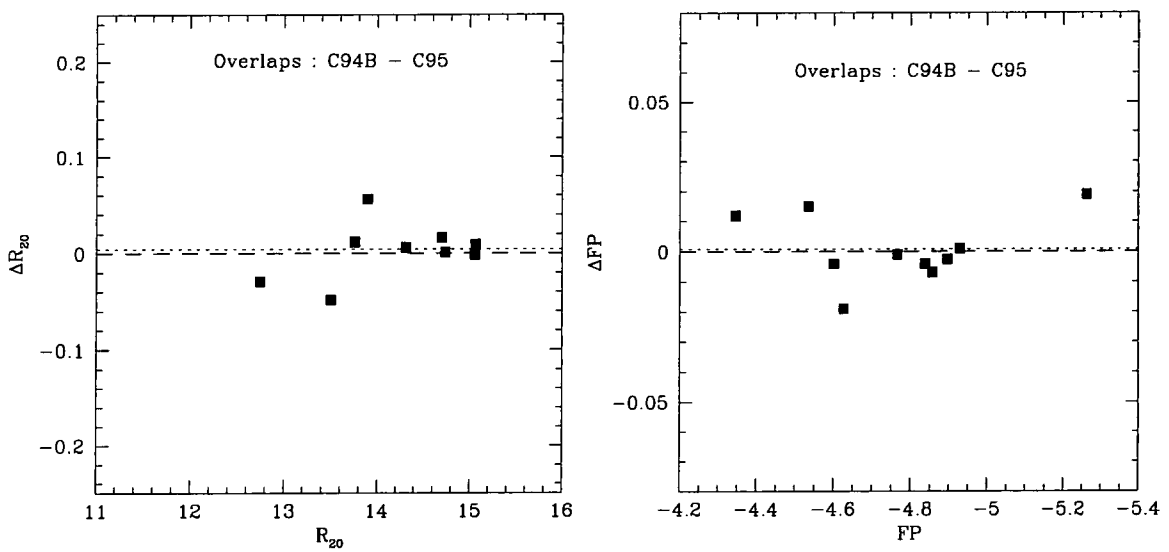

Figure 4.2: Comparison of photometric parameters from the C94B and C95 datasets, for galaxies in common. The comparisons are performed for the magnitude at 20 arcsec (R_{20}) and for the FP parameter, $\log A_e - 0.32\langle\mu\rangle_e$. The dotted line shows the mean difference in each case.

hand panels of Figure 4.3, and quantified in Table 4.4. Since most authors have not published full photometric profiles, it is not possible to compare all sources at the same size of aperture. Where possible (comparisons against Smith et al. and Steel) a 'standard' aperture diameter of 20 arcseconds is adopted, as justified above. For comparisons with Colless et al. and Postman & Lauer, larger apertures were used.

All the aperture photometry comparisons reveal evidence for a slight zero-point offset, with the SMAC data 0.01–0.04 mag brighter than comparison sources. If the aperture photometry were used directly in distance estimation, this would translate into a 0.5–2.0% systematic error in distance. The scatter in the comparison with PL is reduced to 0.034 mag if the two outliers are rejected. The discrepant galaxies are I1565 and I0664. The PL photometry for I1565 (in A0076) is too faint by more than 0.1 mag with respect to our data, and also (as PL themselves point out) with respect to Colless et al. It appears then, that for this galaxy the PL data are affected by a photometric calibration error. The second outlier is I0664, observed twice in C95, and also discrepant in the internal comparisons. Re-examination of the profiles reveals masking of one observation very close to the galaxy centre. This appears to be a 'one-off' data reduction error. The galaxy, in A1142, is *not* part of the final FP sample presented in Chapter 5.

In principle, dividing the comparisons between the individual SMAC datasets

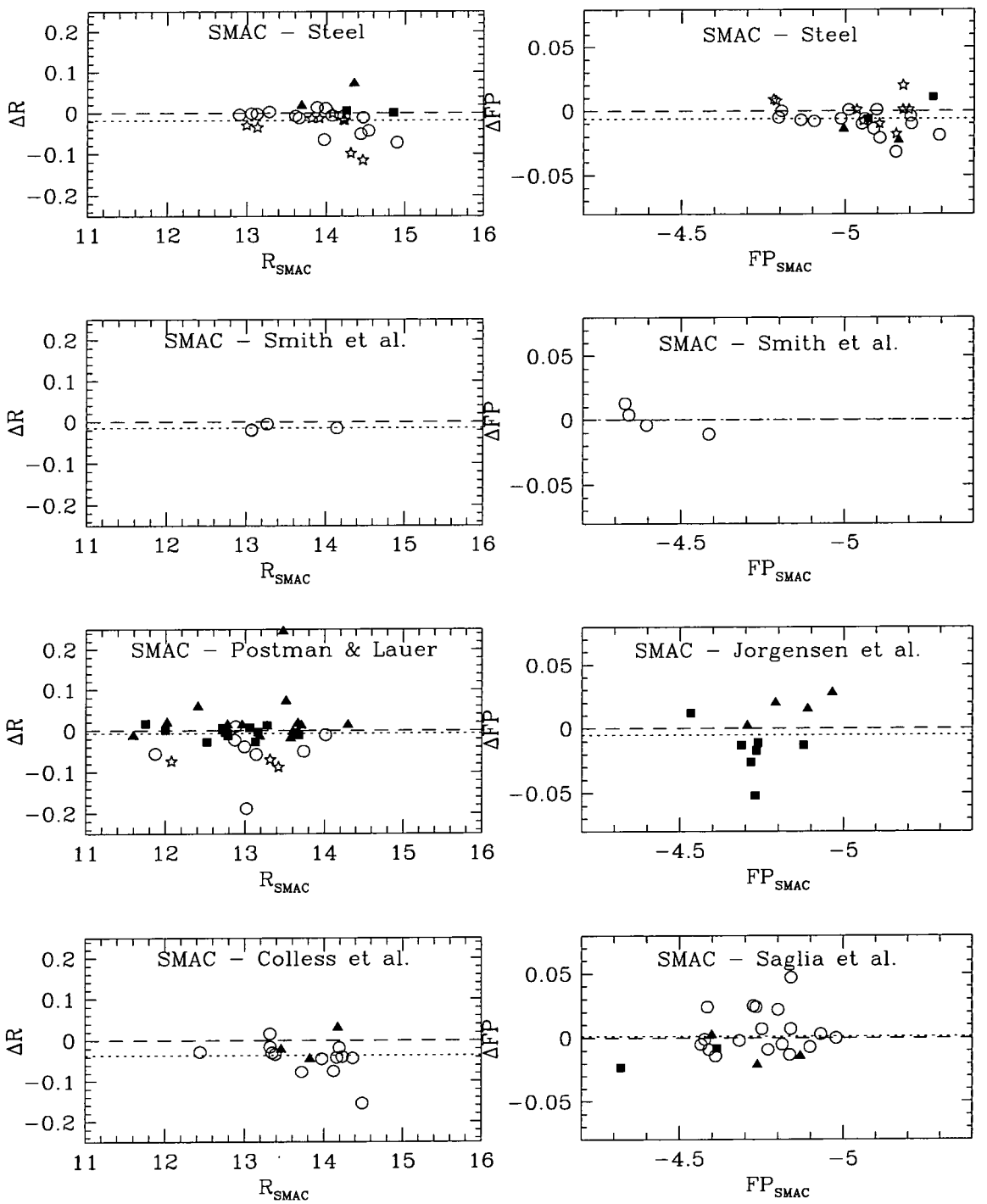

Figure 4.3: Comparison of SMAC photometry with data from external sources. Left hand panels compare the magnitude within the apertures given by Table 4.4, while right hand panels compare the FP parameter $FP = \log A_e - 0.32\langle\mu\rangle_e$. In all cases $\Delta R = R_{\rm SMAC} - R_{\rm others}$ and $\Delta FP = FP_{\rm SMAC} - FP_{\rm others}$. Symbols are coded to reflect the four observing runs from which the SMAC data are drawn: Open symbols are from JKT runs (stars=J95, circles=J97) and filled symbols from CTIO runs (triangles=C95, squares=C94B). Measurements from each SMAC run have been combined as a simple mean prior to the comparison.

Table 4.4: External comparisons of aperture photometry with R-band work from other sources. Offsets are given in the sense $R_{\rm SMAC} - R_{\rm others}$, the comparison being made at diameter(s) $D_{\rm ap}$. Prior to the comparison, repeat observations within each SMAC observing run (but not *between* runs) were combined, leaving $N_{\rm comp}$ comparison data.

Comparison Source	$D_{\rm ap}$ (arcsec)	$N_{\rm comp}$	Mean offset	Dispersion
Steel (1998)	20	28	-0.018±0.007	0.037
Smith et al. (1997)	20	4	-0.015±0.003	0.007
Postman & Lauer (1995)	50, 79	37	-0.007±0.010	0.061
Colless et al. (1993)	19.2, 29.9	17	-0.037±0.010	0.041

provides a further test of the internal homogeneity of the new data. Most striking, among the R_{20} comparisons is the offset of J95 magnitudes with those of PL. While there are only three galaxies in common, the J95 data appear to be offset from the PL data, and from the remainder of the SMAC data by ~0.6 mag. While this is initially alarming, it appears that the offsets can be ascribed to a slight underestimate of the sky value, which has a substantial effect at the very large apertures considered here. In the comparison with Steel's aperture photometry, conducted at 20 arcsec, only a small offset of ~ 0.03 mag is found for these galaxies. (Note that the two outlying J95 points in the comparison with Steel are *not* for the same galaxies which cause the offset with respect to PL.)

4.5.2 Profile comparisons

Saglia et al. (1997b) have compared CCD aperture photometry from the EFAR project with profiles of brightest cluster galaxies (BCGs) tabulated by PL. Of 30 galaxies compared, 18 display strong gradients in the profile difference as a function of radius. The effect is in the sense that at large radii, the PL data become progressively brighter than the EFAR magnitudes. Saglia et al. attribute this effect to a 1–2% underestimate, by PL, of the sky value.

In a similar spirit, Figure 4.4 presents comparisons of the SMAC profiles with those of PL, for 33 galaxies in common. In 20 cases, the plot reveals a significant trend with aperture size, in the same sense as found by Saglia et al., ie such that the PL data become fainter at large apertures. Where repeat observations exist within the SMAC data, the profile trends are generally consistent between exposures. The profile comparisons therefore support the conclusion that either the PL photometry is affected by a systematic under-estimation of the sky, or both the SMAC and EFAR have over-estimated sky values, at least for the BCGs in these samples.

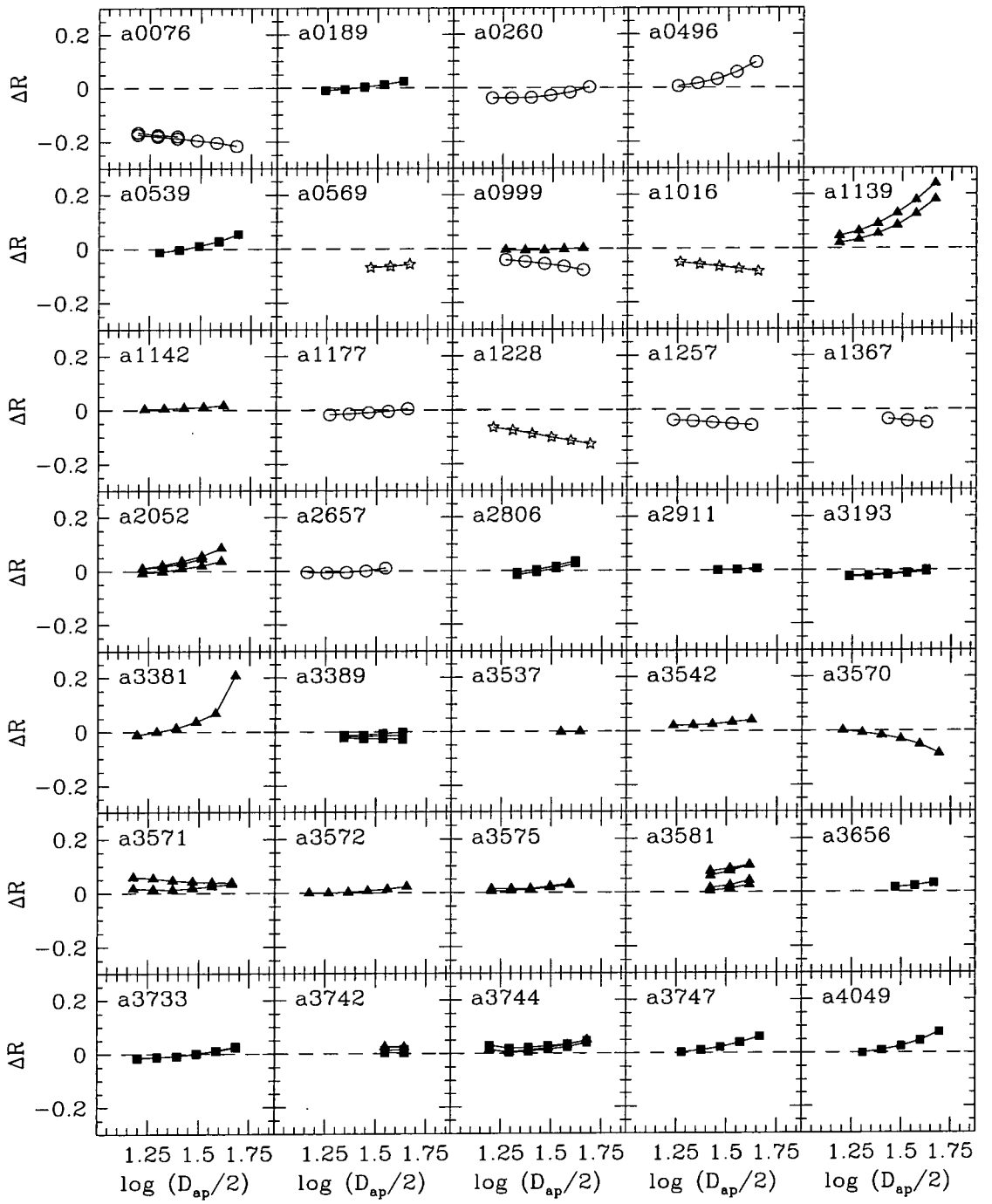

Figure 4.4: Comparison of profiles between the SMAC photometry and that of Postman & Lauer (1995). The SMAC data have been interpolated to match the tabulated apertures (diameter $D_{\rm ap}$ arcsec) of Postman & Lauer, and compared to yield $\Delta R = R_{\rm SMAC} - R_{PL}$. The panels are identified by the Abell cluster number, the galaxy being always the brightest cluster member as selected by Postman & Lauer. The source of the SMAC data is coded by run, as in Figure 4.3. For galaxies with more than one SMAC observation, the profile comparisons are plotted separately. The highly discrepant C95 observation of I0664 in A1142 is not shown.

4.5.3 Derived parameters

Table 4.5 and the right-hand panels of Figure 4.3 present comparisons between SMAC data and published work, in terms of parameters derived from profile fits. The comparisons are made for the robust quantity $FP = \log A_e - 0.32\langle\mu\rangle_e$, which gives a nearly edge-on projection of the Fundamental Plane. For the EFAR data of Saglia et al., FP has been computed from their tabulated half-light parameters R_e and $\langle SB\rangle_e$.

The dispersion in these comparisons is indicative of uncertainties smaller than 0.02 dex per measurement of the FP parameter. Photometric errors therefore contribute less than ~4% to the distance uncertainty per measurement. This estimate includes contributions from the many systematic effects which may affect surface photometry (eg calibration errors, sky errors, masking differences etc). The photometric measurement errors contribute negligibly, therefore, to the total FP scatter of ~20%.

An offset of $\Delta FP = 0.005$ between datasets would translate into a systematic distance error of ~150 km s^{-1} for clusters at the limit of the SMAC survey[3]. Taken as a whole, it appears that the SMAC photometry is not significantly offset in FP with respect to the external sources considered here. However, there is some weak evidence for run-to-run offsets within SMAC, relative to external datasets. The comparison with Steel suggests an offset of $\Delta FP = 0.009 \pm 0.004$ between the J95 data and the other SMAC data, with J95 the brighter. In the comparison with Jørgensen et al., there is evidence for a more substantial offset between the CTIO datasets. Since all the C94B observations in the Jørgensen et al. comparison are of galaxies in A0539, and all the C95 data are for A3381, the simplest explanation for the apparent offsets is a calibration error in either the SMAC or the Jørgensen et al. photometry for one of these two clusters. The direct comparison between the CTIO datasets (Figure 4.2) precludes a *global* offset of this size in the SMAC data.

4.6 Summary

This chapter has presented new photometric data obtained for the SMAC programme. The FP photometric parameters, $\log A_e$ and $\langle\mu\rangle_e$ have been determined from $R^{1/4}$ profile fits, and fully corrected for k-correction and cosmological surface brightness dimming effects. Comparisons of the raw aperture photometry with data from the literature indicate offsets of a 0.01–0.04 mag. Comparisons of results for the parameter combination $\log A_e - 0.32\langle\mu\rangle_e$ suggest that the total external errors are less than 4% per

[3]Since the final SMAC catalogue includes photometric data from many sources, a systematic offset of one dataset by 0.005 in $\log A_e - 0.32\langle\mu\rangle_e$ would *not* translate directly into a spurious bulk-flow of 150 km s^{-1}. Rather, only those clusters observed only (or predominantly) in that run would be strongly affected.

Table 4.5: External comparisons of $FP = \log A_e - 0.32\langle\mu\rangle_e$ with published parameters from other sources. The Gunn-r data of Jørgensen et al. (1995b) have been corrected to the R-band, assuming a mean $r - R = 0.33$ (see Smith et al. 1997). Offsets are given in the sense $R_{SMAC} - R_{others}$. Again, results from repeated observations within each SMAC run are combined prior to the comparison.

Comparison Source	N_{comp}	Mean offset	Dispersion
Steel (1998)	28	−0.006±0.002	0.011
Smith et al. (1997)	4	+0.001±0.005	0.010
Saglia et al. (1997b)	23	+0.001±0.004	0.017
Jørgensen et al. (1995a)	11	−0.005±0.007	0.023

measurement. Although photometric calibration errors for individual clusters cannot be excluded, there are no global substantial offsets between the four SMAC datasets, nor between SMAC data and measurements from the literature. Further photometric comparisons are presented in Section 5.3.

References

Bower R. G., Lucey J. R., Ellis R. S. 1992, MNRAS, 254, 589

Burstein D., Heiles C. 1984, ApJS, 54, 33

Colless M., Burstein D., Wegner G., Saglia R. P., McMahon R. K., Davies R. L., Bertschinger E., Baggley G. 1993, MNRAS, 262, 475

Frei Z., Gunn J. E. 1968, AJ, 108, 1476

Fukugita M., Shimasaku K., Ichikawa T. 1995, PASP, 107, 945

Hudson M. J. 1998, PASP, in press

Jørgensen I., Franx M., Kjærgaard P. 1995a, MNRAS, 273, 1097 (JFK95a)

Landolt A. U. 1983, AJ, 88, 439

Landolt A. U. 1992, AJ, 104, 340

Lucey J. R. 1997, MNRAS, 289, 415

Lucey J. R., Guzmán R., Carter D., Terlevich R. J. 1991b, MNRAS, 253, 584

Lucey J. R., Lahav O., Lynden-Bell D., Terlevich R. J., Infante, L., Melnick J. 1999, in preparation

Oke J. B., Sandage A. 1968, ApJ., 154, 21

Postman M., Lauer T. R. 1995, ApJ, 440, 28 (PL)

Saglia R. P., Bertschinger E., Baggley G., Burstein D., Colless M. M., Davies R. L., McMahan R. K., Wegner G. 1997a, ApJS, 109, 79

Saglia R. P., Burstein D., Bertschinger E., Baggley G., Colless M. M., Davies R. L., McMahan R. K., Wegner G. 1997b, MNRAS, 292, 499

Schlegel D. J., Finkbeiner D. P., Davis M. 1998, ApJ, 500, 525

Smith R. J., Lucey J. R., Hudson M. J., Steel J. 1997, MNRAS, 291, 461

Steel J. 1998, PhD thesis, University of Durham

Chapter 5

Construction of a merged catalogue of FP data

5.1 Introduction

Previous chapters have reported the acquisition and reduction of spectroscopic and photometric data obtained specifically for the SMAC programme. In this chapter, these new data are compared and carefully combined with measurements taken from a variety of literature sources, to yield a homogeneous merged catalogue of FP data.

For the velocity dispersion measurements, which are subject to random errors equivalent to 5–15% in distance, and to systematic offsets of up to 10%, the need for accurate 'system-matching' is especially severe. Section 5.2 describes the application of a technique to determine, and correct for, systematic effects in the spectroscopic parameters, through inter-comparison of an extensive body of overlap data. In Section 5.3, a similar process is employed in a comparison between new photometric datasets and sources from the literature.

Since insufficient data was gathered for some of the target clusters of Chapter 2, and since substantial data is available for a few clusters *not* in the original sample, it is necessary to define a revised sample, based upon the availability of FP data for at least four cluster members. This final sample is constructed in Section 5.4, using objective cluster membership criteria, Finally, the merged catalogue of FP data itself is presented and described in Section 5.6.

5.2 Spectroscopic system matching

Table 5.1 presents a summary of velocity dispersion datasets chosen for incorporation into the the SMAC merged catalogue. These datasets ('systems') generally derive

Table 5.1: Sources of spectroscopic data. Each separately treated 'system' is listed with dates, references and other information. In the 'mode' column, 'S' signifies single-slit spectroscopy, while 'F' refers to multi-fibre observations. The listed number of spectra is the number of velocity dispersion measurements contributed by a given system to our master catalogue.

Project	Code	Dates of observation	Telescope	Mode	Spectra	Ref.
SMAC	I97A	Jan. 1997	INT[1]	S	226	a
	I95	Feb. 1995	INT	S	140	a
	A95B	Sep. 1995	AAT[2]	S	106	a
	A95A	Apr. 1995	AAT	S	134	a
	A94	Apr. 1994	AAT	S	112	a
Perseus–Pisces	TEK94	Sep. 1994	INT	S	211	b
	EEV94	Sep. 1994	INT	S	16	b
	EEV93	Nov. 1993	INT	S	104	b
Coma–Virgo	I97B	Mar. 1997	INT	S	201	c
	INT90	May 1990	INT	S	118	d
A2199/A2634	INT92	Jul. 1992	INT	S	119	e
FOCAP	LC	May 1984 – Sep. 1984	AAT	F	214	f
	FOCP2	Apr. 1987 – Apr. 1988	AAT	F	438	g
7 Samurai	LICK	Sep. 1972 – Aug. 1984	LICK[3]	S	492	h
	PAL	May 1984 – Sep. 1985	PAL[4]	S	30	h
	KPNO	Sep. 1980	KPNO[5]	S	31	h
	LCOHF	Feb. 1982	LCO[6]	S	62	h
	LCOHM	Mar. 1983	LCO	S	82	h
	LCOHJ	Jan. 1984	LCO	S	63	h
	LCOLO	Mar. 1981 & Nov. 1981	LCO	S	93	h
	A1	Aug. 1980 & Aug. 1981	AAT	S	66	h
	A2	Jan. 1981 & Jan. 1982	AAT	S	53	h
Other Published	DF	Mar. 1988 & Mar. 1989	LCO	S	136	i
	JBC12	Oct. 1990 & Apr. 1991	ESO1[7]	S	103	j
	JBC3	Jan. 1992	ESO1	S	32	j
	JFKOP	Feb. 1992	ESO4[8]	F	171	j
	GONZA	Aug. 1985 – Sep. 1989	LICK	S	41	k
	SGH	Sep. 1992 – Sep. 1996	PAL	S	61	l
Total					3806	

Telescope Codes

[1] : 2.5m Isaac Newton Telescope
[2] : 3.9m Anglo-Australian Telescope
[3] : 3m Shane Telescope
[4] : Hale 5m Telescope
[5] : Kitt Peak 2.1m Telescope
[6] : 2.4m Du Pont Telescope
[7] : ESO 1.5m Telescope
[8] : ESO 3.6m Telescope

Reference Codes

a : This thesis
b : Smith et al. (1997)
c : Smith et al. (1998)
d : Lucey et al. (1991)
e : Lucey et al. (1997)
f : Lucey & Carter (1988)
g : Lucey et al. (1999)
h : Davies et al. (1987)
i : Dressler et al. (1991)
j : Jørgensen et al. (1995b)
k : Gonzalez (1993)
l : Scodeggio (1997)

from peculiar velocity field studies, rather than from studies of galaxy kinematics, which typically target fewer galaxies. The systems span a date range of 25 years, a period in which dramatic advances were made in spectrograph and detector efficiency, data reduction techniques, etc. However, spectra from all of these datasets have sufficient resolution for reliable determination of central velocity dispersions, as demonstrated in the original papers, and, *a posteriori*, by the intercomparisons presented in this thesis.

At the limit the SMAC sample ($\sim$ 12000 km s^{-1}), a 1% systematic error in σ corresponds to 170 km s^{-1} in peculiar velocity. A systematic difference between the velocity dispersions measured on telescopes in opposite hemispheres would thus generate a spurious bulk-flow signal, of magnitude comparable to the expected random errors. Despite careful attempts to correct the velocity dispersions for aperture effects, there remain significant systematic differences offsets between datasets, as found previously by several studies (Davies et al., 1987; McElroy, 1995; Smith et al., 1997). Such offsets are present between the sets of data presented in this thesis, even where the data derive from the same telescope, and despite the use of similar observational methods and data reduction techniques (see Table 3.3).

Smith et al. (1997) introduced a simultaneous intercomparison method to determine offsets between spectroscopic systems. In this thesis, the Smith et al. algorithm is applied to an enlarged input catalogue consisting of $\sim$3800 velocity dispersion measurements, on 28 systems (including the five reported in this thesis), for $\sim$1700 different galaxies. The input datasets are those of Table 5.1. The method is also used to determine and correct for systematic offsets between Mg_2 datasets.

5.2.1 Method

The determination of systematic offsets can be achieved by intercomparison of results for galaxies common to two or more datasets, or 'systems', each of which is assumed to be internally homogeneous. Corrective offsets are then derived for each system, in order to bring all data sources into an optimally homogeneous catalogue. Since many galaxies have measurements on more than two systems, a simultaneous determination of these offsets is necessary to derive self-consistent offsets. All input velocity dispersion data are are corrected to the standard physical aperture size of $1.19h^{-1}$ kpc, according to Equation 3.5. and the (aperture-corrected) LICK system (Davies et al. 1987) is adopted as a fiducial standard. For the remaining systems, the offsets relative to LICK are obtained as follows:

Let $s = \log \sigma$ and let i,j and k index the measurement, galaxy and system respectively. The corrections Δ_k, needed to bring each system into agreement with

LICK, are determined by minimising a χ^2 statistic

$$\chi^2 = \sum_i \frac{(s_i + \Delta_k - \overline{s}_j)^2}{e_k^2} \tag{5.1}$$

where e_k is the error in s_i (assumed to be the same for all galaxies in a given system) and $\overline{s}_j$ is the error-weighted mean of all corrected measurements of the same galaxy.

The errors, e_k, for each system are determined by adjusting them such that the reduced χ^2 is unity, both when the system is included and when it is excluded from the comparisons. This external error ($e_{\rm ext}$) is typically 10–25% larger than the internal error ($e_{\rm int}$) estimated from repeat measurements on the same system, reflecting effects which cause systematic differences between datasets, but which vary from galaxy to galaxy. Variable seeing is one possible cause, since the effect of poor seeing will depend upon the luminosity profile and velocity dispersion profile of the galaxies observed.

5.2.2 Velocity dispersion

The overlap data set of velocity dispersion measurements (galaxies with velocity dispersions on more than one system) consists of 2226 measurements on 28 systems, for 534 different galaxies.

The many 7S data sources of Davies et al. (1987), have been treated separately, and in order to take account of zero-point differences first reported by Dressler (1984), the 7S LCOHI data have further been subdivided into the three constituent runs from which they derive; these runs are coded LCOHJ, LCOHM, LCOHF. The PAL system contains 7S Palomar observations (see Dressler et al. 1987b) wrongly attributed by Davies et al. (1987) to the LCOHI dataset. Similarly, the data of Jørgensen et al. (1995b) are divided into three subsets: JBC12 represents a merger of their B&C-1 and B&C-2 runs, which used identical instrumentation. Their B&C-3 dataset used a different aperture size, and is accordingly assigned to a separate system, JBC3. The Jørgensen et al. multifibre ('Optopus') data is assigned to the system coded JFKOP.

In deriving the offsets, those galaxies with $\overline{s} < 2$ are excluded from the fit, as these may be subject to larger random and systematic errors (Jørgensen et al. 1995b). Also excluded are those individual velocity dispersion measurements which are inconsistent at the 3.5 standard deviation level with the other data for the same galaxy (it is likely that some of these highly discrepant data result from misidentifications). The inconsistent velocity dispersion measurements are recorded in Table 5.2.

The results of the velocity-dispersion intercomparison are shown in Table 5.3, which presents the *corrections* required to bring all datasets onto a common system. Note that, because of the interdependencies between the different corrections, the simple

Table 5.2: Velocity dispersion measurements in conflict (at the 3.5 standard deviation level) with other measurements for the same galaxy. These data were not used in determining the system offsets.

Galaxy	Dataset	$(\log\sigma)_{Ex}$	Discrepancy (std. dev.)
A1656:D-136	INT90	2.0890	3.8
A1656:D-239	LCOHM	2.3891	4.0
A4038:D-040	FOCAP	1.9339	4.9
A4038:D-040	FOCAP	2.2116	4.9
N0386	KPNO	1.7879	4.3
N0548	LICK	1.8848	4.8
N3377	I97M	2.2214	3.6

pair offsets quoted in Table 3.5, eg for I95 – LICK, are not trivially related to those derived here by simultaneous fits. The required corrections are span a range from -0.03 (equivalent to rescaling FP distances by a factor 0.91) for PAL, to $+0.04$ (FP distance rescaling of 1.14) for I97A. Around half of the systems, including those of Chapter 3 require corrections which are significant at the $>2\sigma$ level.

The comparison of each dataset with the merged system is shown in Figures 5.1–5.2. Here the 'merged' system is the error-weighted mean of the *rest* of the data, after correction for system offsets. Figure 5.3 summarizes the offsets found for the 28 systems, and demonstrates graphically the magnitude and significance of the necessary corrections. Note that some systems are subject to offsets of $\sim$7% relative to LICK.

5.2.3 Errors in the system matching process

The correction errors, e_Δ, in Table 5.3 indicate the success of the homogenization procedure, in terms of the 'rigidity' of the resulting merged catalogue of velocity dispersions. The new systems of Chapter 3 are tied to the standard system to a mean uncertainty of 0.0055 dex, equivalent to a 1.8% distance error from the Fundamental Plane relation. This small systematic uncertainty reflects the care taken to obtain high-quality spectra and a sufficient number of overlapping observations. If the offsets had been deduced directly from the SMAC – LICK offsets of Table 3.5, then the mean systematic uncertainties in the corrections would have been 3.3%, so the simultaneous intercomparison method represents a factor of $\sim$2 improvement on more simplistic schemes. For systems other than those of Chapter 3, the system matching errors are rather larger. For those datasets which contribute substantially to the final FP catalogue for SMAC clusters eg (TEK94, EEV93, FOCP2, JBC12, JFKOP), the systematic errors are rather larger, at $\sim$0.008 in $\log\sigma$, or $\sim$2.5% in distance.

Table 5.3: Results of the velocity dispersion system-matching process. The systems are coded as in Table 5.1. For each system, $N_{\rm gal}^{\rm (ov)}$ is the number of galaxies in common with other datasets, and $N_{\rm meas}^{\rm (ov)}$ is the total number of observations of those galaxies. The aperture correction applied (prior to comparison) is defined by the value of $2r_{\rm ap}$ (see Equation 3.8), expressed in arcsec. The correction required to bring each dataset into agreement with the standard system is Δ, while its uncertainty is e_Δ. Each system's random error per measurement is given by $e_{\rm ext}$ (see text).

Name	$N_{\rm gal}^{\rm (ov)}$	$N_{\rm meas}^{\rm (ov)}$	$2r_{\rm ap}$	$e_{\rm ext}$	Δ	e_Δ
LICK	168	320	2.95	0.055	$\equiv 0$	$\equiv 0$
A94	51	79	3.91	0.018	+0.0263	0.0054
A95A	51	69	3.91	0.022	+0.0165	0.0051
A95B	40	52	3.91	0.027	+0.0288	0.0068
I95	74	101	3.69	0.029	+0.0187	0.0053
I97A	121	134	3.69	0.035	+0.0398	0.0044
I97B	131	187	3.69	0.029	−0.0061	0.0042
TEK94	103	162	3.69	0.030	−0.0081	0.0055
EEV94	16	16	3.64	0.040	−0.0112	0.0103
EEV93	72	92	3.64	0.042	+0.0001	0.0068
INT92	67	82	3.64	0.054	+0.0104	0.0087
INT90	66	99	3.94	0.041	−0.0166	0.0065
FOCP2	51	81	2.70	0.043	−0.0024	0.0089
LC	59	72	2.70	0.040	−0.0135	0.0078
JBC12	43	50	5.00	0.036	+0.0249	0.0073
JBC3	19	20	4.70	0.045	−0.0172	0.0130
JFKOP	49	88	2.60	0.042	+0.0154	0.0106
GONZA	38	38	3.69	0.011	+0.0271	0.0046
SGH	83	83	4.01	0.045	+0.0086	0.0077
DF	48	48	3.28	0.041	+0.0102	0.0089
PAL	23	23	3.28	0.045	−0.0304	0.0121
KPNO	26	27	3.57	0.065	+0.0160	0.0136
LCOHF	31	31	4.56	0.030	−0.0173	0.0076
LCOHM	64	72	4.56	0.031	+0.0100	0.0062
LCOHJ	42	61	4.56	0.036	+0.0091	0.0085
LCOLO	31	63	3.28	0.041	+0.0188	0.0082
A1	29	34	4.50	0.042	−0.0006	0.0107
A2	25	42	4.50	0.057	+0.0240	0.0097

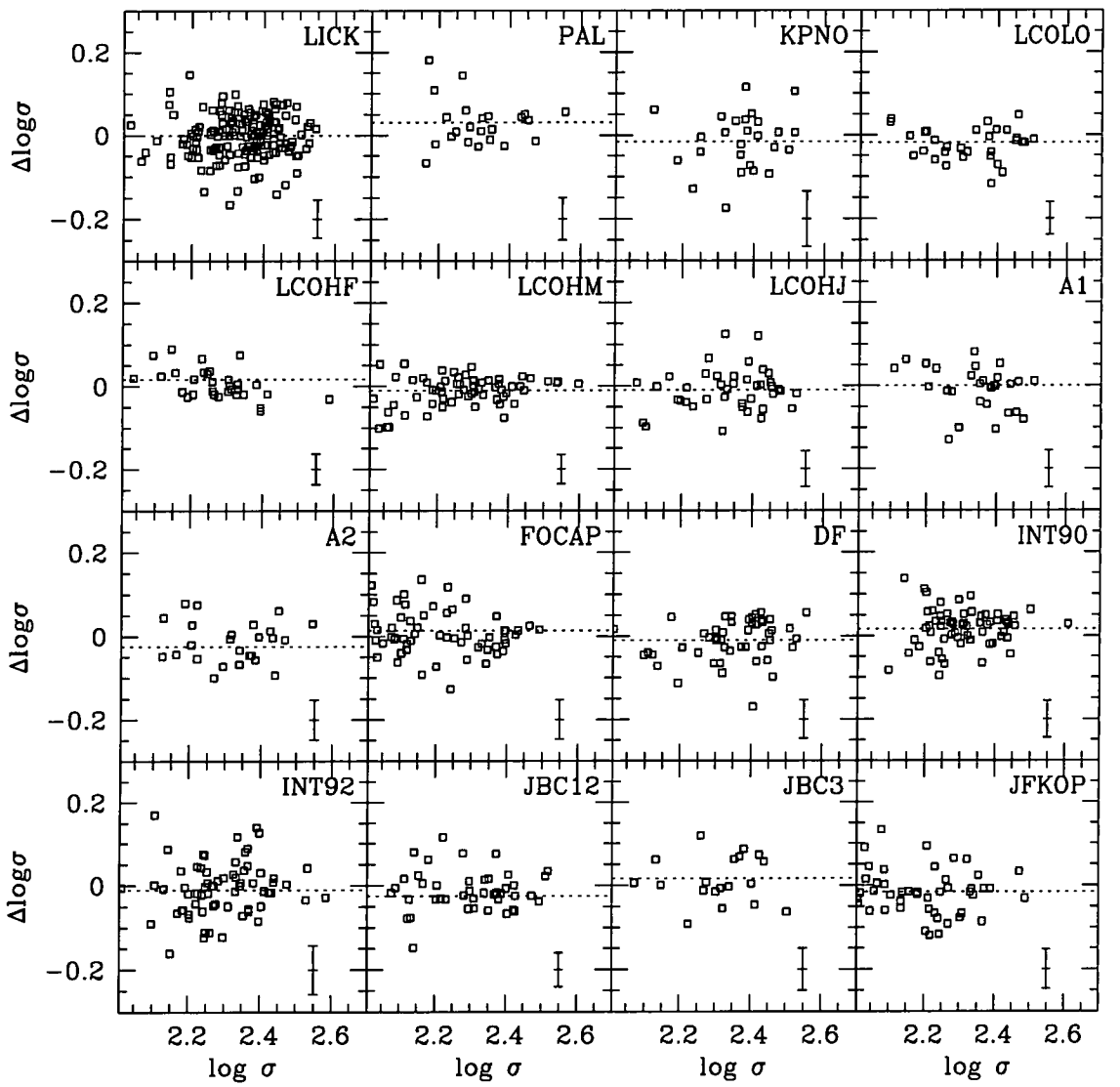

Figure 5.1: Velocity dispersion system-matching results for 16 datasets. For each galaxy on system PAL (for instance), we calculate: (1) the weighted mean of $\log\sigma$ from PAL (aperture corrected, but with *no* system offset), and (2) the weighted mean $\log\sigma$ from merging the *fully*-corrected data from all *other* systems. The plots show the differences $\Delta(\log\sigma)$ between these 'PAL-only' and 'corrected all-but-PAL' averages. The mean difference from zero therefore represents the systematic offset of the dataset from the standard defined by all others after correction. The bar in the lower-left of each panel represents the external random error per galaxy, $e_{\rm ext}$.

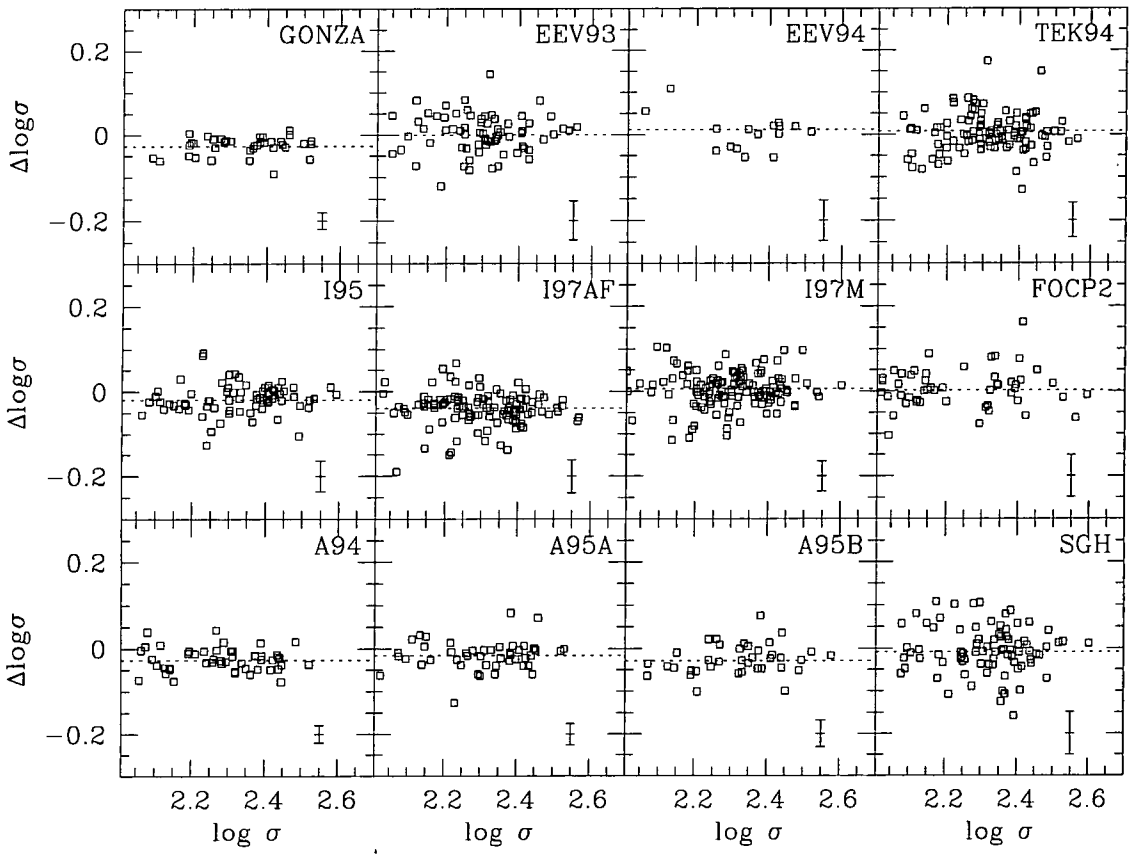

Figure 5.2: As for Figure 5.1 for the remaining systems.

The errors were determined by constructing realisations of the input catalogue, through bootstrap resampling the master data file, and recomputing the the corrections from these resampled catalogues. The use of these bootstrap corrections allows determination of not only the errors, but also the correlations between the system offsets. This covariance arises because some pairs of systems (eg A94 and A95A) have extensive overlap, and thus 'float together' in the fits. From the sets of bootstrap-determined corrections, a series of perturbed realisations of the final merged dataset were constructed. In Chapters 6–7, these catalogues are used to determine systematic errors on cluster distances, bulk flows etc, fully accounting for the covariance between the system corrections.

These bootstrap datasets will be employed in Chapter 6 to determine the 'system-matching' errors on the cluster distance estimates, and in Chapter 7 to quantify the resulting systematic uncertainty in measurement of the bulk-flow and other parameters of the velocity field.

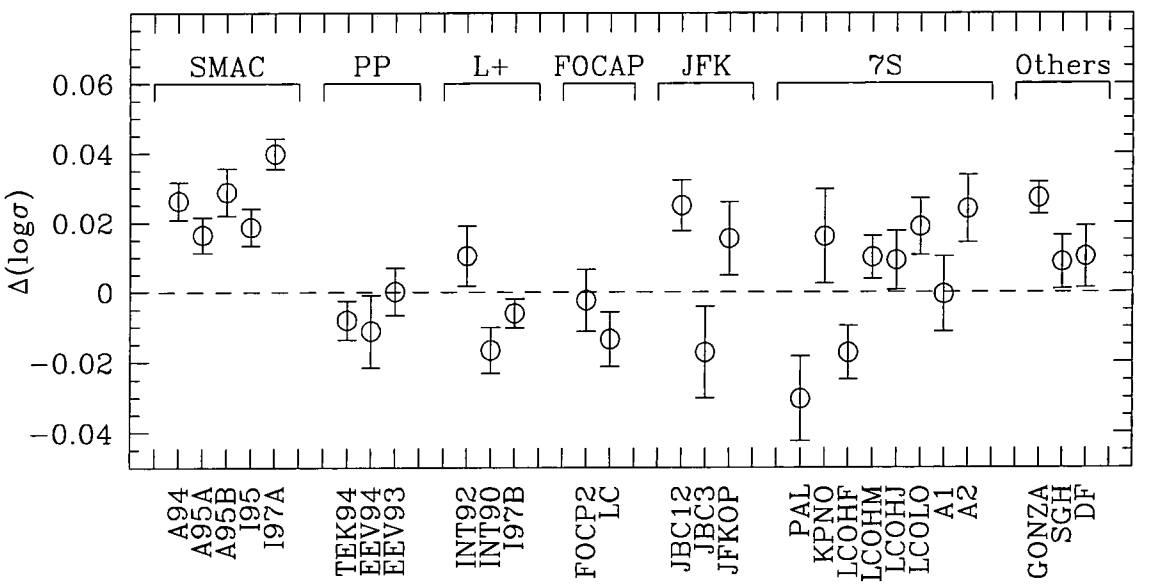

Figure 5.3: Illustration of the magnitude, sense and significance of the offsets of the input datasets relative to the standard system defined by LICK. The systems are grouped according to roughly the same scheme as in Table 5.1. Note that the five SMAC systems have amongst the most significant offsets ($\sim 6 \pm 1\%$ in σ). However, the hypothesis that no offsets are observed is rejected at the $> 99.9\%$ confidence level, even after exclusion of A94, A95A, A95B, I95 I97A and GONZA.

Table 5.4: Magnesium index measurements in conflict ($> 3.5\sigma$) with other measurements for the same galaxy. These data are excluded prior to determination of the system offsets, as are all those excluded from the velocity dispersion matching.

Galaxy	Dataset	$(Mg_2)_{Ex}$	Discrepancy (σ)
A0539:D-053	JFKOP	0.2337	3.5
A1016:SMC-A	A95A	0.1823	4.6
N1282	PAL	0.2296	5.2
N1403	JBC12	0.2093	4.5
N1549	A2	0.3444	4.1
N1549	JBC12	0.2533	4.1
N4486	A94	0.3186	4.0
N4564	EEV93	0.3499	4.3
N6702	TEK94	0.2883	4.0

5.2.4 Magnesium index

The same simultaneous intercomparison scheme has been used to determine the corrections required to bring the various sources of magnesium index data onto a common system.

The overlap dataset of Mg_2 measurements (galaxies with measurements on more than one system) consists of 1854 measurements of 434 different galaxies on 24 systems (the LC, FOCP2, EEV94, SGH) systems have no Mg_2 data). Mg_2 measurements inconsistent at the 3.5σ level with other data for the same galaxy are excluded from the comparison, as are data for the galaxies excluded in the velocity dispersion matching.

Table 5.5 presents the required corrections to the Mg_2 index measurements, and Figure 5.4 illustrates the result of the procedure, as shown previously for the velocity dispersions. Many systems exhibit highly significant offsets of 0.01–0.02 mag in Mg_2. The Mg_2 offsets can be determined with precision of $\sim$0.003 mag or better.

5.2.5 Correction and combination of spectroscopic data

Having determined the corrections between systems, the fully-corrected velocity dispersion and magnesium indices can be computed, and all measurements for each galaxy can be combined to yield the final data for that galaxy. The recipe for this process is as follows:

1. The velocity dispersion and Mg_2 from the published source (Table A.1 for new data) are, where necessary, de-corrected by the original aperture correction. The standard aperture corrections (as given by r_{ap} in Table 5.3) are then applied. The distance used in calculating the aperture correction is the redshift of the cluster,

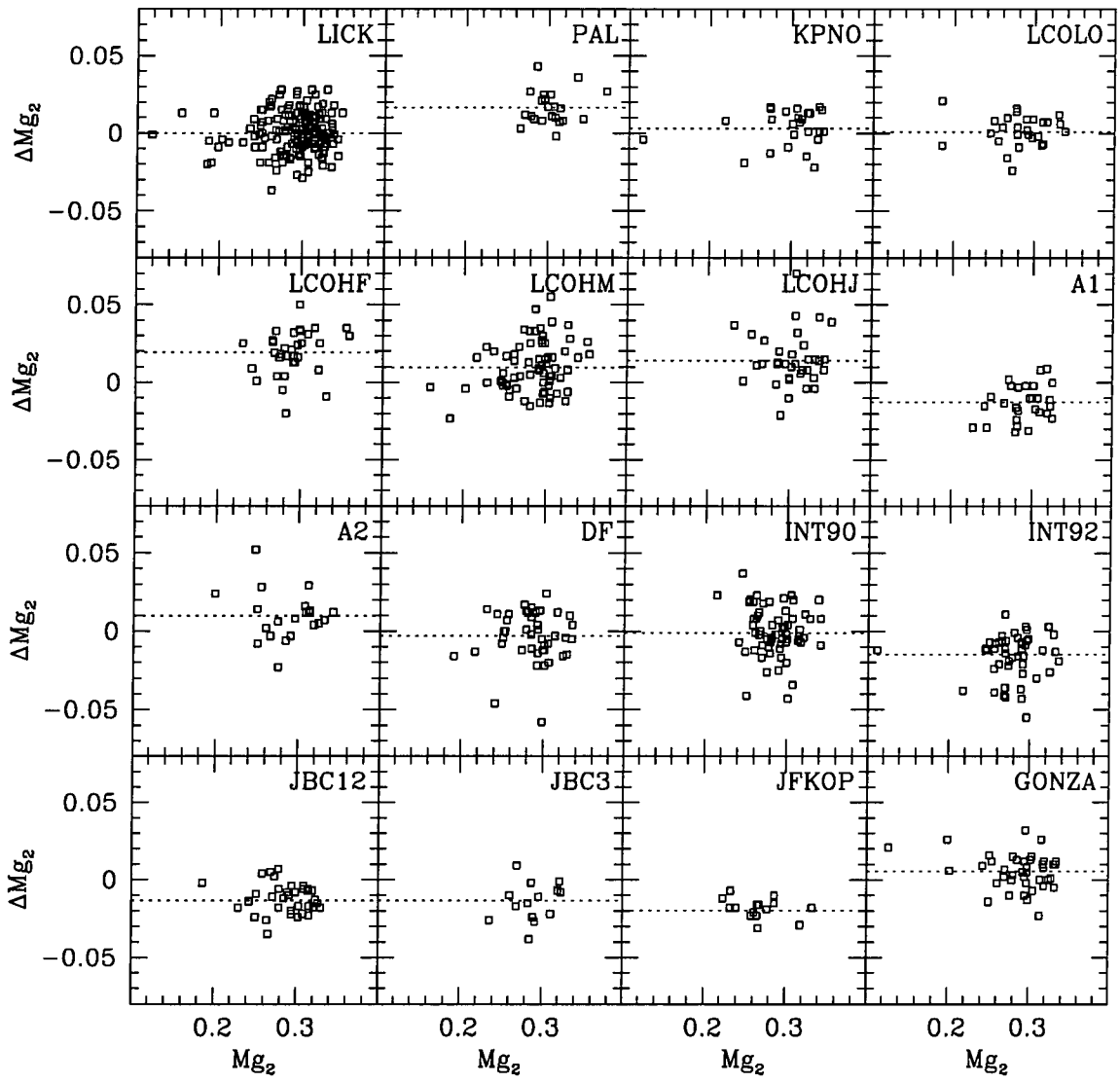

Figure 5.4: Mg_2 system matching results for 16 datasets. Details are as for Figure 5.1.

Table 5.5: As for Table 5.3, but for the Mg_2 measurements.

Name	$N_{\rm gal}^{\rm (ov)}$	$N_{\rm meas}^{\rm (ov)}$	$2r_{\rm ap}$	$e_{\rm ext}$	Δ	e_Δ
LICK	174	340	2.95	0.010	$\equiv 0$	$\equiv 0$
PAL	22	22	3.28	0.009	−0.0164	0.0029
LCOLO	28	57	3.28	0.011	−0.0008	0.0024
LCOHF	33	33	4.56	0.013	−0.0193	0.0032
LCOHM	69	77	4.56	0.014	−0.0095	0.0020
LCOHJ	35	53	4.56	0.016	−0.0141	0.0032
KPNO	25	28	3.57	0.011	−0.0032	0.0025
A1	28	33	4.50	0.010	+0.0123	0.0024
A2	21	33	4.50	0.012	−0.0096	0.0027
DF	43	43	3.28	0.014	+0.0030	0.0026
JBC12	35	41	5.00	0.010	+0.0134	0.0020
JBC3	14	15	4.70	0.010	+0.0136	0.0032
JFKOP	15	28	2.60	0.010	+0.0198	0.0028
INT90	66	99	3.94	0.015	+0.0012	0.0019
INT92	49	59	3.64	0.013	+0.0149	0.0023
GONZA	40	40	3.69	0.009	−0.0054	0.0019
EEV93	67	87	3.64	0.012	+0.0140	0.0019
TEK94	92	144	3.69	0.009	+0.0051	0.0015
A94	47	72	3.91	0.008	−0.0006	0.0014
A95A	52	70	3.91	0.009	+0.0032	0.0016
A95B	39	51	3.91	0.007	+0.0073	0.0017
I95	75	102	3.69	0.010	+0.0142	0.0013
I97A	122	136	3.69	0.011	+0.0110	0.0012
I97B	132	191	3.69	0.009	+0.0118	0.0011

or (in the case of field galaxies) the redshift of the galaxy itself.

2. The $\log\sigma$ and Mg_2 are further adjusted by the system corrections listed in Tables 5.3 and 5.5.

3. The corrected velocity dispersion measurements are combined as a weighted mean of $\log\sigma$, with weights accorded as the square of the external errors $e_{\rm ext}$. The measurements flagged as $> 3.5\sigma$ deviants are not included in the mean. A $\log\sigma$ error is calculated for the weighted mean in the standard way. An equivalent combination scheme is employed for the Mg_2 data.

4. A mean heliocentric redshift is computed from the reliable sources (generally the same data from which the velocity dispersion data are drawn).

Table A.3 presents the fully corrected and combined spectroscopic data, scaled to the 'standard' system, for galaxies in the cluster sample. This table includes only those galaxies for which complementary photometric data is available.

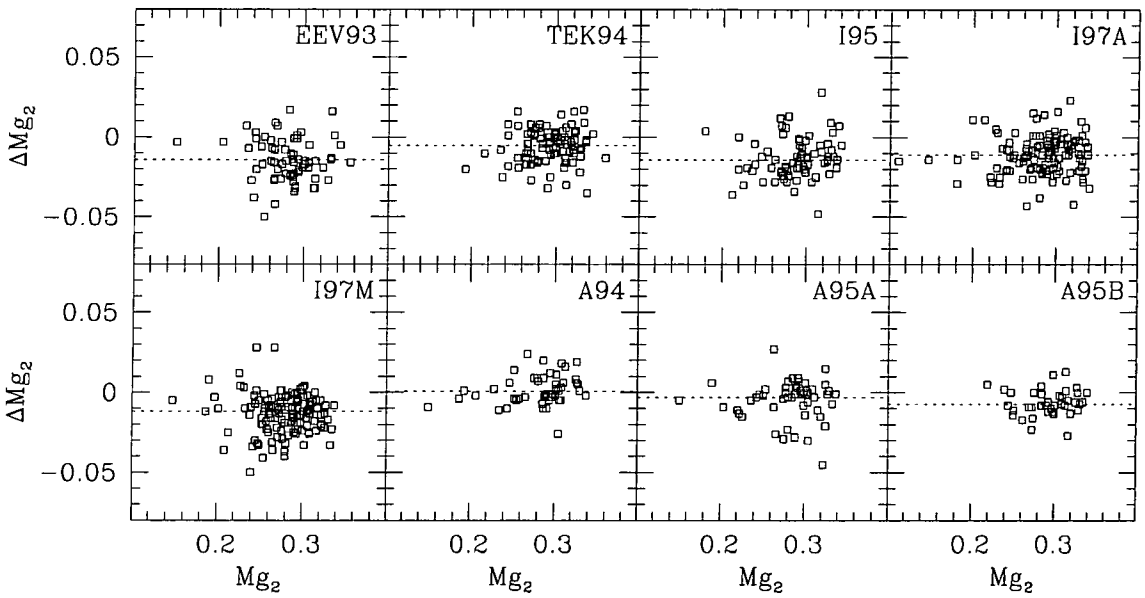

Figure 5.5: As for Figure 5.4, for the remaining Mg_2 systems.

Table 5.6: Sources of photometric data

System	Band	Telescope	Dates	Reference
JKT	R	1.0m JKT	Feb. 1995 & Jan. 1997	This thesis
CTIO	R	CTIO 0.9m	Feb. 1995 & Jan. 1997	This thesis
MSO98	R	MSSS0 40"	Apr. 1998	Unpublished
STEEL	R	2.5m INT	Mar. 1994	Steel (1998)
EFAR	R	Many	Mar. 1987 – Oct. 1993	Saglia et al. (1997b)
FOCAP	V	Many	Mar. 1988 – Apr 1993	Lucey et al. (1999)
JFK	r	Danish 1.5m	Apr. 1989 – Sep. 1992	Jørgensen et al. (1995a)
PP	R	1.0m JKT	Nov. 1993 & Sep. 1994	Smith et al. (1997)
LGSC	V	1.0m JKT	Jun. 1991	Lucey et al. (1997)

5.3 Standardization of photometric data

Photometric data for the catalogue is drawn from the new data reported in Chapter 4, and from a number of literature sources as summarized in Table 4.1. Prior to intercomparing photometric sources, all photometric data have been corrected for galactic extinction according to the map of Schlegel, Finkbeiner & Davis (1998), after decorrecting for the extinction term (generally from Burstein & Heiles 1984), applied by the original authors.

In contrast to the spectroscopic data, the FP photometric parameter combination ($\log A_e - 0.32\langle\mu\rangle_e$) is subject to small (~2%) random errors (Table 4.3), so that systematic offsets between datasets can be determined very precisely. In the photometric

Table 5.7: Measurements of $\log A_e - 0.32\langle\mu\rangle_e$ in conflict at the $> 3.5\sigma$ level with other data for the same galaxy (after allowance for early-type galaxy colours). These measurements are excluded from the photometric system-matching fits.

Galaxy	Dataset	$(\log A_e - 0.32\langle\mu\rangle_e)_{Ex}$	Discrepancy (σ)
A1060:JFK-R261	MSO98	-5.7978	3.0
A1060:JFK-R261	MSO98	-5.8234	3.0
A1656:D-120	JFK	-5.2780	13.4
A1656:D-120	STEEL	-5.5194	13.4
A1656:D-121	JFK	-5.4824	10.6
A1656:D-121	STEEL	-5.2918	10.6
A1656:D-149	JFK	-5.8260	4.2
A1656:D-171	JFK	-5.7188	4.3
A1656:D-171	STEEL	-5.6406	4.3
A1656:D-191	JFK	-5.5984	4.7
A1656:D-191	STEEL	-5.6826	4.7
A1656:D-192	JFK	-5.5724	5.7
A1656:D-192	STEEL	-5.6756	5.7
A1656:D-193	JFK	-5.6872	3.4
A3558:FCP-26	MSO98	-5.5380	3.1
N3311	JFK	-5.0120	3.8
N4850	JFK	-5.3268	3.8
N4876	STEEL	-5.4572	3.9
A2199:B-095	LGSC	-5.6114	3.5
A3558:FCP-26	FOCAP	-5.5740	3.1
S0761:FCP-26	FOCAP	-5.7608	6.2

case, substantial offsets are to be expected between data in different passbands, reflecting the average colours of early-type galaxies.

In order to test for any global systematic offsets between photometry systems, the system matching algorithm has been applied to the sample of galaxies with repeated photometric measurements. The comparison is made for the parameter combination $\log A_e - 0.32\langle\mu\rangle_e$ which enters into the FP distance indicator. Nine systems are compared; the overlap sample comprises 803 photometric measurements for 266 galaxies. The R-band dataset of Steel (1998) is adopted as a fiducial standard in the fits. Figure 5.6 presents results in a format analogous to those for $\log\sigma$ and Mg_2. In the photometric case, large offsets are observed (as expected) for systems based on V-band and r-band imaging. The slight trends visible in the panels for V-band systems (LGSC and FOCAP) are a manifestation of the well-known colour–magnitude relation for early-type galaxies (Bower, Lucey & Ellis 1992). The offsets and their errors are summarised in Table 5.8.

The photometric offsets obtained by the above process are determined to a precision of 0.015–0.055 in $\log A_e - 0.32\langle\mu\rangle_e$ (equivalent to 0.5–1.3% in distance) and are

Table 5.8: Photometric system offsets. The offsets Δ are in the quantity $\log A_e - 0.32\langle\mu\rangle_e$. The zero-offset Δ_0 is that expected from the average colours of early-type galaxies, taken to be $< r - R >= 0.33$ and $< V - R >= 0.57$. Note that here the number of overlap measurements ($N^{(ov)}_{meas}$) is not always well defined since some sources (eg EFAR) quote only averaged parameters for each galaxy.

Name	band	$N^{(ov)}_{gal}$	$N^{(ov)}_{meas}$	e_{ext}	Δ	e_Δ	Δ_0
STEEL	R	114	208	0.010	$\equiv 0$	$\equiv 0$	0.0000
PP	R	57	83	0.010	+0.0001	0.0021	0.0000
JKT	R	47	50	0.010	+0.0031	0.0030	0.0000
CTIO	R	20	25	0.013	-0.0012	0.0055	0.0000
EFAR	R	100	100	0.021	+0.0006	0.0027	0.0000
MSO98	R	53	80	0.006	+0.0002	0.0030	0.0000
JFK	r	120	120	0.015	+0.1046	0.0019	0.1056
FOCAP	V	47	47	0.010	+0.1880	0.0038	0.1824
LGSC	V	90	90	0.010	+0.1846	0.0016	0.1824

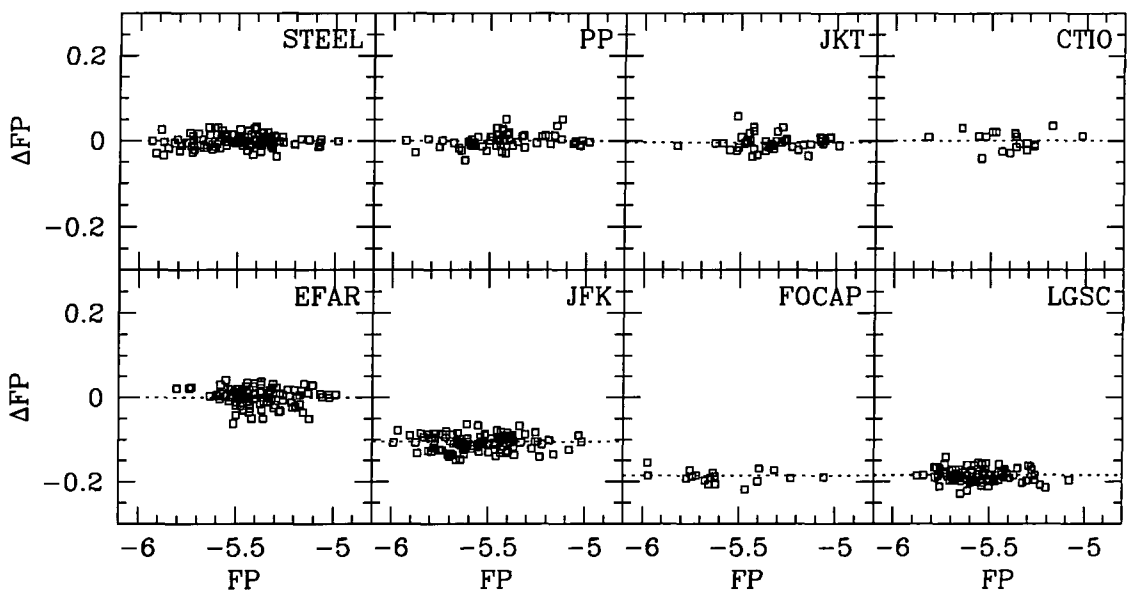

Figure 5.6: System matching results for photometric parameter $FP = \log A_e - 0.32\langle\mu\rangle_e$. Details as for Figure 5.1. The large offsets observed in the case of JFK, FOCAP and LGSC are a result of the different photometric passbands used for this data. The slight trends in the residuals for FOCAP and LGSC reflect the colour-magnitude relation for early-type galaxies.

consistent with zero (at the 1.5σ level) in all cases, after accounting for the mean colours. The assumed colours are those determined by Smith et al. 1997, from a smaller sample of galaxies. Since any offsets at this level are negligible in comparison to other sources of random and systematic error, the parameters are corrected only for the mean colours of early-type galaxies ($< r - R >= 0.33$ and $< V - R >= 0.57$). The parameters $\log R_e$ and $\langle\mu\rangle_e$ are combined as simple means, after these colour corrections have been applied.

5.4 Definition of a revised cluster sample

Having constructed fully corrected and merged spectroscopic and photometric catalogues, attention is now turned to the final selection of a cluster sample for use in determination of distances and peculiar velocities.

The total merged datasets contain velocity dispersion data for 1629 galaxies, Mg_2 data for 1209 galaxies and photometric parameters for 1759 galaxies. For only 903 galaxies, however, does the catalogue contain both velocity dispersion *and* photometric parameters, as necessary for construction of the FP[1]. In order to realise distance errors of $\sim 10\%$ per cluster, each cluster in the final sample must be sampled by *at least four* member galaxies, each with spectroscopic and photometric data. The following sections discuss the method by which galaxies have been assigned to clusters, and discuss the details of the revised cluster sample which results from this process.

5.4.1 Cluster membership criteria

To avoid selection biases in a 'Method-I' velocity field analysis (as is performed in Chapters 6–7), it is necessary to define clusters by criteria which are independent of the FP data itself. The cluster definition procedure is therefore based only upon angular position and redshift data. In defining cluster redshifts and velocity dispersions, galaxy redshifts for an extended sample of early-type galaxies (including galaxies without full FP data) is employed. The following iterative scheme is followed:

1. The projected centre of each cluster is defined by the position of the brightest cluster galaxy (BCG), defined here to be the galaxy with brightest total magnitude. The BCG selected on this definition usually accords with that of Lauer & Postman (1994, LP) for clusters in their sample.

[1]There are 856 galaxies with photometry but no dispersions, mostly from the EFAR project, whose spectroscopic data is as yet unpublished. Of 726 galaxies with spectroscopy but no photometry, approximately two thirds are local 'standards', field galaxies or members of groups and clusters which do not make it into the final SMAC cluster sample.

2. Initial estimates for the mean cluster redshift, $cz_{\rm cl}$, and and velocity dispersion, $\sigma_{\rm cl}$, are obtained from the compilation of Fadda et al. (1996). Where no values are tabulated by Fadda et al., the initial estimate is made from the early-type galaxy sample.

3. Cluster membership is then limited to those galaxies within $2.6\sigma_{\rm c}$ of $cz_{\rm cl}$, and within a projected radius of $R_{\rm cl}$ of the cluster centre. This defining projected radius also scales with the cluster velocity dispersion: $R_{\rm cl} = 3 \times [cz_{\rm cl}/(1000 \text{ km s}^{-1})]\, h^{-1}$ Mpc.

4. The above procedure is iterated, removing outliers from the clusters at each stage, and recomputing the mean cluster redshift $cz_{\rm cl}$. The cluster velocity dispersion $\sigma_{\rm cl}$ is held fixed where a literature value is available. In other cases, a value is iteratively determined from the early-type galaxy data. A minimum of 500 km s^{-1} is adopted to prevent cluster redshift errors from being underestimated through undersampling of the redshift histogram. Note that this also ensures $R_{\rm cl} \geq 1.5h^{-1}$ Mpc, ie an Abell radius.

5. Finally, a few galaxies lie satisfy the membership criteria for two clusters. In such cases, the galaxy is assigned to the cluster which minimizes the quantity

$$C = \left[\frac{cz_{\rm gal} - cz_{\rm clus}}{\sigma_{\rm cl}}\right]^2 - 4\log(1 - R_{\rm gal}/R_{\rm cl}), \qquad (5.2)$$

where $cz_{\rm gal}$ is the redshift of the galaxy, and $R_{\rm gal}$ is its separation from the cluster centre, in h^{-1}Mpc.

Galaxies with morphological types later than S0 are rejected from the catalogue outright, as are galaxies which show obvious disturbances, signs of interaction, dust lanes, and those whose photometric parameters have been flagged as unreliable.

Finally, clusters are defined to be 'adequately sampled' if *four or more* early-type galaxies, carrying complementary spectroscopic and photometric data, remain in the sample after applying the above criteria. For a typical FP scatter of $\sim$ 20%, this population cut ensures that the largest distance error, for a cluster at the limit of the survey, is $\sim$1200 km s^{-1}, or approximately three times the expected rms peculiar velocity of clusters.

The distribution of galaxies within the SMAC sample clusters is illustrated, along with other details of the cluster definition criteria, in the charts of Appendix B.

5.4.2 Drop-out clusters

After removal of interlopers and galaxies with unsuitable morphologies a total of 25 clusters from the originally selected sample (ie LP clusters with $cz < 12000$km s^{-1}),

are found to have fewer than four members with FP data. These 'drop-outs' are in some cases clusters for which EFAR spectroscopy is awaited (9 clusters), while in other cases SMAC observations yielded insufficient data. The following notes summarize the individual cases:

A0260 : EFAR cluster, SMAC observed 5 galaxies (drawn from EFAR candidates list, of which 2 spirals rejected.)

A0397 : EFAR cluster, not observed by SMAC.

A0496 : EFAR cluster, SMAC observed 3 galaxies (drawn from EFAR candidate list).

A0634 : SMAC spectroscopy for 7 galaxies, of which 3 have photometry.

A0779 : SMAC spectroscopy for 6 galaxies, of which 2 have photometry.

A1142 : Background contamination. 3 member galaxies have SMAC spectroscopy, of which two have photometry.

A1185 : 4 galaxies with SMAC spectroscopy, no photometry.

A1267 : Background contamination. 2 member galaxies have SMAC spectroscopy, no photometry.

A1836 : No spectroscopy.

A2147 : EFAR cluster, not observed by SMAC.

A2151 : EFAR cluster, not observed by SMAC.

A2162 : EFAR cluster, not observed by SMAC.

A2197 : EFAR cluster. Three galaxies included with A2199 (see below).

A2247 : EFAR cluster, not observed by SMAC.

A2666 : EFAR cluster, FP data for 2 galaxies. Not included with A2634 (see below).

A2731 : No spectroscopy.

A2870 : No spectroscopy.

A2896 : No spectroscopy.

A2911 : 3 galaxies observed.

A3542 : Severe background contamination. Only 1 galaxy observed has the nominal cluster redshift of $cz \sim 10000$km s^{-1}. From background group at $cz \sim 15000$km s^{-1}, 4 have spectroscopy but no photometry.

A3560 : Close pair with A3565. 1 galaxy observed.

A3565 : Close pair with A3560. Spectroscopy (mostly FOCAP) for 7 galaxies, of which 6 have no photometry.

A3572 : Merged with A3571 (see below).

A3575 : Merged with A3571 (see below).

A3698 : No spectroscopy.

A3747 : Photometry for 6 galaxies, of which 3 have no spectroscopy.

5.4.3 Extra clusters

While a number of clusters drop out of our original sample, others may be added to it, where sufficient data is available. These 'extra' clusters are in some cases Abell clusters which, having anomalous BCGs, were excluded from the sample of LP. In addition, there are a number of extra clusters which are not included in the Abell catalogue. The following notes provide information on the extra clusters included in the catalogue:

7S21 : (=PCC S49-147), PP region; Smith et al. (1997) observed 7 galaxies.

A0400 : LP reject (anomalously faint BCG); EFAR cluster; SMAC observed 7 galaxies (from EFAR candidate lists).

A0426 : (=PERSEUS), PP region; LP reject (BCG has E+A spectrum); 28 galaxies mostly from Smith et al. (1997).

A3558 : Beyond nominal SMAC depth ($cz \sim 14500$); Shapley region; 29 galaxies from Lucey et al (1999).

A3716 : Beyond nominal SMAC depth ($cz \sim 13500$); 17 galaxies from Lucey et al (1999).

H0122 : (=HMS0122+3305, =N0507grp); PP region; 8 galaxies mostly from Smith et al. (1997).

J8 : EFAR cluster; PP region; 10 galaxies mostly from Smith et al. (1997).

MKW12 : (=Z74-23, =PCC N67-336); 4 galaxies from Lucey et al. (1999).

PISC : (=PISCES, =N0383grp); PP region; 22 galaxies mostly from Smith et al. (1997).

S0301 : (=DC0247-31); 14 galaxies from Lucey et al. (1999).

S0753 : GA region; 15 galaxies from Jørgensen et al. (1996).

S0761 : GA region; 10 galaxies from Lucey et al. (1999).

S0805 : (=PAVO-II); GA region; 9 galaxies mostly from Lucey et al. (1999).

Very local ($cz < 2000$km s^{-1}) clusters and groups such as Virgo, Leo, Fornax, Doradus are not included as 'extras' in the sample. These systems would carry a very high weight in the FP and flow model fitting. Furthermore, the following clusters, which have been the target of previous FP observations are *not* included as extras:

A3627 : Spectroscopy for 11 galaxies from Lucey et al. (1999), but no photometry due to stellar contamination ($b = -7°$)

S0639 : (=VELA) 10 galaxies from Jørgensen et al. (1996); Rejected here due to stellar contamination ($b = +11°$)

GRM15 : 4 galaxies from Jørgensen et al. (1996), but only 2 have reliable morphology.

5.4.4 Treatment of double clusters

A fraction of the sample clusters exhibit substructure on the sky, in redshift space, or both. In some cases, the subclusters are distinguished by different names, in others a single nominal cluster includes several structures. The treatment of such cases in the SMAC sample follows the objective criteria of Section 5.4.1. The following cases are worth noting:

A0548 : Substructure on sky. Field observed by Lucey et al. falls between two subclusters.

A0569 : Substructure on sky and in cz. Two components (A0569S, A0569N) separated by $2 - 3\,h^{-1}$Mpc. Adopting either component, the majority of galaxies from the other component are excluded by the assignment criteria.

A1736 : Substructure in cz. The BCG of LP is in background group at $cz \sim 13000$. SMAC sample lies at $cz \sim 10000$.

A2197/A2199 : Cluster pair. Three galaxies nominally associated with A2197 satisfy the membership criteria for A2199, and are assigned to this cluster.

A2634/2666 : Cluster pair with separation $\sim 3\,h^{-1}$Mpc. The two observed A2666 galaxies do not satisfy the criteria for inclusion with A2634.

A3526 : (=CENTAURUS). Well known cz substructure (Lucey, Currie & Dickens 1986). The iterative scheme assigns most galaxies to a single cluster, which includes both the Cen30 and Cen45 systems.

A3571/A3572/A3575 : There are very few galaxies nominally assigned to clusters A3572 and A3575. All these galaxies lie satisfy the membership criteria for A3571, and are assigned to this cluster.

5.4.5 Properties of the revised cluster sample

The final SMAC sample includes 56 clusters, with a total of 725 early-type galaxies satisfying the membership criteria. The cluster sample is presented in Table 5.9, and its distribution on the sky is shown by Figure 5.7. Note that while the 25 clusters within $cz = 8000\,\mathrm{km\ s^{-1}}$ are concentrated towards the GA ($l \sim 310°, b \sim +30°$) and PP ($l \sim 140°, b \sim -30°$) directions, the more distant half of the sample has a fairly uniform distribution. The final sample has a median depth of $8400\,\mathrm{km\ s^{-1}}$, which is $\sim 1000\,\mathrm{km\ s^{-1}}$, smaller than the median depth of the original target sample.

5.5 Summary

In this chapter, the final SMAC sample has been constructed by merging newly-obtained spectroscopic and photometric data with an extensive compilation of data from the literature. A careful process of simultaneous comparisons has been employed to fit for the required 'system corrections', which can be significant in the case of spectroscopic datasets. The method presented here allows the corrections to be determined to 1–4%, and for the effects of the remaining errors (including covariance) to be propogated into bulk-flow determinations.

Galaxies have been assigned to 56 clusters according to objective criteria based on coordinates in redshift-space. The fully corrected and merged catalogue of FP data, for 725 galaxies, has been presented.

Table 5.9: The revised SMAC cluster sample. Equatorial and galactic coordinates are given, followed by the mean B-band galactic extinction (from Schlegel, Finkbeiner & Davis 1998). The adopted mean (heliocentric) redshift and cluster velocity dispersion are given as $cz_\odot$ and σ_c. N_{FP} is the number of cluster members in the final FP catalogue.

Cluster	RA (2000)	Dec (2000)	l	b	A_B	$cz_\odot$	σ_c	N_{FP}
S21	00 : 21.2	+22 : 21	113.8	−40.0	0.26	5991	500	7
A0076	00 : 39.4	+06 : 44	117.6	−56.0	0.16	11498	500	6
A0189	01 : 24.6	+02 : 3	139.6	−59.8	0.13	9554	500	5
A0194	01 : 26.0	−01 : 20	142.2	−62.9	0.16	5226	500	18
A0262	01 : 52.8	+36 : 9	136.6	−25.1	0.30	4844	525	14
A0347	02 : 25.4	+41 : 49	141.1	−17.7	0.28	5707	736	9
A0400	02 : 58.4	+06 : 36	169.9	−44.4	0.72	6768	599	8
A0426	03 : 19.8	+41 : 31	150.6	−13.3	0.67	5183	1026	28
A0539	05 : 16.6	+06 : 26	195.7	−17.7	0.68	8621	629	24

(Continued)

Cluster	RA (2000)	Dec (2000)	l	b	A_B	$cz_\odot$	σ_c	N_{FP}
A0548SE	05 : 44.5	−26 : 4	230.5	−25.5	0.10	12687	863	5
A0569N	07 : 13.9	+50 : 24	166.9	+24.0	0.31	5729	500	7
A0569S	07 : 9.1	+48 : 37	168.6	+22.8	0.29	5975	500	6
A0576	07 : 21.3	+55 : 49	161.3	+26.2	0.31	11084	945	6
A0999	10 : 23.4	+12 : 50	227.9	+52.6	0.16	9764	500	5
A1016	10 : 27.1	+11 : 1	231.3	+52.5	0.13	9717	500	7
A1060	10 : 36.7	−27 : 32	269.6	+26.5	0.31	3859	610	18
A1139	10 : 58.2	+01 : 36	251.4	+52.7	0.12	11701	500	10
A1177	11 : 9.7	+21 : 46	220.4	+66.3	0.07	9507	500	6
A1228	11 : 21.4	+34 : 21	186.9	+69.4	0.09	10553	500	5
A1257	11 : 26.3	+35 : 20	183.3	+70.1	0.09	10622	500	5
A1314	11 : 34.8	+49 : 5	151.8	+63.5	0.07	9951	500	7
A1367	11 : 44.0	+19 : 57	234.3	+73.0	0.10	6600	641	10
A1656	12 : 59.6	+27 : 58	58.2	+88.0	0.04	7003	821	85
A1736	13 : 26.7	−27 : 26	312.5	+34.8	0.22	10510	500	4
A2052	15 : 16.7	+07 : 1	9.4	+50.1	0.15	10250	533	5
A2063	15 : 23.1	+08 : 37	12.8	+49.7	0.14	10563	667	16
A2199	16 : 28.6	+39 : 33	62.9	+43.7	0.04	8859	801	40
A2634	23 : 38.5	+27 : 2	103.5	−33.1	0.31	9279	700	35
A2657	23 : 44.5	+09 : 16	96.6	−50.2	0.50	12400	500	6
A2806	00 : 40.2	−56 : 9	306.1	−60.9	0.06	8297	500	6
A2877	01 : 9.9	−45 : 56	293.1	−70.8	0.05	7195	887	21
A3193	03 : 58.2	−52 : 20	262.0	−47.2	0.06	10303	500	4
A3381	06 : 9.9	−33 : 36	240.3	−22.7	0.15	11256	500	14
A3389	06 : 22.4	−64 : 56	274.7	−27.4	0.29	8174	595	7
A3526	12 : 48.8	−41 : 19	302.4	+21.6	0.49	3547	897	41
A3537	13 : 1.0	−32 : 26	305.3	+30.4	0.35	5157	500	4
A3558	13 : 27.9	−31 : 30	312.0	+30.7	0.22	14313	977	26
A3570	13 : 43.6	−38 : 10	314.1	+23.6	0.29	11054	798	5
A3571	13 : 47.5	−32 : 52	316.3	+28.5	0.22	11272	1045	11
A3574	13 : 49.1	−30 : 18	317.4	+30.9	0.24	4647	500	8
A3581	14 : 7.5	−27 : 1	323.1	+32.9	0.26	6457	500	8
A3656	20 : 0.8	−38 : 35	1.9	−29.5	0.31	6024	500	5
A3716	20 : 51.9	−52 : 50	345.4	−39.3	0.14	13729	804	16

(Continued)

Cluster	RA (2000)	Dec (2000)	l	b	A_B	$cz_\odot$	σ_c	N_{FP}
A3733	21 : 2.0	−28 : 4	17.8	−39.6	0.44	11183	608	10
A3742	21 : 7.9	−47 : 11	352.5	−42.4	0.14	4944	500	5
A3744	21 : 7.3	−25 : 28	21.4	−40.2	0.29	11384	508	5
A4038	23 : 47.5	−28 : 7	25.3	−75.8	0.08	8405	517	19
A4049	23 : 51.6	−28 : 22	24.1	−76.7	0.08	9310	774	12
H0122	01 : 23.7	+33 : 15	130.6	−29.1	0.25	4986	500	8
J8	02 : 29.8	+23 : 6	150.6	−34.4	0.59	9721	500	12
MKW12	14 : 2.9	+09 : 25	349.9	+65.5	0.12	6014	500	4
PISC	01 : 11.0	+33 : 9	127.6	−29.5	0.25	5077	500	22
S0301	02 : 49.1	−31 : 10	229.0	−64.1	0.09	7121	546	11
S0753	14 : 3.6	−33 : 59	319.6	+26.5	0.29	4276	536	15
S0761	14 : 18.4	−27 : 23	325.7	+31.6	0.31	6961	500	9
S0805	18 : 47.3	−63 : 20	332.3	−23.6	0.41	4406	541	10

5.6 The catalogue

Table A.3 presents the final catalogue of FP data for galaxies in the revised cluster sample. All analyses presented in the following chapters are based upon this version of the SMAC catalogue.

References

Bower R. G., Lucey J. R., Ellis R. S. 1992, MNRAS, 254, 589

Burstein D., Heiles C. 1984, ApJS, 54, 33

Davies R. L., Burstein D., Dressler A., Faber S. M., Lynden-Bell D., Terlevich R. J., Wegner G. 1987, ApJS, 64, 581

Dressler A. 1984, ApJ, 281, 512

Dressler A., Lynden-Bell D., Burstein D., Davies R. L., Faber S. M., Terlevich R. J., Wegner G. 1987b, ApJ, 313, 42

Dressler A., Faber S. M., Burstein D. 1991, ApJ, 368, 54

González J. J. 1993, PhD thesis, University of California, Santa Cruz

Fadda D., Girardi M., Giuricin G., Mardirossian F., Mezzetti M. 1996, ApJ, 473, 670

Jørgensen I., Franx M., Kjærgaard P. 1995a, MNRAS, 273, 1097

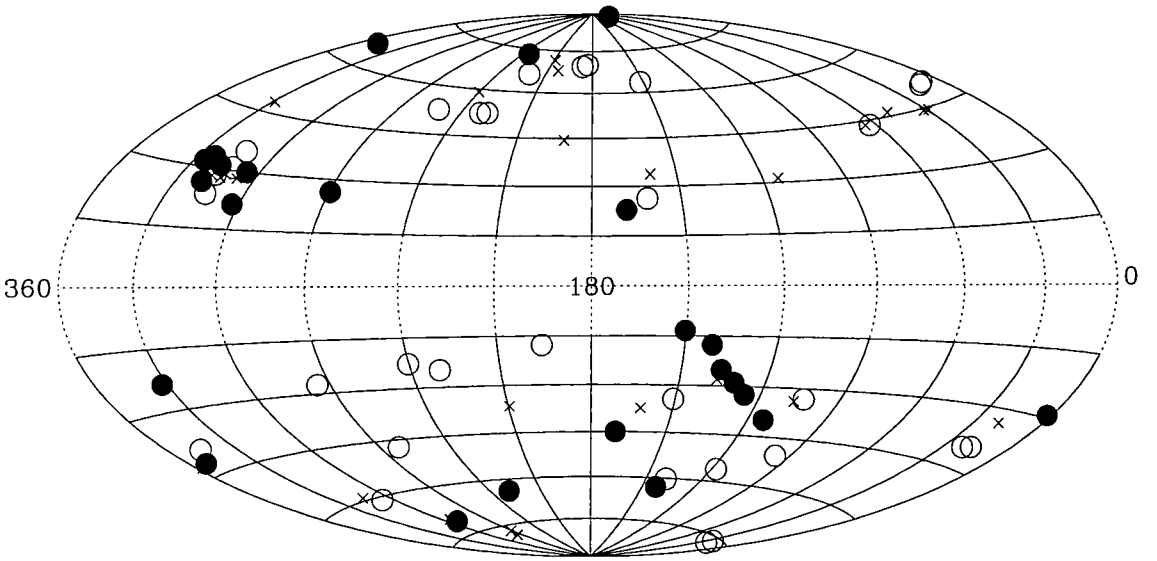

Figure 5.7: The SMAC cluster sample after removal of 'drop-out' clusters and addition of 'extra' clusters. Filled symbols indicate clusters with redshifts $cz < 8000\,\mathrm{km\ s^{-1}}$, while open symbols mark clusters more distant than this. The positions of 'drop-out' clusters are indicated by small crosses.

Jørgensen I., Franx M., Kjærgaard P. 1995b, MNRAS, 276, 1341

Jørgensen I., Franx M., Kjærgaard P. 1996, MNRAS, 280, 167

Lauer T. R., Postman M. 1994, ApJ, 425, 418

Lucey J. R., Carter D. 1988, MNRAS, 235, 1177

Lucey J. R., Currie M. J., Dickens R. J. 1986, MNRAS, 221, 453

Lucey J. R., Guzmán R., Carter D., Terlevich R. J. 1991b, MNRAS, 253, 584

Lucey J. R., Guzmán R., Steel J., Carter D. 1997, MNRAS, 287, 899

Lucey J. R., Lahav O., Lynden-Bell D., Terlevich R. J., Infante, L., Melnick J. 1999, in preparation

Saglia R. P., Burstein D., Bertschinger E., Baggley G., Colless M. M., Davies R. L., McMahan R. K., Wegner G. 1997b, MNRAS, 292, 499

Schlegel D. J., Finkbeiner D. P., Davis M. 1998, ApJ, 500, 525

Smith R. J., Lucey J. R., Hudson M. J., Steel J. 1997, MNRAS, 291, 461

Smith R. J., Lucey J. R., Hudson M. J., Schlegel D. J., Davies R. L. 1998, in preparation

Steel J. 1998, PhD thesis, University of Durham

Scodeggio M. 1997, PhD thesis, Cornell University

Chapter 6

The Fundamental Plane and distance determination

6.1 Introduction

Having derived fully-corrected spectroscopic and photometric parameters for the SMAC programme galaxies, the Fundamental Plane can now be constructed and used to determine cluster distances and peculiar velocities.

Section 6.2 presents a brief discussion of various methods for analysing the distance indicator data, and a justification of the 'Inverse Method I' approach adopted in this thesis. Section 6.3 reports the parameters of the inverse FP fit to the SMAC data, which are corrected and converted to distances in Section 6.4. The final set of cluster distances and peculiar velocities are tabulated in Section 6.5. The potential for systematic effects in the cluster distance estimates are explored in Section 6.6, through the use of the $\mathrm{Mg} - \sigma$ relation and other tests. Finally, Section 6.7 presents comparisons of the SMAC distances and peculiar velocities with those from published studies.

6.2 Fitting the FP : Method

Various methods have been published for analysing peculiar velocity data, resulting in some confusing and conflicting nomenclature. Strauss & Willick (1995) have described the so-called 'method matrix', which divides analyses into Method I or Method II according to the choice of real-space versus redshift-space for the fitting of model velocity fields, and into forward or inverse fits defined by the quantity whose residuals are minimized in constructing the distance-indicator relationship. The terminology of Strauss & Willick will be adopted in the following sections, and this review, and references therein, should be consulted for a full discussion. The alternative treatment of

Lynden-Bell et al. (1993) is also informative.

6.2.1 Method I and Method II analyses

The Method I / Method II distinction applies strictly not to determining the distance indicator relationship (here the FP), but rather to the philosophy underlying the determination of velocity field parameters from the data. The two questions are related, however, and should be treated together. The terms Method I and Method II refer to whether redshift information or distance information (from the FP) should be treated as the best indicator of distance. In effect, the choice is between the conducting the analysis in real space (more intuitive, but with larger errors), or in redshift space (small errors, but less helpful for picturing the velocity field).

In the approach referred to as Method I, the FP (or other distance indicator) data is regarded as the best measure of distance for each cluster. The FP scatter is minimised with the assumption that all galaxies in a given cluster have the same distance, which is to be found. The fit therefore results in a direct determination of each cluster distance. Flow models can then be fit, *a posteriori*, to the peculiar velocity field. However, since the flow models are defined in real-space, there is a large uncertainty in the position of a cluster within the flow. The notorious Malmquist bias is the result of a coupling of the large random errors with the unknown underlying density field. The effects of Malmquist bias are discussed in greater detail in Section 6.4.2 below.

The alternative, Method II, analysis regards redshift information as an *a priori* indicator of distance. The FP scatter is minimised under the assumption of a parametrised flow model, with the best-fitting flow model derived simultaneously with the individual distances. Since the redshifts are accurately known, Malmquist bias does not affect analyses conducted on this basis. However, the individual cluster velocities are not determined directly, but rather depend on the form of the flow model. As a result, Method II does not result in a uniquely defined map of the velocity field.

6.2.2 Forward and Inverse fits

This second distinction refers to the quantity in which the scatter is minimized when the FP fit is performed.

A forward FP fit is one which minimises the scatter in the distance-dependent variable, ie $\log A_e$. The FP slope and zero point derived by this method are biased if the sample is selected by magnitude, or other photometric variables. The bias can be corrected for, if the selection function is known, through a schemes such as those of Lynden-Bell et al. (1988) and Willick (1994). In practice, however, observational

selection criteria are rarely defined sufficiently cleanly for bias corrections to be well constrained.

In contrast, the inverse fit, in which the scatter is minimised in the distance-independent variable, ie $\log \sigma$, is unbiased by photometric selection. However, the inverse fit is biased (in the opposite sense) by any explicit selection on $\log \sigma$. Again, bias corrections can be calculated, in the case of known, well defined selection functions.

Note that a further alternative technique, in which the residuals are minimised orthogonal to the plane, has been adopted by a number of recent studies (Jørgensen et al. 1996, Baggley 1996, Scodeggio 1997). In this an approach, both the photometric and spectroscopic selection biases are present, increasing the complexity of any correction procedure. More recently still, Saglia et al. (1996, 1998) have developed an elaborate Maximum-likelihood algorithm for fitting the FP. This very careful approach is necessitated by the particularly severe selection effects in the EFAR dataset to which it is applied.

6.2.3 Adopted Approach

The determination of cluster distances from the SMAC FP data will be achieved through an inverse Method I analysis. This approach was adopted by Hudson et al. (1997) for a study of a much smaller cluster sample, and is justified here by the following observations:

1. The SMAC sample subsumes many different studies, each with its own photometric selection criteria. Consequently, the selection function for the resulting catalogue is complex (involving magnitude and surface brightness cuts), non-uniform (with different limits from cluster to cluster and from dataset to dataset) and imprecise (fuzzy limits). It is essentially impossible to quantify these selection criteria, and therefore impractical to implement a photometric bias correction scheme.

2. The samples combined into the SMAC catalogue were *not explicitly* selected according to velocity dispersion, σ. The spectra were obtained using instrumentation of sufficient resolution that those galaxies not cut by photometric criteria yield reliable velocity dispersions. While this is not identically true of all the spectroscopic datasets combined in Chapter 5 (especially the older data), it *is* true of those systems which contribute substantially to the final sample of cluster data. Thus, spectroscopic selection biases are expected to be minimal.

The inverse forms of distance indicators have traditionally been combined with a Method II analysis, using a parametrised model such as that of Virgocentric flow (Davis &

Peebles 1983, and references therein). Here, however, the Method I analysis is preferred, since a key objective of the SMAC programme is to provide a model-independent map of the local velocity field. While the analysis to be presented is therefore subject to the effects of Malmquist biases, these effects are substantially ameliorated through the use of a cluster sample, which carries smaller random errors per object than a field sample.

6.3 Fitting the FP : Results

The dataset employed in the FP fits is that constructed in Chapter 5 and presented in Table A.3. Recall that this catalogue contains 725 galaxies in 56 clusters, with a median of eight galaxies per cluster and a minimum of four. The data has been matched into a homogeneous catalogue through extensive intercomparisons between the many original sources. The principal parameters employed are the effective radius $R_e = A_e/2$ (in arcsec), the effective surface brightness $\langle\mu\rangle_e$ (in magnitudes per square arcsec) and velocity dispersion σ in km s^{-1}.

6.3.1 The global FP

As discussed above, the inverse FP relation is applied in this work, such that we regard the photometric parameters as the predictor of the velocity dispersion:

$$\log\sigma = \frac{1}{\alpha}\log R_e - \frac{\beta}{\alpha}\langle\mu\rangle_e - \frac{1}{\alpha}\gamma_{cl} \tag{6.1}$$

and minimize residuals in $\log\sigma$ over all galaxies in the FP sample. The slope parameters (α,β) are determined from the fit, but are constrained to be the same for all clusters. The zero-points γ_{cl} are allowed to vary independently for each cluster, as is necessary since they depend upon cluster distance. Note that β is defined here, as by Hudson et al. (1997), as the coefficient of the surface brightness, which differs by a factor -2.5 from the β defined by Jørgensen et al. (1996).

Table 6.1 summarises the results of the global FP fit. The derived slope parameters, (α,β), are consistent with the values obtained from a similar treatment of a smaller dataset, by Hudson et al. (1997) (Note that the FP parameters from an inverse fit cannot be directly compared with results from forward or orthogonal fitting schemes). The errors in (α,β), which are strongly correlated, were determined by bootstrap resampling the FP sample. The global scatter is equivalent to a distance error of 22.4%, per galaxy, again similar to the results of Hudson et al. Figure 6.1 shows the FP for the combined sample. Galaxies in all clusters have been shifted to the distance of A1656, using the zero-point offsets, $\gamma_{cl} - \gamma_{A1656}$. Three galaxies have residuals of more than

Table 6.1: Parameters of the global Fundamental Plane fit.

Sample size	$N_{\rm gal}$	725
	$N_{\rm cl}$	56
Slope parameters	α	1.418 ± 0.034
	β	0.338 ± 0.005
Scatter in σ	Δ_σ	0.062 dex
Fractional distance error per galaxy	$\Delta_{\rm inv}$	0.224

three standard deviations from the global FP: N4661 in A3526 (3.4σ), U01308 in A0262 (3.2σ) and A1656:D-120 in A1656 (3.1σ). In Figure 6.1, the FP is appropriately shown in that projection which isolates the parameter, σ, whose residuals are minimised in the fit. Note that other possible (and misleading) projections show less apparent scatter, due to the correlated errors in $R_{\rm e}$ and $\langle\mu\rangle_{\rm e}$.

6.3.2 The cluster FPs

Figures 6.2–6.3 present the FP data for each cluster, in individual panels, together with the mean line of slope α (from the global fit), and a fiducial line defined by the zero-point of the Coma cluster, A1656.

Table 6.2 presents the FP fitting results for individual clusters. Neglecting a number of correction terms (see below), the tabulated zero-points, $\gamma_{\rm cl}$ (from the globally-determined FP slope) are related to the cluster distances, $d_{\rm cl}$ through

$$d_{\rm cl}/d_0 = 10^{(\gamma_0 - \gamma_{\rm cl})} \tag{6.2}$$

where d_0, γ_0 are the distance and FP zero-point of some calibrating cluster.

The zero-point errors are computed from the scatter around the global best fit FP, or from the individual cluster rms, whichever is the larger. This reduces the weight of clusters which exhibit greater scatter than the global FP, without according undue influence to those poorly sampled clusters for which the FP scatter is not reliably determined.

The globally-determined FP provides a good fit to the cluster data for most well-sampled cases. However, for a few clusters, the global slope is a rather poor fit to the data. The most discrepant cluster (at the 4.5σ level) is A0576, which prefers a smaller α. A marginally smaller slope is also found for A2806, A3558, A1139, and PISC. For A1060, a larger slope provides a better fit. The α slope defines the exponent in the power law dependance of mass-to-light ratio on luminosity (Faber et al. 1987).

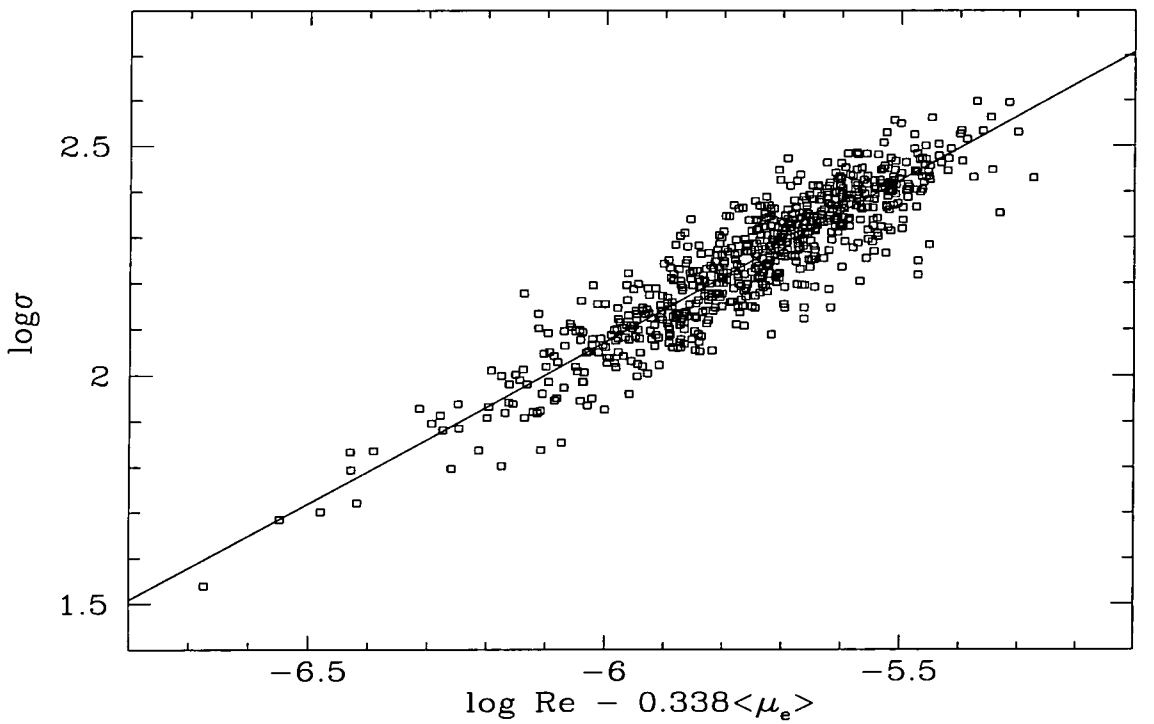

Figure 6.1: The FP for the combined SMAC sample of 725 galaxies in 56 clusters. The clusters have been shifted to the same distance, as described in the text. The dashed line is that given by (α, β) from the global inverse FP fit.

Restricting attention only to the nine clusters with > 20 observed members, the scatter in $\alpha_{\rm cl}/\alpha_{\rm gl}$ is inconsistent with a universal FP slope, at the 95% confidence level. An intrinsic dispersion in FP slope of $\sim$5% from cluster to cluster is required to explain the observed scatter. While these differences might be interesting in the context of galaxy formation and evolution models, the concern here is the effect they might have on distance estimates. The effect of fitting a global FP to a cluster with a significantly different slope will depend upon the sampling of the cluster. Specifically, for a cluster with smaller α, and FP data restricted to the brightest few galaxies, the FP distance will be systematically overestimated. There are too few well-sampled clusters to determine the magnitude of these effects with confidence. To first order however, the effects should lead to a systematic error which is *not* correlated with position on the sky, and therefore should not unduly influence determination of a bulk-flow signal.

The analysis presented here is founded on the assumption that all galaxies assigned to a given cluster do indeed lie at the same distance. In constructing the Mark III Tully–Fisher catalogue, Willick et al. (1995) found that cluster samples were sometimes best modelled as 'expanding clusters', suggesting that the spirals were not drawn from fully collapsed structures. Figures 6.4 -6.5 examine the possibility that a similar effect

acts in the case of early-type galaxy samples. The figure compares the distance of each galaxy (as determined from its FP residual) with its CMB redshift. In an 'expanding cluster', there would be a tendency for galaxies to lie along the Hubble line. In the majority of cases, no such effect is manifest, and the data are consistent with the assumption of equidistance, indicating that observation of early-type galaxies efficiently picks out the collapsed cluster cores. Deviations from equidistance (at the $>2.5\sigma$ level) suggest 'collapse' rather than expansion in the case of A2877, A3574, and A4038. In fact, rather than physical infall, this effect is due to inhomogeneous Malmquist bias: individual galaxies scatter preferentially out of the cluster in *distance* but retain the cluster velocity, producing a spurious inflow pattern around the cluster. The only apparently expanding cluster in the SMAC sample is the poor system MKW12 (3σ significance). This 'cluster' may be a chance alignment of field galaxies, but there are only four galaxies in the SMAC sample, and a strong conclusion cannot be drawn.

The equidistance assumption would also be violated if a sample is drawn from a superposition of two clusters. A cluster with bimodality in distance-space might not be apparent in the previous test, depending on the peculiar motion of the subclusters. Such subclustering can instead be investigated through the distribution of residuals from the FP. Figure 6.6 presents histograms of these residuals (in the unbiased $\log \sigma$ direction) for galaxies in the nine clusters with $N_{\rm gal} > 20$. For these cases, no significant bimodality is detected by the KMM algorithm of Ashman, Bird & Zepf (1994), although it should be noted that the samples have populations smaller than the $\sim$50 recommended by Ashman et al. The clusters investigated here include the Centaurus cluster (A3526), which exhibits clear substructure in velocity-space (Lucey et al. 1986).

6.4 From zero-points to distances

While the relationship between FP zero-points and cluster distances is approximately that of Equation 6.2, there are a number of corrections which must be applied prior to deriving distance estimates. In the absence of selection biases, the corrections applied here account for Malmquist bias, cosmological curvature and passive evolution of stellar populations.

6.4.1 Galaxy selection biases

It has been argued, above, that the inverse fit adopted here is insensitive to sample selection on photometric parameters (magnitude, diameter, surface brightness or combinations thereof). Such a fit would be sensitive, however, to *explicit* selection

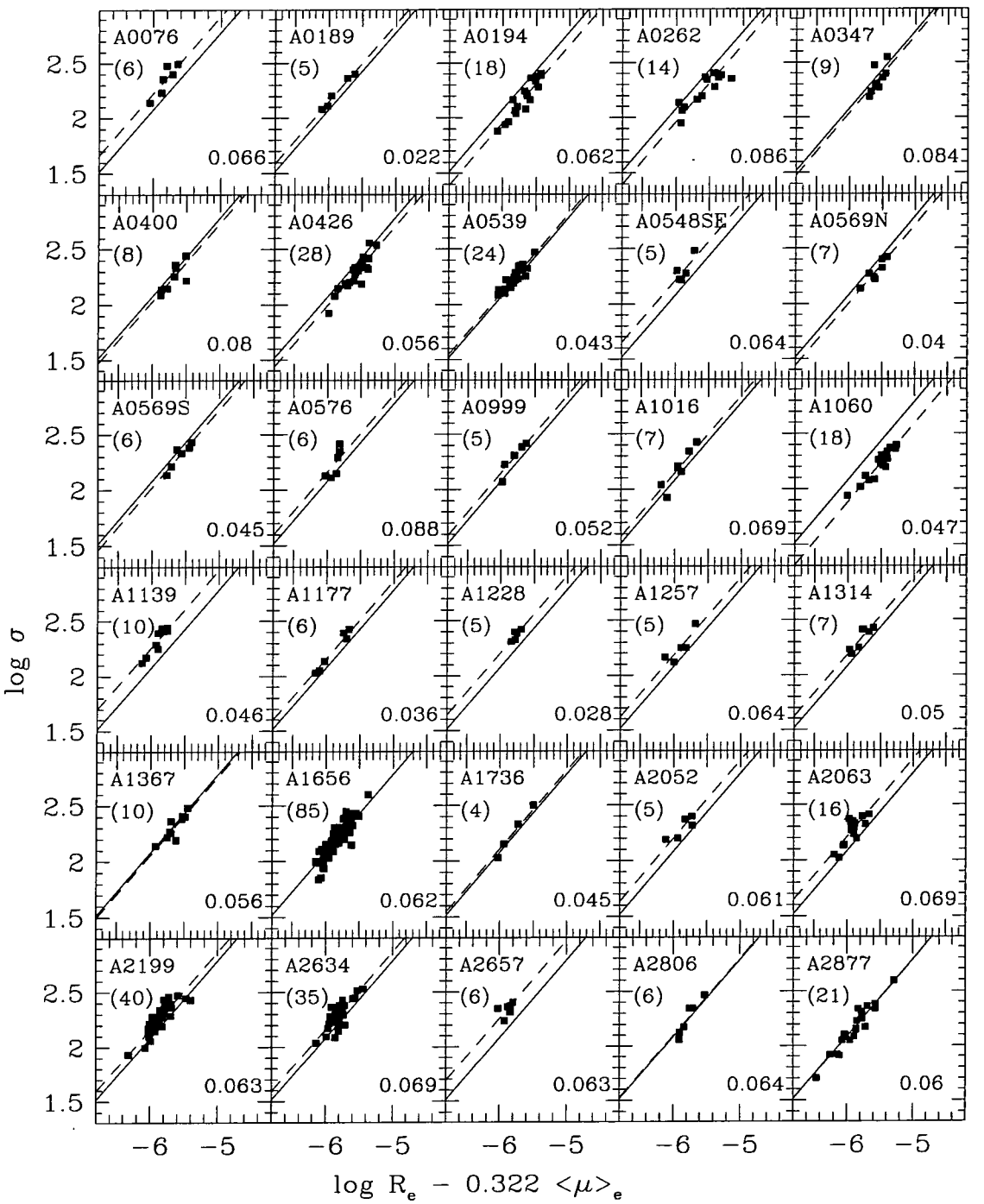

Figure 6.2: Individual cluster FPs for 30 SMAC clusters. In each panel, the dotted line is the mean line of slope α (from the global inverse FP fit). In all panels, the solid line is a fiducial defined by the zero-point of the Coma cluster (A1656). The number of cluster members in the FP fit is given at the top left, and the rms scatter (in $\log\sigma$) about the FP for each cluster is indicated at lower right.

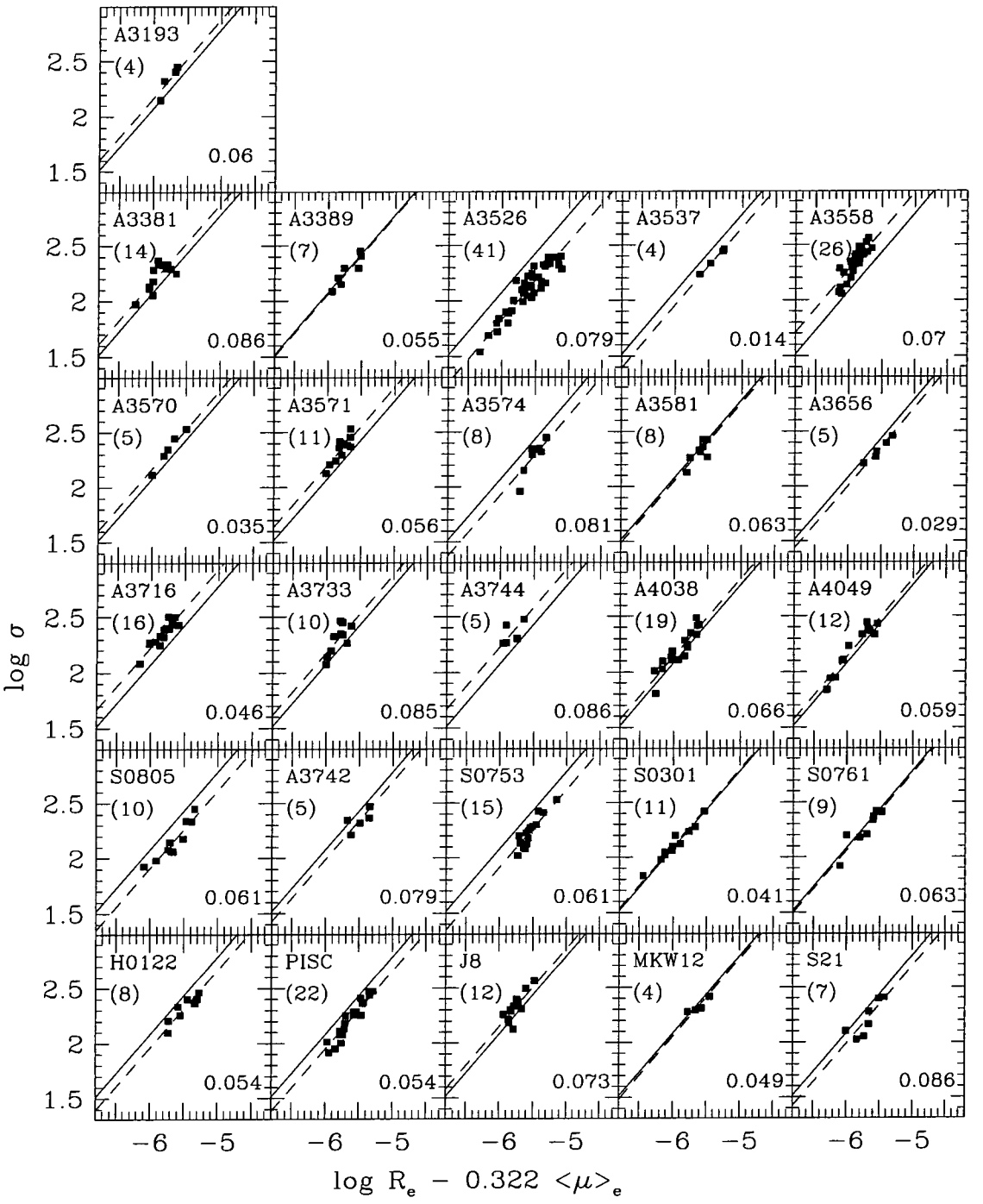

Figure 6.3: Individual cluster FPs for the remaining 26 clusters. Details are as for Figure 6.2.

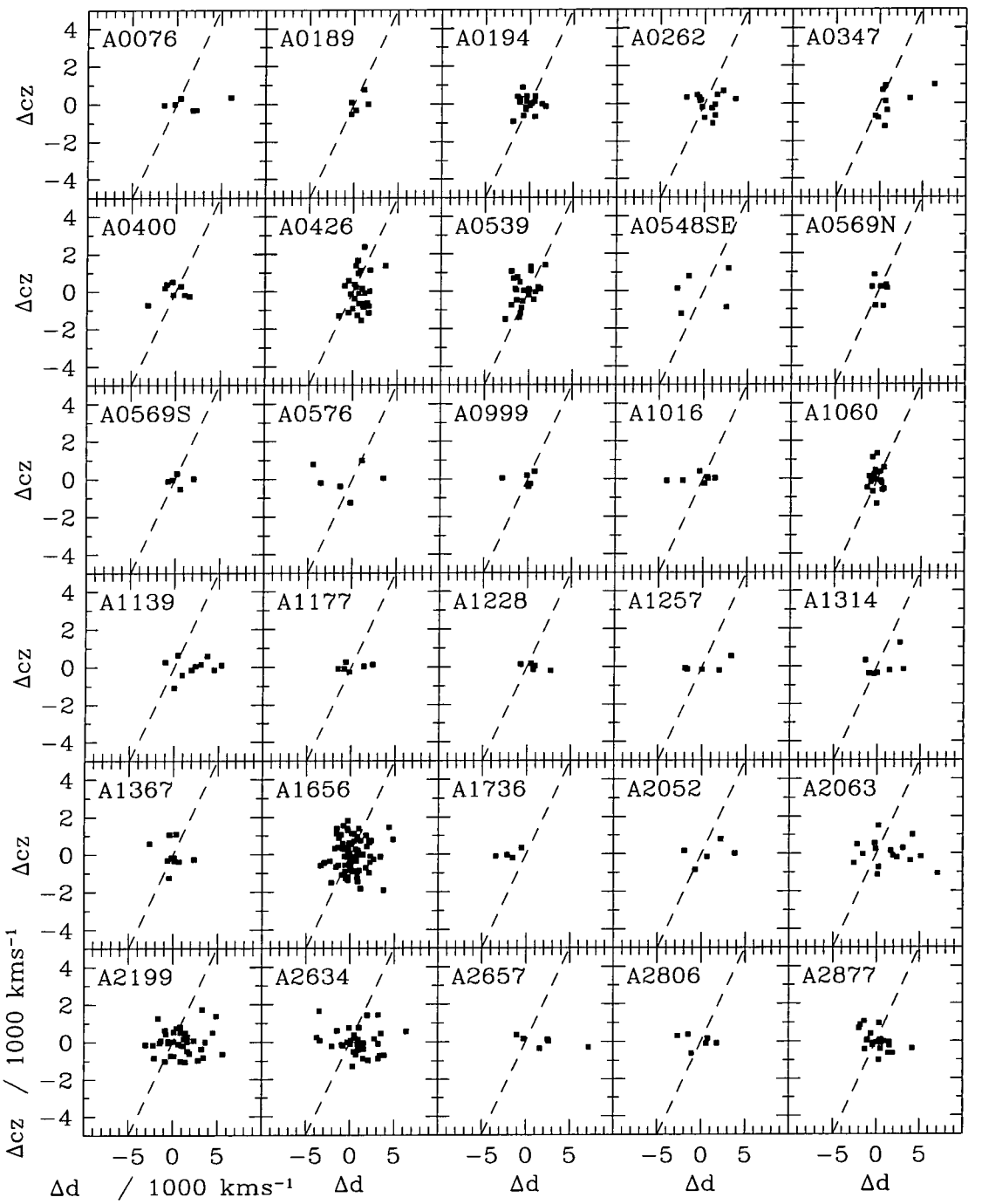

Figure 6.4: Distance–velocity plots by cluster for the first 30 clusters. The individual galaxy redshifts (in the CMB frame), cz, are plotted against the respective galaxy distances d, (determined from the FP residual) The dashed line is of unit slope, so that a positive peculiar velocity is indicated by a mean offset of points to the left of this line, and a negative velocity by an offset to the right.

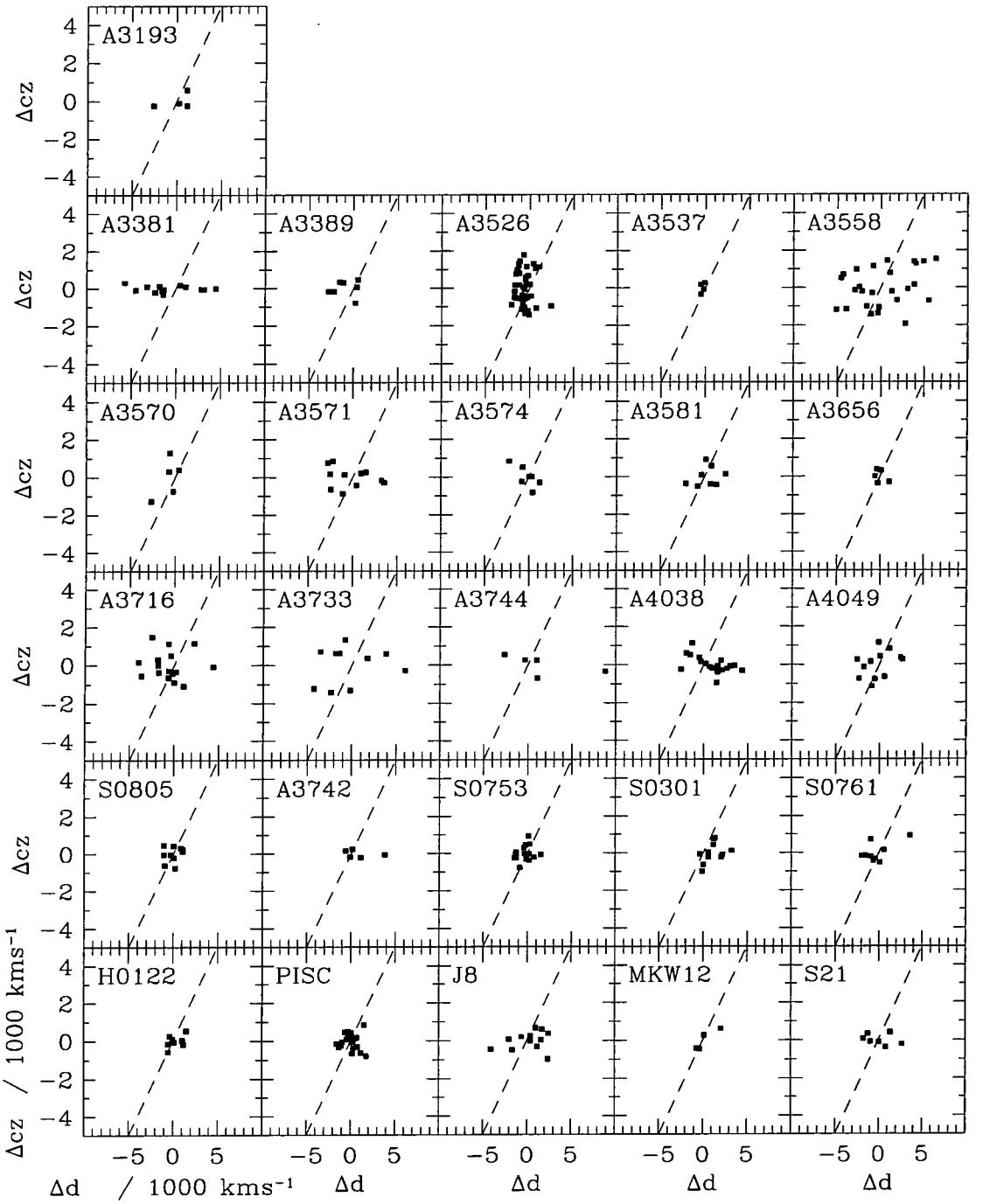

Figure 6.5: As Figure 6.4, for the remaining 26 clusters.

Table 6.2: Results of FP fit, by cluster. For each cluster, N_{gal} is the number of galaxies used in the fit, and γ_{cl} is the FP zero-point for the cluster. The global FP slope parameters are used in determining the zero-points. The column headed α_{cl}/α_{gl} gives the FP slope (relative to the global fit) derived using data for the given cluster only, with bootstrap errors. Where this free-fit slope is very poorly determined, no value is given. The zero-point errors are those determined from the global FP scatter or the cluster FP scatter, whichever is the larger. Asterisks mark cases where the individual cluster scatter is used.

Cluster	N_{gal}	α_{cl}/α_{gl}	γ_{cl}	Cluster	N_{gal}	α_{cl}/α_{gl}	γ_{cl}
A0076	6	0.75±0.39	−9.137±0.036*	A2806	6	0.68±0.11	−8.939±0.036*
A0189	5	1.03±0.93	−9.029±0.039	A2877	21	0.95±0.07	−8.919±0.019
A0194	18	0.88±0.07	−8.746±0.021	A3193	4	0.93±0.47	−9.047±0.044
A0262	14	1.43±0.46	−8.756±0.032*	A3381	14	1.13±0.34	−9.059±0.032*
A0347	9	0.95±0.22	−8.875±0.038*	A3389	7	1.07±0.52	−8.902±0.033
A0400	8	1.15±0.61	−8.857±0.037*	A3526	41	1.12±0.06	−8.567±0.017*
A0426	28	1.02±0.12	−8.811±0.017	A3537	4	1.12±0.26	−8.747±0.044
A0539	24	1.06±0.16	−8.961±0.018	A3558	26	0.81±0.08	−9.198±0.019*
A0548SE	5	—	−9.116±0.040*	A3570	5	0.83±0.15	−9.057±0.039
A0569N	7	1.11±0.25	−8.824±0.033	A3571	11	0.86±0.21	−9.099±0.027
A0569S	6	1.01±0.38	−8.848±0.036	A3574	8	0.69±0.29	−8.718±0.038*
A0576	6	0.54±0.10	−9.044±0.047*	A3581	8	1.22±0.71	−8.890±0.031*
A0999	5	0.84±0.48	−9.019±0.039	A3656	5	1.16±0.17	−8.818±0.039
A1016	7	0.79±0.21	−9.015±0.035*	A3716	16	1.12±0.21	−9.140±0.022
A1060	18	1.14±0.06	−8.642±0.021	A3733	10	0.84±0.19	−9.063±0.038*
A1139	10	0.81±0.08	−9.185±0.028	A3742	5	—	−8.799±0.049*
A1177	6	0.85±0.16	−9.041±0.036	A3744	5	1.78±1.32	−9.135±0.053*
A1228	5	1.10±0.92	−9.101±0.039	A4038	19	0.97±0.14	−9.000±0.022*
A1257	5	1.09±0.63	−9.073±0.039*	A4049	12	0.99±0.17	−8.997±0.025
A1314	7	1.74±0.66	−9.071±0.033	H0122	8	1.18±0.15	−8.754±0.031
A1367	10	1.05±0.11	−8.891±0.028	J8	12	0.82±0.26	−9.020±0.029*
A1656	85	0.92±0.07	−8.927±0.010	MKW12	4	—	−8.890±0.044
A1736	4	0.79±0.11	−8.975±0.044	PISC	22	0.89±0.05	−8.743±0.019
A2052	5	1.54±1.19	−9.081±0.039	S0301	11	1.16±0.09	−8.956±0.027
A2063	16	1.04±0.17	−9.112±0.024*	S0753	15	0.87±0.19	−8.680±0.023
A2199	40	1.05±0.20	−9.041±0.014*	S0761	9	1.00±0.11	−8.893±0.029*
A2634	35	1.07±0.14	−9.041±0.017*	S0805	10	0.98±0.09	−8.683±0.028
A2657	6	—	−9.173±0.036*	S21	7	1.03±0.34	−8.798±0.043*

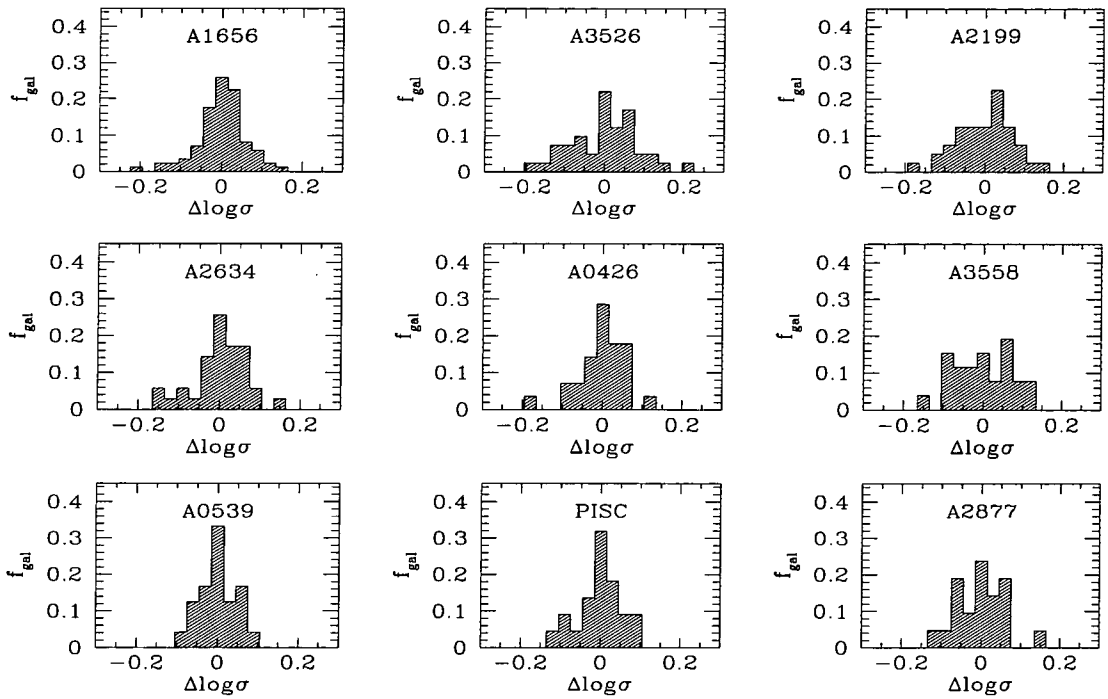

Figure 6.6: Histograms of FP residuals for clusters with N_{gal} >20. Bins are of width 0.03 in $\log\sigma$, with f_{gal} the fraction of cluster members falling inside each bin.

on velocity dispersion. In general, our sample is not subject to such selection. While there are few galaxies with $\sigma < 100\,\mathrm{km\,s^{-1}}$ in the SMAC sample, the low-σ galaxies have been excluded on photometric criteria: reliable dispersions cannot be determined due to the low signal-to-noise ratio of the spectra obtained for them. The spectra are of a resolution sufficient to measure velocity dispersions down to approximately $50\,\mathrm{km\ s^{-1}}$. For the other spectroscopic datasets which contribute substantially to the sample, the dispersions should be reliable to similar limits. Whilst galaxies of smaller dispersion than these limits are excluded in principle, it is unlikely, in practice, that such galaxies are the 'bona fide' E/S0 types to which the FP applies. In all but the nearest clusters, these galaxies have in any case dropped out of the sample as a result of *a priori* magnitude selection.

Finally, note that the sample used here for A1656 is based upon that of Lucey et al. (1991), which *was* explicitly selected to exclude $\sigma < 100\,\mathrm{km\,s^{-1}}$ galaxies. The bias caused by this selection can be calculated by a method analogous to that of Willick (1994) for a strict magnitude-selection bias in the forward-fit method. In practice, for A1656, the correction is extremely small, in consequence of the large range in σ of the observed sample. This correction is neglected here.

6.4.2 Malmquist bias

The Method I approach is subject to Malmquist biases arising from the coupling of (substantial) distance errors with the underlying density field. In the case of a uniform distribution of clusters, the expansion of the volume element as r^2 renders more likely the prospect of a cluster being scattered in from larger true distances, than its being scattered out from smaller true distances (homogeneous Malmquist bias, HMB). This effect (which is not dependent on any selection) occurs at all distances, not only near the limit of the sample. Its effect is that of a rescaling of distances by the multiplicative factor $\exp(3.5\varepsilon_d^2)$. The correction depends upon the fractional distance error ε_d, which for a cluster sample gives

$$d_{\rm corr} = d \cdot \exp(3.5\Delta^2/N_{\rm gal}), \tag{6.3}$$

where $N_{\rm gal}$ is the number of observed galaxies in the cluster and $\Delta = \alpha \ln(10)\Delta_\sigma$ is the fractional distance error per galaxy. For the SMAC sample, the median HMB correction is $\sim 1.5\%$, while the largest corrections (for clusters with only four observed members) are 3.9%.

In the more general case, when the underlying density field is non-uniform, the problem is that of inhomogeneous Malmquist bias (Hudson 1994, Strauss & Willick 1995), hereafter IMB. In this case, the preferential scattering out of density-field peaks produces a spurious contribution to the apparent infall pattern. Hudson (1994) derived corrections based upon a reconstruction of the underlying density field of optical galaxies. In the far-side of the Great Attractor ($cz \sim 6000\,{\rm km\ s^{-1}}$), where Malmquist effects are particularly severe, Hudson finds that the IMB correction is $\sim 500\,{\rm km\ s^{-1}}$ for single galaxies.

In the present context, IMB corrections cannot be determined since the underlying density field of clusters is not sufficiently well determined. However, IMB effects, like the homogeneous case, scale inversely as $N_{\rm gal}$, such that even in the GA background case considered by Hudson, the IMB correction would be $\sim 60\,{\rm km\ s^{-1}}$ for a cluster with $N_{\rm gal} = 8$. Here then, only the homogeneous Malmquist bias correction is applied, but it should be stressed that this is adequate only in the case of a cluster sample.

6.4.3 Cluster selection bias

A further statistical bias arises as a result of the $12000\,{\rm km\,s^{-1}}$ redshift limit of the SMAC sample, which constrains the measured peculiar velocities of clusters towards the limit of the sample. By way of example, a cluster at real-space distance $130\,h^{-1}$ Mpc is constrained to have a negative peculiar velocity, whilst a cluster at $110\,{\rm h^{-1}}$ Mpc with

$v_p = 2000\,\mathrm{km\,s^{-1}}$ (eg in the foreground of a major supercluster) would be excluded from the sample by the redshift limit. (Except in the case of the 'extra' clusters of Chapter 5, which were subject to no strict redshift cut.)

No correction is made for the redshift limit bias in the present study. Indeed the necessary bias correction requires assumptions about the form of the velocity field, which should not be made in a Method I analysis. In the approach taken here, all data-points are individually valid, even at the limit of the sample, and should form part of the velocity field map. It must only be borne in mind that when the data-points are treated as an ensemble, the cluster selection bias can affect the statistical properties of the sample. The redshift limit bias does not affect the recovery of a bulk-flow signal in the velocity field. The behaviour of the velocity monopole, however, will be strongly affected beyond $\sim$10000 km s^{-1}.

An alternative, Method II analysis of the SMAC data, to be conducted in forthcoming papers, will allow for a more natural treatment of cluster selection effects.

6.4.4 Evolutionary corrections

Passive evolution of stellar populations causes a dimming of a few hundredths of a magnitude, between $z \sim 0.04$ and the present day. At the limit of our sample, therefore, evolutionary effects are liable to cause a $\sim 2\%$ distance error if uncorrected, in the sense that the distance will be underestimated.

For a single-burst, passively evolving population, the population synthesis models of Worthey (1994) may be employed to construct a first-order evolutionary correction. For this purpose, it is assumed that the age of ellipticals at the present day is 13 Gyr, and that their age at redshift z is $13\,\mathrm{Gyr}/(1+z)$. Solar metallicity is assumed throughout. The Worthey model gives an R-band surface brightness correction of $(\Delta\langle\mu\rangle_e) = +1.0 \times z$, so a distance correction of $(\Delta \log d)_{\mathrm{Evol}} = +0.33 \times z$ is applied. The correction is not highly sensitive to the input parameters chosen here.

6.4.5 Cosmological corrections and distance calibration

As a preliminary step, the cluster distance estimates are calibrated by adopting zero peculiar velocity for A1656 (Coma), thereby assuming that its distance is given by its CMB redshift. Then, for each cluster, the zero-point difference $(\gamma_{\mathrm{cl}} - \gamma_{\mathrm{A1656}})$ determines the ratio of apparent angular diameter (at the same $\sigma, \langle\mu\rangle_e$) of galaxies in the cluster, relative to galaxies in Coma:

$$\theta_{\mathrm{cl}}/\theta_{\mathrm{A1656}} = 10^{(\gamma_{\mathrm{cl}} - \gamma_{\mathrm{A1656}})}. \qquad (6.4)$$

The angular diameter ratio can be converted to a distance through iterative solution of the equation

$$\theta_{\rm cl}/\theta_{\rm A1656} = \frac{(1+z'_{\rm cl})}{1+z'_{\rm A1656}} \cdot \frac{1-(1+z'_{\rm A1656})^{-1/2}}{1-(1+z'_{\rm cl})^{-1/2}} \tag{6.5}$$

where $cz' = d_{\rm FP}$. The above equation holds for a $q_0 = 0.5$ cosmology (Sandage 1975), but the distances are insensitive to the input deceleration parameter.

Finally, before quoting results, the best-fitting monopole (ie Hubble-like) flow model is subtracted from the distances . Such a flow is of no interest here, since it is absorbed into the (unknown) value for the Hubble constant. In fact, after removal of the monopole term, A1656 exhibits a peculiar velocity of less than 50 km s^{-1}, so no significant rescaling of distances occurs at this stage. Setting the velocity zero-point from a shell of clusters at $cz = 6000 - 9000$ km s^{-1} effects only a $\sim 1\%$ distance scaling relative to the global calibration.

6.5 Cluster distances and peculiar velocities

The following items summarize relevant aspects of the FP distance and velocity results:

1. The cluster redshifts, determined in Chapter 5 are translated from heliocentric to the CMB frame by subtracting a the vector 369 km s^{-1} directed towards $l = 264°, b = 48°$ (Lineweaver et al. 1996).

2. Redshift errors are computed as $\sigma_{\rm c}/N_{\rm gal}^{1/2}$ where $\sigma_{\rm c}$ is the cluster velocity dispersion as in Table 5.9.

3. Distances are corrected for homogeneous Malmquist bias (according to Equation 6.3), for the passive evolution of stellar populations, as discussed in Section 6.4.4 and for the effects of cosmological curvature (with $q_0 = 0.5$, Equation 6.5).

4. Distance errors are calculated from the scatter in the FP residuals for the cluster in question, or from the global FP scatter, whichever is the larger.

5. The best-fitting velocity monopole is subtracted from the resulting distances.

6. Systematic errors remaining from the spectroscopic standardization process are determined as the rms of cluster distance estimates derived from the bootstrap-matched datasets of Section 5.2.3.

7. No correction is made for cluster selection bias, σ-selection bias in the galaxy sample, or inhomogeneous Malmquist bias.

Table 6.3 presents distances and peculiar velocities as determined from the FP zero points after the corrections described above. In Figure 6.7, the results are shown as a Hubble plot. Random distance errors are in the range 3–13%, with median 8%.

The system-matching errors on cluster distances are always smaller than the quoted random error. Accordingly these systematic errors can generally be neglected in considering individual clusters. However, since there are correlations between the corrections to different spectroscopic systems, the systematic errors are frequently correlated from cluster to cluster, as illustrated by Figure 6.8. In particular, neighbouring clusters are likely to have common data sources, leading to spatially correlated systematic errors.

The following flags have been assigned in Table 6.3, to warn of potentially damaging systematic effects: A – mean extinction $A_B > 0.45$; S – cluster FP slope discordant from global slope at $>2.5\sigma$ level; O – sensitive to outlier rejection at >10% level (see Section 6.6.1); M – offset from global Mg $-$ σ relation by $>2.5\sigma$ (see Section 6.6.2).

Table 6.3: Cluster distance and peculiar velocity results. The quoted mean redshifts are those computed in Chapter 5, translated into the CMB frame. The adopted distance errors are discussed in the text. The column headed $e_{\rm syst}$ gives the systematic error due to uncertainties in the spectroscopic system matching process. Finally, flags are assigned to clusters according to criteria discussed in the text.

Cluster	l	b	$N_{\rm gal}$	$cz_{\rm CMB}$	$d_{\rm FP}$	$v_{\rm p}$	$e_{\rm syst}$	flags
A3656	2	-30	5	5864 ± 224	5727 ± 551	137 ± 595	72	
A2052	9	50	5	10438 ± 238	11052 ± 1050	-614 ± 1077	145	
A2063	13	50	16	10741 ± 167	11710 ± 673	-969 ± 693	219	
A3733	18	-40	10	10933 ± 192	10430 ± 966	503 ± 984	197	
A3744	21	-40	5	11121 ± 227	12664 ± 1660	-1543 ± 1676	251	O
A4049	24	-77	12	9004 ± 223	8797 ± 529	207 ± 574	127	
A4038	25	-76	19	8097 ± 119	8802 ± 464	-705 ± 479	141	
A1656	58	88	85	7284 ± 89	7298 ± 173	-14 ± 195	123	
A2199	63	44	40	8899 ± 127	9719 ± 323	-821 ± 347	176	
A2657	97	-50	6	12025 ± 204	13894 ± 1212	-1869 ± 1229	187	A
A2634	104	-33	35	8927 ± 118	9725 ± 393	-798 ± 411	155	
S21	114	-40	7	5640 ± 189	5406 ± 577	234 ± 607	97	
A0076	118	-56	6	11142 ± 204	12667 ± 1106	-1525 ± 1124	161	M
PISC	128	-30	22	4775 ± 107	4649 ± 214	126 ± 239	97	
H0122	131	-29	8	4692 ± 177	4831 ± 368	-138 ± 408	93	

(Continued)

Cluster	l	b	$N_{\rm gal}$	$cz_{\rm CMB}$	$d_{\rm FP}$	$v_{\rm p}$	$e_{\rm syst}$	flags
A0262	137	-25	14	4579 ± 140	4815 ± 379	-235 ± 404	93	M
A0189	140	-60	5	9230 ± 224	9688 ± 923	-457 ± 949	84	
A0347	141	-18	9	5484 ± 245	6490 ± 606	-1006 ± 654	107	
A0194	142	-63	18	4906 ± 118	4691 ± 239	214 ± 267	86	
A0426	151	-13	28	5012 ± 194	5483 ± 224	-472 ± 297	93	A
J8	151	-34	12	9469 ± 144	9321 ± 653	148 ± 668	135	A
A1314	152	64	7	10163 ± 189	10684 ± 854	-521 ± 874	131	
A0576	161	26	6	11153 ± 386	10054 ± 1164	1099 ± 1226	120	S
A0569N	167	24	7	5808 ± 189	5762 ± 466	46 ± 503	86	
A0569S	169	23	6	6054 ± 204	6135 ± 542	-81 ± 579	96	
A0400	170	-44	8	6545 ± 212	6241 ± 567	304 ± 605	90	A
A1257	183	70	5	10903 ± 224	10848 ± 1031	55 ± 1055	139	
A1228	187	69	5	10838 ± 224	11627 ± 1104	-789 ± 1127	181	
A0539	196	-18	24	8607 ± 128	7995 ± 344	612 ± 367	157	A
A1177	220	66	6	9838 ± 204	9946 ± 871	-108 ± 894	120	
A0999	228	53	5	10108 ± 224	9473 ± 902	635 ± 930	118	
S0301	229	-64	11	6945 ± 165	7920 ± 517	-976 ± 542	165	
A0548SE	231	-26	5	12738 ± 386	12128 ± 1182	610 ± 1244	299	
A1016	231	53	7	10066 ± 189	9301 ± 792	765 ± 814	78	
A1367	234	73	10	6936 ± 203	6764 ± 459	172 ± 502	81	
A3381	240	-23	14	11344 ± 134	10295 ± 797	1049 ± 808	285	M
A1139	251	53	10	12072 ± 158	14184 ± 953	-2112 ± 966	126	
A3193	262	-47	4	10255 ± 250	10229 ± 1105	26 ± 1132	190	OM
A1060	270	27	18	4205 ± 144	3632 ± 187	572 ± 236	112	M
A3389	275	-27	7	8254 ± 225	7016 ± 564	1239 ± 608	80	
A2877	293	-71	21	6994 ± 194	7189 ± 327	-195 ± 381	138	
A3526	302	22	41	3837 ± 140	3005 ± 126	832 ± 188	78	A
A3537	305	30	4	5467 ± 250	4847 ± 532	620 ± 587	73	
A2806	306	-61	6	8136 ± 204	7705 ± 677	431 ± 708	139	SM
A3558	312	31	26	14608 ± 192	14621 ± 659	-13 ± 687	392	S
A1736	313	35	4	10814 ± 250	8579 ± 929	2235 ± 962	92	
A3570	314	24	5	11321 ± 357	10438 ± 993	883 ± 1055	134	
A3571	316	29	11	11549 ± 315	11408 ± 740	141 ± 804	149	
A3574	317	31	8	4928 ± 177	4427 ± 417	501 ± 453	74	M

(Continued)

Cluster	l	b	$N_{\rm gal}$	$cz_{\rm CMB}$	$d_{\rm FP}$	$v_{\rm p}$	$e_{\rm syst}$	flags
S0753	320	27	15	4537 ± 138	3996 ± 225	541 ± 264	107	
A3581	323	33	8	6727 ± 177	6768 ± 511	-41 ± 541	75	
S0761	326	32	9	7220 ± 167	6813 ± 480	407 ± 508	126	
S0805	332	-24	10	4383 ± 171	4044 ± 279	339 ± 327	72	
A3716	345	-39	16	13584 ± 201	12649 ± 664	934 ± 694	321	
MKW12	350	66	4	6289 ± 250	6886 ± 749	-596 ± 789	119	
A3742	353	-42	5	4763 ± 224	5452 ± 668	-689 ± 704	100	O

6.6 Systematic effects in FP distance determination

Is it possible that the zero-point shifts in the FP do not reflect peculiar velocities, but instead a variation, from cluster to cluster, in star-formation history or other systematic effect? This section considers the evidence for any such 'spurious motions', using the extra information at our disposal: the Mg $-$ σ relation, the morphological properties of the SMAC galaxies, and cluster parameters such as velocity dispersion and intra-cluster gas temperature.

6.6.1 Effect of outliers in the FP

Since many galaxies in the SMAC sample have only a single spectroscopic and photometric observation, there is a potential for an aberrant measurement for a single galaxy to influence unduly the distance estimate for a whole cluster.

The sensitivity of cluster distances to outlying galaxies has been investigated by means of a jackknife procedure, in which the fits were recomputed after excluding each galaxy in turn. In a few cases the exclusion of individual members affects the derived distance by >10%. The offending galaxies are E286-029 (in A3742), A3193:SMC-B (in A3193) and A3744:SMC-I and A3744:SMC-E (both in A3744). The effect of excluding outliers is only larger than the quoted random error in the case of A3193. These three clusters have been flagged as potentially unreliable in Table 6.3.

6.6.2 The Mg $-$ σ relation

The relationship between magnesium line-strength and velocity dispersion is potentially a probe of systematic effects associated with stellar population differences. The presence of a young stellar population in a galaxy raises its luminosity, while leaving

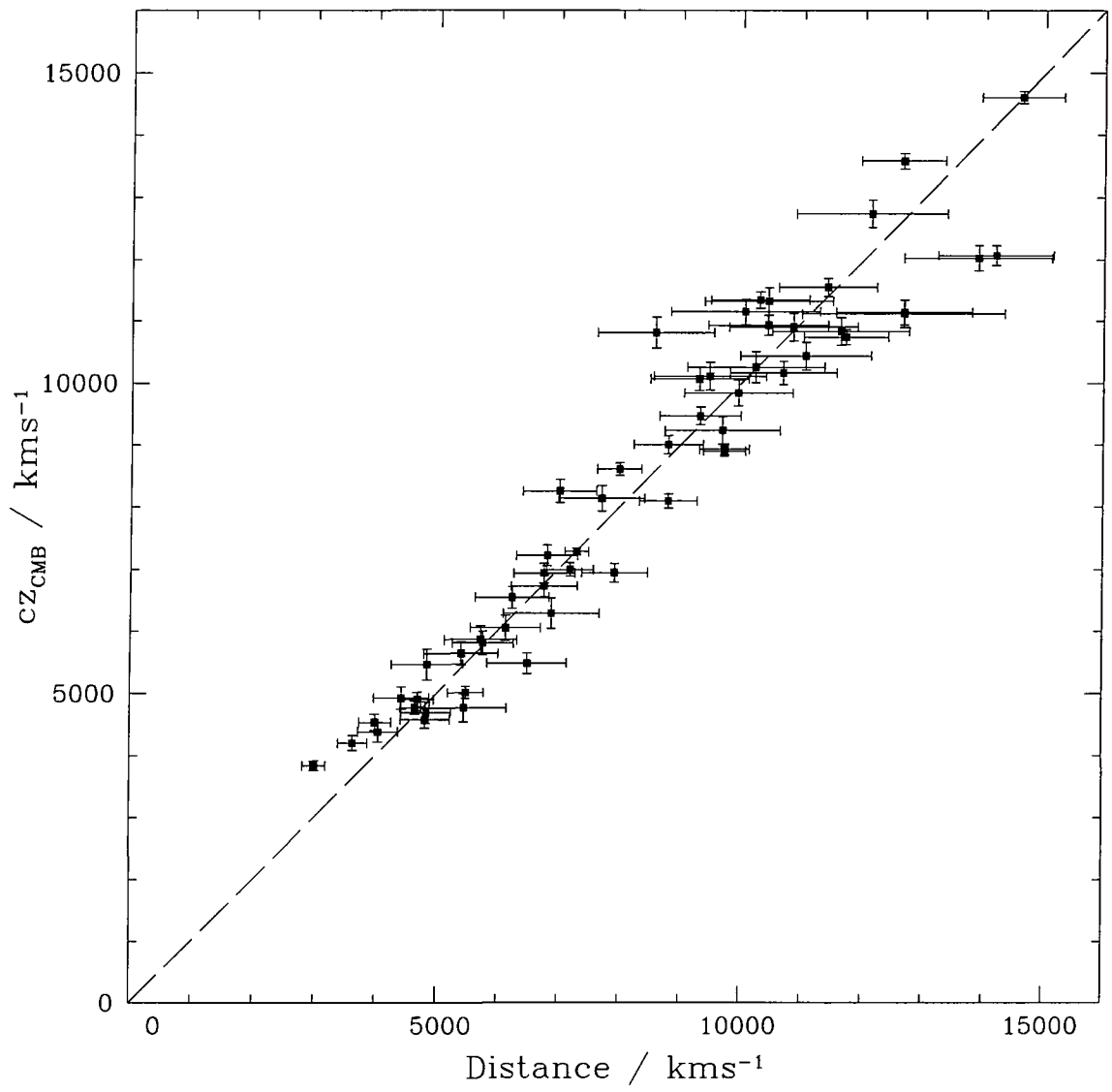

Figure 6.7: Hubble plot for the 56 clusters in the SMAC peculiar velocity sample. The error bars give the random errors, with system-matching errors neglected.

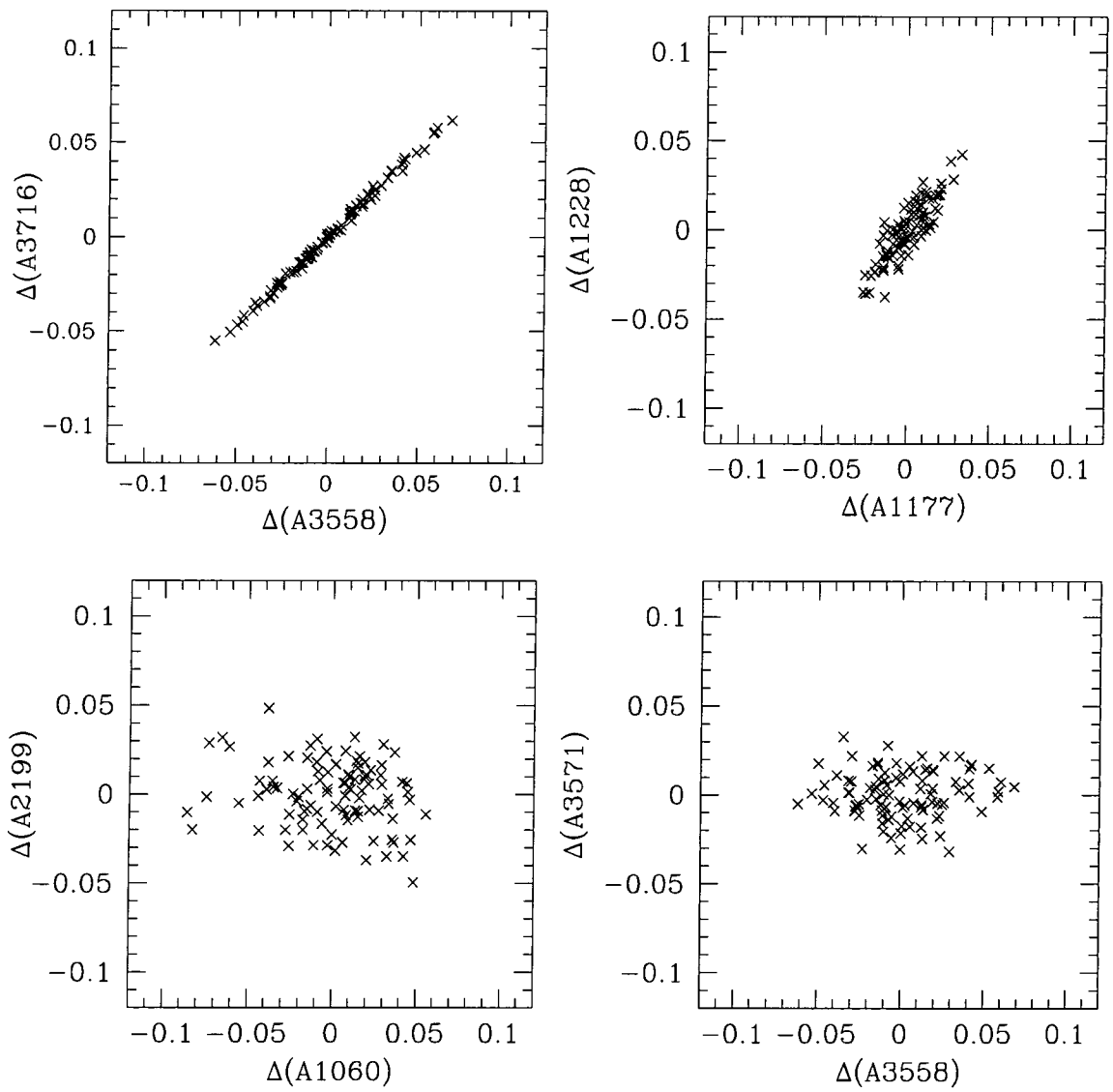

Figure 6.8: Cluster-to-cluster correlations between systematic distance errors. FP catalogues have been constructed for each of 100 bootstrap realisations of the system matching process, and used to determine new sets of cluster distances. The resulting fractional offsets in distance, Δ, are compared here between four illustrative pairs of clusters. For the clusters A3558 and A3716, *all* spectroscopic data derives from a single source (FOCP2) resulting in fully-correlated systematic errors. For A1177 and A1228, spectroscopic data is from the same two sources (I95 and I97A) for each cluster. The correlation is generated since these datasets have large mutual overlap, and tend to 'float together' in the fit. For A2199 vs A1060 and A3558 vs A3571, the data are from distinct data sources and little or no correlation is observed.

Table 6.4: $Mg_2 - \sigma$ relation for the SMAC sample, compared with determinations in the literature. We describe the relation as $Mg_2 = \xi \log \sigma + \zeta$. Note that the results of Baggley are converted from fits to $Mgb - \sigma$ data..

Data	N_{gal}	ξ	ζ	reference
SMAC	570	0.180 ± 0.006	0.123 ± 0.001	This thesis
EFAR(subset)	117	0.181 ± 0.020	0.118 ± 0.033	Baggley (1996)
JFK	207	0.196 ± 0.016	0.155	Jørgensen et al. (1996)
7S	455	0.175	0.110	Burstein et al. (1988)

velocity dispersion unchanged. The resulting displacement from the FP would be interpreted incorrectly as a peculiar motion. However, the light of the younger population would also cause a decrease in the magnesium line-strength at given velocity dispersion. Effects due to stellar-population differences will correlate, therefore, with the zero-point of the $Mg - \sigma$ relation. Indeed a number of studies (Guzmán & Lucey 1992, Jørgensen et al. 1996, Hudson et al. 1997) have used Mg_2 data as part of a more general 'age-independent' distance indicator relation. Here, the $Mg - \sigma$ relation is used only to place limits on the level of any stellar-population effect on the FP-derived distances, and to flag clusters for which the FP distance estimates may be unreliable.

In this analysis, the Mg_2 index will be employed in constructing the $Mg - \sigma$ relation. While the advantageous properties of Mgb were discussed in Chapter 3, the Mg_2 index is preferred for this purpose, since Mg_2 data exist for most clusters in the SMAC sample, whereas Mgb has been determined only from the the most recent observations.

Of the 725 galaxies in the SMAC FP sample, 570 have reliable Mg_2 data. The remaining 155 are mostly from the Lucey & Carter (1988) and Lucey et al. (1999) samples based upon multi-fibre spectroscopic observations, for which large sky-count uncertainties restrict the accuracy of line strength measurements. The $Mg_2 - \sigma$ data can be described adequately by a fit which minimises residuals in the Mg_2 direction. Such a fit is not strongly affected by the degradation of the relationship for the lower luminosity-galaxies. Application of an iterative 3.25σ residual clipping removes five galaxies from the fit (I1548 in 7S21; J8:EFR-H; A1257:SMC-C; A3381:D-064; A3571:SMC-10). The global $Mg_2 - \sigma$ relation is presented in Figure 6.9. The best-fit relation is compared in Table 6.4 with previous determinations. The scatter in the global relation is 0.019 mag.

Peculiar velocity estimates will be compromised if stellar populations differ systematically from cluster to cluster. Figure 6.10 displays the $Mg_2 - \sigma$ relation for 48 clusters in the SMAC sample. For the remaining eight clusters, fewer than four cluster members have reliable $Mg - \sigma$ data. The offset between cluster and global zero-point is

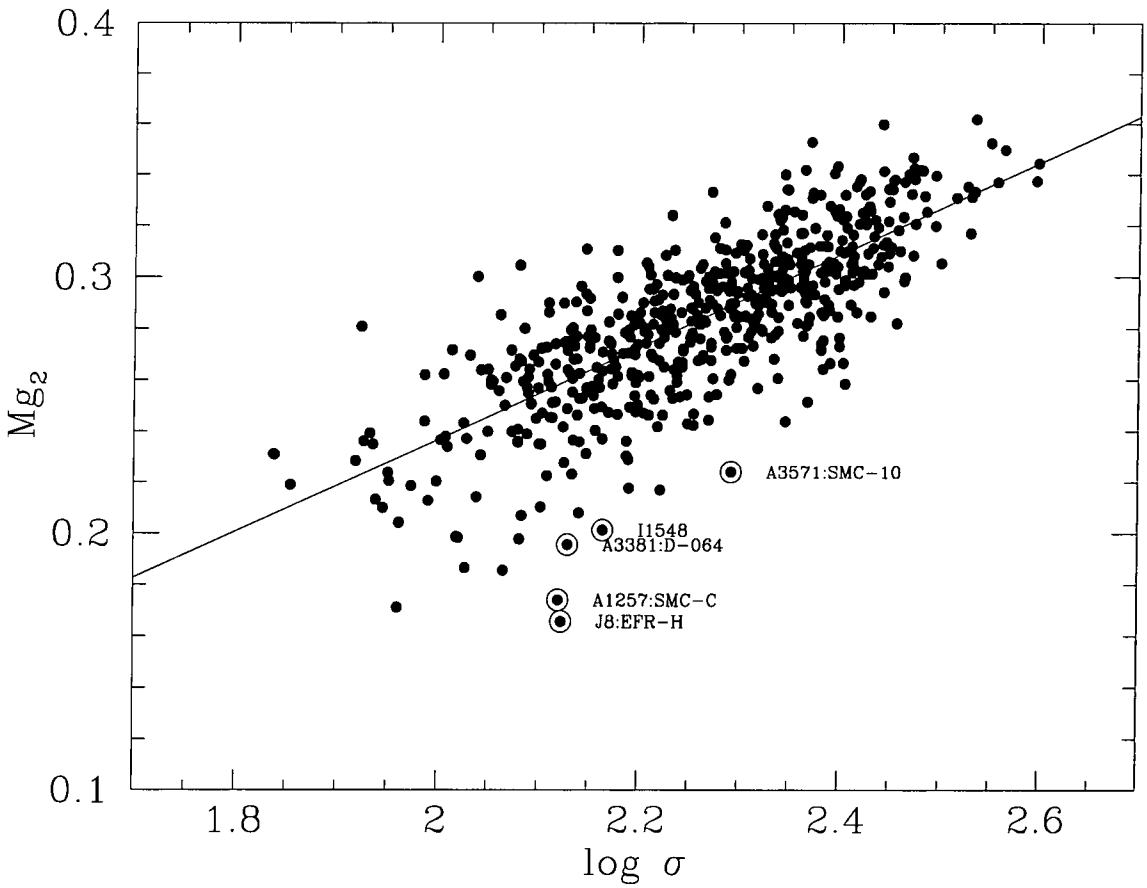

Figure 6.9: The $Mg_2 - \sigma$ relation for the 570 SMAC galaxies with measurements of both parameters. The highlighted galaxies are rejected by an iterative 3.25σ clipping scheme applied in fitting the global relation.

computed with the slope constrained to that of the global fit. Since for many clusters there are few data points, the errors are computed using the cluster rms or that of the global relation, whichever is the larger.

The absolute zero-point offsets are smaller than 0.02 mag for all clusters, and are significant (at the 2σ level) for only three clusters (A0076, A1177, A3571). The distribution of the cluster zero-point offsets is shown in Figure 6.11. The rms deviation of the cluster $Mg-\sigma$ zero-points from that global relation is 0.009 mag. The median random uncertainty in determining the zero-points (for the same subsample) is 0.008 mag, leaving an upper limit of 0.004 mag to be ascribed to systematic effects, or to intrinsic scatter. Recall from Section 3.3.6, however, that the Mg_2 index may be subject to redshift-dependent (and therefore cluster-dependent) systematic errors of $\sim$0.01 mag. It can be concluded, therefore, that intrinsic cluster-to-cluster differences in stellar populations must therefore contribute negligibly to the dispersion in cluster zero-points. The same conclusion is reached if the sample is restricted to clusters with offsets determined with

smaller (<0.006 mag) errors.

The potential contribution by stellar-population effects to spurious peculiar velocities can be estimated from the spread in Mg_2 zero-points. The FP offset $\Delta\gamma$ can be determined from a linear relationship $\Delta\gamma/\Delta Mg_2 = 0.11/0.02 = 5.5$, based on the models of Worthey (1994) (according to Jørgensen et al., 1996). For a 0.008 mag rms in ΔMg_2, the 'spurious velocity' contribution is $\Delta\gamma \sim 0.04$, a value which is closely comparable to the observed rms FP offset. While this might be taken as evidence that age-differences can reproduce the observed FP zero-point offsets, it should be stressed that a very extreme case has been considered. If the Mg_2 offsets are partially the result of metallicity effects, then the limits on spurious velocities are tightened. Further, it has been shown above that there is no evidence for *intrinsic* scatter in the $Mg - \sigma$ zero-point distribution, whereas the analysis above assumes that all of the observed scatter is intrinsic. Finally, and most convincingly, the measured peculiar velocities do not correlate significantly with the $Mg - \sigma$ relation offsets, as demonstrated in Section 6.6.5 below.

6.6.3 The FP as a function of morphological type

The galaxy sample selected for the SMAC programme (in common with most other FP surveys) contains not only (apparently-)pure ellipticals, but also S0 galaxies of varying degrees of 'diskiness'. A correlation of the FP residual with morphological type would result in spurious peculiar velocities, if the proportions of (observed) E and S0 galaxies vary from cluster to cluster in the sample. While Jørgensen et al. (1996) report no significant offset in the FP between E and S0 galaxies, Hudson et al. (1997) present marginal evidence for such a shift, with E types having slightly larger velocity dispersions than S0 galaxies with the same photometric parameters.

The morphological types of galaxies in the SMAC sample are somewhat uncertain, as the types were assigned by eye, by many observers, from image material of variable quality. However, by restricting the sample to just two classes, E (including cD, D, E, E/S0) and L (including S0, S0/E, SB0), it is possible to test for the presence of any substantial systematic effect in the FP. From 725 galaxies, 421 are classed as E types and 290 as L types. The remaining 14 galaxies have no reliable morphological classification.

Table 6.5 summarises the results of FP fits to the E and L subsamples. For fits with slopes fixed to that of the global FP, the zero-point offset between E and L galaxies is 0.011 ± 0.006, in the same sense as the offset of 0.025 ± 0.011 reported by Hudson et al. Such an offset would translates into a $2.6 \pm 1.4\%$ effect in FP distance measurements. However, the mean S0 fraction of 0.4 within the SMAC sample merely effects a global

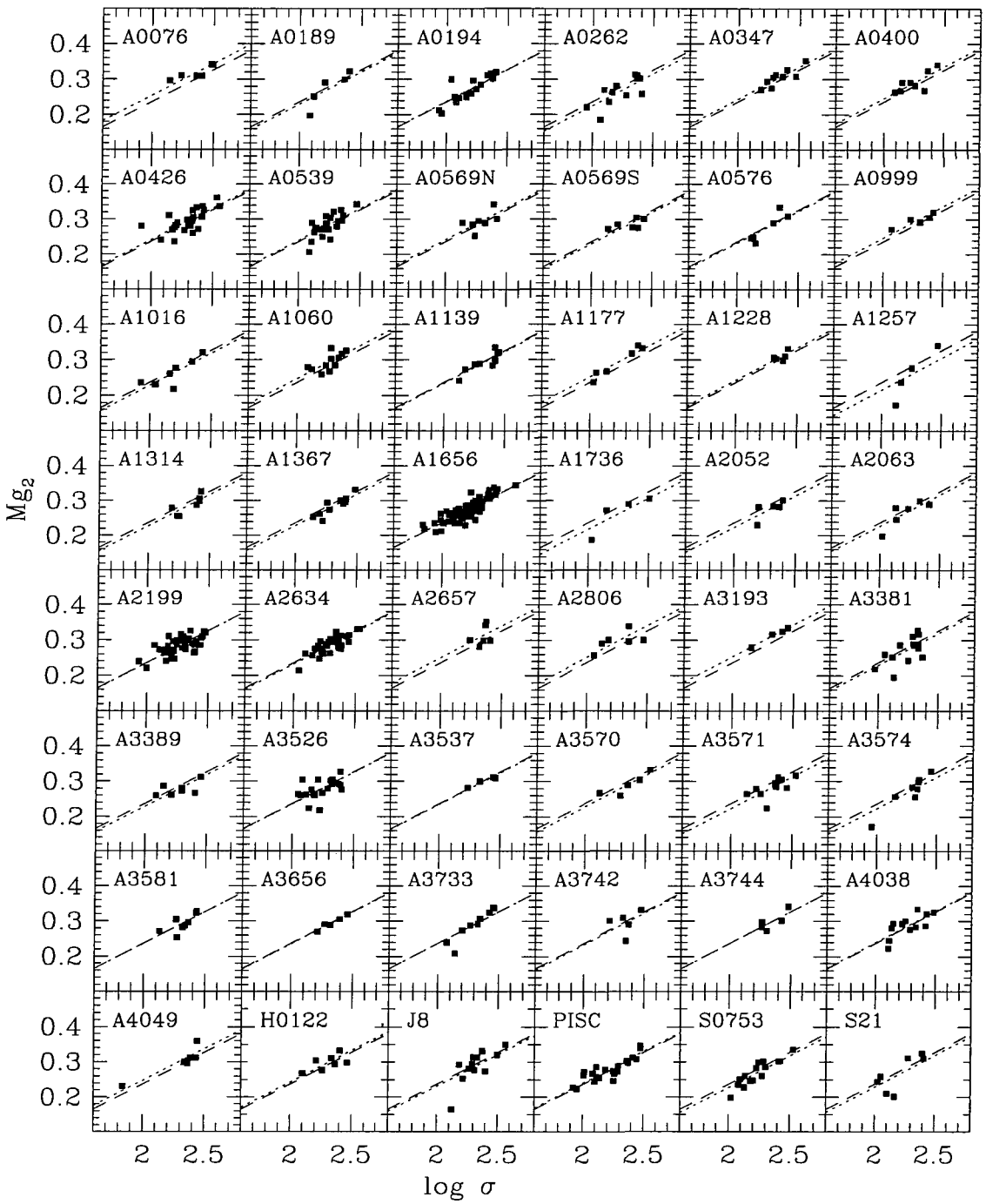

Figure 6.10: The SMAC $Mg_2 - \sigma$ relation, divided cluster by cluster. The 48 clusters shown are those for which at least four data points are available. In each panel, the dotted line corresponds to the global FP fit of Figure 6.9. The dashed line is a fit to the individual cluster data, with the slope constrained to that of the global relation.

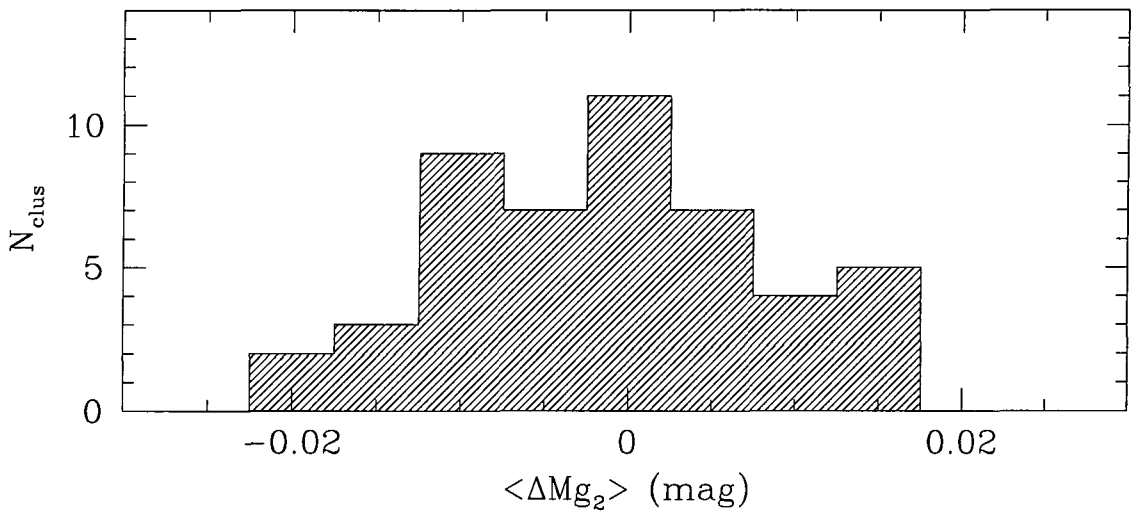

Figure 6.11: Distribution of the cluster $Mg_2 - \sigma$ zero-points, relative to that of the global relation. The dispersion is 0.009 mag, and the typical error on each offset is 0.008 mag.

shift in the FP, which is absorbed into the velocity zero-point. Errors in the FP distances are only introduced by cluster-to-cluster differences in the S0 fraction. For the SMAC sample the cluster-to-cluster scatter in N_{S0}/N_{gal} is 0.18, so the typical systematic error caused by the E vs S0 offset will be $\sim 0.18 \times 0.011 = 0.002$ in FP, which corresponds to only 0.5% in the derived cluster distance.

6.6.4 Effect of low-σ galaxies

Jørgensen et al. (1995b) reported that galaxies with velocity dispersions below 100 km s^{-1} can be subject to large random and systematic errors in $\log\sigma$. It is worthwhile, therefore, to test the sensitivity of the SMAC results to the presence of the 44 galaxies with $\log\sigma < 2.0$ in the FP sample. This test cannot be performed by explicitly excluding galaxies with low *measured* dispersions, since any cut on $\log\sigma$ will bias the inverse FP fit. Instead, a cut is made according to the velocity dispersion *predicted* by the inverse FP relation, given the photometric parameters (and redshift) of each galaxy. This cut excludes 43 galaxies, leaving 682 with $\sigma_{pred} > 2.0$.

A free fit to the high-dispersion subsample yields slope parameters essentially unchanged with respect to the global FP (see Table 6.5). Using the zero-points from this fit to determine distances, four clusters (A4049, S0301, S0761, 7S21) are moved by 3–6%, relative to the default solutions of Table 6.3. In these cases, the galaxies responsible are readily identified in Figures 6.2–6.3. Other cluster distances are perturbed by less than 2%. Finally, the FP slopes are fixed, and the low-σ and high-σ subsamples are

Table 6.5: FP fit parameters for SMAC galaxies divided by morphological type and by velocity dispersion.

Sample	N_{gal}	α	β	Δ_σ	Zero-point
Global	725	1.418 ± 0.034	0.338 ± 0.005	0.062	-8.513±0.003
E type only	421	1.478±0.054	0.333±0.006	0.057	—
E type only	421	(1.418)	(0.338)	0.059	-8.518±0.004
S0 type only	290	(1.418)	(0.338)	0.065	-8.507±0.006
$\log \sigma_{pred} > 2$	682	1.429 ± 0.044	0.337 ± 0.008	0.062	
$\log \sigma_{pred} > 2$	682	(1.418)	(0.338)	0.061	-8.513 ± 0.003
$\log \sigma_{pred} < 2$	43	(1.418)	(0.338)	0.074	-8.509 ± 0.016
				$\gamma_E - \gamma_{S0} =$	-0.011±0.006
				$\gamma_{low-\sigma} - \gamma_{high-\sigma} =$	-0.004±0.016

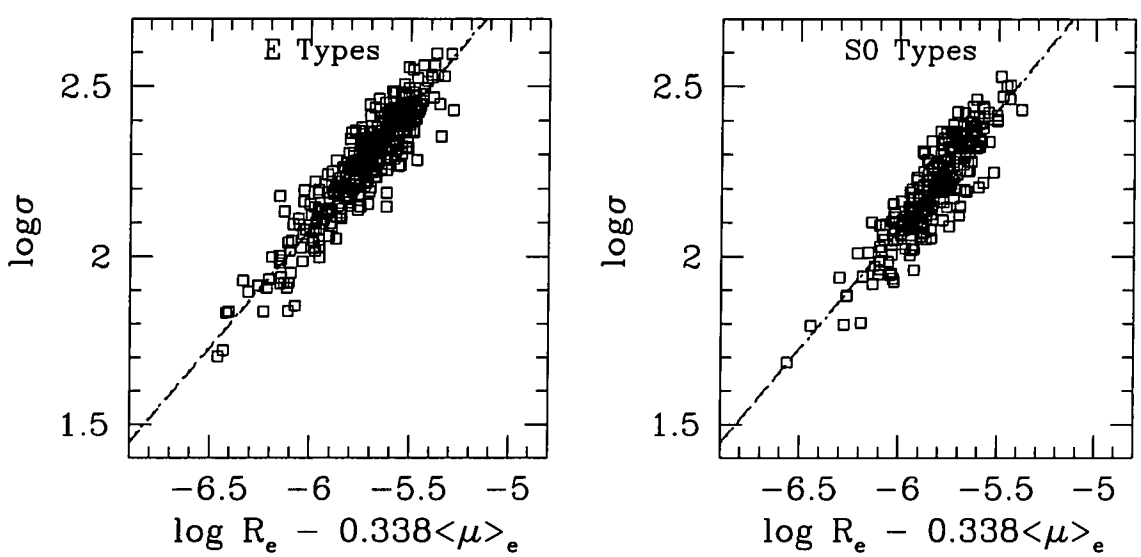

Figure 6.12: The FP subdivided by morphological type. The fits shown are constrained to the slope of the global FP relation.

fit separately, after being shifted to the same distance according to the global zero-points. While the scatter is somewhat larger for the low-σ galaxies, there is no systematic offset relative to the high-σ sample. There is therefore no evidence that errors or biases associated with low-dispersion galaxies cause any systematic effects on the SMAC results. These galaxies are retained in the sample.

6.6.5 Correlations with cluster parameters

A further test for spurious contributions to the velocity measurements is presented in Figure 6.13, in which the derived peculiar velocities are plotted as a function of other cluster parameters. The tests, which do not reveal convincing evidence for any systematic effects, are summarized here:

- The SMAC cluster velocities exhibit no correlation with respect to cluster velocity dispersion (as determined in Chapter 5). This test indicates there are no systematic effects associated with the local environment, and validates *a posteriori* the selection of clusters over a wide range of richness.

- The derived velocities are not correlated with the mean Schlegel et al. (1998) extinction corrections, and therefore reveal no evidence for over- or under-estimation of the extinction in high-reddening regions.

- The comparison of peculiar velocity with a cluster's offset from the global $Mg_2 - \sigma$ relation provides a test for spurious motions associated with cluster to cluster stellar population differences. While the plot appears to provide evidence for just such an effect, the apparent correlation is largely driven by a single cluster (A1736 at $v_p \sim 2000\,\mathrm{km\ s^{-1}}$).

- Finally, the peculiar velocity exhibits a marginal trend with respect to the cluster-to-global slope ratio, in the sense that with apparently larger α have more negative peculiar velocities. The effect is rather small however, at $< 100\,\mathrm{km\ s^{-1}}$, for a cluster with 10% slope deviation, and is neglected here.

6.7 Comparison with published distance estimates

Until cluster distance estimates from different methods can be shown to be consistent within the quoted errors, the claims of coherent motions on large scales will and must be treated with caution, as the possible effects of systematic errors. In this section, the distances and peculiar velocity measurements from SMAC are compared,

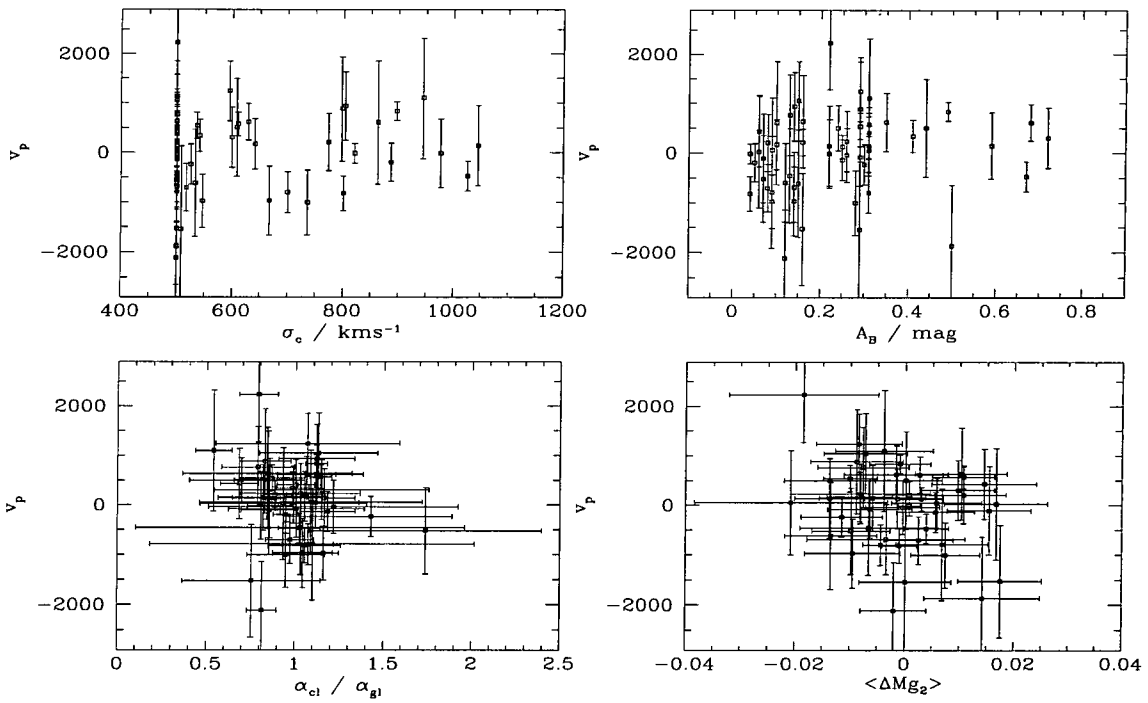

Figure 6.13: Tests for correlations between the measured peculiar velocities and other cluster parameters. The parameters employed are: the cluster velocity dispersion, σ_c (as a measure of cluster richness); the mean B-band extinction correction, A_B; the offset of the cluster from the global $Mg_2 - \sigma$ relation, $< \Delta Mg_2 >$; and the ratio of the cluster FP slope to that of the global FP, $(\alpha_{cl}/\alpha_{gl})$. None of the tests reveal significant correlations.

on a cluster by cluster basis, with those from a number of published studies. It should be borne in mind, however, that the large errors on individual data points can easily hide a spurious bulk motion of a few 100 km s^{-1}. The SMAC distances and velocities used in the comparison are those of Table 6.3. The system-matching errors are neglected at this stage, since they contribute little to the uncertainty for any *individual* cluster. The comparisons are presented in Figures 6.14–6.16 and in Table 6.6. The Centaurus cluster (A3526) has been removed from the comparisons, since the treatment of the two subclusters differs between studies.

6.7.1 Fundamental Plane distances

The most straightforward comparison of cluster distances is with other studies which used the FP or $D_n - \sigma$ relation as a distance indicator. However, raw data from many of these works (Faber et al. 1989; Lucey & Carter 1988; Jørgensen et al. 1995a,b; Smith et al. 1997; Scodeggio 1997) have been used to construct the present sample of distances. The distances and peculiar velocities are, therefore, not wholly independent.

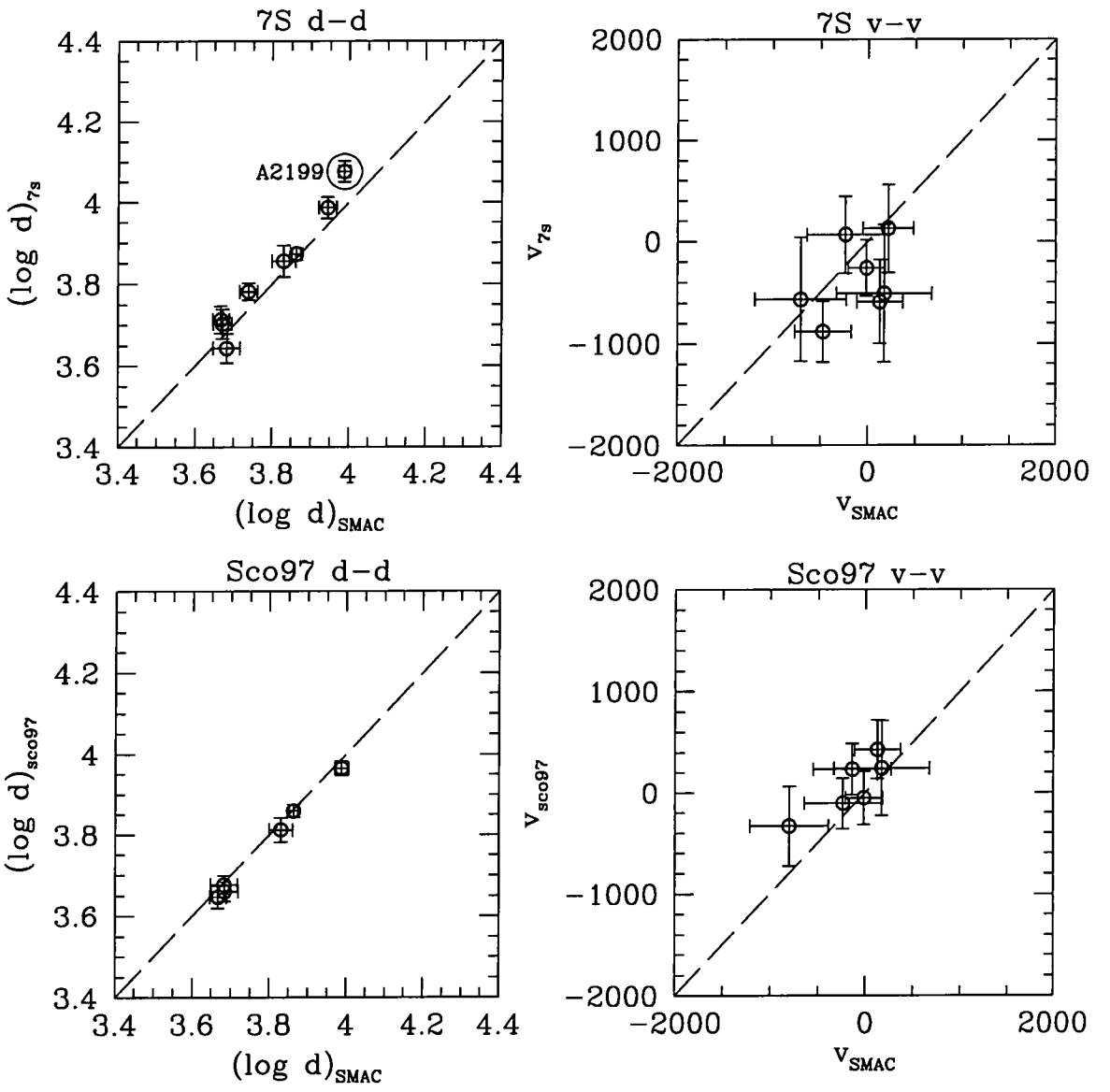

Figure 6.14: Comparison of SMAC distances and peculiar velocities with those from the $D_n - \sigma$ survey of Faber et al. (1989, 7S), and the FP study of Scodeggio (1997, Sco97). Here, and in subsequent plots, highlighted clusters are discrepant at the $>2\sigma$ level. In this comparison Scodeggio's 'N383 group' has been identified as the 'PISC' cluster, and his 'N507 group' with cluster H0122. For A2199, the 7S peculiar velocity lies beyond the plot limits, at -2921 km s^{-1}.

Table 6.6: Comparisons of distance and peculiar velocity estimates from SMAC with determinations from the literature. See text for further details.

		distances (log)		peculiar velocities		
Code	$N_{\rm clus}$	χ^2	$P(>\chi^2)$	χ^2	$P(>\chi^2)$	Source
HM	11	14.96	0.18	9.38	0.59	Willick et al. (1997)
SCI	11	15.01	0.13	13.15	0.22	Giovanelli et al. (1998)
LP	39	63.65	0.01	49.93	0.11	Lauer & Postman (1994)
Sco97	6	1.67	0.95	2.02	0.92	Scodeggio (1997)
7S	8	15.20	0.06	11.61	0.17	Faber et al. (1989)
7S[a]	7	6.36	0.50	4.76	0.69	Faber et al. (1989)

[[a] Excluding cluster A2199.]

However, the data has been differently treated here, and for many clusters the SMAC distances are based on datasets substantially enlarged relative to the comparison study. The comparisons presented are restricted to the $D_{\rm n} - \sigma$ distances of Faber et al. (1989), and with the I-band FP survey of Scodeggio (1997).

The comparison with the 7S distances of Faber et al. (1989) employs only their clusters and groups with four or more observed galaxies. The distances are compatible with those from SMAC, after removal of one highly discrepant cluster (A2199) from the comparison. Note that the 7S distance for A2199 is based on spectra from the PAL system, which requires a large σ-correction (Section 5.2), and photometric parameters uncorrected for seeing effects, which are significant at this distance. Both effects tend to increase their distance estimate, as found in the comparison.

The comparison of SMAC and Scodeggio peculiar velocities yields a significant correlation, and a rather small χ^2, which might indicate some overestimate of the errors. There is also some evidence for a calibration offset between the samples, with SMAC distances slightly the larger.

6.7.2 Tully–Fisher distances

Comparison of FP results with distance estimates derived from TF studies is potentially hampered by differences between the distributions of early- and late-type galaxies: While ellipticals and S0s typically reside in cluster cores, late-type spirals are rare in cluster environments. Accordingly, TF studies are prone to sampling the galaxies in the outer regions of clusters, or even in extended overdensities associated with a surrounding supercluster. In addition, the potential for contamination from foreground and background galaxies is much greater for spiral samples.

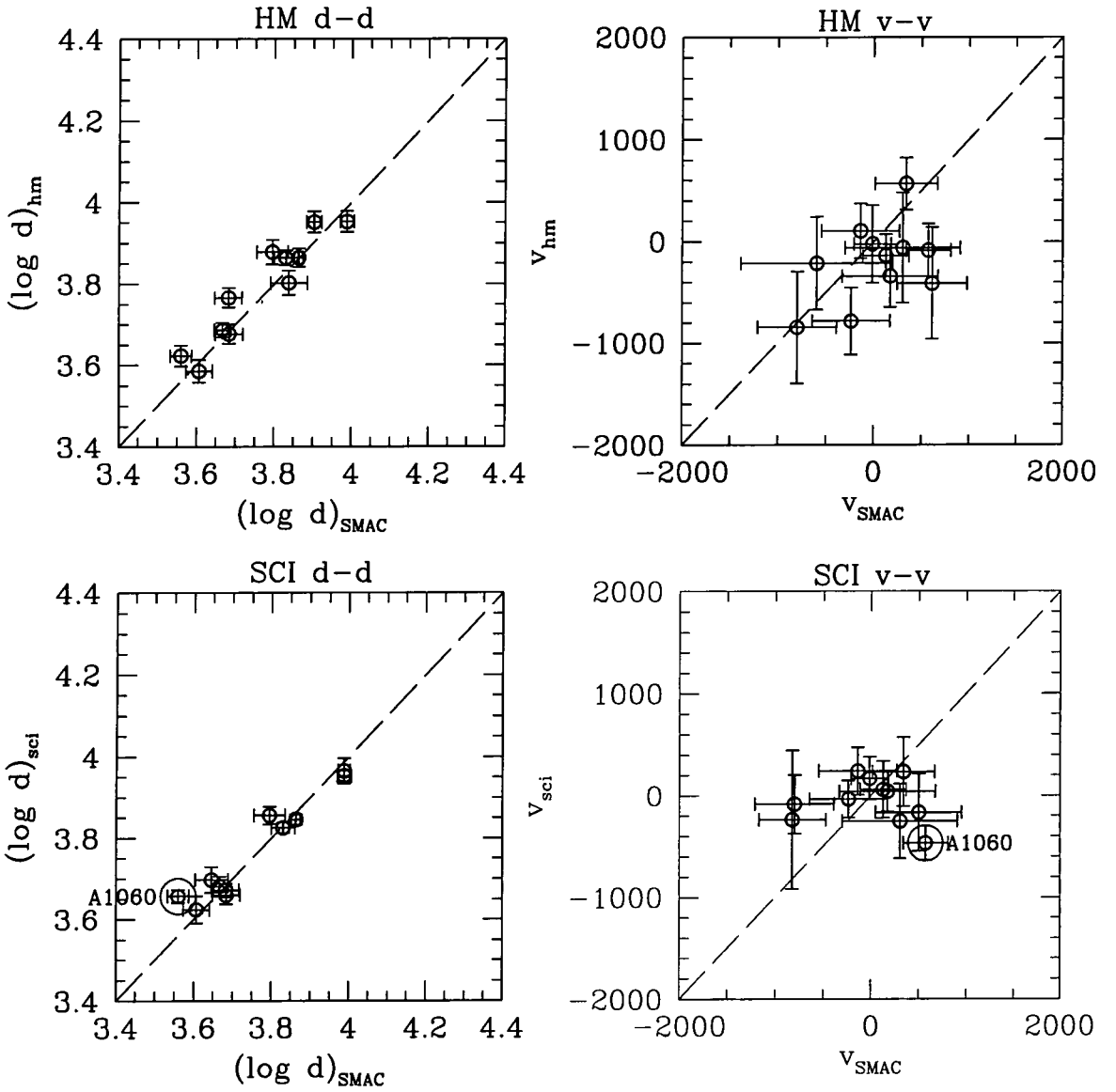

Figure 6.15: Comparison of SMAC distances and peculiar velocities with those derived from TF studies. The upper panels present comparisons with the results of Han & Mould (1992) and Mould et al. (1991, 1993), as re-derived by Willick et al. (1997). Lower panels show the comparison with the SCI results of Giovanelli et al. (1998). In the SCI comparison, the N383 and N507 groups are identified with PISC and H0122 respectively.

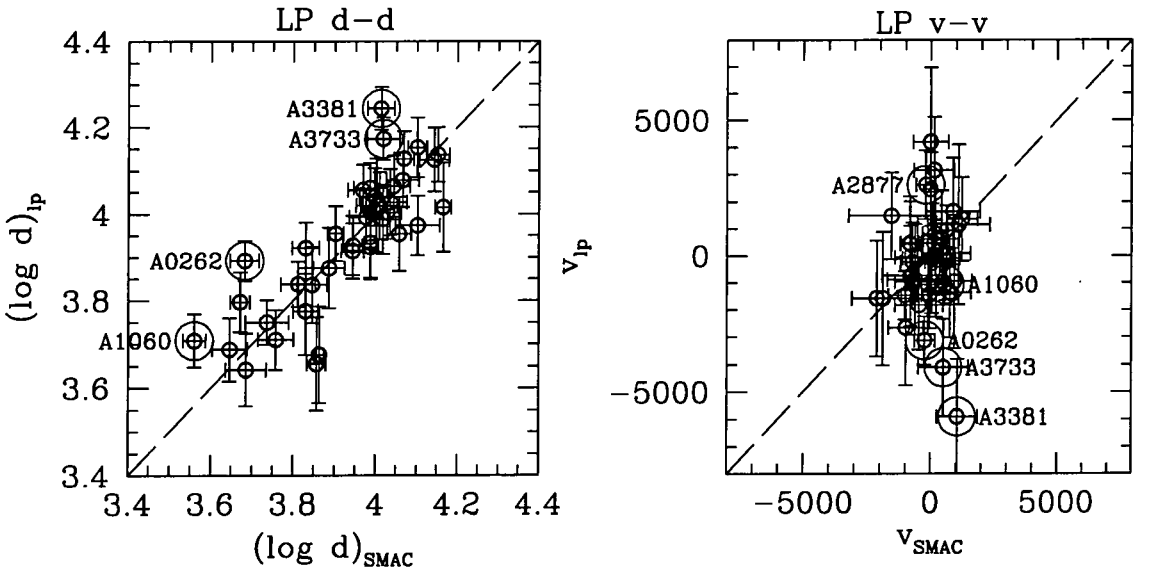

Figure 6.16: Comparison of SMAC distances and peculiar velocities with those of Lauer & Postman (1994). Note the expanded scale in the peculiar velocity comparison, with respect to the previous figures.

The SMAC data are compared in Figure 6.15 with distances from two sources of TF results. The first comparison sample is that of Han, Mould and collaborators (HM: Mould et al. 1991; Han & Mould 1992; Mould et al. 1993), as re-analysed by Willick et al. (1997) for the Mark III peculiar velocity catalogue. The comparison is for the inverse TF distances and errors as quoted by Willick et al. For this sample, the distances and peculiar velocities are both consistent with those of SMAC.

The second comparison source is the SCI sample of Giovanelli et al. (1998), for which the SCI 'in' sample distances are employed (the 'in' sample is a subset of SCI satisfying more rigorous selection criteria). In the SMAC *versus* SCI comparison, the agreement is formally acceptable given the errors, although there is a lack of significant correlation between the peculiar velocity results.

6.7.3 Brightest Cluster Galaxy distances

The BCG distance indicator suffers from errors considerably larger than those of the FP and TF methods. However, the BCG in each cluster is in nearly all cases physically associated with the cluster members probed by FP studies, and indeed is often part of FP samples. It might be hoped then that comparison between these two methods would reliably indicate cases of intrinsic differences in performance of the distance indicators.

In performing the comparison with distances from Lauer & Postman (1994),

the cluster A1736 is excluded, since the observed 'BCG' lies in a background group at $cz \sim 13000\,\mathrm{km\ s^{-1}}$, while the galaxies in the SMAC sample lie in a cluster at $cz \sim 11000\,\mathrm{km\ s^{-1}}$. Also excluded is A0076, for which the photometry of Postman & Lauer (1995) is affected by a calibration error (see Section 4.5.1).

For the 39 clusters remaining, the χ^2 for the distance comparison indicates inconsistency between the two sets of results, at the 99.3% confidence level. Since the errors are expected to be Gaussian in log(distance), the greater apparent consistency of the peculiar velocities may result from non-Gaussian errors in this quantity. This effect will be larger in this case, where the errors are sometimes $\sim 2000\,\mathrm{km\ s^{-1}}$.

Figure 6.16 reveals that the inconsistency between the distances is largely driven by four highly discrepant clusters, removal of which restores an acceptable χ^2. For one of these clusters (A0262) the BCG has recently been observed with HST, revealing alarming dust features (Lauer et al. 1998). The effects of internal extinction in the BCG would of course more strongly affect the LP distance than the SMAC distance based on many cluster members, with the LP distance being too large compared to SMAC, as is observed. It is interesting to note that the other three highly discrepant BCG distances are all in the same sense as for A0262. Whether or not internal extinction is responsible for these outliers too, cannot be ascertained at this time. However, it should be noted that culling all four outliers from the LP sample does *not* significantly reduce the BCG bulk flow.

6.8 Summary

The Inverse Fundamental Plane distance indicator relation has been applied to the SMAC sample of 725 galaxies in 56 clusters. The scatter of 0.062 in $\log \sigma$ is equivalent to a distance error of 22% per galaxy, consistent with previous work. Distances have been corrected for homogeneous Malmquist bias, cosmological curvature and passive evolution effects. Selection bias corrections are not required for the inverse distance indicator. Inhomogeneous Malmquist effects are small. The distances have random errors of 3–13%, and systematic errors of 1–3% associated with spectroscopic system matching uncertainties. These latter uncertainties are in some cases correlated from cluster to cluster.

A range of tests has been applied to search for potential systematic effects in the FP results. In particular, the $\mathrm{Mg}_2 - \sigma$ relation for the clusters is consistent with stellar populations being identical from cluster to cluster, once the errors are accounted for. The cluster distances are generally insensitive to rejection of outlying galaxies, and to the exclusion of galaxies with low (predicted) velocity dispersions. The SMAC

sample efficiently probes the collapsed cluster cores, with no evidence for subclustering in distance space, or for correlation of distance and velocity residuals. The clusters appear to conform to a nearly uniform FP, with intrinsic slope differences of $\sim$ 5%. There is a weak (and marginal) correlation of cluster velocities with the cluster FP slope. A slight offset in the FP (equivalent to $\sim$2.5% in distance) is found between E and S0 type galaxies.

Comparisons of the SMAC cluster distances with results from the literature do not reveal any gross discrepancies. The SMAC results are compatible with those from TF studies and from earlier FP surveys. Comparison with distance estimates from LP reveal four galaxies for which the BCG distance is $\sim$50% larger than that from SMAC. When these clusters are removed from the comparison, the LP and SMAC results are compatible.

References

Ashman K. M., Bird C. M., Zepf S. E. 1994, AJ,108 ,2348

Baggley G. 1996, DPhil Thesis, Oxford University

Burstein D., Davies R. L., Dressler A., Faber S. M., Lynden-Bell D., Terlevich R. J., Wegner G. 1988, in *Towards Understanding Galaxies at Large Redshift*, 17, Eds. Kron R. G., Renzini A.

Davis M., Peebles P. J. E. 1983, ARA&A, 21, 109

Faber S. M., Wegner G., Burstein D., Davies R. L., Dressler A., Lynden-Bell D., Terlevich R. J., 1989, ApJS, 69, 763

Faber S. M., Dressler A., Davies R. L., Burstein D., Lynden-Bell D., Terlevich R. J., Wegner G. 1987, in *Nearly Normal Galaxies*, 175, Ed. Faber S. M.

Giovanelli R., Haynes M. P., Salzer J. J.,, Wegner G., da Costa L. N, Freudling W. 1998, preprint (astro-ph/9808158)

Guzmán R., Lucey J. R. 1992, MNRAS, 263, L47

Han M., Mould J. R., 1992, ApJ, 396, 453

Hudson, M. J., Lucey J. R., Smith R. J., Steel J. 1997, MNRAS, 291, 488

Jørgensen I, Franx M., Kjærgaard P. 1995a MNRAS, 273, 1097

Jørgensen I, Franx M., Kjærgaard P. 1995b MNRAS, 276, 1341

Jørgensen I., Franx M., Kjærgaard P. 1996, MNRAS, 280, 167

Lauer T. R., Postman M. 1994, ApJ, 425, 418

Lauer T. R., Tonry J. L., Postman M., Ajhar E. A., Holtzman J. A.1998, ApJ, 499, 577

Lineweaver C. H., Tenorio L., Smoot G. F., Keegstra P., Banday A. J., Lubin P. 1996, ApJ, 470, 38

Lucey J. R., Carter D. 1988, MNRAS, 235, 1177

Lucey J. R., Currie M. J., Dickens R. J. 1986, MNRAS, 221, 453

Lucey J. R., Guzmán R., Carter D., Terlevich R. J. 1991, MNRAS, 253, 584

Lucey J. R., Lahav O., Lynden-Bell D., Terlevich R. J., Infante, L., Melnick J. 1999, in preparation

Lynden-Bell D., Faber S. M., Burstein D., Davies R. L., Dressler A., Terlevich R. J., Wegner G., 1988, ApJ, 326, 19

Lynden-Bell D., Burstein D., Davies R. L., Dressler A., Faber S. M., Terlevich R.J., Wegner G. 1993, in *Statistical Challenges in Modern Astronomy*, 307, eds Feigelson E. D., Babu G. J.

Mould J. R. et al. 1991, ApJ, 383, 467

Mould J. R., Akeson R. L., Bothun G. D., Han M., Huchra J. P, Roth J., Schommer R. A. 1993, ApJ, 409, 14

Postman M., Lauer T. R. 1995, ApJ, 440, 28 (PL)

Schlegel D. J., Finkbeiner D. P., Davis M. 1998, ApJ., *in press*

Saglia R. P., Colless M. M., Baggley G., Bertschinger E., Burstein D., Davies R. L., McMahan R. K., Wegner G. 1997, in *Galaxy Scaling Relations: Origins, Evolution and Applications*, eds da Costa L.N., Renzini A., p. 306

Saglia R. P., Colless M. M., Burstein D., Davies R. L., McMahan R. K., Wegner G. A 1998, *in preparation*

Sandage A. 1975, in *Galaxies and the Universe*, eds. Sandage A. et al., University of Chicago Press, p761

Scodeggio M. 1997, PhD Thesis, Cornell University

Smith R. J., Lucey J. R., Hudson M. J., Steel J. 1997, MNRAS, 291, 461

Strauss M. A., Willick J. A. 1995, Phys. Rep., 261, 271

Willick J. A. 1994, ApJS, 92, 1

Willick J. A., Courteau S., Faber S. M., Burstein D., Dekel A. 1995, ApJ, 446, 12

Willick J. A., Courteau S., Faber S. M., Burstein D., Dekel A., Strauss M. A., 1997, ApJS, 109, 333

Worthey G. 1994, ApJS, 95, 107

Chapter 7

The peculiar velocity field

7.1 Introduction

This chapter presents an analysis of the local peculiar velocity field as determined from the SMAC survey. Section 7.2 provides a qualitative description of the major features of the velocity field, after which Section 7.3 investigates the most striking aspect of the field: a coherent bulk flow of large amplitude. In Section 7.4, net peculiar motions are determined of some prominent supercluster structures. Section 7.5 presents results from a simplified model of the velocity field in the direction of the Great Attractor and Shapley Concentration. The 'coldness' of the observed flow is investigated in Section 7.6. Section 7.7 compares these results to those of previous velocity field studies, while Section 7.8 presents a more general discussion of the SMAC results in the cosmological context.

7.2 A qualitative tour of the local velocity field

The cluster distances and peculiar velocities of Table 6.3 are shown in graphical form by Figures 7.1–7.3. In the first of these figures, the velocities are shown projected onto the sky (in galactic coordinates). The latter plots project the peculiar velocity vectors onto the principal planes of the supergalactic coordinate system. Each panel shows only the clusters within 30° of the appropriate plane, such that Figure 7.2 displays motions of clusters approximately in the Supergalactic Plane (SGP), and Figure 7.3 the motions perpendicular to that plane. For clarity, the peculiar velocity vectors are shown expanded by a factor of three with respect to the spatial coordinates. Bold vectors indicate clusters with significant peculiar velocities (at the 2σ level, random error only). In these plots, and in all other results quoted here, peculiar velocities are referenced to the CMB frame.

Here, we highlight some of the qualitative features of the velocity field as suggested by Figures 7.1–7.3. The significance of these features is discussed in subsequent sections of this chapter.

- A dipole (bulk-flow) component, visible in Figure 7.1 as a predominance of negative velocity clusters at $0° < l < 180°$ and of positive velocities at $180° < l < 270°$. The bulk motion is also evident in Figure 7.3, as a streaming from positive to negative SGX.

- The Great Attractor / Hydra–Centaurus (GA/HC) region lies at $\sim 50\,h^{-1}$Mpc distance, in the (–X,+Y) quadrant of Figure 7.2. Strong outflow is observed in this region, with only one cluster exhibiting a negative velocity.

- Beyond the GA, three clusters lie in the foreground of the Shapley Concentration (SC), and exhibit a marginally significant mean flow away from the LG, suggesting that the influence of SC dominates over that of the GA in this region. The cluster A3558, at the core of SC, is at rest within the errors.

- Three clusters exhibit a marginally significant positive mean flow, at (–Y, –Z) (Figure 7.3), corresponding to $(l, b) \sim (240°, -25°)$. The region is in the foreground of the Horologium–Reticulum supercluster. Together with the Shapley foreground, this flow pattern provides the outflow pole of the dipole.

- In the Perseus–Pisces (PP) ridge at $(l, b) \sim (140°, -20°)$, a few clusters have significant peculiar velocities, but taken as a whole there is no coherent motion of the structure. In the background of PP, negative velocities predominate.

- Generally more negative velocities are found in the background of PP, and in the Hercules–Corona–Borealis region at $(l, b) \sim (40°, +45°)$. These regions provide the inflow pole of the dipole.

7.3 The bulk motion

The bulk velocity vector $\mathbf{v}_B$ can be visualised as the vector average of the full three dimensional velocity field, computed over some chosen volume. If the velocity field can be sampled with arbitrary density, the bulk-flow will be primarily sensitive to the distribution of mass outside or at the edges of the survey volume. It is for this reason that the bulk velocity is a sensitive probe of the mass clustering power on very large scales, and potentially a discriminant between cosmological structure-formation models.

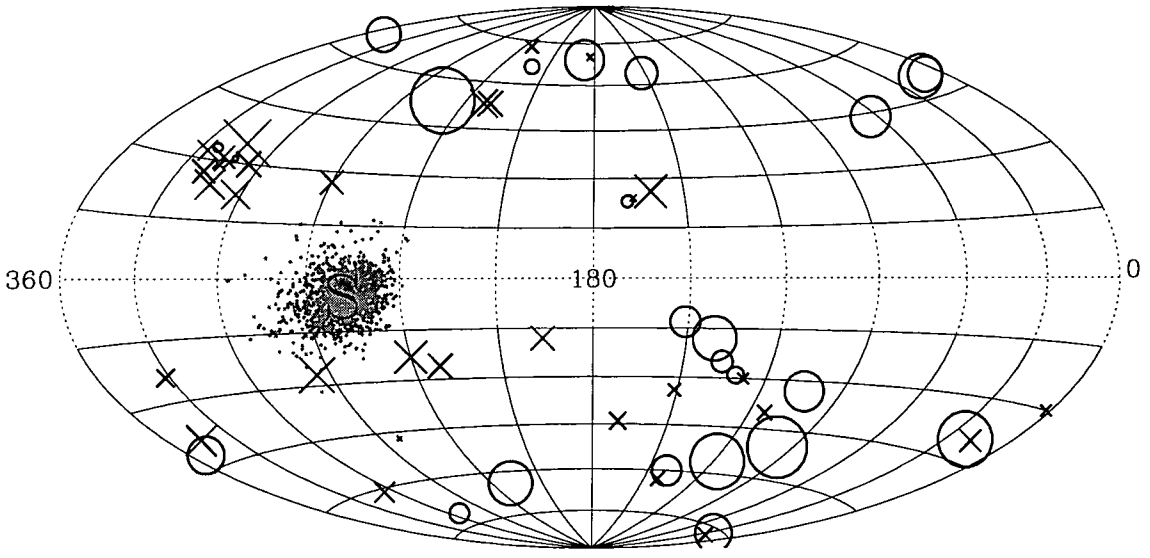

Figure 7.1: Sky-projection of the SMAC peculiar velocity field (with respect to the CMB), in galactic coordinates. Clusters with negative peculiar velocities are indicated by circles, and those with positive peculiar velocities denoted by crosses. The symbol size is proportional to the magnitude of the peculiar velocity. Note that the significance of the velocities is not indicated. The 'S' marks the direction of the best fit bulk flow vector, and the cloud of points around it are the flow directions from 1000 Monte-Carlo realisations of the random errors.

In practice, however, the peculiar velocity field is sampled sparsely, according to the location of the observed galaxies or clusters. While the best-fitting bulk-flow of a sample of velocity tracers can still be defined, this observational quantity will be sensitive, to a greater or lesser degree, to mass-density fluctuations on scales smaller than the survey diameter. The exact extent of these contributions from small and intermediate scales depends upon the sample geometry and the underlying mass power spectrum (Feldman & Watkins 1994). In the following discussion of observational results from SMAC, the term 'bulk-flow' will generally refer to the best-fitting pure bulk-flow model; this should not be interpreted as the underlying bulk motion of all galaxies within $120\,h^{-1}$Mpc, which is clearly not determined from the survey.

The peculiar velocity field of a survey such as SMAC can be modelled as the sum of a monopole (Hubble-like) and a dipole (bulk-flow) component:

$$\mathbf{v}_{\rm mod}(\mathbf{r}) = \Delta_{\rm H} r + \mathbf{v}_{\rm B}\,, \tag{7.1}$$

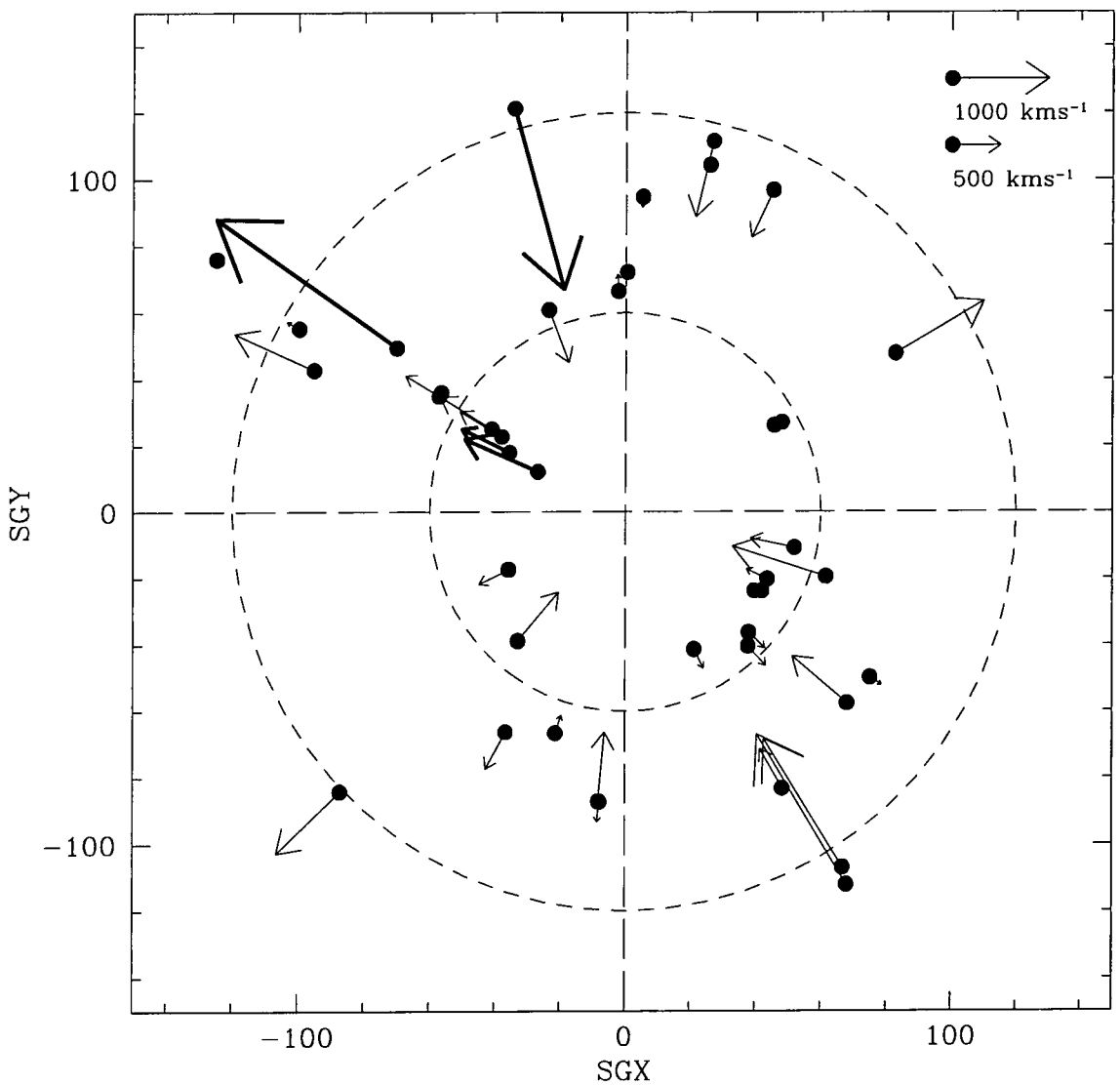

Figure 7.2: SMAC peculiar velocity vectors (in the CMB frame) projected onto the SGX–SGY plane. Clusters are plotted by filled points at the distance given by their FP-derived distance in h^{-1}Mpc. The vectors give the direction and magnitude of the radial peculiar velocity, but note that for clarity the vectors have been expanded by a factor of three, relative to the spatial coordinates. Bold vectors highlight peculiar velocities significant at the $>2\sigma$ level. To reduce projection distortions, only those clusters within 30° of the SGX–SGY plane have been plotted. The galactic plane lies along the SGX axis.

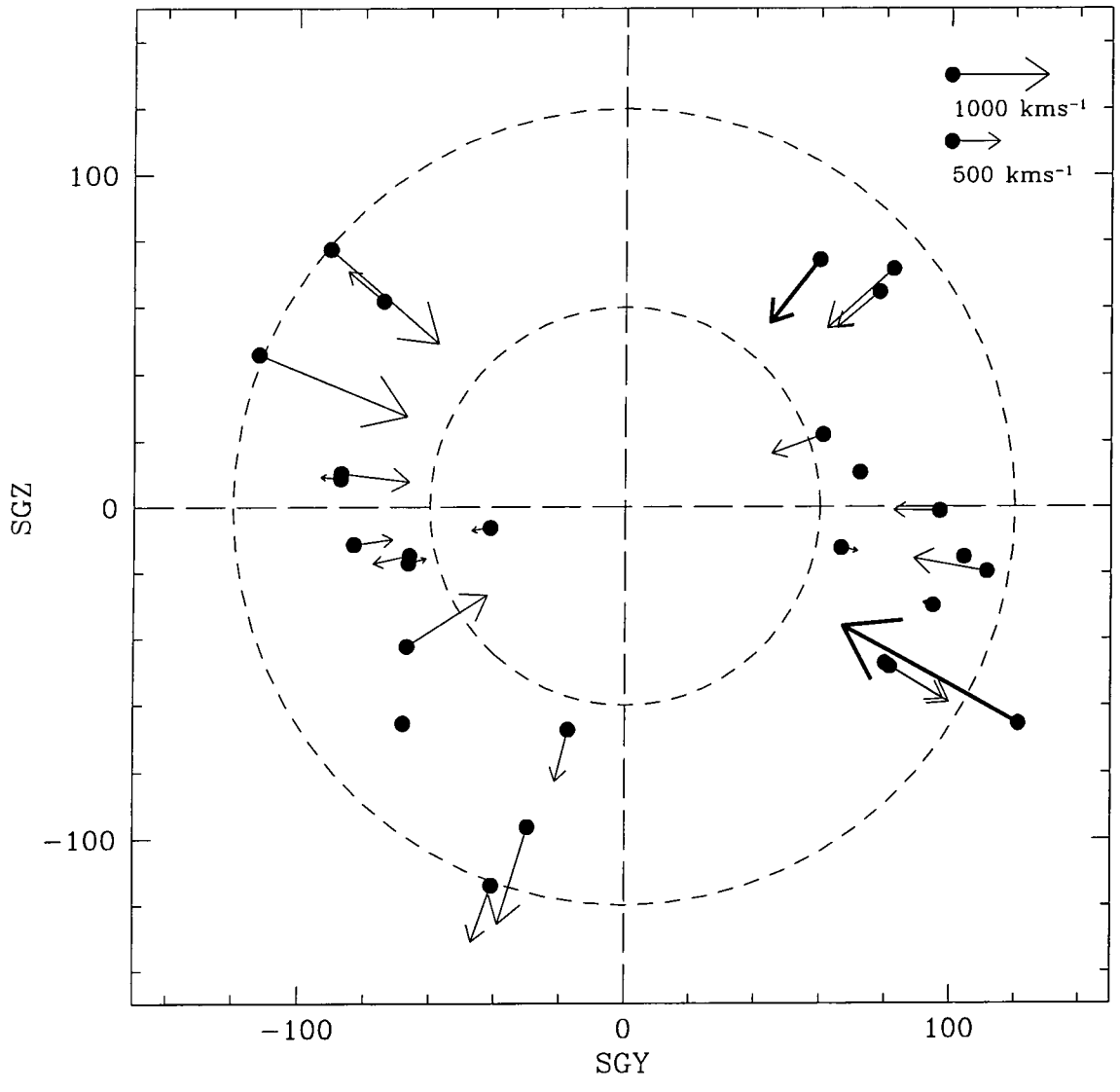

Figure 7.3: SMAC peculiar velocity vectors (CMB frame) on the SGY–SGZ plane. Details are as for Figure 7.2. The galactic plane lies approximately along the SGZ axis.

where $\mathbf{v}_{\rm mod}$ is the model-predicted peculiar velocity vector at position $\mathbf{r}$, the position independent vector $\mathbf{v}_{\rm B}$ is the bulk-flow vector, and the monopole term is $\Delta_{\rm H}$.

This model can be fitted to the observed radial peculiar velocities v_i by constructing the statistic

$$\chi^2 = \sum_i \frac{[\mathbf{v}_{\rm mod}(r_i) \cdot \hat{\mathbf{r}}_i - v_i]^2}{\sigma_i^2 + \sigma_v^2} \tag{7.2}$$

and minimising with respect to the four free parameters – $\Delta_{\rm H}$ and the three components of $\mathbf{v}_{\rm B}$. In the above, $\mathbf{r}_i$ are the position vectors of the clusters (with distances given by the FP results). The weighting accounts for the measurement errors in the peculiar velocities (σ_i), and for a 'thermal' component in the velocity field (σ_v). This latter component allows for an intrinsic scatter around the best fitting model, presumably generated on scales much smaller than the survey volume. For the bulk-flow fits, the rms velocity dispersion is set to $\sigma_v = 150$ km s^{-1}. The fits are not sensitive to this choice: $\mathbf{v}_{\rm B}$ moves by $\sim$10 km s^{-1}, if $\sigma_v = 350$ km s^{-1} is adopted instead.

7.3.1 The default solution

Initially, the bulk-flow solution is determined using all 56 clusters, with peculiar velocities taken directly from Table 6.3. For this sample the best fit bulk flow vector has amplitude 811 ± 180 km s^{-1}, directed towards $(l, b) = (258°, -5°)$.

The error estimate here is derived from Monte-Carlo realisations of the *random* errors on each cluster distance estimate. The Monte-Carlo datasets are analysed in precisely the same way as for the real data, fitting simultaneously for $\Delta_{\rm H}$ and $\mathbf{v}_{\rm B}$. These errors are used in correcting the bulk-flow amplitude for 'error biasing' as discussed by Lauer & Postman (1994, LP). Specifically, the 'raw flow amplitude is biased high by the errors on the individual components and should be corrected to

$$|\mathbf{v}_{\rm B}| = [v_{\rm B}^2 - (e_X^2 + e_Y^2 + e_Z^2)]^{\frac{1}{2}} . \tag{7.3}$$

The flow amplitude quoted above is already corrected for this bias, which amounts to only 30 km s^{-1}. Figure 7.4 shows the Monte-Carlo bulk-flow solutions, projected into the principal planes of the supergalactic coordinate system. Note that the error ellipsoid is not isotropic, and that its long axis is close to the SGZ axis, and to the direction of the SMAC flow. The large error in the SGZ component is due in part to the Zone of Avoidance (ZoA) and in part to a lack of clusters in the region at $l \sim 60°$, and more generally far from the SGP. While the SGX component should also be affected by the ZoA, the cluster sample typically extends to lower galactic latitude within the SGP. While it is true that the GA and PP regions, in the SGP, dominate the local density field, the poor sampling at high supergalactic latitude can perhaps be partially ascribed

Table 7.1: Default bulk-flow solution for the SMAC peculiar velocity field. All velocities are in km s^{-1}. The direction of the flow vector is given in galactic coordinates (l, b).

	N_{gal}	N_{cl}	Δ_H	v_X	v_Y	v_Z	$\|v_B\|$	l	b
Best fit solution:	725	56	−0.003	−431	+6	−722	811	258.3	−5.0
Random errors :			±0.009	±92	±95	±181	±158	±8.9	±6.4
System matching errors :			±0.003	±66	±48	±92	±87	±5.1	±3.0

to an 'SGP-centric' bias in observational programmes to date. The EFAR survey of Wegner et al. (1996) has better coverage along the SGZ axis. Improved constraints on this bulk flow component would result from incorporation of the SMAC and EFAR datasets into a single homogeneous catalogue.

The cluster distance estimates are also subject to systematic errors arising from the uncertainties in the spectroscopic system matching procedure of Section 5.2. As noted in Section 6.5, these errors are small for individual clusters, but can be correlated from cluster to cluster. Since such correlations are likely to exhibit spatial coherence (neighbouring clusters often have identical data sources), this effect can translate into substantial errors in the bulk-flow. The system-matching errors are determined by fitting flow models to the bootstrap realisations of the merged data catalogue (see Section 5.2.3), and computing the resulting dispersion in the flow components. The system-matching error in the bulk motion amplitude is found in this way to be 87 km s^{-1}, which has already been added in quadrature to the error quoted above[1].

7.3.2 Robustness tests

The large amplitude of the SMAC bulk-flow is quite unexpected, given the depth of the survey, and it is vital to investigate the reliability robustness of this result. In this section, a range of tests are performed to assess the sensitivity of the SMAC flow vector to potential systematic effects. Many of the results of these tests are summarized in Table 7.3

The jackknife test, in which each cluster in turn is deleted from the sample and the bulk-flow recomputed, is a simple method for identifying clusters with 'undue influence' on the fit. Such clusters may have highly significant (but spurious) peculiar velocity measurements as a result of systematic errors, or may instead be reliable measurements which nevertheless have high weight in the fit. Either way, their presence may inval-

[1]It was argued in Chapter 5 that the system matching procedure employed here yields a catalogue with approximately half that which would be obtained by simply comparing each spectroscopic dataset, one-by-one, with a fiducial standard. Had this more simple method been used, the resulting systematic uncertainties in the bulk-flow would have been comparable to the random errors.

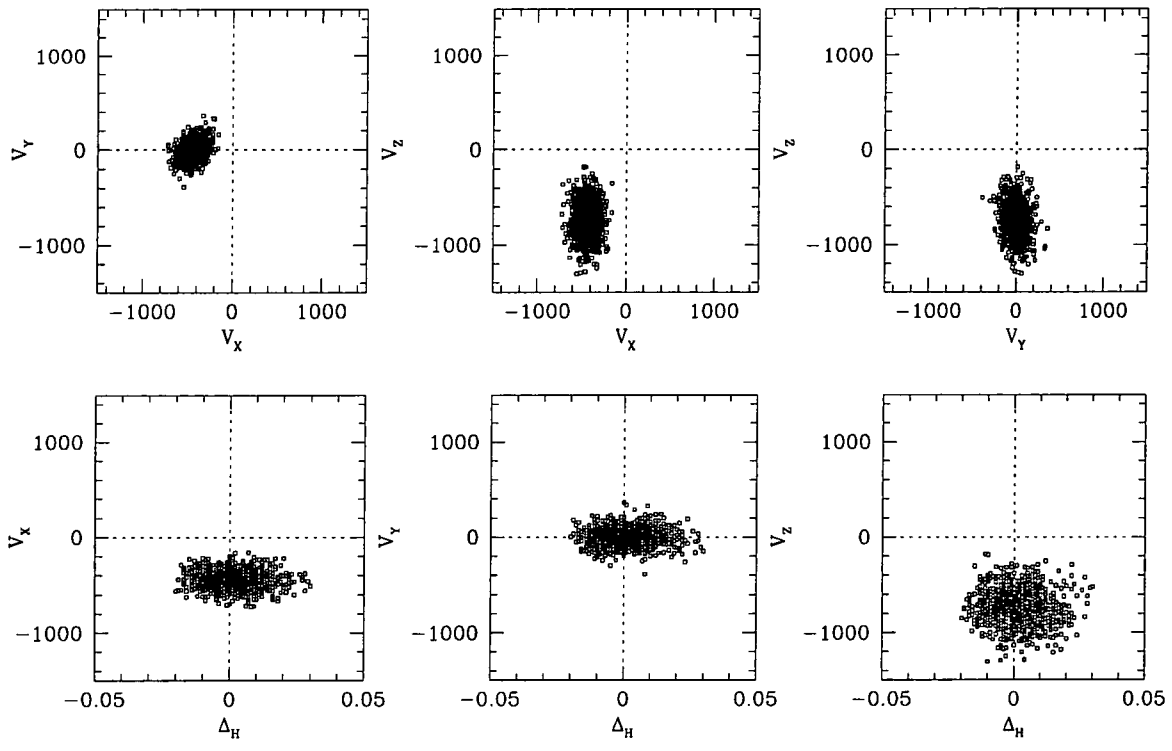

Figure 7.4: Distribution of flow model parameters over 1000 Monte-Carlo realisations of the FP distances. The upper panels show the bulk-flow error ellipsoid, projected into supergalactic coordinates. In the lower panels, the derived velocity components are plotted against the monopole parameter Δ_H. All velocities are in km s^{-1}.

idate the interpretation of the flow as a *coherent* streaming across the survey volume. Figure 7.5 presents the results of a jackknife test for the SMAC bulk-flow components. The principal result of the test is that no single cluster dominates the flow, or influences the fit by more than the quoted 1σ error. The amplitude of the flow is *increased* by $> 50\,\mathrm{km\ s^{-1}}$ by excluding A1656, S0301 or PISC. Only by removing A3526 (Centaurus) can the flow amplitude be appreciably *reduced*: by $65\,\mathrm{km\ s^{-1}}$.

For a more brutal test, entire superclusters may be deleted from the sample, to test whether any single prominent structure dominates the SMAC bulk motion. Groups of clusters have been objectively identified from the cluster sample, by means of a simple friends-of-friends algorithm. At a linking length of $30\,h^{-1}$Mpc (in redshift space), 13 superclusters are found with two or more members (Table 7.2). While some of these are close pairs (eg A4038 and A4049, collectively known as Klemola 44), others are extended structures such as PP and HC/GA. Note that only 11 clusters have no neighbours within $30\,h^{-1}$Mpc. The influence of each supercluster on the bulk-flow solution is shown in Figure 7.6. The bulk-flow components are robust against the removal of these

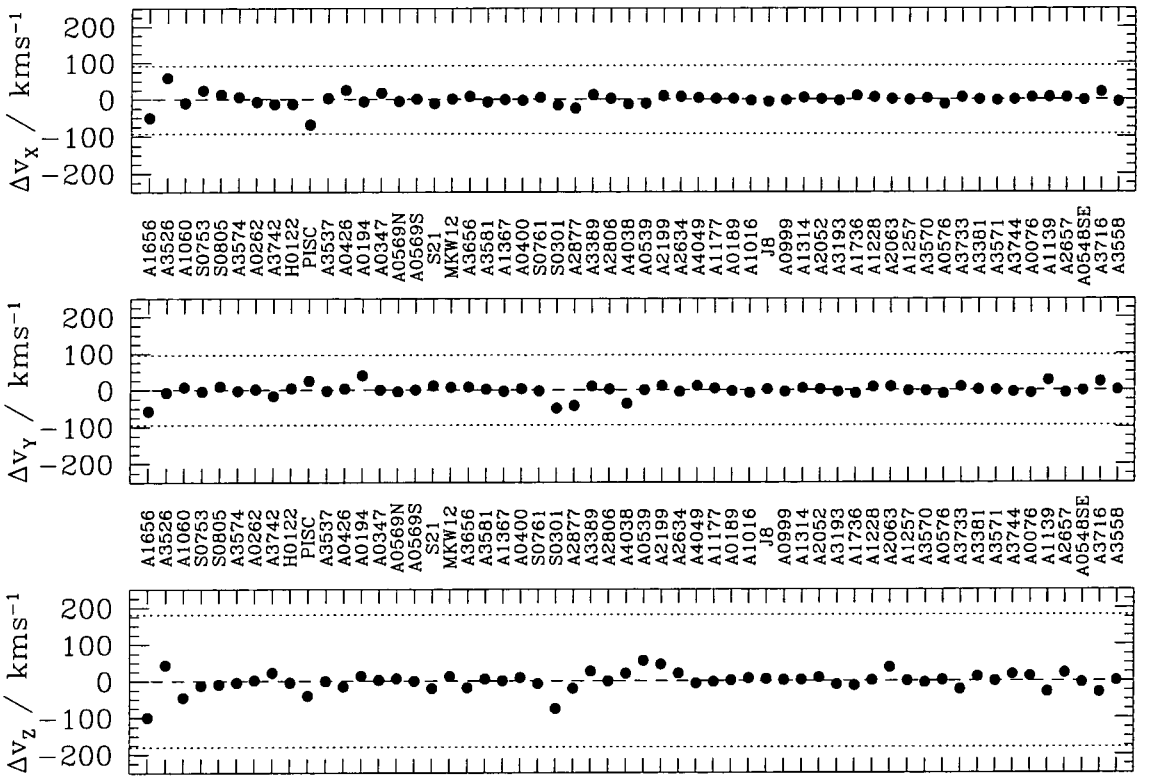

Figure 7.5: Jackknife test for bulk-flow components. The top panel shows the change (relative to the default solution) of the SGX component of the bulk-flow vector, caused by excluding each cluster in turn from the sample. The remaining panels show the same for the SGY and SGZ components. The dotted lines show the 1σ error bars (random error) in each component, as derived from Monte-Carlo simulations.

superclusters. As expected, the largest superclusters, HC/GA and PP, have the greatest effect. However, the bulk-flow amplitude is reduced by only $\sim$100 km s^{-1} when HC/GA is deleted from the sample, and increases when PP is removed. The SMAC bulk-flow is not, therefore driven by the streaming motion of any single supercluster structure.

Of the various systematic effects which may be suspected of affecting the FP distances, many are monopolar in character, depending only on distance. While these corrections principally affect only the monopolar flow component, the non-uniformity of the sample sky coverage will introduce correlation between the bulk-flow and monopole terms. For the SMAC sample, the sky-coverage is generally good for $|b| > 15°$, except towards $(l, b) = (\sim 60°, 0°)$, where an angular region of $60° \times 60°$ is unsurveyed. This direction lies roughly towards the positive SGZ axis and it is therefore to be expected that the SGZ component of the bulk flow will be correlate with the monopole term. In order to test for such an effect, bulk-flow fits have been performed in which the monopole parameter is held fixed at each of a range of values. The SGZ component

Table 7.2: Superclusters used in exclusion test. These structures have been identified by a friends-of-friends algorithm with linking length $30\,h^{-1}$Mpc

ID	member clusters	Notes
1	A0076 A0189	Cetus
2	A0569N A0569S	
3	A0999 A1016 A1177 A1228 A1257 A1314	Leo
4	A2052 A2063	
5	A0548SE A3381	
6	A1736 A3570 A3571	Shapley Foreground
7	A3733 A3744	
8	A4038 A4049	
9	A1367 A1656 MKW12	Coma
10	S21 A0194 A0262 A0347 A0400 A0426 H0122 PISC	Perseus–Pisces
11	A2806 A2877 S0301	
12	A1060 A3526 A3537 A3574 A3581 S0753 S0761	Hydra–Cen / Great Attractor
13	A3656 A3742 S0805	Pavo–Indus

does indeed correlate with the monopole varying by $\sim$150 km s^{-1} over an interval of 0.1 in $\Delta_{\rm H}$. However, a 10% error in the monopole is a very large effect (equivalent to changing the distance of Coma by 700km s^{-1}). Thus any inadequacy in the treatment of distance-dependent corrections to the SMAC cluster distances cannot be the cause of the bulk motion. Over the 3σ range of $\Delta_{\rm H}$ allowed in the default solution, the bulk-flow amplitude varies by just $\sim$80 km s^{-1}.

In Chapter 6, the FP slope was determined to be $\alpha = 1.418 \pm 0.034$. However, it was remarked there that a small number of clusters were better fit by slopes as low as $\alpha \sim 1.2$. The variation in the SMAC bulk-flow, as the slope is varied, has been assessed by recomputing the cluster peculiar velocities with the slope fixed at each of a range of values. Again, the SGZ component is the most sensitive, changing by $\sim$35 km s^{-1} for each 1σ (ie 0.034) step in α. The sense is such that the magnitude of the SGZ flow component (and consequently of the bulk-flow) is reduced for smaller adopted α. However, for a 3σ change to $\alpha \sim 1.3$, the bulk-flow amplitude is only reduced by 100 km s^{-1}. For a slope of $\alpha \sim 1.2$, the flow amplitude is 600 ± 150 km s^{-1}. Hence no 'reasonable' global slope can be adopted which substantially suppresses the apparent bulk-motion.

No evidence was found, in Chapter 6, for a systematic bias affecting galaxies with predicted velocity dispersions lower than 100 km s^{-1}. Excluding these galaxies from the sample does not affect the bulk-flow solution.

Deleting from the sample those clusters with a mean extinction $A_B > 0.45$ mag has a more substantial effect on the bulk flow, with the SGZ component reduced by 150 km s^{-1}. By means of Figure 7.5, the clusters A3526 and A0539 can be identified as the cause of this effect. Indeed, cutting only these points from the sample yields

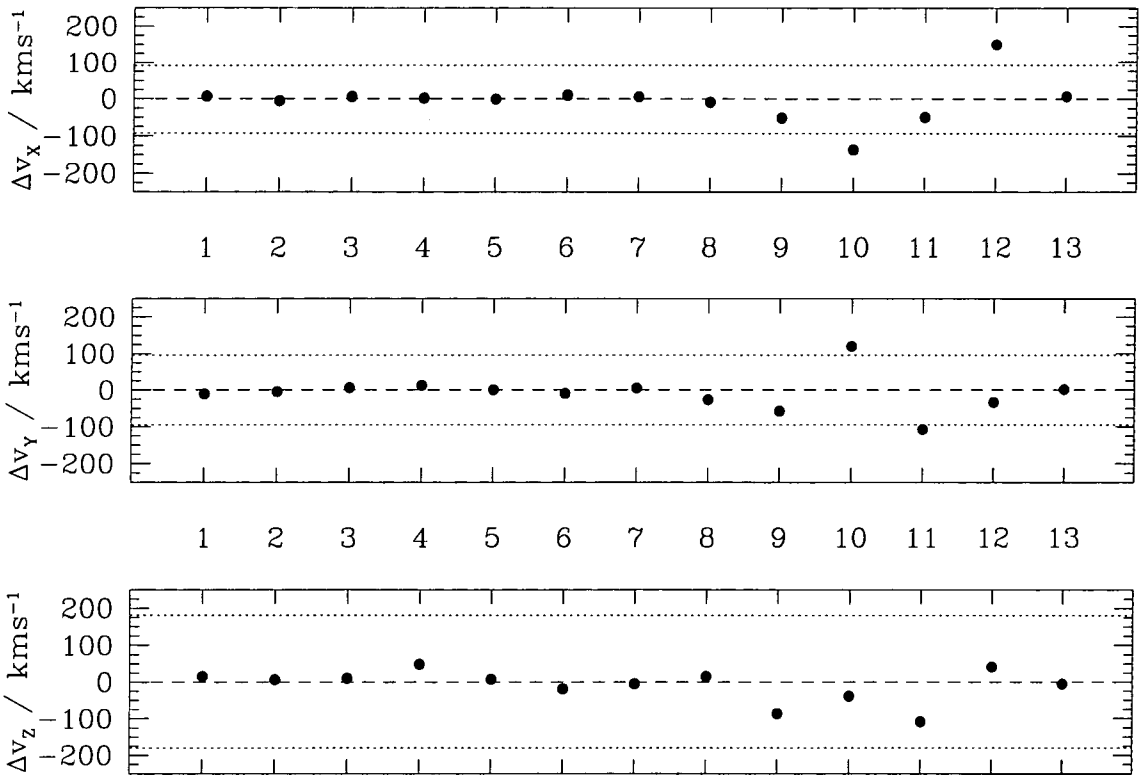

Figure 7.6: Supercluster exclusion test for bulk motion components. Points show the change in bulk motion components, when the superclusters of Table 7.2 are deleted in turn from the sample. The excluded superclusters are identified by the number given in the first column of Table 7.2. Dotted lines indicate the 1σ random errors on the default solution.

approximately the same flow found by cutting all the high-extinction clusters. This test reveals no strong evidence against the reliability of distances for clusters with moderately high A_B.

Table 7.3 summarizes a range of additional tests for systematic effects on the bulk motion. The flow vector is not significantly affected by the exclusion of clusters with random errors $> 10\%$, nor by deleting the 'extra' clusters of Section 5.4. Removing the most distant clusters (in real or redshift space) makes little difference to the flow. Clusters can also be excluded on the basis of the reliability flags assigned to clusters in Section 6.5. Deleting clusters with outlier-sensitive distances does not affect the flow. Cutting out the clusters with apparently discrepant FP slopes makes no difference to the flow. Removing clusters flagged for significant offsets from the Mg $-\ \sigma$ relation, the bulk motion is unchanged.

Table 7.3: Robustness tests for the SMAC bulk-flow solution. The numbers of galaxies and clusters used in the fit is given by $N_{\rm gal}$ and $N_{\rm clus}$. All velocities are in km s^{-1}, and all flow amplitudes have been corrected for error-biasing. See text for further details.

	$N_{\rm gal}$	$N_{\rm cl}$	$\Delta_{\rm H}$	v_X	v_Y	v_Z	$\|v\|$	l	b
Default solution:	725	56	−0.003	−431	+6	−722	811	258.3	−5.0
			±0.009	±92	±95	±181	±158	±8.9	±6.4
$e_d/d < 0.1$	654	43	+0.003	−422	−14	−749	826±171	257.0	−6.4
No 'extra' clusters	574	43	−0.010	−502	+39	−887	1020±164	256.9	−3.3
$cz < 10000$ km s^{-1}	566	38	−0.004	−393	+50	−713	786±137	256.2	−2.0
$d < 12000$ km s^{-1}	651	49	−0.012	−398	+41	−728	804±137	256.0	−2.7
$d < 10000$ km s^{-1}	563	38	−0.012	−393	+69	−689	767±130	256.9	−0.6
Exclude Hydra–Cen	622	49	0.000	−282	−27	−681	697±202	250.1	−8.0
Exclude PP	611	48	−0.983	−567	+126	−761	923±183	263.7	+2.5
Exclude supercl. 11	687	53	+0.002	−480	−101	−831	933±188	257.8	−11.5
$A_B < 0.45$	606	50	−0.006	−363	+2	−595	658±160	258.9	−5.2
No A3526, A0539	660	54	−0.002	−382	−1	−617	690±167	259.3	−5.5
No 'O-flag'	711	53	−0.006	−447	−19	−690	796±132	260.6	−6.6
No 'M-flag'	655	49	0.000	−440	+4	−755	833±196	257.7	−5.2
No 'S-flag'	687	53	+0.001	−448	+2	−720	823±135	259.4	−5.2
$\sigma_{\rm pred} > 2.0$	682	56	−0.005	−431	−23	−746	824±188	257.6	−7.0
3σ monopole tweak	725	56	(−0.030)	−432	+17	−772	855±179	256.7	−4.4
3σ monopole tweak	725	56	(+0.024)	−429	−4	−673	768±175	260.1	−5.6
3σ α-tweak (1.520)	725	56	+0.006	−478	−29	−821	910±200	257.8	−7.2
3σ α-tweak (1.316)	725	56	−0.011	−389	+34	−621	697±164	259.5	−2.7

7.4 Peculiar velocities of superclusters

The net radial peculiar velocity of the 13 friends-of-friends superclusters have been determined directly from the velocities of their member clusters, and are presented in Table 7.4. These results should be treated with some caution, since the 'superclusters' are merely groupings of an incomplete underlying cluster sample. However, these supercluster motions, with smaller errors than the individual cluster velocities, provide an illustrative 'smoothing' of the SMAC velocity field. Note that since different clusters within a supercluster often share spectroscopic data, it is necessary to calculate the system matching error for the supercluster velocities. This error is determined by computing the rms of the supercluster motion, over all the bootstrap perturbed realisations

Table 7.4: Peculiar velocities of superclusters. For each of the structures identified by the friends-of-friends algorithm, the table gives the variance-weighted mean radial peculiar velocity of the supercluster, with its associated error. The final column gives the system-matching error, as discussed in the text. Note that supercluster 10* is added by hand, to reflect the definition of the 'PP ridge' used by Hudson et al. (1997).

ID	Member clusters	v_p (km s^{-1})	e_{syst}
1	A0076 A0189	−903±725	±100
2	A0569N A0569S	−4±379	±89
3	A0999 A1016 A1177 A1228 A1257 A1314	71±380	±107
4	A2052 A2063	−867±583	±159
5	A0548SE A3381	936±676	±223
6	A1736 A3570 A3571	971±533	±118
7	A3733 A3744	−23±849	±210
8	A4038 A4049	−332±368	±131
9	A1367 A1656 MKW12	−20±177	±108
10	S21 A0194 A0262 A0347 A0400 A0426 H0122 PISC	−54±126	±81
10*	S21 A0262 A0347 A0426 H0122 PISC	−157±147	±93
11	A2806 A2877 S0301	−311±285	±114
12	A1060 A3526 A3537 A3574 A3581 S0753 S0761	623±115	±70
13	A3656 A3742 S0805	151±265	±63

of the spectroscopic catalogue.

Significant peculiar velocities (at the $>1.5\sigma$ level) are determined for only two systems: the HC/GA structure (supercluster 12), and the Shapley Foreground group (supercluster 6) behind it. No significant peculiar velocity is observed for the PP supercluster (supercluster 10). Restricting the extent of PP to match the 'ridge' sample of Hudson et al. 1997 (supercluster 10*), the net motion remains insignificant at $-157 \pm 174\,\mathrm{km\ s^{-1}}$.

7.5 Shapley and the Great Attractor : A simple toy model

A striking feature of the SMAC velocity field is the lack of 'far-side' infall behind the HC/GA, and the apparent continuation of positive peculiar velocities into the foreground of SC. The overall impression is that SC generates a significant fraction of the streaming traditionally attributed to the 'Great Attractor', and retards the infall in the GA background. In this section, a simple two-component 'toy model' is employed to determine the relative dynamical influence of these two mass complexes.

The GA+SC model velocity field is a superposition of two spherical infall models, each of which is of the form introduced by Faber & Burstein (1988, FB88). The first

term accounts for the peculiar motions generated by the GA:

$$\mathbf{v}_{\rm GA} = v^0_{\rm GA} \frac{\mathbf{r}_{\rm GA} - \mathbf{r}}{r_{\rm GA}} \left[\frac{r^2_{\rm GA} + c^2}{|\mathbf{r}_{\rm GA} - \mathbf{r}|^2 + c^2_{\rm GA}} \right]^{(n+1)/2} . \tag{7.4}$$

Here, $\mathbf{r}_{\rm GA}$ is the position of the GA, $\mathbf{r}$ the position of the cluster considered, and $v^0_{\rm GA}$ the peculiar motion induced by the GA at the Local Group (LG). The 'concentration' of the attracting mass is characterised by a core radius $c_{\rm GA}$ and the index n. These parameters are held fixed at the FB88 values: $n = 1.7$ and $c = 0.35 \times r_{\rm GA} \approx 1500$ km s^{-1}. To take include the effects of a second attractor, representing Shapley, the second element of the model is analogous to the above:

$$\mathbf{v}_{\rm SC} = v^0_{\rm SC} \frac{\mathbf{r}_{\rm SC} - \mathbf{r}}{r_{\rm SC}} \left[\frac{r^2_{\rm SC} + c^2}{|\mathbf{r}_{\rm SC} - \mathbf{r}|^2 + c^2_{\rm SC}} \right]^{(n+1)/2} . \tag{7.5}$$

SC is given the same values of n as for the GA, but the core radius is enlarged over that of GA by a factor 1.5. The attractor positions are held fixed at $(l, b, cz) = (309°, 18°, 4200$ km s$^{-1})$, for the GA, and $(l, b, cz) = (312°, 31°, 14500$ km s$^{-1})$, for SC. The GA+SC flow model then predicts the velocity of each cluster to be

$$\mathbf{v}_{\rm mod} = \mathbf{v}_{\rm GA} + \mathbf{v}_{\rm SC} . \tag{7.6}$$

The component of the LG motion in the direction of GA and SC is 475 km s^{-1}, and the model can be normalised by demanding that it predict this velocity at the LG. The model is then completely specified by the fractional contribution of SC to this total.

The statistic

$$\chi^2 = \sum_i \frac{[\mathbf{v}_{\rm mod}(r_i) \cdot \hat{\mathbf{r}}_i - v_i]^2}{\sigma_i^2 + \sigma_v^2} \tag{7.7}$$

(with σ_v=150 km s^{-1}, as for the bulk-flow fits) is then minimized with respect to the only free parameter, $v^0_{\rm SC}/v_{\rm LG}$. This very simplistic model is certainly not expected to perform adequately over whole the volume of the SMAC survey (since other attractors and voids can not be neglected), so the fit is restricted to the ten clusters which lie within 15° of SC. These clusters (A3526, S0753, A3574, A3537, A3581, S0761, A1736, A3570, A3571 and A3558) span a distance range from 3000 km s^{-1} to 14600 km s^{-1}.

Using the peculiar velocities from Table 6.3, the best fit is found for $v^0_{\rm SC} = 231 \pm 54$ km s^{-1}, ie $v^0_{\rm SC}/v_{\rm LG} = 0.49 \pm 0.12$, where the error includes system matching errors (determined by the same procedure as used previously for the bulk-flow components). Scaling by the square of the distance to each attractor, the implied ratio of excess mass in the two superclusters is $M_{\rm SC}/M_{\rm GA} = 10 \pm 2$. A jackknife test confirms that no individual cluster has undue influence on the fit, though deletion of A3571 moves the results by slightly more than 1σ, resulting in an even larger amplitude for the SC infall.

Tests indicate that the SC infall amplitude is somewhat degenerate with the assumed SC core radius. Forcing the SC core radius to the same value as for GA, the best fit SC contribution is reduced to $v_{SC}^0/v_{LG} = 0.39$.

Figure 7.7 illustrates the results of the GA+SC fits. The GA flow alone is a very poor fit ($\chi^2 = 27$) to the data beyond 4000 km s^{-1}, where the expected far-side infall is not observed. However, the flow cannot be entirely generated by SC, since the large mass required (to give the correct LG motion) would dramatically overproduce the velocities at ~10000 km s^{-1} ($\chi^2 = 30$). The final panel shows the best-fitting GA+SC model, with 37% of the LG velocity generated by SC and the rest by the GA. This model is formally a good fit ($\chi^2 = 8.4$ with 9 degrees of freedom) and reproduces to the broad features of the data: outflow at ~4000 km s^{-1}, a retardation of the flow (but no strong far-side infall) at 6000–7000 km s^{-1}, and renewed outflow at 10000 km s^{-1}.

At face value, then, the SMAC data argue that SC generates ~40–50% of the LG's peculiar velocity in this direction. However, the toy model presented here is necessarily over simplistic. It should be noted that a bulk streaming model, with 475 km s^{-1} outflow throughout the region, also provides an acceptable fit to the data for these ten clusters. Improved peculiar velocity data, especially beyond 10000km s^{-1} distance, are required for a clear detection of the shear induced by SC.

7.6 The RMS cluster velocity

The bulk-flow statistic, discussed above, provides a probe of the clustering power of mass on large scales. By contrast, the rms dispersion of cluster velocities *around* the bulk-flow is sensitive to the power on scales smaller than the survey volume.

Estimation of the the rms cluster velocity, σ_v, requires careful treatment of the measurement errors, which vary significantly from cluster to cluster, and are generally larger than the intrinsic dispersion. Watkins (1997, W97) has presented a maximum likelihood technique in which σ_v is determined by maximizing the probability of the observed cluster velocities, given the measurement errors. In this method, the velocity v_i of cluster i is assumed to be drawn from a Gaussian distribution with variance $\sigma_v^2 + \sigma_i^2$. This variance arises from the intrinsic rms velocity of the sample (σ_v), and from the measurement error (σ_i) associated with v_i. The probability of measuring velocity v_i for cluster i is then given by

$$P(v_i) = \frac{1}{(2\pi)^{1/2}(\sigma_v^2 + \sigma_i^2)^{1/2}} \exp\left[\frac{-v_i^2}{2(\sigma_v^2 + \sigma_i^2)}\right], \tag{7.8}$$

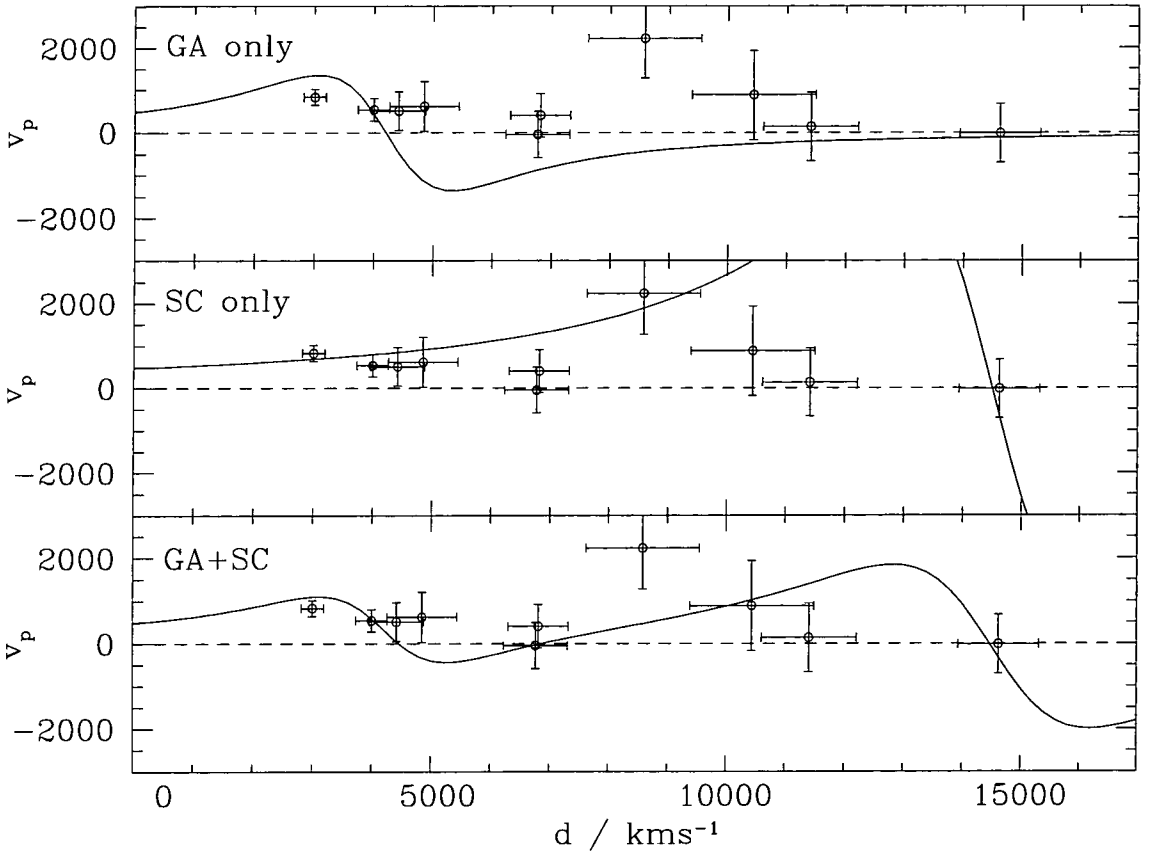

Figure 7.7: Peculiar velocities of ten clusters in the direction of the Great Attractor (GA) and Shapley Concentration (SC). The peculiar velocity is plotted against FP distance for each cluster, so the errors are correlated (in the sense that scattering to higher distance also moves the cluster to more negative velocity). The data points are the same in all three panels. The models are, from top to bottom: pure SC infall; pure GA infall; a combination of GA and SC flow patterns. All models are normalised to generate 475 km s^{-1} infall velocity at the LG.

and the likelihood function is formed from the joint probability over all observed clusters,

$$L(\sigma_i) = \prod_i P(v_i)\,. \tag{7.9}$$

To exclude contributions to σ_v from the large scale streaming in the SMAC velocity field, the v_i are the cluster velocity *residuals* from the best-fit bulk flow solution. In this respect, the analysis differs from that of W97, who employed the CMB frame velocities clusters from TF surveys.

The normalized likelihood function $L(\sigma_v)$, is presented in Figure 7.8. Its maximum is attained at $\sigma_v = 110$ km s^{-1}, with an upper limit of $\sigma_v = 270$ km s^{-1} at the 90% confidence level. At the same confidence level, the intrinsic velocity dispersion is consistent with zero. Cutting the sample to clusters with $cz < 8000$ km s^{-1}, where the observational errors are smaller, does not significantly alter this result, although the 90%

confidence upper limit on σ_v is extended to 325 km s^{-1}.

W97 showed that, in linear theory, the rms cluster velocity can be approximately related to the mass density parameter Ω_0 and to the power spectrum normalisation σ_8 according to

$$\Omega_0^{0.6}\sigma_8 = \frac{\sigma_v}{580 \text{ km s}^{-1}} . \tag{7.10}$$

for $\Gamma = \Omega_0 h$ in the range 0.2–0.5. By this argument, the SMAC measurement of σ_v requires $\Omega^{0.6}\sigma_8 < 0.47$, at 90% confidence. However, N-body simulations, such as those of Colberg et al. (1998), demonstrate that nonlinear effects in superclusters cannot be neglected in determining model predictions for σ_v. They also show that when simulations are normalised to reproduce the observed abundance of rich clusters, the predicted rms cluster velocities are quite insensitive to the parameters of the underlying cosmology. The rms cluster velocities determined from N-body simulations of standard Cold Dark Matter ($\Omega_0 = 1$, SCDM) and low-density Cold Dark Matter ($\Omega_0 = 0.3$, with or without cosmological constant) models lie in the range 235–250 km s^{-1}. Thus, the SMAC measurement for σ_v is compatible with the predictions of these cluster-normalised models. By contrast, COBE-normalised models, as used in the N-body simulations of Bahcall et al. (1994), differ widely in their predictions for σ_v. Specifically, the COBE-normalised SCDM model predicts $\sigma_v = 490$ km s^{-1}, which is strongly rejected by the SMAC data. COBE-normalised low density models have $\sigma_v = 270$ km s^{-1}, marginally consistent with the SMAC result.

While the bulk-flow and rms dispersion measure the amplitude of the mass power spectrum at different scales, the ratio of these quantities, the cosmic Mach number (Ostriker & Suto 1990), provides a normalisation-independent probe of the power spectrum shape. For the SMAC sample, the Mach number is > 3 at the 90% confidence level indicating an extremely cold flow.

7.7 Comparison with previous results

The following sections discuss the principal results of this chapter, in relation to the results of previous peculiar velocity surveys.

7.7.1 The bulk motion

As reviewed in Chapter 1, there is a long history of bulk-flow measurements, dating at least to the work of Rubin et al. (1976). Over the past decade, bulk motions have been inferred on ever larger scales through a variety of methods (Dressler et al. 1987, Courteau et al. 1993, Lauer & Postman 1994). Many of these results are summarized

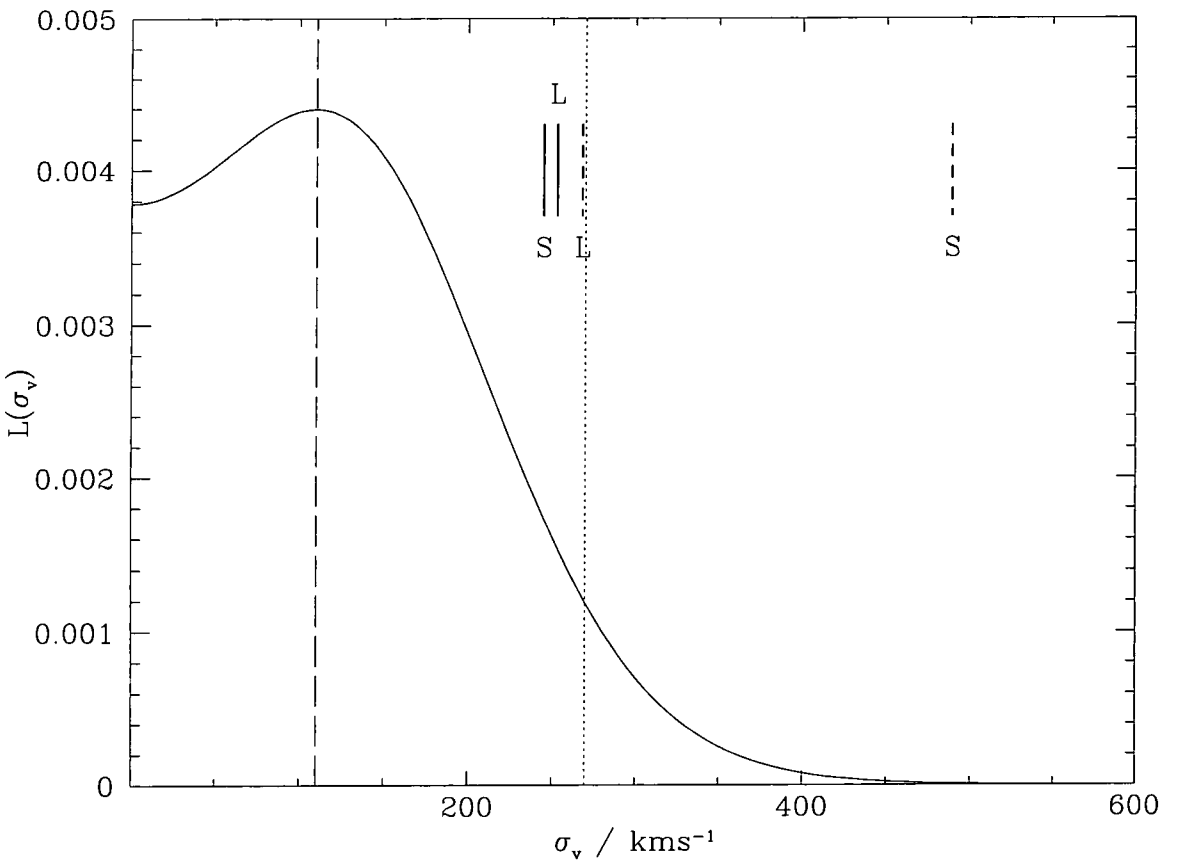

Figure 7.8: Likelihood function for the rms cluster velocity, σ_v, determined in the frame of the SMAC bulk-flow. The maximum likelihood σ_v is marked by the long dashed line, and the 90% upper limit is indicated by the dotted line. The short vertical bars mark the predictions for σ_v, based on N-body simulations. Here, low density ($\Omega_0 = 0.3$) and high density ($\Omega_0 = 1.0$) models are distinguished by 'L' and 'S', respectively. Dashed bars are the predictions of Bahcall et al. (1994), for COBE-normalised models. The solid bars give the predictions in cluster-normalised models, from Colberg et al. (1998).

in Figure 7.9 and Table 7.5. While very-large scale coherent flows pose a significant challenge to current cosmological models (Feldman & Watkins 1994; Strauss et al. 1995), the apparent conflict between different surveys has engendered scepticism towards the distance indicator techniques (eg Hudson & Ebeling 1997).

Comparison between bulk-flow solutions from different surveys is a far from trivial exercise, as demonstrated by Watkins & Feldman (1995, WF95). Especially in the case of sparse samples based on clusters, surveys with different sampling geometry are differently affected by the incomplete cancellation of flow patterns on scales smaller than the survey volume. Moreover, these effects are model-dependent since they are sensitive to the ratio of small- to large-scale power in the underlying cosmology. As an example, WF95 showed that the SNIa results of Riess, Press & Kirshner (1995) are not

necessarily incompatible with the bulk-flow of Lauer & Postman (1994, LP), despite the apparently gross difference between the flow vectors. It is beyond the scope of this thesis to embark upon a full and rigorous treatment of the comparison between the SMAC, LP and other bulk streaming results, in the spirit of WF95. Some general comments may however be advanced:

- The majority of published surveys have a depth considerably smaller than that of SMAC. The flow solutions for these local surveys generally cluster around the region $l = 300°, b = 0°$, this being close to the original Seven Samurai bulk motion apex (Dressler et al. 1987). It is unlikely that the SMAC bulk-flow vector conflicts with these measurements given the great difference in sample depths and the relatively small angular difference.

- The SMAC flow vector is separated from that of LP by approximately 90°. At first sight this appears to constitute an irreconcilable conflict. In particular, the LP flow component perpendicular to the galactic plane is highly significant and positive, while the SMAC flow points south of this plane. However, the WF95 results caution against over-interpretation of this disagreement.

- The flow solution recently announced by Giovanelli et al. (1998a), supports a small amplitude (100–300 km s^{-1}) flow. This result is based upon the SCI Tully–Fisher survey, which despite a small sample size (24 clusters), has fairly uniform sky-coverage and a limiting depth of ∼9000 km s^{-1}. It seems likely, therefore, that the SCI and SMAC flow vectors are in conflict, a conclusion supported by Figure 7.10, which shows no dependance of SCI velocity on angle from the SMAC bulk-flow.

- Fitting bulk-flow models to the recently enlarged SNIa dataset (Riess et al. 1997), yields a flow of moderate amplitude (400 km s^{-1}) directed within 20° of the SMAC dipole. A comparison of the SNIa velocities with angle from the SMAC bulk-flow (Figure 7.10) demonstrates the apparent agreement between these two surveys.

- The SMAC bulk-flow result is also supported by results very recently reported by Willick (1998). His TF study of 15 clusters in a shell at $cz = 9000 - 13000$ km s^{-1} yields a bulk-flow of 900 ± 375 km s^{-1} in the direction of the CMB dipole. The sample was selected to have good sky coverage, despite the small number of clusters.

- The direction of the SMAC bulk flow is close to the flow direction reconstructed from the new IRAS PSCz survey (Branchini et al. 1998). A rigorous comparison to the PSCz velocity field would require radial velocities predictions for the SMAC cluster positions, which are currently unavailable. Qualitatively, however, the PSCz

Table 7.5: Comparison of the SMAC bulk-flow with determinations from other samples. See also Figure 7.9. Note however, that different samples have grossly different effective depths and sky-coverage, so that the comparison is not a trivial one. Notes : For the SNIa bulk-flow, the fit is by Hudson (priv. comm.) from data presented by Riess et al. Willick's free-fit bulk-flow solution was close, in direction, to the LG motion with respect to the CMB. The quoted result is from a fit *fixed* to this direction. The flow of Schechter 1977 is from a reanalysis of the Rubin et al. 1976 Sc galaxy sample.

Code	Method	v_B			l	b	Ref.
SMAC	FP (clusters)	810	$\pm$	180	258	-5	This thesis
LCO/Pal	TF (clusters)	900	$\pm$	375	(273)	(+27)	Willick (1998)
SCI	TF (clusters)	310	$\pm$	120	337	-15	Giovanelli et al. (1998a)
SFI	TF (field)	200	$\pm$	65	295	+25	Giovanelli et al. (1998b)
RDBK	SNIa	400	$\pm$	163	282	-8	Riess et al. (1997)
H97	FP (clusters)	420	$\pm$	280	262	-25	Hudson et al. (1997)
LP	BCG	689	$\pm$	178	343	+53	Lauer & Postman (1994)
M93	TF (clusters)	559	$\pm$	107	326	-9	Mould et al. (1993)
C93	TF (field)	360	$\pm$	40	294	0	Courteau et al. (1993)
7S	$D_n - \sigma$	599	$\pm$	104	312	+6	Dressler et al. (1987)
R76	Spirals	730	$\pm$	250	329	+33	Schechter et al. (1977)

velocity field is dominated by a coherent large-scale streaming motion along a ridge extending from Perseus–Pisces to Shapley, broadly similar to the results obtained from SMAC.

While no clear consensus has emerged from the most recent peculiar velocity surveys, the three deepest samples (LP, SMAC, Willick) argue for coherent flows of > 500 km s^{-1} amplitude on scales > 10000 km s^{-1}. The direction of the bulk-flow is relatively consistent between the SMAC, SNIa and Willick surveys. The very small bulk-flow determined from the SCI survey appears to be inconsistent with SMAC, LP and Willick. Preliminary reports (Giovanelli 1998) on the extension of SCI to greater depths (see Dale et al. 1997, 1998) also find no bulk-flow. This rather confusing picture highlights the need for a full and careful analysis of all the available results, including the effects of the different survey depths and sampling geometries.

7.7.2 Coherent streaming in Perseus–Pisces?

From a TF survey of field spirals in the PP direction, Willick (1990, 1991) found evidence for a net flow towards the LG of 441 ± 49 km s^{-1}. Since PP lies opposite the GA on the sky, Willick (and others, eg Matthewson et al. 1992) argued that the PP streaming added to the evidence for a bulk motion with coherence length $> 100\,h^{-1}$Mpc.

The cluster sample of Han & Mould (1992) supported these claims, but was based upon the same calibration as Willick's study, and was not therefore an independent test.

By contrast, the error-weighted mean velocity of six clusters in the PP ridge, from the SMAC velocity field, is only $-157 \pm 147\,\mathrm{km\ s^{-1}}$, which accords with the PP velocity of of $-60 \pm 220\,\mathrm{km\ s^{-1}}$, found by Hudson et al. (1997). The Hudson et al. result was on a subset of the data now employed in SMAC, but was subject to greater calibration uncertainty, since their sample was smaller and had much poorer sky coverage.

In the PP region, the SMAC results are consistent with the work of Giovanelli et al. (1998a), who found a net streaming of $+75 \pm 134\,\mathrm{km\ s^{-1}}$ from TF distances to three clusters (PISC, HMS0122 and A0262). The field TF study of da Costa et al. (1996) also revealed no coherent streaming of the PP structure.

7.7.3 The Great Attractor and the Shapley Concentration

In the Centaurus direction, the SMAC survey reveals little evidence for far-side infall into a 'Great Attractor' at $cz \sim 4500\,\mathrm{km\ s^{-1}}$. Rather, SMAC argues for a high amplitude flow towards the Shapley Concentration, at three times this distance, which retards the expected infall in the background of the GA, and enhances the motions on its near side. The model presented here is in good accord with the results of Hudson (1994), who argued from the Mark II compilation of TF and $D_\mathrm{n} - \sigma$ data that the GA could not account for more than about 60% of the local flow amplitude. The SMAC results in this region are also consistent with evidence from the TF survey of of Matthewson et al. (1992), which shows large positive peculiar motions in the GA direction at distances 6000–10000 km s^{-1}. The SMAC data conflict with the claims of Dressler & Faber (1990), whose TF and $D_\mathrm{n} - \sigma$ survey of the GA background was severely affected by inhomogeneous Malmquist bias (Hudson 1994).

While it seems clear that positive peculiar velocities persist far into the background of the GA, improved data for distant ($> 10000\,\mathrm{km\ s^{-1}}$) clusters will be necessary to determine whether infall into the SC region can fully account for the observed motions.

7.7.4 The RMS cluster velocity

The dispersion of SMAC cluster velocities around the best fitting bulk-flow model is extremely small ($\sigma_v = 110$ km s^{-1}, $\sigma_v < 270$ km s^{-1} at 90% confidence) but roughly consistent with published results. The most recent analysis, by W97 found an rms velocity of $247^{+123}_{-80}\,\mathrm{km\ s^{-1}}$ for SCI clusters, with a similar result for clusters in the Mark III catalogue (after some trimming of the sample).

7.8 Discussion

The bulk-flow revealed by the SMAC project is of similar amplitude to that determined by LP. Their results found little support from related cosmological observations, and it might be tempting to suppose that the same would be true of the results presented here. However, while the amplitude of the SMAC flow is indeed surprising, its *direction* is supported by several independent observations.

Figure 7.9 shows the SMAC flow apex in relation to some other important cosmological directions. First, the SMAC flow is relatively close (35°) to the apex of the CMB dipole, which is suggestive that some significant fraction of the LG motion is generated by sources near or beyond the limit of the survey volume. The proximity of the SMAC solution to that recovered from more local samples, such as those of Dressler et al. (1987) and Courteau et al. (1993), provides evidence that these local flows, too, are generated by distant ($> 60\,h^{-1}$Mpc) perturbations. (Note that this latter observation is more robust than the comparison with the CMB dipole, since the LG velocity will be more strongly influenced by very local contributions such as Virgocentric infall.)

Also shown in Figure 7.9 are the directions of two distant structures prominent in the distribution of Abell clusters: the Shapley Concentration (SC) and the Horologium–Reticulum Supercluster (HR). The SC and HR structures are by far the most extreme concentrations of Abell clusters in the local ($z < 0.1$) universe (Tully et al. 1992). If structures beyond 12000 km s^{-1} indeed contribute significantly to the local motions, it is not unreasonable to suspect that the SC and HR regions are largely responsible. Indeed the role of SC in the generation of the local flows has been a source of speculation for some time (Scaramella et al. 1989; Raychaudhury et al. 1991; Quintana et al. 1995). The SMAC bulk motion is directed to within 30° of an average taken between the HR and SC directions. Given that these two structures are so prominent in rich clusters, it comes as no surprise to find that the dipole of X-ray selected clusters also lies very close (∼20°) to the direction of the SMAC bulk-flow (Plionis & Kolokotronis 1998: XBACs dipole corrected to real-space with $L_{\rm X}^{5/11}$ weighting). These results may suggest that on large scales, the underlying mass distribution. is well-traced by the distribution of rich clusters. It is interesting to note also that the antapex of the SMAC flow lies ∼50° from the direction of the Boötes Void at 15500 km s^{-1} (Kirshner et al. 1987). It is possible that this underdensity exerts a 'push' on clusters within the SMAC survey.

A preliminary analysis (Hudson et al. 1998, following Kaiser 1988) suggests that the SMAC bulk-flow, like that of Lauer & Postman, is very difficult to accommodate in the context of current cosmological models. While the SMAC flow is more probable in models with very high normalisation (such as COBE normalised Standard CDM,

and Mixed Dark Matter models), these models dramatically overpredict the small scale dispersion of cluster velocities. The 'coldness' of the SMAC flow argues, therefore, not for a change of normalisation, but for a change in the *shape* of the power spectrum. Models with excess power on scales of $60 - 150\,h^{-1}$Mpc (eg the 'Isocurvature–Baryon' models of Peebles 1987) are likely to be more consistent with the observed velocity field.

A peak or 'spike' in the power spectrum of *galaxies*, at 120–$130\,h^{-1}$Mpc has indeed been suggested by Broadhurst et al. (1990) and by Landy et al. (1996) from one- and two-dimensional redshift surveys. More recently, Einasto et al. (1997) have argued for excess power at $120\,h^{-1}$Mpc scales, from the distribution of *Abell clusters* The SMAC survey results appear to supplement this circumstantial (and controversial) evidence, with the suggestion that *mass*, too, may exhibit excess clustering on very large scales.

7.9 Summary

The SMAC velocity field is dominated by a coherent streaming component of $810 \pm 180\,\mathrm{km\ s^{-1}}$. The flow is not dominated by any cluster of supercluster region, but appears instead to be shared by the entire sample. The Shapley Concentration appears to play a significant role in generating the local motions, producing approximately 40% of the LG motion with respect to the CMB. However, the direction of the bulk-flow vector is such that Shapley cannot account fully for the observed streaming. The net motion of the Perseus–Pisces region is consistent with zero. The cluster velocities exhibit a dispersion of less than $270\,\mathrm{km\ s^{-1}}$. around the SMAC bulk-flow solution.

The SMAC results add to a growing number of claims for coherent flows on large scales. However, there is by no means a comprehensive agreement between the latest survey results. Detailed comparisons will be necessary to determine the compatibility of the many recent bulk-flow determinations. If confirmed, the existence of coherent bulk-flows, on $> 100\,h^{-1}$ Mpc scales, will pose a significant challenge to current cosmological models.

References

Bahcall N. A., Cen R., Gramman M. 1994, ApJ, 430, L13

Branchini E. et al. 1998 reported at the ESO/MPA Cosmology Conference "Evolution of Large Scale Structure".

Broadhurst T. J., Ellis R. S., Koo D. C., Szalay A. S. 1990, Nature, 343, 726

Colberg J. M., White, S. D. M., MacFarland T. J., Jenkins A., Pearce F. R., Frenk C. F., Thomas P. A., Couchman H. M. P. 1998, preprint (astro-ph/9805078)

Courteau S., Faber S. M., Dressler A., Willick J. A., 1993, ApJ, 412, L51

da Costa L. N., Freudling W., Wegner G., Giovanelli R., Haynes M. P., Salzer J. J., 1996, ApJ, 468, L5

Dale D. A., Giovanelli R., Haynes M. P., Scodeggio, M., Hardy E., Campusano, L. E. 1997, AJ, 114, 455

Dale D. A., Giovanelli R. Haynes M. P., Scodeggio M., Hardy E., Campusano L. E. 1998, AJ, 115, 418

Dressler A., Faber S. M. 1990, ApJ, 354, 13

Dressler A., Faber S. M., Burstein D., Davies R. L., Lynden-Bell D., Terlevich R. J., Wegner G. 1987, ApJ, 313, L37

Einasto J., Einasto M., Göttlober S., Müller V., Saar E., Starobinsky A. A., Tago E., Tucker D., Andernach H., Frisch P. 1997, Nature, 385, 139

Faber S. M., Bu rstein D., 1988, in Coyne G., Rubin V.C., eds, Proceedings of the Vatican Study Week, Large Scale Motions in the Universe. Princeton Univ. Press, Princeton, p. 135 (FB88)

Feldman H. A., Watkins R. 1994, ApJ, 430, L17

Giovanelli R., Haynes M. P., Salzer J. J., Wegner G., da Costa L. N., Freudling W. 1998a, preprint (astro-ph/9808158)

Giovanelli R., Haynes M. P., Freudling W, da Costa L. N., Salzer J. J., Wegner G. 1998b, ApJ, 505, L91

Giovanelli R. 1998, preprint (astro-ph/9809041)

Han M., Mould J. R., 1992, ApJ, 396, 453

Hudson M. J. 1994, MNRAS, 266, 468

Hudson M. J., Smith R. J., Lucey J. R., Schlegel D. J., Davies R. L. 1998, in preparation

Hudson M. J., Ebeling H. 1997, ApJ, 479, 621

Hudson, M. J., Lucey J. R., Smith R. J., Steel J. 1997, MNRAS, 291, 488

Kaiser N., 1988, 231, 149

Kirshner R. P., Oemler A. A., Schechter P. L., Schectman S. A. 1987, ApJ, 314, 493

Landy S. D., Shechtman S. A., Lin H., Kirshner R. P., Oemler A. A., Tucker D., 1996, ApJ, 456, L1

Lauer T. R., Postman M. 1994, ApJ, 425, 418 (LP)

Matthewson D. S., Ford V. L., Buchhorn M. 1992, ApJ, 389, L5

Mould J. R., Akeson R. L., Bothun G. D., Han M., Huchra J. P, Roth J., Schommer R. A. 1993, ApJ, 409, 14

Ostriker J. P., Suto Y., 1990, ApJ, 348, 378

Peebles P. J. E. 1987, Nature, 327, 210

Plionis M., Kolokotronis V. 1998, ApJ, 500, 1

Quintana H., Ramirez A., Melnick J., Raychaudhury S., Slezak E. 1995, AJ, 110, 463

Raychaudhury S., Fabian A. C., Edge A. C., Jones C., Forman W. 1991, MNRAS, 248, 101

Riess A. G., Press W. H., Kirshner R. P. 1995, ApJ, 445, L91

Riess A. G., Davis M., Baker J., Kirshner R. P. 1997, ApJ, 488, L1

Rubin V. C.., Thonnard N., Ford W. K., Roberts M. S 1976, AJ, 81, 719

Scaramella R., Baiesi-Pillastrini G., Chincarini G., Vettolani G., Zamorani G. 1989, Nature, 338, 562

Schechter P. L. 1977, AJ, 82, 569

Strauss M. A., Cen R., Ostriker J. P., Lauer T. R., Postman M. 1995, ApJ, 444, 507

Tully R. B., Scaramella R., Vettolani G., Zamorani G. 1992, 388, 9

Watkins R., Feldman H. A. 1995, ApJ, 453, L73

Watkins R. 1997, MNRAS, 292, L59 (W97)

Wegner G., Colless M., Baggley, G. Davies R. L., Bertschinger E., Burstein D., McMahan R. K. Jr., Saglia R. P. 1996, ApJS, 106, 1

Willick J. A., 1990, ApJ, 351, L45

Willick J. A., 1991, PhD thesis, University of California, Berkeley

Willick J. A. 1998, preprint (http://astrophys.Stanford.EDU:80/jeffw/survey/)

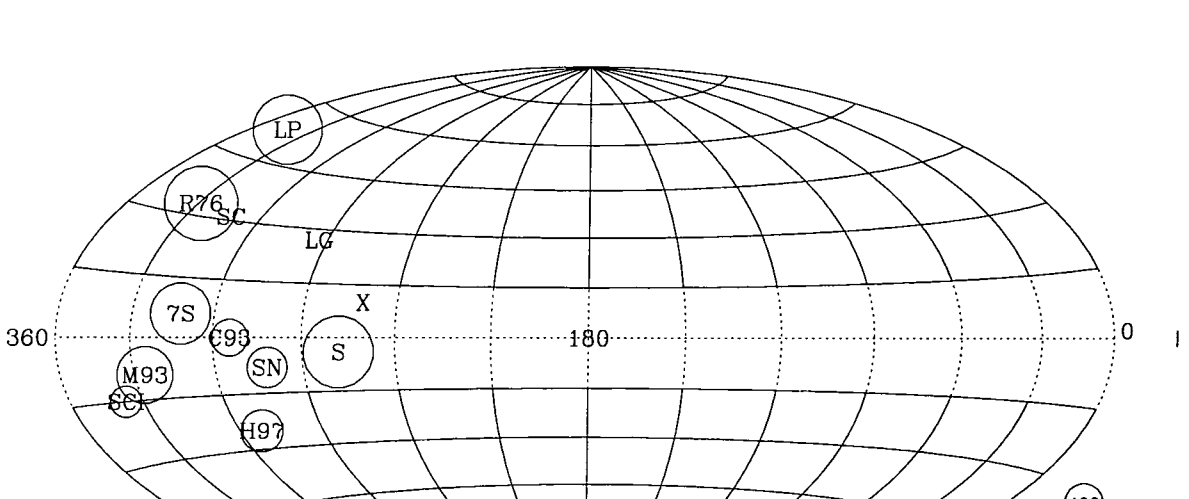

Figure 7.9: Comparison of the SMAC bulk-flow direction (S) with other bulk-flow determinations, and with other relevant extragalactic directions. Bulk-flow directions are highlighted by circles proportional to the bulk motion amplitude (see key). The symbols are: S=SMAC (this thesis), LP = BCG sample (Lauer & Postman 1994), SCI = cluster TF sample (Giovanelli et al. 1998a), H97 = FP sample of 16 clusters from Hudson et al. (1997), SN = bulk-flow fit to enlarged SNIa dataset of Riess et al. (1997), M93 = cluster TF sample of Mould et al. (1993), C93 = field TF sample of Courteau et al. (1993), 7S = elliptical galaxy bulk motion (Dressler et al. 1987), R76 = Reanalysis by Schechter (1977) of the Rubin et al. (1976) Sc galaxy sample. Other interesting directions are: LG = direction of Local Group motion with respect to the CMB, SC = position of Shapley Concentration (Tully et al. 1992), HR = position of Horologium-Reticulum Supercluster (Tully et al. 1992), X = direction of X-ray cluster dipole (Plionis & Kolokotronis 1998).

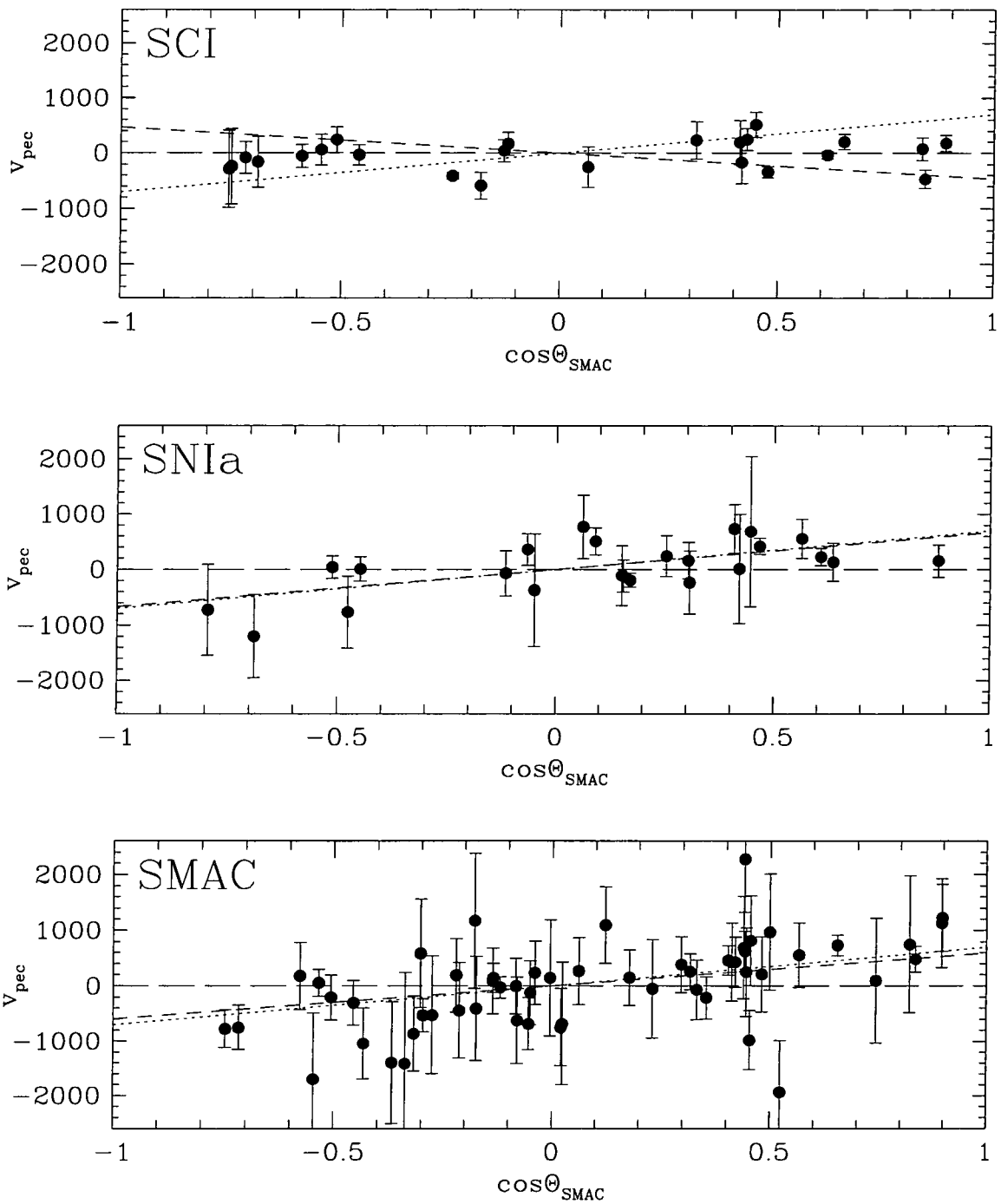

Figure 7.10: Peculiar velocities for SMAC clusters, SCI clusters and SNIa, as a function of angle from the SMAC bulk-flow apex, Θ_{SMAC}. The dotted line shows the predictions of the best fitting SMAC bulk-flow model. Note that the SCI cluster velocities show no trend with $\cos\Theta_{SMAC}$, but that there is a clear correlation in the SNIa case.

Chapter 8

Conclusions

8.1 Thesis summary

This thesis has presented results from the 'Streaming Motions of Abell Clusters' (SMAC) survey of cluster peculiar velocities to 12000 km s^{-1}. This survey aimed towards a reliable determination of the local bulk-flow vector, and to provide velocity field data for a variety of cosmological applications. The following sections present a brief summary of the catalogue construction, and of the analyses presented in previous chapters.

8.1.1 Sample and data

An initial sample was constructed from the set of 65 Abell/ACO clusters in the Lauer & Postman sample, limited to a depth of 12000 km s^{-1}. New observations were made for galaxies in 36 of these clusters, with data being drawn from a variety of literature sources for the remaining clusters.

Five new spectroscopic datasets yielded measurements of recession velocity, central velocity dispersion and magnesium index for 429 early-type galaxies. The velocity dispersion datasets have internal errors of 0.016–0.042 dex, equivalent to 5–15% error in the FP distance. The Mg_2 and Mgb measurements have internal errors of $\sim$0.010 mag.

R-band photometric parameters were determined for 324 galaxies, from four new datasets. The effective (ie half-light) diameter A_e and the surface brightness within this diameter, $\langle\mu\rangle_e$, were obtained by fitting $R^{1/4}$ law profiles to the aperture photometry. The combination $\log A_e - 0.32\langle\mu\rangle_e$, which enters into the FP, has internal errors of 1–2% in distance.

The new spectroscopic and photometric measurements have been combined with an extensive compilation of data from the literature. Velocity dispersion systems are subject to systematic offsets of up to 7%, equivalent to $\sim$10% in distance, which if untreated would severely compromise peculiar velocity measurements. Correction for

these effects has been achieved through simultaneous intercomparison of data for galaxies in common between datasets. The system corrections are determined with a precision of 0.004–0.014 in $\log \sigma$, equivalent to 1–4% in distance.

The final sample is restricted to clusters for which complementary spectroscopic and photometric data is available for four or more early-type members, and the original sample is augmented with data for additional clusters which satisfy these criteria. The completed survey has data for 725 galaxies in 56 clusters. The sample has excellent sky coverage to a depth of $\sim$12000 km s^{-1}.

8.1.2 The fundamental plane and distance estimates

Cluster distances have been derived from the inverse formulation of the FP, which is unbiased by photometric selection effects. The scatter around this relation is equivalent to a distance error of 22% per galaxy, resulting in random errors of 3–13% per cluster. The distances are also subject to systematic errors, introduced by the uncertainties in matching spectroscopic datasets, at the level of 1–3%. The systematic errors are in some cases correlated from cluster to cluster.

The SMAC distances are compatible with distances derived from the TF relation, for clusters in common. While the SMAC distances are generally consistent with those derived from the BCG study of LP, a comparison reveals a small number of highly discrepant clusters, for which the LP distances are too large by $\sim$ 50%.

8.1.3 The local peculiar velocity field and implications for cosmology

The cluster sample exhibits a coherent bulk motion of 810$\pm$180 km s^{-1}, with respect to the CMB, in the direction (l, b)=(258°,–5°). The error includes contribution from uncertainties in the spectroscopic system offsets. The bulk-flow solution is robust against a range of tests for systematic errors: no single cluster, or supercluster structure dominates the flow; the flow is insensitive to the changing the slope of the FP within reasonable limits; there is no strong correlation between the monopole and dipole flow components.

The SMAC bulk-flow vector is approximately 90° from that of Lauer & Postman (1994), suggesting a conflict between the two results. A rigorous comparison, however, requires that the different window-functions of the two surveys be properly taken into account (Watkins & Feldman 1995). The SMAC bulk-flow also appears to be inconsistent with the determination from cluster spiral galaxies by Giovanelli et al. (1998), which is rather shallower than SMAC. The SMAC flow is, however, supported by the recent TF survey of Willick (1998), and perhaps by the new sample of SNIa sample of Riess et al.

(1997).

The SMAC bulk-flow apex lies close to the mean direction of the Shapley and Horologium–Reticulum superclusters. The direction of the SMAC bulk flow is in excellent agreement (15°) with the dipole of X-ray clusters (Plionis & Kolokotronis 1998), which also is strongly influenced by these supercluster structures, the most prominent in the $z < 0.1$ universe. There is some evidence in the SMAC velocity field for infall around the Shapley Concentration, although the coherence length of the flow in this direction remains essentially unconstrained.

The presence of coherent motions on $>100h^{-1}$Mpc scales is unexpected in current models when normalised to give the correct cluster abundances (Jenkins et al. 1998). Whilst models with a higher normalisation would render such flows more likely, this would be at the expense of small-scale velocity dispersions much higher than observed. In consequence, the SMAC results argue not for an increase in the normalisation of the models, but for a change in the power spectrum shape, so as to enhance the power on $\sim 120\,h^{-1}$Mpc scales, *relative* to the small scale power.

8.2 Directions for future research

This thesis has presented only the basic analyses of the SMAC peculiar velocity field. A brief summary of more advanced applications of these results, and of some observational extensions to the project, is presented in the following sections.

8.2.1 Comparison with the IRAS PSCz velocity field

From a full-sky redshift catalogue, such as those selected from the IRAS point source catalogue, the real-space density and peculiar velocity fields can be reconstructed by a variety of methods (see Strauss & Willick 1995 and references therein). The deepest of the IRAS redshift surveys, PSCz, has recently been employed in such analysis by Branchini et al. (1998). The reconstruction requires an input value for the density parameter $\beta_{\rm IRAS} = \Omega^{0.6}/b_{\rm IRAS}$, usually taken to be $\beta_{\rm IRAS} = 1.0$. Since velocities scale linearly with $\Omega^{0.6}$ in the linear régime, the value of $\beta_{\rm IRAS}$ can be determined through comparison between reconstructed velocities and those measured from surveys like SMAC.

While a full and careful comparison of the SMAC and PSCz velocity fields will be the subject of a future paper, some very preliminary results can be reported here. Most significantly, *direction* of the SMAC bulk-flow is in good agreement with the predictions of PSCz for this sample. (Note that this is a prediction for a sparse and discrete set of points, and will differ from the bulk-motion determined from the flow derived from all

points in the PSCz reconstruction.) The agreement in direction leads to the conclusion that the SMAC bulk-flow can be accounted for by the PSCz redshift survey, if $\beta_{\rm IRAS}$ is sufficiently large. In addition, a good agreement is seen between the PSCz predictions and SMAC velocities for individual clusters, with a preferred value for $\beta_{\rm IRAS}$ in the range 0.6–1.3 (Hudson et al. 1998).

8.2.2 Detailed tests of consistency with other bulk-flow determinations

The $\sim 90^\circ$ separation of the SMAC bulk-flow vector from that of Lauer & Postman (1994) at face value suggests a highly significant conflict between the two results. However Watkins & Feldman (1995) have demonstrated that comparison between bulk-flow determinations is non-trivial, since different sampling geometries, cause bulk-flow fits to be differently affected by the incomplete cancellation of smaller scale flows *even in the absence of random errors.*

In future work, the bulk-flow vectors determined from a number of recent surveys will be compared, with a full and rigorous treatment sampling differences between the surveys. The comparison will consider, not only the SMAC and LP results, but also those from the SCI survey of Giovanelli et al. (1998), the LCO/Palomar survey of Willick (1998), the EFAR project (Saglia et al. 1998), and the SNIa velocity field (Riess et al. 1997).

8.2.3 Comparison of the SMAC bulk-flow with model predictions

Like the comparison between bulk-flow vectors from different surveys, the comparison between bulk motion measurements and the predictions from models is far from trivial. Again, as emphasized by Feldman & Watkins (1994), the survey geometry must be accounted for, in order to determine effective depth, and to include the effects of incomplete cancellation between small-scale flows.

A preliminary analysis of this type has already been performed for the SMAC survey (Hudson et al. 1998), but again, a more careful treatment will be required. In particular, the analysis should include the effects of system-matching errors on cluster distances, which introduce covariance into the noise matrix. This analysis will be conducted shortly.

As a 'brute-force' complement to this analytic approach, large N-body simulations can be used to determine expectation values for velocity-field parameters in various cosmological models (eg Strauss et al. 1995, for an application to the LP bulk-flow). Since the SMAC results seem to favour excess power on large scales relative to small, for any normalisation of current models, the Cosmic Mach Number promises to

be a powerful statistic for model rejection (Strauss et al. 1993). Forthcoming work will investigate the distribution function of this statistic in conventional cosmologies (eg variants of the Cold Dark Matter model), and in baryon-dominated models with more large scale power. Again, a full analysis should account for the survey geometry, random errors and for covariance in the systematic errors.

8.2.4 Reconstruction of the mass power spectrum from the SMAC velocity field

The principal advantage of peculiar velocity surveys in studies of large-scale structure is their sensitivity to the distribution of *mass* rather than to that of galaxies. Consequently, the peculiar velocity field can in principle place constraints on parameters of the mass power spectrum (its amplitude, primordial slope, turn-over scale), independent of the unknown effects of (probably scale-dependent) galaxy biasing.

Zaroubi et al. (1997) have developed a likelihood analysis by which parameters of various model power-spectra can be estimated from sparsely-sampled peculiar velocity data. Application of the method to the Mark III and SFI catalogues (Zehavi 1998) provides only weak constraints on the power spectrum shape-parameter: $\Gamma = 0.4 \pm 0.2$.

The SMAC data probe scales comparable to the expected turnover scale in the power spectrum. It can be hoped, therefore, that more precise constraints on Γ can be obtained by using this survey (possibly in combination with more local data) in the Zaroubi et al. analysis. An extension of the method, to include more general models for the power spectrum, will provide a test for the presence of a 'spike' of excess power on $120\,h^{-1}$Mpc scales.

8.2.5 An enlarged catalogue?

Two observational extensions to the SMAC survey are planned, both of which target specific, dynamically interesting regions of the local Universe.

The first such program will improve the extent of the sample in the direction of the Shapley Supercluster, with the aim of detecting infall around this extreme concentration of rich clusters. Direct determination of the infall amplitude for this region will permit an improved estimate of the influence of distant superclusters on the local peculiar velocity field.

A second observational effort aims to improve the constraints on the SGZ component of the flow, which dominates the bulk-flow amplitude, but is at present rather imprecisely determined. To this end, observations will be obtained for small samples of clusters at $z = 0.04-0.06$, with high galactic latitudes. Another strategy for constraining

the flow perpendicular to the SGP involves incorporating data from the EFAR survey (Wegner et al. 1996) into a new, and much enlarged Fundamental Plane catalogue.

8.3 Concluding remarks

The field of large-scale motions, controversial since the work of Rubin et al. (1976), continues to present unexpected results after twenty years. To depths beyond 10000 km s^{-1}, three surveys (LP; SMAC; Willick 1998) have now detected coherent flows, far in excess of model predictions. However, the experience of the past two decades should caution that 'serious implications for cosmological models' are often overstated in the immediate aftermath of a bulk-flow detection. Reliable constraints on cosmological parameters require sophisticated analysis techniques, and the application of such methods to the new surveys may yield truly exciting results within the next two years.

References

Branchini E. et al. 1998 reported at the ESO/MPA Cosmology Conference "Evolution of Large Scale Structure".

Feldman H. A., Watkins R. 1994, ApJ, 430, L17

Giovanelli R., Haynes M. P., Salzer J. J., Wegner G., da Costa L. N., Freudling W. 1998, preprint (astro-ph/9808158)

Hudson M. J. et al. 1998 reported at the ESO/MPA Cosmology Conference "Evolution of Large Scale Structure".

Jenkins A. R., Frenk C. S., Thomas P. A., Colburg J. M., White S. D. M., Couchman H. M. P., Peacock J. A., Efstathiou G. P., Nelson A. H. 1998, ApJ, 499, 20

Lauer T. R., Postman M. 1994, ApJ, 425, 418 (LP)

Plionis M., Kolokotronis V. 1998, ApJ, 500, 1

Riess A. G., Davis M., Baker J., Kirshner R. P. 1997, ApJ, 488, L1

Rubin V. C.., Thonnard N., Ford W. K., Roberts M. S 1976, AJ, 81, 719

Saglia R. P. et al. 1998 reported at the ESO/MPA Cosmology Conference "Evolution of Large Scale Structure".

Strauss M. A., Willick J. A. 1995, Phys. Rep., 261, 271

Strauss M. A., Cen R., Ostriker J. P., Lauer T. R., Postman M. 1995, ApJ, 444, 507

Strauss M. A., Cen R., Ostriker J. P. 1993, ApJ, 408, 389

Tully R. B., Scaramella R., Vettolani G., Zamorani G. 1992, 388, 9

Watkins R., Feldman H. A. 1995, ApJ, 453, L73

Wegner G., Colless M., Baggley, G. Davies R. L., Bertschinger E., Burstein D., McMahan R. K. Jr., Saglia R. P. 1996, ApJS, 106, 1

Willick J. A. 1998, preprint (http://astrophys.Stanford.EDU:80/jeffw/survey/)

Zaroubi S., Zehavi I., Dekel A., Hoffman Y., Kolatt T. 1997, ApJ, 486, 21

Zehavi I. 1998, preprint (astro-ph/9807092)

Appendix A

Data tables

This Appendix presents tables of new spectroscopic data (discussed in Chapter 3), new photometric data (Chapter 4), and the final merged catalogue used in the determination of cluster distances from the FP (Chapter 6).

Table A.1, presents new spectroscopic data from five datasets. Positions have been drawn from the NED database. S/N gives the signal-to-noise ratio per angstrom. The tabulated spectroscopic parameters are: helicentric recession velocity, $cz_{\odot}$, in km s^{-1}; central velocity dispersion, σ, in km s^{-1}; and magnesium line indices Mg_2 and Mgb' in magnitudes. Velocity dispersion and magniesium index measurements quoted here are *prior* to correction for aperture effects and for the system offsets of Section 5.2.

Raw photometric data from the four new imaging runs are reported in Table A.2. Each observation is reported separately. Together with the galaxy identification and coordinates the table gives the name of the dataset (run) from which the observation derives, and the B-band galactic extinction values from Burstein & Hieles (1984) and from Schlegel, Finkbeiner & Davis (1998). The raw R-band magnitude within 20 arcsec (R_{20}) is quoted prior to extinction correction. The measured FP parameters $\log A_e$ and $\langle\mu\rangle_e$ are quoted with A_e in arcsec and $\langle\mu\rangle_e$ in mag. per square arcsec. Extinction corrections applied to the latter are those of Burstien & Hieles, for ease of comparison to published work. The FWHM seeing is given by psf, and the final column give gives the rms residual from the best-fitting $R^{1/4}$ law profile.

Table A.3 presents the final catalogue of fully-corrected, merged and standarized FP parameters for 725 galaxies in the SMAC peculiar velocity sample. This table is divided by cluster, with NED positions given for each galaxy. The tabulated parameters are $cz_{\odot}$ (heliocentric redshift in km s^{-1}), $\log\sigma$ (where σ is the central velocity dispersion in km s^{-1}, on the standard system of Section 5.2), Mg_2 (fully corrected Mg_2 index, on the standard system), $\log R_e$ (where R_e is the effective radius in arcsec.), $\langle\mu\rangle_e$(effective surface brightness translated to the R-band). Note that the extinction corrections of

Schlegel, Finkbeiner & Davis (1998) have been applied to $\langle\mu\rangle_e$ at this stage. The final colmun gives the broad morphological type: 'E' denotes broadly elliptical types (E, E/S0, D, cD) and 'L' signifies 'lenticulars' (S0, S0/E, SB0). In this column, a 'Q' flags galaxies without reliable morphological information.

Table A.1: Raw spectroscopic data from the SMAC project. See text of Appendix A for details.

Identification	R.A. (J2000)	Dec. (J2000)	Source	S/N	$cz_\odot$	σ	Mgb'	Mg_2
A2806:SMC-F	00 37 56.94	−56 03 43.4	A95B	28	8651	106	0.133	0.243
A0076:D-018	00 39 15.62	+06 41 21.5	I97A	14	11591	216	0.175	0.299
A0076:D-018	00 39 15.62	+06 41 21.5	I97A	20	11597	164	0.163	0.279
I1565	00 39 26.27	+06 44 03.3	I97A	26	11335	317	0.179	0.318
I1566	00 39 33.35	+06 48 54.5	I97A	19	11941	250	0.148	0.280
I1566	00 39 33.35	+06 48 54.5	I97A	26	11975	277	0.170	0.296
A0076:D-016	00 39 36.63	+06 39 54.2	I97A	22	11650	144	0.162	0.275
I1568	00 39 55.96	+06 50 54.9	I97A	28	11998	305	0.178	0.320
A2806:SMC-C	00 40 04.23	−56 10 50.2	A95B	46	8508	204	0.160	0.283
N0212	00 40 13.31	−56 09 10.8	A95B	26	8271	216	0.164	0.328
N0212	00 40 13.31	−56 09 10.8	A95B	26	8260	193	0.197	0.326
A2806:SMC-D	00 40 24.59	−56 13 22.9	A95B	32	8720	123	0.165	0.277
I1569	00 40 28.02	+06 43 10.9	I97A	25	11346	232	0.170	0.288
A2806:SMC-E	00 40 43.21	−55 55 46.9	A95B	32	7718	139	0.162	0.287
N0215	00 40 48.93	−56 12 51.1	A95B	49	8245	269	0.162	0.287
N0221	00 42 41.85	+40 51 51.8	I97A	67	-145	112	0.099	0.182
N0224	00 42 44.23	+41 16 07.7	I97A	31	-203	202	0.183	0.311
N0380	01 07 17.60	+32 28 58.0	I97A	24	4426	324	0.182	0.327
N0383	01 07 24.98	+32 24 44.8	I97A	18	5119	272	0.176	0.305
N0383	01 07 24.98	+32 24 44.8	I97A	29	5098	283	0.166	0.285
I1633	01 09 55.35	−45 55 52.8	A95B	38	7270	368	0.171	0.327
A0189:SMC-C	01 23 23.69	+01 46 03.6	I97A	24	9555	171	0.161	0.264
A0189:SMC-C	01 23 23.69	+01 46 03.6	A95B	27	9523	144	0.167	0.278
A0189:SMC-A	01 23 26.33	+01 42 17.8	I97A	27	10259	198	0.176	0.275
A0189:SMC-A	01 23 26.33	+01 42 17.8	I97A	31	10258	254	0.169	0.290
A0189:SMC-A	01 23 26.33	+01 42 17.8	A95B	36	10297	221	0.151	0.283

(*Continued*)

Identification	R.A. (J2000)	Dec. (J2000)	Source	S/N	$cz_{\odot}$	σ	Mgb'	Mg$_2$
N0507	01 23 39.77	+33 15 23.2	I97A	34	4940	290	0.162	0.281
A0189:SMC-K	01 24 22.85	+01 45 00.3	I97A	14	5368	118	0.139	0.253
I0103	01 24 36.44	+02 02 39.3	A95B	42	9600	232	0.164	0.307
A0189:SMC-J	01 24 43.94	+01 22 01.6	I97A	25	8997	134	0.117	0.233
N0534	01 24 44.66	−38 07 44.5	A95B	35	5824	173	0.169	0.285
A0189:SMC-I	01 24 58.92	+01 33 23.2	I97A	16	9200	127	0.141	0.198
A0189:SMC-I	01 24 58.92	+01 33 23.2	I97A	16	9206	142	0.091	0.161
N0544	01 25 12.01	−38 05 37.6	A95B	40	5939	185	0.166	0.300
N0533	01 25 31.36	+01 45 32.8	I97A	34	5549	262	0.166	0.311
A2911:SMC-D	01 25 32.37	−38 17 02.5	A95B	36	6093	112	0.121	0.225
N0541	01 25 44.29	−01 22 46.0	I97A	25	5410	228	0.189	0.296
N0541	01 25 44.29	−01 22 46.0	A95B	38	5422	213	0.179	0.310
N0545	01 25 59.21	−01 20 25.3	I97A	29	5330	248	0.166	0.314
N0545	01 25 59.21	−01 20 25.3	A95B	37	5338	238	0.173	0.311
N0547	01 26 00.68	−01 20 44.4	I97A	29	5550	248	0.186	0.314
N0547	01 26 00.68	−01 20 44.4	A95B	36	5553	261	0.171	0.316
N0548	01 26 02.49	−01 13 31.7	I97A	23	5389	156	0.138	0.234
N0548	01 26 02.49	−01 13 31.7	A95B	27	5404	141	0.164	0.250
N0584	01 31 21.01	−06 52 16.1	I97A	56	1802	195	0.155	0.278
A0260:EFR-E	01 49 12.88	+33 05 44.8	I97A	25	11778	301	0.187	0.304
A0260:SMC-1	01 50 32.13	+33 02 49.7	I97A	24	10195	159	0.128	0.224
I1733	01 50 43.02	+33 04 54.4	I97A	29	10685	291	0.176	0.306
A0260:SMC-D	01 51 21.29	+33 11 11.2	I97A	17	11747	125	0.145	0.239
A0260:SMC-D	01 51 21.29	+33 11 11.2	I97A	18	11768	136	0.137	0.217
A0260:SMC-D	01 51 21.29	+33 11 11.2	I97A	20	11772	128	0.149	0.264
A0260:EFR-G	01 51 45.53	+33 32 14.1	I97A	24	10608	237	0.146	0.297
A0260:EFR-G	01 51 45.53	+33 32 14.1	I97A	24	10624	258	0.154	0.269
N0720	01 53 00.46	−13 44 18.4	I97A	41	1745	260	0.191	0.342
N0821	02 08 20.98	+10 59 44.2	I97A	46	1735	197	0.172	0.307
N0936	02 27 37.67	−01 09 17.2	I97A	54	1415	192	0.176	0.284
N0936	02 27 37.67	−01 09 17.2	A95B	55	1430	199	0.164	0.293
A0400:D-070	02 55 14.85	+06 10 39.3	I97A	26	7564	187	0.154	0.270
A0400:D-044	02 57 33.67	+05 58 36.9	I97A	29	6861	283	0.185	0.329
A0400:D-052	02 57 37.45	+06 02 50.1	I97A	19	7466	158	0.181	0.284
A0400:D-052	02 57 37.45	+06 02 50.1	I97A	21	7436	147	0.166	0.275
A0400:D-041	02 57 47.41	+06 01 39.6	I97A	33	7346	217	0.146	0.256
A0400:D-058	02 58 21.02	+06 05 42.5	I97A	26	6796	238	0.177	0.312
A0400:D-089	02 58 24.58	+06 35 30.5	I97A	25	6333	173	0.166	0.279
A0400:D-057	02 58 54.22	+06 06 59.6	I97A	25	7241	128	0.153	0.252
A0400:D-017	02 59 48.58	+05 44 33.1	I97A	25	6886	143	0.141	0.256
A0426:PP-P08	03 18 22.52	+41 24 36.0	I97A	23	6468	173	0.163	0.263
A0426:7S-PER199	03 19 09.80	+41 05 01.5	I97A	28	5109	226	0.168	0.271
N1272	03 19 21.30	+41 29 26.7	I95	17	3741	252	0.165	0.327
N1272	03 19 21.30	+41 29 26.7	I95	19	3805	250	0.172	0.311
N1272	03 19 21.30	+41 29 26.7	I97A	21	3877	286	0.197	0.342
N1272	03 19 21.30	+41 29 26.7	I97A	31	3815	265	0.197	0.331
N1278	03 19 54.15	+41 33 47.9	I95	22	6067	249	0.168	0.292
N1278	03 19 54.15	+41 33 47.9	I95	22	6088	251	0.164	0.301
N1278	03 19 54.15	+41 33 47.9	I97A	33	6090	258	0.189	0.305
N1282	03 20 12.13	+41 22 00.9	I95	17	2222	209	0.164	0.261

(*Continued*)

Identification	R.A. (J2000)	Dec. (J2000)	Source	S/N	$cz_\odot$	σ	Mgb'	Mg$_2$
N1282	03 20 12.13	+41 22 00.9	I95	23	2202	217	0.163	0.272
N1282	03 20 12.13	+41 22 00.9	I97A	38	2139	195	0.163	0.275
N1282	03 20 12.13	+41 22 00.9	I97A	38	2253	226	0.154	0.266
A0426:7S-PER163	03 20 28.65	+41 29 18.2	I95	14	5460	154	0.179	0.288
A0426:7S-PER163	03 20 28.65	+41 29 18.2	I95	14	5439	162	0.172	0.275
A0426:7S-PER163	03 20 28.65	+41 29 18.2	I95	21	5470	133	0.122	0.243
A0426:7S-PER163	03 20 28.65	+41 29 18.2	I97A	26	5498	137	0.150	0.261
N1293	03 21 36.46	+41 23 34.2	I97A	35	4175	222	0.176	0.317
N1293	03 21 36.46	+41 23 34.2	I97A	38	4173	233	0.174	0.300
N1339	03 28 06.57	−32 17 04.3	A95B	43	1358	152	0.170	0.312
N1339	03 28 06.57	−32 17 04.3	A95B	45	1361	154	0.169	0.310
N1351	03 30 34.76	−34 51 12.3	A95B	38	1514	141	0.168	0.277
N1351	03 30 34.76	−34 51 12.3	A95B	40	1524	153	0.166	0.287
N1351	03 30 34.76	−34 51 12.3	A95B	44	1525	129	0.157	0.271
N1374	03 35 16.66	−35 13 34.3	A95B	39	1339	178	0.193	0.321
N1379	03 36 03.26	−35 26 25.5	A95B	34	1361	116	0.146	0.265
N1399	03 38 29.32	−35 27 00.7	A95B	42	1437	322	0.185	0.353
N1395	03 38 29.57	−23 01 39.8	A95B	41	1717	238	0.176	0.327
N1404	03 38 52.01	−35 35 34.0	A95B	50	1930	228	0.177	0.322
N1404	03 38 52.01	−35 35 34.0	A95B	65	1914	228	0.174	0.314
I2006	03 54 28.53	−35 57 54.8	A95B	39	1382	120	0.151	0.290
A3193:SMC-F	03 56 40.80	−51 33 28.0	A95B	36	10944	192	0.160	0.300
A3193:SMC-B	03 58 12.49	−52 27 09.5	A95B	26	10128	139	0.165	0.264
A3193:SMC-B	03 58 12.49	−52 27 09.5	A95B	27	10112	121	0.143	0.262
N1500	03 58 13.96	−52 19 43.8	A95B	32	10141	260	0.175	0.312
N1500	03 58 13.96	−52 19 43.8	A95B	39	10114	258	0.164	0.323
N1506	04 00 21.28	−52 34 26.6	A95B	37	10258	229	0.172	0.304
N1506	04 00 21.28	−52 34 26.6	A95B	43	10271	236	0.177	0.310
A3193:SMC-I	04 03 03.74	−52 44 22.9	A95B	30	10642	165	0.158	0.280
N1600	04 31 39.89	−05 05 10.1	A95B	23	4716	307	0.163	0.323
N1600	04 31 39.89	−05 05 10.1	A95B	28	4701	363	0.163	0.330
A0496:D-046	04 33 37.84	−13 15 43.0	A95B	27	9858	241	0.206	0.309
A0496:D-015	04 33 57.05	−13 27 45.7	A95B	32	9705	165	0.160	0.297
A0496:D-025	04 34 10.43	−13 22 11.9	A95B	29	10428	201	0.161	0.303
N1700	04 56 56.21	−04 51 55.8	A95B	29	3915	234	0.159	0.284
N1700	04 56 56.21	−04 51 55.8	A95B	36	3901	222	0.161	0.281
A0539:D-031	05 15 35.90	+06 15 51.7	I97A	21	8747	165	0.152	0.232
A0539:D-039	05 15 47.86	+06 19 19.9	I97A	23	8627	199	0.158	0.256
A0539:D-053	05 16 13.71	+06 26 50.0	I97A	31	6693	199	0.164	0.280
A0539:D-045	05 16 25.49	+06 20 33.2	I97A	24	8739	228	0.187	0.316
A0539:D-044	05 16 28.86	+06 24 08.9	I97A	24	7489	230	0.148	0.260
A0539:D-064	05 16 33.58	+06 30 14.6	I97A	13	8650	121	0.103	0.213
A0539:D-063	05 16 35.68	+06 30 13.4	I97A	23	7138	189	0.099	0.211
A0539:D-063	05 16 35.68	+06 30 13.4	A95B	29	7136	166	0.129	0.234
A0539:D-062	05 16 36.26	+06 29 19.4	I97A	21	9310	187	0.164	0.271
A0539:D-062	05 16 36.26	+06 29 19.4	A95B	24	9334	142	0.128	0.274
A0539:D-050	05 16 37.01	+06 27 06.4	A95B	22	8549	199	0.151	0.283
A0539:D-050	05 16 37.01	+06 27 06.4	I97A	30	8566	244	0.162	0.271
A0539:D-049	05 16 37.15	+06 26 53.0	I97A	21	8739	246	0.166	0.284
A0539:D-049	05 16 37.15	+06 26 53.0	A95B	23	8722	194	0.142	0.280

(*Continued*)

Identification	R.A. (J2000)	Dec. (J2000)	Source	S/N	$cz_{\odot}$	σ	Mgb'	Mg$_2$
A0539:D-049	05 16 37.15	+06 26 53.0	I97A	28	8742	223	0.161	0.279
A0539:D-047	05 16 37.33	+06 26 27.3	A95B	19	8177	177	0.149	0.306
A0539:D-047	05 16 37.33	+06 26 27.3	I97A	19	8177	209	0.167	0.309
A0539:D-051	05 16 38.94	+06 27 52.2	I97A	25	9374	174	0.152	0.266
A0539:D-042	05 16 49.45	+06 23 20.5	I97A	17	8714	201	0.134	0.260
A0539:D-068	05 16 55.12	+06 33 09.5	I97A	21	9728	332	0.167	0.313
A0539:D-068	05 16 55.12	+06 33 09.5	A95B	33	9685	249	0.176	0.333
A0539:D-016	05 17 17.86	+06 08 14.4	I97A	31	9680	224	0.173	0.285
A0539:D-040	05 18 32.26	+06 23 07.1	I97A	21	9839	223	0.151	0.287
A3389:D-043	06 21 13.85	−65 00 59.4	A95A	21	7832	140	0.177	0.288
A3389:D-043	06 21 13.85	−65 00 59.4	A95A	30	7844	127	0.150	0.269
N2229	06 21 23.67	−64 57 26.3	A94	35	8429	229	0.171	0.277
N2230	06 21 27.47	−64 59 37.2	A94	36	8074	262	0.178	0.307
A3389:D-053	06 22 04.85	−64 57 37.9	A95A	30	8344	116	0.144	0.249
A3389:D-053	06 22 04.85	−64 57 37.9	A95A	34	8355	115	0.146	0.253
A3389:D-060	06 22 19.57	−64 14 08.8	A95A	53	7830	188	0.157	0.264
N2235	06 22 22.04	−64 56 05.5	A94	38	8335	235	0.147	0.262
A3389:D-049	06 23 07.44	−64 55 52.0	A95A	41	8471	188	0.145	0.272
A3389:D-082	06 23 35.72	−64 34 42.4	A94	28	13900	260	0.158	0.298
A3389:D-048	06 23 48.97	−64 57 17.1	A95A	38	7237	154	0.143	0.253
A0569:SMC-S	07 00 17.34	+48 24 01.4	I95	17	15693	201	0.151	0.300
N2320	07 05 42.00	+50 34 50.8	I95	19	5892	296	0.181	0.282
N2320	07 05 42.00	+50 34 50.8	I95	26	5944	306	0.174	0.299
A0569:SMC-Q	07 06 40.14	+48 29 24.5	I95	16	5839	225	0.190	0.294
A0569:SMC-Q	07 06 40.14	+48 29 24.5	I95	17	5862	204	0.151	0.291
A0569:SMC-Q	07 06 40.14	+48 29 24.5	I95	25	5895	244	0.175	0.290
A0569:SMC-M	07 07 27.72	+48 40 18.1	I95	13	14963	159	0.164	0.262
A0569:SMC-N	07 07 59.60	+48 39 58.7	I95	33	5341	203	0.155	0.259
A0569:SMC-G	07 08 24.18	+50 08 11.7	I95	14	5794	175	0.148	0.284
A0569:SMC-G	07 08 24.18	+50 08 11.7	I97A	30	5748	195	0.167	0.285
A0569:SMC-R	07 08 52.74	+48 27 00.0	I95	23	6156	157	0.151	0.273
N2329	07 09 08.01	+48 36 55.5	I95	24	5826	225	0.161	0.275
N2329	07 09 08.01	+48 36 55.5	I95	24	5819	246	0.172	0.272
U03696	07 09 23.05	+48 38 07.5	I97A	44	6150	271	0.167	0.282
N2330	07 09 28.40	+50 09 09.1	I97A	29	4820	142	0.156	0.281
N2332	07 09 34.20	+50 10 54.5	I95	27	5845	261	0.177	0.293
N2332	07 09 34.20	+50 10 54.5	I97A	34	5836	254	0.148	0.288
A0569:SMC-L	07 09 44.85	+48 41 25.7	I95	24	5742	131	0.131	0.260
I0458	07 10 34.01	+50 07 06.3	I97A	34	6500	212	0.167	0.281
I0461	07 10 45.03	+50 04 51.5	I97A	20	5714	116	0.116	0.242
I0461	07 10 45.03	+50 04 51.5	I97A	28	5747	160	0.141	0.245
I0464	07 11 04.79	+50 08 11.2	I95	17	4864	151	0.150	0.242
I0464	07 11 04.79	+50 08 11.2	I97A	45	4820	200	0.147	0.243
N2340	07 11 10.84	+50 10 27.7	I95	24	5919	248	0.185	0.331
N2340	07 11 10.84	+50 10 27.7	I97A	36	5925	249	0.193	0.334
I0465	07 11 33.65	+50 14 53.7	I95	26	6102	240	0.170	0.293
U03725	07 11 41.65	+49 51 42.6	I95	30	6171	266	0.171	0.304
A0569:SMC-B	07 13 54.02	+50 23 54.4	I95	16	5836	164	0.157	0.272
A0569:SMC-B	07 13 54.02	+50 23 54.4	I95	20	5823	155	0.160	0.274
U03758	07 15 04.72	+50 32 09.6	I95	23	5678	245	0.161	0.269

(*Continued*)

Identification	R.A. (J2000)	Dec. (J2000)	Source	S/N	$cz_{\odot}$	σ	Mgb'	Mg$_2$
A0576:SMC-I	07 19 28.53	+55 36 31.8	I97A	26	9874	201	0.142	0.269
A0576:SMC-B	07 20 20.43	+55 53 11.3	I95	15	11906	130	0.108	0.200
A0576:SMC-B	07 20 20.43	+55 53 11.3	I97A	29	11875	142	0.107	0.219
A0576:SMC-C	07 21 19.42	+55 48 38.2	I95	14	11176	262	0.174	0.285
A0576:SMC-C	07 21 19.42	+55 48 38.2	I95	18	11177	232	0.169	0.290
A0576:SMC-C	07 21 19.42	+55 48 38.2	I97A	28	11142	249	0.171	0.279
A0576:SMC-D	07 21 21.55	+55 47 52.1	I95	14	12100	222	0.178	0.303
A0576:SMC-D	07 21 21.55	+55 47 52.1	I95	18	12111	199	0.160	0.323
A0576:SMC-D	07 21 21.55	+55 47 52.1	I97A	27	12095	217	0.177	0.306
A0576:SMC-E2	07 21 29.64	+55 45 39.2	I95	15	12312	229	0.172	0.288
A0576:SMC-E2	07 21 29.64	+55 45 39.2	I97A	27	12332	244	0.161	0.303
A0576:SMC-E2	07 21 29.64	+55 45 39.2	I97A	31	12338	271	0.167	0.302
A0576:SMC-E1	07 21 32.06	+55 45 24.5	I95	15	11414	267	0.177	0.332
A0576:SMC-E1	07 21 32.06	+55 45 24.5	I97A	28	11415	279	0.174	0.301
A0576:SMC-E1	07 21 32.06	+55 45 24.5	I97A	32	11430	273	0.182	0.327
A0576:SMC-A	07 21 36.44	+56 10 16.5	I95	15	10936	122	0.125	0.226
A0576:SMC-A	07 21 36.44	+56 10 16.5	I97A	26	10906	130	0.115	0.219
A0576:SMC-G	07 21 43.96	+55 40 42.8	I97A	31	9967	180	0.155	0.264
A0576:SMC-H	07 22 09.36	+55 39 48.0	I97A	23	12332	213	0.170	0.281
A0576:SMC-J	07 25 48.27	+55 29 40.7	I97A	23	10737	139	0.132	0.228
N2300	07 32 21.98	+85 42 27.4	I95	25	1916	276	0.189	0.324
A0634:SMC-B	08 09 31.47	+58 44 22.9	I95	15	20635	279	0.182	0.282
A0634:SMC-I	08 09 52.60	+57 54 46.5	I95	15	7916	293	0.182	0.313
A0634:SMC-I	08 09 52.60	+57 54 46.5	I97A	44	7948	297	0.188	0.317
A0634:SMC-F	08 13 39.42	+58 08 06.8	I97A	31	8133	211	0.161	0.294
A0634:SMC-J	08 14 20.15	+57 52 26.0	I95	14	8080	211	0.157	0.269
A0634:SMC-J	08 14 20.15	+57 52 26.0	I95	15	8065	204	0.151	0.253
A0634:SMC-J	08 14 20.15	+57 52 26.0	I97A	25	8078	198	0.150	0.269
A0634:SMC-H	08 14 43.16	+57 57 38.6	I95	14	8247	204	0.141	0.249
A0634:SMC-H	08 14 43.16	+57 57 38.6	I95	21	8210	191	0.147	0.267
U04289	08 15 44.75	+58 19 15.6	I95	14	8118	247	0.183	0.290
U04289	08 15 44.75	+58 19 15.6	I95	20	8158	225	0.154	0.286
U04289	08 15 44.75	+58 19 15.6	I97A	32	8151	247	0.191	0.305
A0634:SMC-G	08 16 05.37	+58 00 32.6	I95	18	7893	200	0.154	0.263
A0634:SMC-G	08 16 05.37	+58 00 32.6	I95	28	7901	191	0.158	0.260
A0634:SMC-C	08 16 15.09	+58 35 22.1	I97A	20	7924	92	0.146	0.263
N2634	08 48 25.12	+73 58 03.1	I95	25	2249	174	0.170	0.277
N2831	09 19 45.47	+33 44 42.3	I95	15	5134	175	0.132	0.259
N2831	09 19 45.47	+33 44 42.3	I97A	39	5180	207	0.151	0.262
N2832	09 19 46.86	+33 44 59.3	I95	23	6898	333	0.188	0.324
N2832	09 19 46.86	+33 44 59.3	I97A	55	6948	339	0.185	0.322
A0779:SMC-G	09 19 52.28	+33 38 57.7	I95	18	6702	139	0.181	0.286
A0779:SMC-G	09 19 52.28	+33 38 57.7	I97A	27	6689	158	0.178	0.293
U04972	09 21 51.43	+33 24 07.0	I95	16	7098	199	0.158	0.292
U04972	09 21 51.43	+33 24 07.0	I95	25	7075	232	0.154	0.286
U04972	09 21 51.43	+33 24 07.0	I97A	25	7108	256	0.170	0.287
U04974	09 22 10.38	+33 50 54.6	I95	19	7040	225	0.147	0.284
U04974	09 22 10.38	+33 50 54.6	I97A	27	7023	235	0.171	0.297
N2865	09 23 30.69	−23 09 48.5	I97A	29	2639	195	0.095	0.189
N2865	09 23 30.69	−23 09 48.5	A94	34	2609	172	0.099	0.197

(*Continued*)

Identification	R.A. (J2000)	Dec. (J2000)	Source	S/N	$cz_{\odot}$	σ	Mgb'	Mg$_2$
N2865	09 23 30.69	−23 09 48.5	A95A	36	2614	177	0.120	0.200
N2865	09 23 30.69	−23 09 48.5	A95A	43	2622	169	0.118	0.214
N2865	09 23 30.69	−23 09 48.5	A94	54	2627	181	0.111	0.202
A0779:SMC-F	09 23 32.64	+33 45 17.4	I95	19	6648	152	0.157	0.218
A0779:SMC-F	09 23 32.64	+33 45 17.4	I97A	30	6657	145	0.135	0.207
N2986	09 44 16.19	−21 16 42.8	I97A	32	2332	289	0.170	0.315
N2986	09 44 16.19	−21 16 42.8	A95A	37	2313	262	0.182	0.342
N2986	09 44 16.19	−21 16 42.8	A94	42	2320	274	0.189	0.351
N2986	09 44 16.19	−21 16 42.8	A95A	57	2294	278	0.174	0.345
N2986	09 44 16.19	−21 16 42.8	A94	65	2302	259	0.176	0.342
N3115	10 05 13.42	−07 43 06.5	A94	47	746	239	0.175	0.322
N3115	10 05 13.42	−07 43 06.5	A95A	57	697	269	0.181	0.330
N3115	10 05 13.42	−07 43 06.5	A95A	57	720	269	0.166	0.325
N3115	10 05 13.42	−07 43 06.5	A94	61	739	257	0.180	0.328
A0999:SMC-C	10 23 22.53	+13 05 34.9	I97A	21	9630	125	0.166	0.253
A0999:SMC-D	10 23 23.85	+12 50 05.8	I97A	29	9764	264	0.174	0.302
A0999:SMC-E	10 23 26.29	+12 48 54.8	I97A	30	9314	204	0.164	0.274
A0999:SMC-F	10 23 43.10	+12 42 55.8	I97A	29	9179	245	0.162	0.286
A0999:SMC-A	10 24 22.36	+13 40 27.1	I97A	26	5657	84	0.139	0.211
A0999:SMC-G	10 25 06.66	+12 24 52.8	I97A	28	9979	171	0.159	0.282
A0999:SMC-B	10 25 08.93	+13 36 05.1	I97A	20	5599	78	0.090	0.115
A1016:SMC-F	10 26 23.50	+10 55 06.2	I95	15	9594	134	0.140	0.241
A1016:SMC-F	10 26 23.50	+10 55 06.2	I97A	26	9615	150	0.129	0.239
A1016:SMC-E	10 26 36.48	+10 56 06.4	I95	14	10090	144	0.132	0.186
A1016:SMC-E	10 26 36.48	+10 56 06.4	I97A	24	10101	163	0.130	0.211
A1016:SMC-B	10 27 05.83	+11 03 16.8	I95	17	9722	217	0.157	0.267
A1016:SMC-B	10 27 05.83	+11 03 16.8	I97A	31	9722	204	0.162	0.283
I0613	10 27 07.79	+11 00 38.5	I95	22	9729	261	0.164	0.306
I0613	10 27 07.79	+11 00 38.5	A95A	48	9722	239	0.161	0.300
I0613	10 27 07.79	+11 00 38.5	A95A	53	9724	254	0.190	0.307
A1016:SMC-C	10 27 10.58	+11 01 15.8	I95	14	9814	185	0.155	0.270
A1016:SMC-C	10 27 10.58	+11 01 15.8	A95A	32	9793	142	0.140	0.257
A1016:SMC-C	10 27 10.58	+11 01 15.8	A95A	33	9774	146	0.165	0.264
A1016:SMC-G	10 27 42.58	+10 49 28.1	I97A	17	9474	126	0.122	0.196
A1016:SMC-G	10 27 42.58	+10 49 28.1	I97A	18	9465	130	0.138	0.204
A1016:SMC-G	10 27 42.58	+10 49 28.1	A95A	20	9441	97	0.115	0.210
A1016:SMC-A	10 30 00.79	+11 08 18.2	I97A	17	9630	101	0.103	0.222
A1016:SMC-A	10 30 00.79	+11 08 18.2	I97A	18	9623	95	0.125	0.201
A1016:SMC-A	10 30 00.79	+11 08 18.2	A95A	9	9602	74	0.087	0.174
N3308	10 36 22.22	−27 26 20.0	A94	36	3573	181	0.167	0.309
N3308	10 36 22.22	−27 26 20.0	A95A	44	3553	184	0.161	0.310
N3308	10 36 22.22	−27 26 20.0	A94	53	3554	180	0.172	0.313
N3309	10 36 35.72	−27 31 03.2	A94	57	4075	232	0.184	0.337
A1060:SMC-S135	10 37 09.62	−27 39 29.3	A94	37	4119	124	0.156	0.264
A1060:SMC-S135	10 37 09.62	−27 39 29.3	A94	37	4114	133	0.143	0.270
N3377	10 47 42.05	+13 59 09.1	I95	38	679	134	0.153	0.259
N3377	10 47 42.05	+13 59 09.1	A94	42	683	132	0.150	0.265
N3377	10 47 42.05	+13 59 09.1	A95A	44	655	131	0.156	0.272
N3377	10 47 42.05	+13 59 09.1	I97A	44	679	138	0.148	0.270
N3377	10 47 42.05	+13 59 09.1	A95A	45	665	134	0.152	0.271

(*Continued*)

Identification	R.A. (J2000)	Dec. (J2000)	Source	S/N	$cz_{\odot}$	σ	Mgb'	Mg$_2$
N3377	10 47 42.05	+13 59 09.1	I95	48	659	146	0.158	0.257
N3377	10 47 42.05	+13 59 09.1	A94	62	695	132	0.156	0.269
N3379	10 47 49.50	+12 34 56.9	A95A	27	913	202	0.183	0.318
N3379	10 47 49.50	+12 34 56.9	I97A	32	932	212	0.160	0.294
N3379	10 47 49.50	+12 34 56.9	I95	38	910	215	0.174	0.297
N3379	10 47 49.50	+12 34 56.9	I97A	41	930	215	0.174	0.312
N3379	10 47 49.50	+12 34 56.9	I95	41	919	207	0.181	0.302
N3379	10 47 49.50	+12 34 56.9	A94	43	905	204	0.177	0.324
N3379	10 47 49.50	+12 34 56.9	A95A	45	911	217	0.184	0.320
N3379	10 47 49.50	+12 34 56.9	A95A	51	914	217	0.174	0.319
N3379	10 47 49.50	+12 34 56.9	A95A	52	895	209	0.170	0.319
N3379	10 47 49.50	+12 34 56.9	A95A	55	918	212	0.170	0.326
N3379	10 47 49.50	+12 34 56.9	A94	63	904	208	0.180	0.320
N3379	10 47 49.50	+12 34 56.9	A94	70	911	205	0.175	0.314
N3384	10 48 17.19	+12 37 49.3	I97A	42	741	181	0.154	0.288
N3384	10 48 17.19	+12 37 49.3	I97A	48	738	144	0.164	0.295
N3384	10 48 17.19	+12 37 49.3	A95A	52	687	140	0.160	0.289
N3384	10 48 17.19	+12 37 49.3	A95A	56	704	149	0.156	0.303
N3384	10 48 17.19	+12 37 49.3	A94	62	698	138	0.164	0.301
N3412	10 50 53.12	+13 24 45.8	I97A	41	846	113	0.126	0.231
N3412	10 50 53.12	+13 24 45.8	A95A	42	845	104	0.133	0.233
N3412	10 50 53.12	+13 24 45.8	A94	55	841	98	0.132	0.240
A1139:D-030	10 57 01.60	+01 33 59.9	I97A	24	11287	197	0.161	0.260
A1139:D-030	10 57 01.60	+01 33 59.9	A95A	31	11264	184	0.167	0.279
A1139:D-041	10 57 32.91	+01 37 16.3	I97A	22	10589	157	0.157	0.268
A1139:D-041	10 57 32.91	+01 37 16.3	A95A	26	10573	138	0.151	0.249
A1142:SMC-C	10 57 42.28	+10 36 22.5	I97A	14	25673	329	0.137	0.246
A1139:D-029	10 57 43.29	+01 34 01.1	A95A	42	11778	234	0.172	0.270
A1139:D-039	10 58 11.02	+01 36 15.4	I95	15	11526	255	0.187	0.319
A1139:D-039	10 58 11.02	+01 36 15.4	I95	16	11546	228	0.160	0.325
A1139:D-039	10 58 11.02	+01 36 15.4	I97A	29	11565	253	0.175	0.289
A1139:D-039	10 58 11.02	+01 36 15.4	A95A	42	11537	248	0.187	0.318
A1139:D-037	10 58 13.10	+01 36 24.5	I95	14	11582	245	0.162	0.279
A1139:D-037	10 58 13.10	+01 36 24.5	I97A	30	11525	291	0.178	0.316
A1139:D-036	10 58 15.23	+01 36 56.9	I95	15	11855	279	0.183	0.320
A1139:D-036	10 58 15.23	+01 36 56.9	A95A	44	11824	253	0.179	0.288
I0660	10 58 26.67	+01 22 57.9	I97A	29	12276	220	0.164	0.298
I0660	10 58 26.67	+01 22 57.9	A95A	30	12274	259	0.161	0.278
A1139:D-016	10 58 38.93	+01 22 55.0	I97A	19	12339	142	0.154	0.220
I0661	10 58 51.49	+01 39 02.2	I97A	24	11962	190	0.172	0.281
I0661	10 58 51.49	+01 39 02.2	A95A	28	11941	165	0.155	0.263
I0662	10 59 20.55	+01 35 55.3	I95	14	11732	248	0.167	0.271
I0662	10 59 20.55	+01 35 55.3	I97A	30	11756	256	0.160	0.279
A1142:D-052	10 59 45.07	+10 47 58.8	I97A	19	11640	99	0.150	0.240
A1142:D-052	10 59 45.07	+10 47 58.8	I97A	19	11639	98	0.118	0.204
N3489	11 00 18.14	+13 54 08.2	I97A	47	697	114	0.114	0.181
N3489	11 00 18.14	+13 54 08.2	I97A	53	683	118	0.101	0.175
N3489	11 00 18.14	+13 54 08.2	A95A	57	682	105	0.104	0.186
N3489	11 00 18.14	+13 54 08.2	A94	69	677	108	0.108	0.184
I0664	11 00 45.39	+10 33 11.6	I97A	30	10169	325	0.173	0.316

(*Continued*)

Identification	R.A. (J2000)	Dec. (J2000)	Source	S/N	$cz_{\odot}$	σ	Mgb'	Mg$_2$
A1142:D-020	11 02 21.36	+10 14 35.8	I97A	21	10720	222	0.163	0.266
A1185:D-021	11 08 10.35	+28 31 48.8	I95	15	9481	231	0.195	0.340
A1185:D-021	11 08 10.35	+28 31 48.8	I95	21	9453	270	0.185	0.308
A1177:SMC-A	11 09 17.59	+22 21 58.9	I95	19	16507	162	0.110	0.185
A1177:SMC-H	11 09 19.73	+21 38 53.4	I97A	19	9285	147	0.164	0.250
U06198	11 09 25.81	+29 34 07.5	I95	18	10429	139	0.117	0.200
A1177:SMC-F	11 09 41.02	+21 44 23.1	I95	27	9675	233	0.181	0.319
A1177:SMC-G	11 09 42.81	+21 44 07.5	I97A	29	9259	191	0.159	0.260
N3551	11 09 44.44	+21 45 31.7	I95	20	9584	255	0.177	0.310
N3551	11 09 44.44	+21 45 31.7	I95	23	9578	250	0.157	0.315
N3551	11 09 44.44	+21 45 31.7	I97A	30	9589	268	0.178	0.314
N3555	11 09 50.33	+21 48 36.7	I95	19	9454	207	0.163	0.297
A1177:SMC-B	11 10 25.84	+22 06 36.4	I97A	18	9446	122	0.166	0.246
A1177:SMC-I	11 10 34.17	+21 34 46.2	I95	16	9926	92	0.059	0.174
A1177:SMC-I	11 10 34.17	+21 34 46.2	I97A	24	9873	82	0.099	0.159
A1185:D-010	11 10 38.53	+28 18 59.8	I95	17	10320	277	0.145	0.280
A1185:D-033	11 10 43.01	+28 41 33.3	I95	13	9975	176	0.152	0.266
A1185:D-033	11 10 43.01	+28 41 33.3	I95	19	9928	212	0.176	0.271
N3554	11 10 47.84	+28 39 36.4	I95	20	8743	215	0.153	0.273
A1177:SMC-C	11 10 48.19	+22 03 33.0	I97A	18	9814	116	0.141	0.219
N3570	11 12 03.36	+27 35 22.8	I95	17	10564	270	0.194	0.327
N3570	11 12 03.36	+27 35 22.8	I95	29	10535	247	0.173	0.327
U06250	11 13 10.40	+27 49 05.0	I95	21	9418	283	0.176	0.289
A1185:SMC-M	11 16 13.48	+29 13 06.1	I95	20	8820	223	0.191	0.306
I2738	11 21 23.06	+34 21 24.0	I95	21	10504	249	0.162	0.309
A1228:SMC-G	11 21 26.94	+34 27 09.1	I95	20	10607	199	0.157	0.280
A1228:SMC-E	11 21 28.43	+34 32 38.8	I95	14	12452	371	0.187	0.320
A1228:SMC-E	11 21 28.43	+34 32 38.8	I97A	38	12474	361	0.183	0.306
I2744	11 21 42.48	+34 21 45.9	I95	26	10635	187	0.161	0.285
I2744	11 21 42.48	+34 21 45.9	I97A	27	10666	214	0.176	0.286
A1228:SMC-H	11 22 07.30	+34 21 57.6	I95	20	10259	235	0.162	0.287
U06394	11 22 56.49	+34 06 41.2	I97A	18	12801	286	0.188	0.315
U06394	11 22 56.49	+34 06 41.2	I97A	19	12878	285	0.181	0.302
A1228:SMC-K	11 22 59.06	+34 17 31.8	I97A	23	12902	147	0.165	0.260
A1228:SMC-C	11 23 20.35	+34 39 39.9	I95	15	12272	115	0.151	0.273
A1228:SMC-C	11 23 20.35	+34 39 39.9	I97A	24	12271	128	0.173	0.249
A1228:SMC-M	11 23 24.52	+33 49 44.6	I95	24	10324	227	0.170	0.275
A1257:SMC-C	11 23 47.02	+35 26 32.1	I97A	23	10218	137	0.110	0.154
A1228:SMC-B	11 24 07.46	+34 39 48.6	I97A	14	8760	177	0.150	0.312
A1228:SMC-B	11 24 07.46	+34 39 48.6	I97A	24	8745	139	0.159	0.279
A1228:SMC-B	11 24 07.46	+34 39 48.6	I97A	30	8737	150	0.169	0.286
A1257:SMC-B	11 25 30.88	+35 30 16.2	I97A	38	10143	287	0.188	0.320
A1257:SMC-GC	11 26 15.69	+35 19 42.5	I97A	19	10915	156	0.119	0.217
A1257:SMC-G	11 26 17.26	+35 20 24.2	I97A	15	10327	198	0.152	0.266
A1257:SMC-G	11 26 17.26	+35 20 24.2	I97A	23	10267	191	0.168	0.254
A1257:SMC-G	11 26 17.26	+35 20 24.2	I97A	31	10278	176	0.163	0.255
A1257:SMC-E	11 26 18.38	+35 20 57.4	I97A	21	10177	196	0.167	0.259
A1257:SMC-E	11 26 18.38	+35 20 57.4	I97A	30	10226	171	0.135	0.254
A1267:SMC-E	11 28 12.55	+26 57 20.2	I97A	17	17261	201	0.128	0.254
A1267:SMC-A	11 28 19.91	+27 37 19.1	I97A	16	9671	87	0.094	0.158

(*Continued*)

Identification	R.A. (J2000)	Dec. (J2000)	Source	S/N	$cz_\odot$	σ	Mgb'	Mg$_2$
A1267:SMC-F	11 28 36.21	+26 54 20.7	I97A	31	9817	259	0.166	0.277
A1314:SMC-B	11 32 34.81	+49 06 34.7	I95	25	10199	183	0.126	0.226
A1314:SMC-B	11 32 34.81	+49 06 34.7	I97A	31	10194	153	0.154	0.243
I0708	11 33 59.22	+49 03 43.4	I95	22	9497	251	0.183	0.304
I0709	11 34 14.54	+49 02 35.3	I95	22	9513	230	0.163	0.265
I0712	11 34 49.24	+49 04 39.7	I95	18	10031	317	0.167	0.318
I0712	11 34 49.24	+49 04 39.7	I97A	38	10059	331	0.173	0.326
A1314:SMC-E	11 34 59.83	+49 04 53.6	I95	18	9503	144	0.154	0.252
A1314:SMC-E	11 34 59.83	+49 04 53.6	I97A	25	9470	161	0.167	0.267
A1314:SMC-D	11 35 26.29	+49 05 13.4	I97A	27	9661	173	0.135	0.237
A1314:SMC-A	11 36 30.55	+49 07 52.8	I97A	27	11129	262	0.156	0.278
A1314:SMC-G	11 36 36.65	+49 03 46.8	I95	15	9707	243	0.152	0.279
A1314:SMC-G	11 36 36.65	+49 03 46.8	I97A	34	9724	255	0.174	0.290
N3837	11 43 56.42	+19 53 40.4	I95	23	6338	257	0.192	0.302
N3837	11 43 56.42	+19 53 40.4	I97A	28	6321	264	0.160	0.289
N3842	11 44 02.17	+19 56 58.7	I95	18	6262	309	0.177	0.314
N3842	11 44 02.17	+19 56 58.7	I95	19	6285	295	0.194	0.319
N3842	11 44 02.17	+19 56 58.7	I97A	39	6316	319	0.189	0.330
N3841	11 44 02.19	+19 58 18.7	I95	14	6342	171	0.168	0.289
N3841	11 44 02.19	+19 58 18.7	I97A	32	6356	175	0.158	0.276
A1367:B-041	11 44 07.69	+19 44 15.5	I97A	23	7765	145	0.153	0.241
N3851	11 44 20.41	+19 58 50.3	I97A	26	6405	222	0.172	0.289
I2955	11 45 03.88	+19 37 14.0	I95	19	6497	160	0.135	0.247
I2955	11 45 03.88	+19 37 14.0	I97A	35	6511	183	0.169	0.280
N3862	11 45 05.00	+19 36 22.7	I95	26	6525	242	0.155	0.281
N3862	11 45 05.00	+19 36 22.7	I97A	47	6511	277	0.179	0.288
A1367:B-021	11 45 14.95	+19 50 42.3	I97A	25	7739	156	0.131	0.230
N3873	11 45 46.06	+19 46 24.9	I95	19	5402	227	0.158	0.275
N3873	11 45 46.06	+19 46 24.9	I97A	39	5434	250	0.154	0.273
A1367:B-020	11 48 03.36	+20 00 22.6	I97A	25	7246	171	0.156	0.250
N3940	11 52 46.33	+20 59 21.2	I95	21	6420	211	0.154	0.271
N4365	12 24 27.87	+07 19 04.9	I95	27	1229	227	0.171	0.315
N4365	12 24 27.87	+07 19 04.9	I97A	27	1250	292	0.191	0.333
N4365	12 24 27.87	+07 19 04.9	A95A	45	1243	248	0.185	0.321
N4365	12 24 27.87	+07 19 04.9	A94	53	1261	265	0.184	0.337
N4374	12 25 03.15	+12 53 11.2	I97A	26	1047	286	0.155	0.318
N4374	12 25 03.15	+12 53 11.2	I95	31	1035	303	0.173	0.294
N4374	12 25 03.15	+12 53 11.2	A94	32	1058	295	0.174	0.315
N4374	12 25 03.15	+12 53 11.2	A95A	42	1032	281	0.174	0.328
N4374	12 25 03.15	+12 53 11.2	A95A	51	1027	275	0.176	0.318
N4374	12 25 03.15	+12 53 11.2	A94	69	1028	280	0.182	0.310
N4382	12 25 24.23	+18 11 23.4	A94	107	729	167	0.129	0.230
N4406	12 26 11.74	+12 56 46.4	I95	17	-268	214	0.183	0.303
N4406	12 26 11.74	+12 56 46.4	I95	29	-234	244	0.189	0.305
N4406	12 26 11.74	+12 56 46.4	I95	31	-251	220	0.185	0.316
N4406	12 26 11.74	+12 56 46.4	I97A	31	-243	260	0.183	0.317
N4406	12 26 11.74	+12 56 46.4	A95A	40	-244	220	0.179	0.323
N4406	12 26 11.74	+12 56 46.4	A94	44	-223	249	0.191	0.318
N4406	12 26 11.74	+12 56 46.4	A94	52	-232	235	0.180	0.315
N4464	12 29 20.67	+08 09 30.3	I95	18	1235	119	0.144	0.230

(Continued)

Identification	R.A. (J2000)	Dec. (J2000)	Source	S/N	$cz_{\odot}$	σ	Mgb'	Mg$_2$
N4464	12 29 20.67	+08 09 30.3	I97A	18	1308	140	0.157	0.258
N4464	12 29 20.67	+08 09 30.3	I95	24	1262	113	0.165	0.244
N4464	12 29 20.67	+08 09 30.3	A95A	39	1256	124	0.135	0.243
N4464	12 29 20.67	+08 09 30.3	A94	67	1243	112	0.148	0.257
N4472	12 29 46.57	+08 00 07.5	I95	31	989	280	0.175	0.324
N4472	12 29 46.57	+08 00 07.5	I97A	31	1009	322	0.195	0.328
N4472	12 29 46.57	+08 00 07.5	I95	34	986	298	0.170	0.311
N4472	12 29 46.57	+08 00 07.5	A94	45	997	279	0.176	0.340
N4472	12 29 46.57	+08 00 07.5	I95	45	1000	299	0.167	0.317
N4472	12 29 46.57	+08 00 07.5	A94	53	982	300	0.181	0.339
N4473	12 29 48.87	+13 25 45.7	A94	105	2244	175	0.176	0.315
N4473	12 29 48.87	+13 25 45.7	I95	21	2250	192	0.164	0.285
N4473	12 29 48.87	+13 25 45.7	I95	35	2231	168	0.175	0.288
N4473	12 29 48.87	+13 25 45.7	I97A	35	2281	192	0.179	0.313
N4478	12 30 17.39	+12 19 43.9	I95	17	1379	143	0.151	0.242
N4478	12 30 17.39	+12 19 43.9	I95	21	1357	126	0.154	0.261
N4478	12 30 17.39	+12 19 43.9	I97A	27	1391	142	0.156	0.268
N4478	12 30 17.39	+12 19 43.9	A95A	41	1349	150	0.142	0.267
N4478	12 30 17.39	+12 19 43.9	A94	53	1336	130	0.164	0.276
N4486B	12 30 31.85	+12 29 26.0	I97A	23	1569	176	0.175	0.310
N4486B	12 30 31.85	+12 29 26.0	A94	34	1555	174	0.164	0.313
N4486B	12 30 31.85	+12 29 26.0	A95A	36	1562	174	0.185	0.320
N4486B	12 30 31.85	+12 29 26.0	A94	47	1555	165	0.177	0.305
N4486	12 30 49.42	+12 23 28.0	I95	17	1308	292	0.167	0.286
N4486	12 30 49.42	+12 23 28.0	I97A	23	1300	403	0.182	0.270
N4486	12 30 49.42	+12 23 28.0	A95A	28	1323	361	0.209	0.305
N4486	12 30 49.42	+12 23 28.0	A94	35	1333	350	0.180	0.323
N4486	12 30 49.42	+12 23 28.0	A94	62	1307	327	0.207	0.345
N4552	12 35 39.91	+12 33 25.1	I95	37	341	265	0.192	0.329
N4552	12 35 39.91	+12 33 25.1	I97A	53	340	258	0.186	0.336
N4552	12 35 39.91	+12 33 25.1	I95	54	350	259	0.192	0.330
N4564	12 36 26.96	+11 26 20.6	I95	26	1115	167	0.196	0.325
N4564	12 36 26.96	+11 26 20.6	I97A	29	1189	205	0.178	0.326
N4564	12 36 26.96	+11 26 20.6	I95	31	1137	169	0.191	0.321
N4564	12 36 26.96	+11 26 20.6	A94	83	1142	166	0.188	0.334
N4594	12 39 58.84	−11 37 28.0	A95A	58	1024	237	0.183	0.338
N4621	12 42 02.49	+11 38 48.7	I95	38	458	233	0.191	0.334
N4636	12 42 49.70	+02 41 18.4	I95	21	949	218	0.200	0.319
N4636	12 42 49.70	+02 41 18.4	I97A	21	948	217	0.181	0.333
N4636	12 42 49.70	+02 41 18.4	I95	23	940	207	0.176	0.321
N4636	12 42 49.70	+02 41 18.4	A94	38	936	202	0.209	0.338
N4636	12 42 49.70	+02 41 18.4	A94	51	938	196	0.183	0.335
N4649	12 43 39.66	+11 33 09.4	I97A	37	1116	361	0.191	0.356
N4649	12 43 39.66	+11 33 09.4	I95	42	1117	338	0.187	0.343
N4645	12 44 10.18	−41 44 58.0	A95A	46	2637	193	0.153	0.293
N4645	12 44 10.18	−41 44 58.0	A94	48	2630	193	0.160	0.288
N4645	12 44 10.18	−41 44 58.0	A94	59	2640	186	0.166	0.298
N4660	12 44 32.35	+11 11 26.6	I95	51	1083	210	0.176	0.297
E322-081	12 47 21.68	−41 14 16.7	A94	46	3111	237	0.159	0.301
N4697	12 48 35.71	−05 48 02.9	I97A	31	1277	187	0.168	0.288

(Continued)

Identification	R.A. (J2000)	Dec. (J2000)	Source	S/N	$cz_\odot$	σ	Mgb'	Mg$_2$
N4697	12 48 35.71	−05 48 02.9	A95A	58	1241	179	0.165	0.305
N4706	12 49 54.15	−41 16 46.4	A94	49	3862	206	0.176	0.301
N4709	12 50 03.88	−41 22 56.0	A94	27	4679	241	0.186	0.338
N4709	12 50 03.88	−41 22 56.0	A94	46	4684	236	0.199	0.345
N4709	12 50 03.88	−41 22 56.0	A95A	51	4678	244	0.175	0.336
N4709	12 50 03.88	−41 22 56.0	A94	54	4678	235	0.189	0.337
A3526:D-049	12 50 11.48	−41 13 17.1	A94	29	2967	118	0.188	0.307
A3526:D-049	12 50 11.48	−41 13 17.1	A95A	32	2960	120	0.176	0.313
A3526:D-049	12 50 11.48	−41 13 17.1	A94	39	2971	117	0.172	0.314
A3526:D-049	12 50 11.48	−41 13 17.1	A94	41	2968	118	0.169	0.322
E323-008	12 50 34.39	−41 28 15.9	A94	31	5302	135	0.135	0.233
N4729	12 51 46.29	−41 07 56.4	A95A	33	3334	135	0.144	0.282
N4729	12 51 46.29	−41 07 56.4	A94	49	3333	137	0.157	0.300
N4729	12 51 46.29	−41 07 56.4	A94	54	3344	132	0.145	0.280
N4730	12 52 00.47	−41 08 50.3	A94	52	2094	200	0.166	0.315
N4730	12 52 00.47	−41 08 50.3	A94	52	2093	200	0.170	0.315
E323-019	12 52 03.13	−41 27 35.7	A95A	35	3945	136	0.151	0.259
E323-034	12 53 26.01	−41 12 11.8	A94	59	4335	219	0.165	0.301
N4767	12 53 52.70	−39 42 52.3	A95A	29	2995	208	0.174	0.306
A3537:SMC-173	12 56 27.40	−31 27 06.4	A94	34	15692	269	0.179	0.340
E443-014	12 56 58.14	−31 19 44.9	A94	23	16929	301	0.198	0.000
N4839	12 57 24.27	+27 29 47.9	I97A	24	7372	258	0.174	0.303
A3537:SMC-156	12 58 41.86	−32 07 17.1	A94	39	5217	161	0.164	0.290
A3537:SMC-156	12 58 41.86	−32 07 17.1	A94	41	5213	163	0.152	0.280
A1656:D-136	12 58 55.87	+27 58 01.5	I97A	27	5701	190	0.149	0.260
N4860	12 59 03.79	+28 07 25.6	I95	11	7938	263	0.191	0.324
N4860	12 59 03.79	+28 07 25.6	I97A	36	7962	275	0.180	0.319
I3959	12 59 08.00	+27 47 02.7	I97A	30	7081	211	0.180	0.294
N4874	12 59 34.77	+27 57 38.2	I97A	23	7214	278	0.193	0.308
N4875	12 59 37.80	+27 54 26.5	I97A	27	8045	191	0.157	0.274
N4876	12 59 44.30	+27 54 44.6	I97A	34	6726	189	0.140	0.234
N4881	12 59 57.60	+28 14 50.6	I95	21	6718	200	0.163	0.287
N4881	12 59 57.60	+28 14 50.6	I97A	33	6740	192	0.174	0.284
N4882	13 00 04.20	+27 59 14.8	I97A	41	6392	165	0.158	0.241
I4011	13 00 06.20	+28 00 14.7	I97A	32	7268	123	0.146	0.244
N4889	13 00 07.68	+27 58 32.8	I95	19	6527	387	0.187	0.337
N4889	13 00 07.68	+27 58 32.8	I97A	28	6540	390	0.194	0.322
E443-024	13 01 00.80	−32 26 29.2	A95A	43	5118	284	0.175	0.313
E443-024	13 01 00.80	−32 26 29.2	A94	56	5109	269	0.166	0.316
N4905	13 01 30.53	−30 52 03.0	A94	33	5306	225	0.176	0.308
N4905	13 01 30.53	−30 52 03.0	A94	44	5291	232	0.183	0.316
I3986	13 01 32.63	−32 17 07.9	A94	60	4606	257	0.170	0.320
N4926	13 01 54.45	+27 37 28.8	I95	18	7886	274	0.167	0.311
N4926	13 01 54.45	+27 37 28.8	I97A	36	7887	282	0.184	0.313
E382-002	13 03 01.12	−32 50 06.2	A95A	40	4841	200	0.168	0.302
E382-002	13 03 01.12	−32 50 06.2	A94	42	4844	200	0.170	0.301
E382-002	13 03 01.12	−32 50 06.2	A94	52	4846	211	0.171	0.305
A3537:SMC-130	13 03 11.14	−31 38 23.0	A95A	31	15886	148	0.124	0.234
E382-011	13 07 42.61	−33 33 31.6	A94	19	14073	113	0.107	0.215
A3542:SMC-94	13 08 41.52	−34 34 31.3	A94	43	10461	277	0.186	0.333

(*Continued*)

Identification	R.A. (J2000)	Dec. (J2000)	Source	S/N	$cz_{\odot}$	σ	Mgb'	Mg$_2$
A3542:SMC-41	13 11 30.69	−34 18 14.7	A94	28	26691	259	0.158	0.000
A3542:SMC-86	13 12 07.15	−34 35 44.9	A94	29	3155	57	0.103	0.186
A3542:SMC-32	13 13 57.54	−33 55 03.4	A94	41	15342	197	0.151	0.278
A3542:SMC-31	13 14 04.35	−33 53 20.3	A94	34	14867	192	0.180	0.308
A3542:SMC-31C	13 14 06.86	−33 53 10.2	A94	32	14832	193	0.171	0.293
A3542:SMC-30	13 14 09.02	−33 48 34.2	A94	27	15557	189	0.158	0.277
E382-024	13 15 21.75	−34 56 02.5	A94	50	7939	220	0.147	0.263
A1736:D-144	13 25 51.13	−26 45 03.1	A94	21	10089	103	0.087	0.167
A1736:D-144	13 25 51.13	−26 45 03.1	A94	21	10110	93	0.110	0.188
A1736:D-137	13 26 11.01	−26 49 35.6	A94	40	10016	196	0.171	0.281
E509-008	13 26 44.11	−27 26 23.7	A95A	40	10523	308	0.178	0.296
E509-008	13 26 44.11	−27 26 23.7	A95A	62	10555	303	0.168	0.292
A1736:D-039	13 27 02.69	−27 26 07.8	A94	18	10159	118	0.141	0.258
A1736:D-039	13 27 02.69	−27 26 07.8	A94	23	10168	140	0.137	0.282
A1736:D-039	13 27 02.69	−27 26 07.8	A95A	32	10168	138	0.136	0.243
A1736:D-028	13 27 27.34	−27 29 25.8	A94	26	10128	146	0.140	0.267
A1736:D-028	13 27 27.34	−27 29 25.8	A94	27	10135	147	0.161	0.284
E509-016	13 27 35.82	−27 02 37.3	A95A	39	10807	206	0.172	0.274
A1736:D-051	13 28 03.35	−27 21 30.6	A94	27	10646	235	0.177	0.284
A1736:D-051	13 28 03.35	−27 21 30.6	A95A	28	10669	230	0.168	0.275
A1736:D-051	13 28 03.35	−27 21 30.6	A94	28	10684	239	0.172	0.278
A1736:D-051	13 28 03.35	−27 21 30.6	A95A	36	10672	245	0.169	0.283
A1736:D-005	13 28 07.69	−27 46 27.5	A95A	32	10109	152	0.156	0.254
N5193	13 31 53.33	−33 14 04.4	A95A	41	3711	209	0.165	0.306
E383-038	13 36 18.25	−33 13 35.6	A95A	40	7395	146	0.119	0.207
I4296	13 36 39.37	−33 57 59.5	A95A	42	3780	338	0.183	0.340
I4296	13 36 39.37	−33 57 59.5	A95A	51	3737	335	0.186	0.340
E383-049	13 38 02.99	−33 52 26.5	A95A	32	3858	76	0.129	0.225
A3570:SMC-71C2	13 43 28.15	−38 11 13.6	A95A	18	10605	125	0.134	0.246
E325-004	13 43 33.36	−38 10 30.5	A95A	37	10179	332	0.172	0.322
E325-004	13 43 33.36	−38 10 30.5	A95A	51	10164	310	0.174	0.317
A3570:SMC-64	13 44 00.44	−38 17 11.6	A95A	31	9637	117	0.143	0.243
A3570:SMC-64	13 44 00.44	−38 17 11.6	A95A	34	9655	129	0.155	0.262
A3570:SMC-60	13 44 18.65	−39 11 19.1	A95A	26	11537	246	0.170	0.296
A3570:SMC-60	13 44 18.65	−39 11 19.1	A95A	36	11534	268	0.178	0.304
E325-013	13 45 17.41	−38 10 23.2	A95A	33	11225	218	0.170	0.268
E325-013	13 45 17.41	−38 10 23.2	A95A	37	11214	201	0.162	0.283
A3570:SMC-50	13 45 46.12	−37 56 46.2	A95A	21	12213	181	0.163	0.231
A3570:SMC-50	13 45 46.12	−37 56 46.2	A95A	30	12212	186	0.166	0.253
A3570:SMC-50	13 45 46.12	−37 56 46.2	A95A	37	12216	181	0.147	0.255
A3570:SMC-105	13 46 01.07	−37 19 57.8	A95A	41	15731	155	0.143	0.246
E325-016	13 46 24.16	−37 58 14.8	A95A	33	11316	251	0.159	0.291
E325-016	13 46 24.16	−37 58 14.8	A95A	49	11309	276	0.167	0.290
A3571:SMC-44	13 47 00.73	−33 16 48.8	A95A	31	10580	151	0.155	0.266
A3571:SMC-40	13 47 16.47	−32 49 00.4	A95A	27	10793	126	0.150	0.250
E445-028	13 47 17.74	−29 48 33.3	A94	51	4550	212	0.176	0.308
A3574:W-024	13 47 23.34	−30 25 01.0	A94	47	4310	198	0.142	0.262
A3571:SMC-187	13 47 28.42	−32 51 51.8	A95A	30	11570	308	0.182	0.302
A3571:SMC-187	13 47 28.42	−32 51 51.8	A95A	35	11567	297	0.166	0.311
A3571:SMC-38	13 47 30.94	−33 35 18.8	A95A	38	11269	317	0.184	0.303

(Continued)

Identification	R.A. (J2000)	Dec. (J2000)	Source	S/N	$cz_\odot$	σ	Mgb'	Mg$_2$
A3571:SMC-32	13 47 37.28	−32 45 04.7	A95A	40	11589	228	0.171	0.298
A3571:SMC-29	13 47 48.91	−33 17 25.4	A95A	33	12297	164	0.157	0.251
A3571:SMC-27	13 47 53.10	−32 59 03.2	A95A	31	11188	225	0.170	0.282
A3571:SMC-171	13 48 06.14	−32 30 31.7	A95A	40	11717	215	0.173	0.282
A3571:SMC-21	13 48 14.26	−33 22 57.8	A95A	40	12210	217	0.168	0.271
A3571:SMC-21	13 48 14.26	−33 22 57.8	A95A	47	12205	222	0.167	0.270
A3574:W-033	13 48 14.68	−30 33 03.5	A94	51	4271	121	0.125	0.211
A3570:SMC-27	13 48 33.26	−37 54 30.8	A95A	20	16976	262	0.178	0.285
E445-040	13 48 38.64	−30 48 37.7	A94	27	5068	132	0.145	0.261
E445-042	13 48 48.92	−31 09 18.4	A94	35	5155	126	0.134	0.246
A3571:SMC-13	13 48 58.08	−32 51 26.1	A95A	43	11646	234	0.170	0.290
I4329	13 49 05.17	−30 17 43.7	A95A	34	4539	273	0.185	0.334
I4329	13 49 05.17	−30 17 43.7	A94	52	4573	274	0.188	0.336
I4329	13 49 05.17	−30 17 43.7	A94	61	4564	266	0.187	0.333
A3570:SMC-24	13 49 17.97	−38 26 55.4	A95A	31	10360	210	0.164	0.285
A3571:SMC-10	13 49 25.59	−33 36 50.1	A95A	34	11604	184	0.114	0.210
A3571:SMC-164	13 49 45.42	−32 22 52.4	A95A	38	11011	268	0.154	0.268
N5304	13 50 01.41	−30 34 42.0	A95A	23	3723	220	0.163	0.272
N5304	13 50 01.41	−30 34 42.0	A95A	25	3718	211	0.177	0.296
N5304	13 50 01.41	−30 34 42.0	A94	48	3718	199	0.178	0.289
A3571:SMC-114	13 51 33.66	−32 49 49.8	A95A	32	12525	113	0.101	0.161
E445-059	13 51 39.47	−30 29 21.7	A94	47	4554	187	0.161	0.287
A3571:SMC-112	13 52 38.36	−32 53 17.3	A95A	40	11148	241	0.170	0.286
A3571:SMC-112	13 52 38.36	−32 53 17.3	A95A	41	11162	244	0.164	0.298
E445-065	13 52 45.63	−29 55 45.4	A94	45	4776	145	0.139	0.256
N5328	13 52 53.63	−28 29 16.1	A94	66	4740	314	0.177	0.325
N5357	13 55 59.42	−30 20 27.8	A94	52	4868	200	0.152	0.264
E510-023	13 57 16.06	−25 23 25.3	A95A	41	11344	221	0.171	0.267
A3578:SMC-115	13 57 17.44	−24 48 37.0	A95A	31	13190	177	0.157	0.251
A3578:SMC-36	13 57 21.12	−24 13 52.7	A95A	39	11005	180	0.132	0.256
E510-034	13 59 41.98	−25 22 41.7	A95A	36	11364	170	0.121	0.230
E510-044	14 01 37.77	−26 25 54.5	A94	50	6680	83	0.122	0.212
E510-053	14 03 35.68	−25 25 41.2	A94	33	6749	174	0.130	0.213
E510-054	14 04 03.31	−26 12 57.2	A94	33	6057	176	0.154	0.256
E510-054	14 04 03.31	−26 12 57.2	A94	42	6024	172	0.133	0.247
E510-054	14 04 03.31	−26 12 57.2	A95A	58	6023	180	0.140	0.253
E510-063	14 06 16.07	−25 47 57.2	A94	35	6966	249	0.170	0.322
E510-066	14 07 15.62	−27 09 30.9	A94	37	7304	211	0.168	0.294
E510-066	14 07 15.62	−27 09 30.9	A95A	47	7295	226	0.171	0.294
A3581:SMC-78	14 07 16.96	−26 32 59.9	A94	47	6005	201	0.158	0.286
A3581:SMC-77	14 07 20.92	−27 00 38.8	A95A	24	5969	171	0.158	0.289
A3581:SMC-77	14 07 20.92	−27 00 38.8	A95A	24	5964	180	0.187	0.312
I4374	14 07 29.76	−27 01 04.2	A94	33	6546	246	0.196	0.335
I4374	14 07 29.76	−27 01 04.2	A95A	43	6535	265	0.190	0.313
A3581:SMC-76	14 07 35.17	−27 02 07.2	A94	34	5903	126	0.149	0.271
A3581:SMC-75	14 07 44.13	−27 04 58.8	A95A	50	6489	198	0.162	0.278
E511-023	14 18 26.58	−27 22 43.1	A94	41	6788	238	0.174	0.299
N5846	15 06 28.73	+01 36 15.6	A95A	38	1717	236	0.172	0.330
N5846	15 06 28.73	+01 36 15.6	A95A	42	1708	230	0.188	0.334
A2052:SMC-M13	15 15 51.37	+07 01 00.9	A95A	19	10183	145	0.133	0.218

(Continued)

Identification	R.A. (J2000)	Dec. (J2000)	Source	S/N	$cz_{\odot}$	σ	Mgb'	Mg$_2$
A3744:SMC-Q	21 06 03.73	−26 10 29.1	A95B	19	11991	172	0.128	0.285
A3744:SMC-Q	21 06 03.73	−26 10 29.1	A95B	23	11981	164	0.146	0.275
E286-049	21 06 47.51	−47 11 16.8	A95B	48	5295	198	0.174	0.305
N7016	21 07 16.19	−25 28 08.4	A95B	36	11047	278	0.166	0.321
N7016	21 07 16.19	−25 28 08.4	A95B	40	11046	270	0.178	0.326
A3744:SMC-E	21 07 22.08	−25 27 20.2	A95B	24	11388	243	0.165	0.283
A3744:SMC-I	21 07 32.35	−25 38 34.7	A95B	33	12276	183	0.127	0.254
N7014	21 07 52.25	−47 10 46.6	A95B	63	4857	291	0.186	0.332
A3747:SMC-C	21 07 54.55	−43 15 43.7	A95B	32	9161	194	0.166	0.294
A3744:SMC-V	21 08 09.95	−26 24 13.8	A95B	32	10433	217	0.157	0.298
E286-059	21 08 39.33	−43 29 08.9	A95B	35	9363	227	0.171	0.296
E286-060	21 08 56.98	−43 41 10.0	A95B	34	9131	226	0.161	0.270
N7454	23 01 06.61	+16 23 23.9	I97A	17	2028	130	0.152	0.228
N7454	23 01 06.61	+16 23 23.9	I97A	22	2032	120	0.150	0.220
N7562	23 15 57.36	+06 41 15.7	I97A	35	3613	248	0.157	0.289
N7562	23 15 57.36	+06 41 15.7	A95B	36	3609	229	0.143	0.270
N7619	23 20 14.68	+08 12 23.2	I97A	26	3806	335	0.180	0.346
N7619	23 20 14.68	+08 12 23.2	A95B	42	3789	296	0.195	0.331
N7626	23 20 42.29	+08 13 02.5	A95B	32	3433	262	0.171	0.312
N7626	23 20 42.29	+08 13 02.5	I97A	35	3407	274	0.184	0.345
A2657:D-015	23 43 42.27	+08 59 31.2	I97A	16	10721	199	0.173	0.256
A2657:D-015	23 43 42.27	+08 59 31.2	I97A	16	10731	161	0.138	0.275
A2657:D-031	23 44 16.10	+09 02 56.3	I97A	19	11877	257	0.168	0.331
A2657:D-031	23 44 16.10	+09 02 56.3	I97A	19	11900	244	0.193	0.329
A2657:D-072	23 44 27.78	+09 16 00.2	I97A	21	12608	180	0.175	0.277
A2657:D-071	23 44 30.50	+09 15 48.2	I97A	23	12359	261	0.163	0.276
A2657:D-070	23 44 43.91	+09 12 55.2	I97A	25	12399	210	0.134	0.259
A2657:D-043	23 44 56.41	+09 07 53.6	I97A	15	11940	273	0.155	0.267
A2657:D-043	23 44 56.41	+09 07 53.6	I97A	20	11960	215	0.141	0.285
A2657:D-064	23 45 17.21	+09 16 15.8	I97A	25	12288	236	0.190	0.319
I5353	23 47 28.59	−28 06 34.1	A95B	48	8240	247	0.176	0.314
A4038:D-055	23 47 31.76	−28 06 25.5	A95B	33	8461	176	0.160	0.286
A4038:D-043	23 47 43.17	−28 08 38.1	A95B	34	8118	186	0.135	0.260
I5358	23 47 45.03	−28 08 26.7	A95B	39	8646	205	0.177	0.321
A4049:D-047	23 51 34.80	−28 04 28.6	A95B	29	9693	254	0.174	0.345
I5362	23 51 36.62	−28 21 52.9	A95B	37	8256	249	0.161	0.294
I5362	23 51 36.62	−28 21 52.9	A95B	41	8288	270	0.160	0.301
A4049:D-055	23 51 54.37	−27 55 48.0	A95B	34	8772	224	0.161	0.297
A4049:SMC-E	23 52 10.10	−29 04 41.5	A95B	38	8684	197	0.153	0.286
A4049:SMC-E	23 52 10.10	−29 04 41.5	A95B	45	8692	204	0.162	0.284
A4049:SMC-D	23 52 24.15	−29 01 22.3	A95B	34	8657	206	0.155	0.274
A4049:SMC-D	23 52 24.15	−29 01 22.3	A95B	52	8677	221	0.165	0.289

Table A.2: New photometric data from the SMAC project. See text of Appendix A for details.

Identification	R.A. (J2000)	Dec. (J2000)	run	R_{20}	A_B^{BH}	A_B^{SFD}	psf	$\log A_e$	SB_e	rms
A0076:D-016	00 39 36.63	+06 39 54.2	J97	21.46	0.07	0.14	1.8	1.178	20.56	0.01
A0076:D-018	00 39 15.62	+06 41 21.5	J97	21.72	0.06	0.16	1.9	1.155	19.99	0.01
A2806:SMC-C	00 40 04.23	−56 10 50.2	C94B	21.81	−0.07	0.06	1.8	1.202	19.60	0.01
A2806:SMC-C	00 40 04.23	−56 10 50.2	C94B	21.82	−0.07	0.06	1.7	1.215	19.63	0.01
A2806:SMC-D	00 40 24.59	−56 13 22.9	C94B	21.65	−0.07	0.07	1.7	1.025	19.69	0.03
A2806:SMC-D	00 40 24.59	−56 13 22.9	C94B	21.65	−0.07	0.07	1.8	1.006	19.62	0.03
A2806:SMC-E	00 40 43.21	−55 55 46.9	C94B	22.04	−0.07	0.05	1.5	0.967	19.31	0.01
A2806:SMC-F	00 37 56.94	−56 03 43.4	C94B	21.87	−0.08	0.06	1.5	0.978	19.56	0.01
A2806:SMC-G	00 41 21.60	−56 09 40.9	C94B	22.04	−0.07	0.08	1.8	0.850	18.97	0.03
A2806:SMC-I	00 43 45.89	−56 27 19.0	C94B	21.38	−0.05	0.08	1.4	1.217	20.93	0.01
A2806:SMC-K	00 40 06.57	−56 09 29.2	C94B	21.90	−0.07	0.06	1.8	1.026	19.77	0.05
A2806:SMC-K	00 40 06.57	−56 09 29.2	C94B	21.94	−0.07	0.06	1.7	1.011	19.72	0.05
I1565	00 39 26.27	+06 44 03.3	J97	21.54	0.06	0.18	1.8	1.522	20.34	0.04
I1565	00 39 26.27	+06 44 03.3	J97	21.54	0.06	0.18	1.9	1.461	20.17	0.02
I1566	00 39 33.35	+06 48 54.5	J97	21.70	0.06	0.18	2.0	1.286	19.90	0.01
I1568	00 39 55.96	+06 50 54.9	J97	21.43	0.06	0.17	1.8	1.414	20.49	0.06
I1569	00 40 28.02	+06 43 10.9	J97	21.60	0.08	0.12	1.6	1.248	20.16	0.03
N0212	00 40 13.31	−56 09 10.8	C94B	21.33	−0.07	0.06	1.8	1.699	21.24	0.01
N0212	00 40 13.31	−56 09 10.8	C94B	21.34	−0.07	0.06	1.7	1.694	21.22	0.01
N0215	00 40 48.93	−56 12 51.1	C94B	21.83	−0.06	0.07	1.7	1.314	19.42	0.01
N0215	00 40 48.93	−56 12 51.1	C94B	21.84	−0.06	0.07	1.8	1.319	19.43	0.01
A0189:SMC-A	01 23 26.33	+01 42 17.8	C94B	21.83	0.03	0.13	1.7	1.174	19.58	0.01
A0189:SMC-B	01 23 23.75	+01 39 02.6	C94B	21.50	0.03	0.13	1.7	1.058	20.01	0.05
A0189:SMC-C	01 23 23.69	+01 46 03.6	C94B	21.77	0.03	0.13	1.7	1.062	19.96	0.02
A0189:SMC-D	01 22 36.84	+01 53 27.8	C94B	22.16	0.02	0.12	1.5	1.027	19.46	0.07
A0189:SMC-G	01 25 17.91	+01 46 11.7	C94B	22.31	0.02	0.12	1.7	0.789	18.59	0.02
A0189:SMC-H	01 25 04.53	+01 42 32.4	C94B	21.72	0.02	0.11	1.7	0.950	19.56	0.03
A0189:SMC-I	01 24 58.92	+01 33 23.2	J97	21.38	0.02	0.11	1.1	1.359	21.25	0.02
A0189:SMC-J	01 24 43.94	+01 22 01.6	J97	21.64	0.02	0.12	1.2	1.054	20.10	0.01
A0189:SMC-K	01 24 22.85	+01 45 00.3	J97	21.66	0.02	0.13	0.9	1.093	20.04	0.02
A0260:EFR-E	01 49 12.88	+33 05 44.8	J97	21.66	0.13	0.17	1.3	1.290	20.05	0.05
A0260:EFR-G	01 51 45.53	+33 32 14.1	J97	21.61	0.15	0.17	1.1	1.327	20.26	0.02
A0260:SMC-1	01 50 32.13	+33 02 49.7	J97	21.84	0.14	0.18	0.9	1.041	19.59	0.05
A0260:SMC-D	01 51 21.29	+33 11 11.2	J97	21.43	0.14	0.20	1.0	1.372	21.01	0.03
A0262:B-042	01 50 14.75	+36 13 43.5	J97	21.64	0.19	0.25	1.5	1.140	20.16	0.02
A2911:SMC-C	01 26 23.43	−38 35 40.0	C94B	21.93	0.00	0.09	1.6	1.213	19.53	0.01
A2911:SMC-D	01 25 32.37	−38 17 02.5	C94B	22.28	0.00	0.09	1.6	0.850	18.44	0.02
A2911:SMC-F	01 26 42.73	−37 12 22.8	C94B	21.98	0.00	0.06	2.0	0.804	18.91	0.02
I0103	01 24 36.44	+02 02 39.3	C94B	21.96	0.05	0.14	1.5	1.128	19.14	0.02
I1733	01 50 43.02	+33 04 54.4	J97	21.51	0.14	0.19	0.9	1.512	20.26	0.03
N0533	01 25 31.36	+01 45 32.8	C94B	21.41	0.02	0.13	1.7	1.934	20.85	0.02
N0534	01 24 44.66	−38 07 44.5	C94B	21.60	0.00	0.08	1.5	1.352	19.74	0.04
N0534	01 24 44.66	−38 07 44.5	C94B	21.60	0.00	0.08	1.5	1.356	19.76	0.04
N0544	01 25 12.01	−38 05 37.6	C94B	21.87	0.00	0.08	1.5	1.234	19.21	0.03
N0584	01 31 21.01	−06 52 16.1	C94B	22.06	0.12	0.17	1.4	1.668	18.64	0.01
N0596	01 32 52.08	−07 01 54.6	C94B	21.78	0.12	0.15	1.5	1.570	18.80	0.03
N0679	01 49 43.79	+35 47 06.8	J97	21.87	0.16	0.25	1.5	1.450	19.27	0.01
N0732	01 56 27.68	+36 48 03.6	J97	21.85	0.21	0.34	1.6	1.266	19.61	0.03
A0400:D-017	02 59 48.58	+05 44 33.1	J97	21.96	0.28	0.46	1.2	0.901	19.27	0.01

(Continued)

Identification	R.A. (J2000)	Dec. (J2000)	run	R_{20}	A_B^{BH}	A_B^{SFD}	psf	$\log A_e$	SB_e	rms
A0400:D-041	02 57 47.41	+06 01 39.6	J97	22.45	0.29	0.72	1.0	0.791	18.48	0.03
A0400:D-044	02 57 33.67	+05 58 36.9	J97	22.15	0.28	0.75	1.4	1.030	18.80	0.01
A0400:D-052	02 57 37.45	+06 02 50.1	J97	22.27	0.29	0.72	1.0	0.809	18.92	0.03
A0400:D-057	02 58 54.22	+06 06 59.6	J97	21.56	0.29	0.63	1.1	1.213	20.37	0.01
A0400:D-058	02 58 21.02	+06 05 42.5	J97	21.73	0.30	0.66	0.9	1.240	19.74	0.02
A0400:D-070	02 55 14.85	+06 10 39.3	J97	21.71	0.27	0.91	1.0	1.260	20.10	0.02
A0400:D-089	02 58 24.58	+06 35 30.5	J97	21.57	0.31	0.93	1.5	1.548	20.46	0.01
N0936	02 27 37.67	−01 09 17.2	C94B	21.41	0.00	0.14	1.9	1.779	19.71	0.02
A0426:PP-P26	03 20 00.69	+41 33 49.7	J97	22.35	0.69	0.66	1.4	0.878	18.21	0.01
A3193:SMC-B	03 58 12.49	−52 27 09.5	C94B	21.79	−0.08	0.05	1.5	0.986	19.58	0.02
A3193:SMC-B	03 58 12.49	−52 27 09.5	C94B	21.80	−0.08	0.05	1.8	0.971	19.52	0.02
A3193:SMC-C	03 58 28.42	−52 21 52.0	C94B	21.35	−0.08	0.05	1.8	1.270	20.80	0.05
A3193:SMC-F	03 56 40.80	−51 33 28.0	C94B	21.52	−0.08	0.06	1.3	1.248	20.17	0.03
A3193:SMC-G	03 59 14.08	−51 32 56.4	C94B	21.70	−0.08	0.05	1.2	1.022	19.86	0.02
N1272	03 19 21.30	+41 29 26.7	J97	21.35	0.67	0.65	1.5	1.803	20.44	0.03
N1273	03 19 26.79	+41 32 25.4	J97	21.98	0.67	0.66	1.5	1.293	18.96	0.02
N1278	03 19 54.15	+41 33 47.9	J97	21.76	0.69	0.66	1.4	1.671	20.04	0.01
N1500	03 58 13.96	−52 19 43.8	C94B	21.60	−0.08	0.05	1.5	1.404	20.10	0.03
N1500	03 58 13.96	−52 19 43.8	C94B	21.60	−0.08	0.05	1.8	1.392	20.05	0.03
A0496:D-046	04 33 37.84	−13 15 43.0	J97	21.18	0.10	0.57	1.3	1.942	21.73	0.01
A3193:SMC-H	04 00 15.54	−51 57 30.9	C94B	21.97	−0.08	0.05	1.6	0.977	19.49	0.03
A3193:SMC-I	04 03 03.74	−52 44 22.9	C94B	21.60	−0.08	0.04	1.2	1.195	20.35	0.02
N1506	04 00 21.28	−52 34 26.6	C94B	21.56	−0.08	0.06	1.4	1.433	20.25	0.03
A0539:D-042	05 16 49.45	+06 23 20.5	C94B	21.69	0.49	0.67	1.5	1.043	19.73	0.04
A0539:D-044	05 16 28.86	+06 24 08.9	C94B	22.11	0.49	0.64	1.5	1.020	19.12	0.01
A0539:D-047	05 16 37.33	+06 26 27.3	C94B	21.23	0.49	0.68	1.3	1.774	21.68	0.05
A0539:D-049	05 16 37.15	+06 26 53.0	C94B	22.30	0.49	0.68	1.3	0.908	18.82	0.03
A0539:D-050	05 16 37.01	+06 27 06.4	C94B	21.89	0.49	0.68	1.3	1.183	19.72	0.10
A0539:D-063	05 16 35.68	+06 30 13.4	C94B	22.01	0.49	0.71	1.2	1.052	19.13	0.01
A0539:D-068	05 16 55.12	+06 33 09.5	C94B	21.70	0.50	0.77	1.5	1.386	19.73	0.03
A3381:D-021	06 09 32.97	−33 50 30.7	C95	21.78	0.03	0.14	1.8	0.952	19.72	0.02
A3381:D-025	06 06 47.50	−33 48 54.6	C95	21.57	−0.07	0.15	1.7	1.403	20.36	0.02
A3381:D-055	06 09 54.49	−33 35 33.2	C95	21.42	0.02	0.15	1.8	1.494	20.95	0.01
A3381:D-056	06 09 49.29	−33 35 47.8	C95	21.75	0.02	0.15	1.8	1.120	20.03	0.04
A3389:D-043	06 21 13.85	−65 00 59.4	C94B	21.88	0.17	0.30	1.3	1.144	19.81	0.02
A3389:D-043	06 21 13.85	−65 00 59.4	C94B	21.91	0.17	0.30	2.3	1.073	19.55	0.01
A3389:D-048	06 23 48.97	−64 57 17.1	C94B	21.98	0.17	0.25	1.4	0.972	19.37	0.02
A3389:D-049	06 23 07.44	−64 55 52.0	C94B	22.31	0.17	0.28	1.3	0.817	18.65	0.01
A3389:D-053	06 22 04.85	−64 57 37.9	C94B	22.01	0.17	0.31	1.2	0.898	19.45	0.03
A3389:D-053	06 22 04.85	−64 57 37.9	C94B	22.01	0.17	0.31	2.3	0.963	19.66	0.05
A3389:D-053	06 22 04.85	−64 57 37.9	C94B	22.03	0.17	0.31	1.4	0.955	19.62	0.05
A3389:D-060	06 22 19.57	−64 14 08.8	C94B	22.08	0.15	0.21	1.3	1.130	18.93	0.01
A3389:D-070	06 25 28.82	−64 44 30.6	C94B	21.85	0.16	0.20	2.0	0.981	19.74	0.03
N2230	06 21 27.47	−64 59 37.2	C94B	21.60	0.17	0.31	1.3	1.548	20.14	0.02
N2230	06 21 27.47	−64 59 37.2	C94B	21.61	0.17	0.31	2.3	1.535	20.09	0.02
N2235	06 22 22.04	−64 56 05.5	C94B	21.53	0.17	0.31	1.4	1.738	20.66	0.02
N2235	06 22 22.04	−64 56 05.5	C94B	21.53	0.17	0.31	2.3	1.739	20.66	0.01
N2235	06 22 22.04	−64 56 05.5	C94B	21.54	0.17	0.31	1.2	1.740	20.68	0.02
A0569:SMC-B	07 13 54.02	+50 23 54.4	J95	21.82	0.29	0.27	2.1	1.248	19.40	0.03
A0569:SMC-G	07 08 24.18	+50 08 11.7	J95	22.05	0.28	0.32	1.9	0.950	18.82	0.03
A0569:SMC-L	07 09 44.85	+48 41 25.7	J97	21.82	0.28	0.28	1.3	1.143	19.61	0.03

(Continued)

Identification	R.A. (J2000)	Dec. (J2000)	run	R_{20}	A_B^{BH}	A_B^{SFD}	psf	$\log A_e$	SB_e	rms
A0569:SMC-N	07 07 59.60	+48 39 58.7	J97	21.82	0.30	0.27	1.1	1.228	19.20	0.05
A0569:SMC-Q	07 06 40.14	+48 29 24.5	J97	21.86	0.32	0.30	1.4	1.213	19.36	0.03
A0569:SMC-R	07 08 52.74	+48 27 00.0	J97	21.82	0.30	0.31	1.3	1.382	20.12	0.04
A0576:SMC-A	07 21 36.44	+56 10 16.5	J95	21.84	0.16	0.27	2.1	0.984	19.70	0.03
A0576:SMC-B	07 20 20.43	+55 53 11.3	J95	21.92	0.15	0.31	1.8	1.055	19.71	0.07
A0576:SMC-C	07 21 19.42	+55 48 38.2	J95	21.44	0.15	0.30	2.3	1.494	20.85	0.06
A0576:SMC-D	07 21 21.55	+55 47 52.1	J95	21.65	0.15	0.30	2.3	1.239	20.11	0.05
A0576:SMC-D	07 21 21.55	+55 47 52.1	J97	21.77	0.15	0.30	0.9	1.167	19.90	0.07
A0576:SMC-E1	07 21 32.06	+55 45 24.5	J97	21.61	0.15	0.30	0.9	1.318	20.36	0.01
A0576:SMC-E2	07 21 29.64	+55 45 39.2	J97	21.49	0.15	0.30	0.9	1.204	19.99	0.02
A0576:SMC-G	07 21 43.96	+55 40 42.8	J97	21.62	0.16	0.32	0.9	1.228	19.97	0.02
A0576:SMC-I	07 19 28.53	+55 36 31.8	J95	21.74	0.15	0.34	2.2	1.154	19.95	0.01
A0576:SMC-J	07 25 48.27	+55 29 40.7	J95	21.79	0.16	0.30	2.2	1.137	20.41	0.08
I0458	07 10 34.01	+50 07 06.3	J95	21.89	0.26	0.35	2.2	1.266	19.20	0.03
I0461	07 10 45.03	+50 04 51.5	J95	21.44	0.25	0.32	2.2	1.324	20.53	0.03
I0464	07 11 04.79	+50 08 11.2	J97	21.88	0.25	0.32	1.3	1.205	19.38	0.01
N2329	07 09 08.01	+48 36 55.5	J95	21.57	0.29	0.29	2.0	1.666	20.17	0.01
N2330	07 09 28.40	+50 09 09.1	J97	21.77	0.27	0.35	1.3	1.046	19.53	0.03
N2332	07 09 34.20	+50 10 54.5	J97	21.70	0.27	0.35	1.3	1.442	19.49	0.03
N2340	07 11 10.84	+50 10 27.7	J97	21.24	0.26	0.31	1.3	2.042	21.48	0.03
U03696	07 09 23.05	+48 38 07.5	J95	21.97	0.29	0.29	2.0	1.175	18.61	0.01
A0634:SMC-C	08 16 15.09	+58 35 22.1	J97	21.71	0.13	0.25	0.8	0.861	19.65	0.02
A0634:SMC-I	08 09 52.60	+57 54 46.5	J97	22.15	0.08	0.17	0.9	1.058	18.74	0.02
A0634:SMC-J	08 14 20.15	+57 52 26.0	J95	21.82	0.11	0.21	1.6	0.953	19.60	0.02
A0634:SMC-J	08 14 20.15	+57 52 26.0	J97	21.82	0.11	0.21	0.9	1.026	19.87	0.04
A0779:SMC-G	09 19 52.28	+33 38 57.7	J97	22.00	−0.03	0.06	1.0	0.858	19.24	0.01
U04974	09 22 10.38	+33 50 54.6	J97	21.82	−0.02	0.07	1.1	1.323	19.55	0.02
A0999:SMC-C	10 23 22.53	+13 05 34.9	C95	21.70	0.10	0.20	2.3	0.968	19.74	0.05
A0999:SMC-D	10 23 23.85	+12 50 05.8	C95	21.71	0.10	0.16	1.9	1.342	19.80	0.03
A0999:SMC-D	10 23 23.85	+12 50 05.8	J97	21.68	0.10	0.16	1.4	1.372	19.87	0.03
A0999:SMC-F	10 23 43.10	+12 42 55.8	C95	22.06	0.09	0.15	1.9	0.988	18.93	0.02
A0999:SMC-G	10 25 06.66	+12 24 52.8	C95	21.86	0.08	0.14	1.7	0.936	19.54	0.01
A1016:SMC-A	10 30 00.79	+11 08 18.2	C95	21.61	0.08	0.14	1.7	0.891	19.87	0.02
A1016:SMC-B	10 27 05.83	+11 03 16.8	J95	21.89	0.04	0.12	1.7	1.160	19.74	0.01
A1016:SMC-C	10 27 10.58	+11 01 15.8	J95	21.99	0.04	0.13	1.7	0.777	19.08	0.01
A1016:SMC-E	10 26 36.48	+10 56 06.4	J95	21.77	0.03	0.13	1.9	1.055	19.91	0.01
A1016:SMC-F	10 26 23.50	+10 55 06.2	J95	21.62	0.03	0.13	1.9	1.175	20.11	0.01
A1016:SMC-G	10 27 42.58	+10 49 28.1	C95	21.51	0.04	0.13	1.7	1.010	20.47	0.01
A1016:SMC-G	10 27 42.58	+10 49 28.1	J97	21.46	0.04	0.13	1.5	1.039	20.60	0.01
A1139:D-016	10 58 38.93	+01 22 55.0	C95	21.51	0.07	0.11	1.3	1.172	20.81	0.02
A1139:D-016	10 58 38.93	+01 22 55.0	C95	21.53	0.07	0.11	1.4	1.127	20.62	0.01
A1139:D-016	10 58 38.93	+01 22 55.0	C95	21.55	0.07	0.11	1.8	1.110	20.55	0.01
A1139:D-029	10 57 43.29	+01 34 01.1	C95	21.74	0.06	0.12	1.6	1.101	19.86	0.02
A1139:D-030	10 57 01.60	+01 33 59.9	C95	21.91	0.06	0.13	1.6	0.920	19.42	0.01
A1139:D-036	10 58 15.23	+01 36 56.9	C95	22.07	0.06	0.12	1.7	0.853	18.76	0.03
A1139:D-036	10 58 15.23	+01 36 56.9	C95	22.09	0.06	0.12	1.4	0.822	18.62	0.04
A1139:D-037	10 58 13.10	+01 36 24.5	C95	21.95	0.06	0.12	1.4	1.054	19.61	0.05
A1139:D-037	10 58 13.10	+01 36 24.5	C95	22.02	0.06	0.12	1.7	0.969	19.26	0.02
A1139:D-038	10 58 13.70	+01 36 07.5	C95	21.68	0.06	0.12	1.4	0.795	19.94	0.01
A1139:D-039	10 58 11.02	+01 36 15.4	C95	21.54	0.06	0.12	1.7	1.407	20.37	0.02
A1139:D-039	10 58 11.02	+01 36 15.4	C95	21.55	0.06	0.12	1.4	1.387	20.33	0.02

(Continued)

Identification	R.A. (J2000)	Dec. (J2000)	run	R_{20}	A_B^{BH}	A_B^{SFD}	psf	$\log A_e$	SB_e	rms
A1139:D-041	10 57 32.91	+01 37 16.3	C95	21.95	0.06	0.13	1.7	0.781	19.46	0.01
A1139:D-041	10 57 32.91	+01 37 16.3	C95	21.97	0.06	0.13	1.5	0.766	19.39	0.01
A1142:SMC-C	10 57 42.28	+10 36 22.5	C95	21.84	0.01	0.10	2.0	1.034	20.03	0.05
I0613	10 27 07.79	+11 00 38.5	J95	21.70	0.04	0.13	1.7	1.307	19.82	0.04
I0660	10 58 26.67	+01 22 57.9	C95	21.72	0.07	0.12	1.4	1.211	19.97	0.01
I0660	10 58 26.67	+01 22 57.9	C95	21.73	0.07	0.12	1.8	1.208	19.96	0.02
I0661	10 58 51.49	+01 39 02.2	C95	21.39	0.07	0.11	1.6	1.435	20.85	0.01
I0662	10 59 20.55	+01 35 55.3	C95	21.83	0.08	0.12	1.6	1.129	19.67	0.02
A1139:D-053	11 00 01.90	+01 46 33.8	C95	21.29	0.12	0.13	1.6	1.398	20.86	0.03
A1142:D-015	11 00 44.39	+10 04 17.9	C95	22.00	0.01	0.12	2.0	0.844	19.53	0.03
A1142:D-020	11 02 21.36	+10 14 35.8	C95	21.72	0.01	0.12	1.9	1.213	19.94	0.01
A1142:D-046	11 00 48.35	+10 35 40.5	C95	22.65	0.01	0.12	1.5	0.478	17.83	0.02
A1177:SMC-B	11 10 25.84	+22 06 36.4	J97	21.29	−0.06	0.07	1.0	1.223	20.87	0.06
A1177:SMC-C	11 10 48.19	+22 03 33.0	J95	21.69	−0.06	0.07	1.9	0.913	20.12	0.01
A1177:SMC-F	11 09 41.02	+21 44 23.1	J97	22.17	−0.06	0.07	1.0	0.886	18.88	0.03
A1177:SMC-G	11 09 42.81	+21 44 07.5	J97	22.09	−0.06	0.07	1.0	0.834	19.14	0.02
A1177:SMC-H	11 09 19.73	+21 38 53.4	J95	21.98	−0.06	0.07	1.6	0.743	19.23	0.01
A1177:SMC-I	11 10 34.17	+21 34 46.2	J97	21.78	−0.06	0.07	1.0	0.876	19.47	0.02
A1185:SMC-M	11 16 13.48	+29 13 06.1	J95	21.70	−0.01	0.07	2.1	1.259	19.87	0.01
A1228:SMC-B	11 24 07.46	+34 39 48.6	J95	21.81	0.10	0.09	1.9	1.119	19.74	0.02
A1228:SMC-C	11 23 20.35	+34 39 39.9	J95	21.46	0.05	0.08	1.8	1.262	20.63	0.02
A1228:SMC-G	11 21 26.94	+34 27 09.1	J97	21.98	0.04	0.09	1.2	0.971	19.12	0.01
A1228:SMC-H	11 22 07.30	+34 21 57.6	J95	21.92	0.04	0.10	1.7	1.017	19.29	0.03
A1228:SMC-K	11 22 59.06	+34 17 31.8	J95	21.71	0.04	0.10	1.8	1.141	20.33	0.04
A1228:SMC-M	11 23 24.52	+33 49 44.6	J95	21.78	0.01	0.09	1.8	1.162	19.62	0.04
A1257:SMC-B	11 25 30.88	+35 30 16.2	J97	21.92	0.02	0.09	0.9	1.020	19.00	0.04
A1257:SMC-C	11 23 47.02	+35 26 32.1	J97	21.88	0.01	0.09	1.3	0.711	19.02	0.02
A1257:SMC-C	11 23 47.02	+35 26 32.1	J97	21.91	0.01	0.09	1.0	0.682	18.90	0.02
A1257:SMC-E	11 26 18.38	+35 20 57.4	J97	21.92	0.01	0.10	1.3	0.967	19.45	0.03
A1257:SMC-E	11 26 18.38	+35 20 57.4	J97	21.94	0.01	0.10	0.9	0.993	19.54	0.04
A1257:SMC-G	11 26 17.26	+35 20 24.2	J97	21.68	0.01	0.10	1.3	1.259	20.10	0.03
A1257:SMC-G	11 26 17.26	+35 20 24.2	J97	21.71	0.01	0.10	0.9	1.275	20.16	0.05
A1257:SMC-GC	11 26 15.69	+35 19 42.5	J97	21.84	0.01	0.09	1.3	0.847	19.76	0.02
A1257:SMC-GC	11 26 15.69	+35 19 42.5	J97	21.88	0.01	0.09	0.9	1.027	20.41	0.09
A1314:SMC-A	11 36 30.55	+49 07 52.8	J97	21.64	−0.01	0.07	1.1	1.327	20.12	0.01
A1314:SMC-B	11 32 34.81	+49 06 34.7	J97	21.91	−0.02	0.08	1.1	1.018	19.44	0.01
A1314:SMC-D	11 35 26.29	+49 05 13.4	J97	21.98	−0.02	0.06	1.1	0.801	19.20	0.00
A1314:SMC-G	11 36 36.65	+49 03 46.8	J97	21.80	−0.01	0.07	1.1	1.179	19.74	0.02
A1367:B-020	11 48 03.36	+20 00 22.6	J97	22.01	0.02	0.14	1.4	1.094	19.06	0.01
A1367:B-021	11 45 14.95	+19 50 42.3	J97	21.69	−0.03	0.11	1.4	1.353	20.22	0.01
I0664	11 00 45.39	+10 33 11.6	C95	21.57	0.01	0.12	1.5	1.433	20.24	0.06
I0664	11 00 45.39	+10 33 11.6	C95	22.07	0.01	0.12	1.6	0.996	18.87	0.03
I0708	11 33 59.22	+49 03 43.4	J97	21.68	−0.02	0.08	1.2	1.383	19.85	0.03
I0709	11 34 14.54	+49 02 35.3	J97	21.88	−0.02	0.08	1.1	1.177	19.47	0.03
I0709	11 34 14.54	+49 02 35.3	J97	21.89	−0.02	0.08	1.2	1.161	19.41	0.03
I2738	11 21 23.06	+34 21 24.0	J95	21.71	0.04	0.10	1.7	1.246	19.69	0.03
I2744	11 21 42.48	+34 21 45.9	J95	21.49	0.04	0.09	2.0	1.433	20.66	0.02
I2955	11 45 03.88	+19 37 14.0	J97	21.85	−0.03	0.10	1.5	1.230	19.80	0.05
N3551	11 09 44.44	+21 45 31.7	J97	21.30	−0.06	0.07	1.0	1.742	21.10	0.05
N3554	11 10 47.84	+28 39 36.4	J95	21.89	−0.01	0.12	2.1	1.097	19.38	0.01
N3555	11 09 50.33	+21 48 36.7	J97	22.39	−0.06	0.07	1.0	0.869	18.64	0.02

(Continued)

Identification	R.A. (J2000)	Dec. (J2000)	run	R_{20}	A_B^{BH}	A_B^{SFD}	psf	log A_e	SB_e	rms
N3837	11 43 56.42	+19 53 40.4	J97	21.89	−0.03	0.09	1.4	1.288	19.35	0.02
N3841	11 44 02.19	+19 58 18.7	J97	21.79	−0.03	0.09	1.7	1.258	19.76	0.04
N3842	11 44 02.17	+19 56 58.7	J97	21.42	−0.03	0.09	1.7	1.753	20.49	0.03
N3851	11 44 20.41	+19 58 50.3	J97	22.08	−0.03	0.09	1.6	1.022	19.09	0.01
N3862	11 45 05.00	+19 36 22.7	J97	21.57	−0.02	0.10	1.5	1.467	19.78	0.05
U06198	11 09 25.81	+29 34 07.5	J95	21.78	−0.04	0.11	2.0	1.182	19.45	0.05
U06250	11 13 10.40	+27 49 05.0	J95	21.79	−0.02	0.07	1.7	1.284	19.43	0.04
A3537:SMC-156	12 58 41.86	−32 07 17.1	C95	22.02	0.34	0.34	1.3	1.215	19.39	0.03
A1736:D-007	13 27 22.87	−27 45 05.7	C95	22.14	0.17	0.22	1.8	0.787	18.68	0.02
A1736:D-036	13 30 01.56	−27 24 55.4	C95	21.88	0.19	0.22	2.1	0.648	19.10	0.02
A1736:D-039	13 27 02.69	−27 26 07.8	C95	22.04	0.19	0.21	1.8	0.833	19.18	0.01
A1736:D-125	13 28 20.17	−26 56 30.1	C95	22.46	0.19	0.22	1.9	0.576	18.44	0.03
A1736:D-137	13 26 11.01	−26 49 35.6	C95	21.74	0.20	0.22	1.8	1.260	19.82	0.02
A1736:D-144	13 25 51.13	−26 45 03.1	C95	21.98	0.21	0.24	1.8	0.770	19.26	0.01
A3542:SMC-51	13 08 27.57	−34 25 27.6	C95	21.75	0.16	0.25	2.0	1.087	20.16	0.04
A3542:SMC-61	13 04 53.73	−34 17 06.0	C95	21.88	0.19	0.23	1.7	0.980	19.49	0.02
A3542:SMC-94	13 08 41.52	−34 34 31.3	C95	21.97	0.16	0.23	1.7	1.092	19.16	0.01
A3542:SMC-999	13 06 04.37	−34 19 32.6	C95	21.51	0.19	0.24	2.0	1.392	20.37	0.04
A3570:SMC-50	13 45 46.12	−37 56 46.2	C95	21.77	0.20	0.31	1.6	1.167	19.89	0.01
A3570:SMC-64	13 44 00.44	−38 17 11.6	C95	21.66	0.18	0.24	1.6	1.020	19.93	0.03
A3571:SMC-10	13 49 25.59	−33 36 50.1	C95	21.74	0.19	0.27	1.7	1.199	19.84	0.02
A3571:SMC-112	13 52 38.36	−32 53 17.3	C95	21.97	0.22	0.23	1.6	1.008	19.35	0.03
A3571:SMC-112	13 52 38.36	−32 53 17.3	C95	22.00	0.22	0.23	2.0	0.996	19.30	0.04
A3571:SMC-114	13 51 33.66	−32 49 49.8	C95	21.83	0.22	0.23	2.1	0.990	19.57	0.04
A3571:SMC-13	13 48 58.08	−32 51 26.1	C95	22.11	0.19	0.22	2.1	0.954	19.03	0.02
A3571:SMC-13	13 48 58.08	−32 51 26.1	C95	22.13	0.19	0.22	2.0	0.969	19.03	0.03
A3571:SMC-154	13 52 50.24	−32 24 14.2	C95	21.81	0.19	0.18	1.8	0.967	19.77	0.03
A3571:SMC-164	13 49 45.42	−32 22 52.4	C95	21.94	0.24	0.20	1.9	1.138	19.22	0.02
A3571:SMC-171	13 48 06.14	−32 30 31.7	C95	21.73	0.22	0.20	2.0	1.268	20.10	0.07
A3571:SMC-174	13 48 03.62	−32 37 43.7	C95	21.79	0.21	0.20	2.2	1.066	19.92	0.03
A3571:SMC-176	13 47 29.78	−32 08 26.8	C95	21.78	0.20	0.21	1.8	1.134	19.80	0.02
A3571:SMC-187	13 47 28.42	−32 51 51.8	C95	20.84	0.19	0.22	1.7	2.438	23.02	0.02
A3571:SMC-187	13 47 28.42	−32 51 51.8	C95	20.86	0.19	0.22	1.6	2.392	22.87	0.02
A3571:SMC-21	13 48 14.26	−33 22 57.8	C95	21.98	0.18	0.22	1.8	1.144	19.28	0.01
A3571:SMC-24	13 48 08.22	−34 04 27.6	C95	21.02	0.17	0.22	1.9	1.189	21.29	0.08
A3571:SMC-29	13 47 48.91	−33 17 25.4	C95	22.02	0.17	0.23	1.8	0.905	19.24	0.01
A3571:SMC-29	13 47 48.91	−33 17 25.4	C95	22.05	0.17	0.23	2.1	0.912	19.24	0.01
A3571:SMC-32	13 47 37.28	−32 45 04.7	C95	22.34	0.20	0.21	1.9	0.832	18.48	0.01
A3571:SMC-32	13 47 37.28	−32 45 04.7	C95	22.35	0.20	0.21	2.4	0.833	18.50	0.02
A3571:SMC-32	13 47 37.28	−32 45 04.7	C95	22.40	0.20	0.21	1.6	0.787	18.30	0.02
A3571:SMC-38	13 47 30.94	−33 35 18.8	C95	22.13	0.18	0.22	1.6	0.953	18.73	0.01
A3571:SMC-38	13 47 30.94	−33 35 18.8	C95	22.16	0.18	0.22	1.7	0.932	18.63	0.01
A3571:SMC-40	13 47 16.47	−32 49 00.4	C95	21.80	0.20	0.22	1.7	0.870	19.52	0.01
A3571:SMC-40	13 47 16.47	−32 49 00.4	C95	21.81	0.20	0.22	1.6	0.874	19.54	0.01
A3571:SMC-40	13 47 16.47	−32 49 00.4	C95	21.82	0.20	0.22	1.7	0.842	19.43	0.02
A3571:SMC-40	13 47 16.47	−32 49 00.4	C95	21.87	0.20	0.22	1.7	0.835	19.39	0.02
A3571:SMC-42	13 47 22.73	−33 36 09.1	C95	21.82	0.18	0.22	1.6	0.940	19.96	0.03
A3571:SMC-42	13 47 22.73	−33 36 09.1	C95	21.91	0.18	0.22	1.7	0.869	19.68	0.03
A3571:SMC-44	13 47 00.73	−33 16 48.8	C95	21.62	0.16	0.25	1.6	1.011	19.87	0.02
A3571:SMC-44	13 47 00.73	−33 16 48.8	C95	21.66	0.16	0.25	2.3	0.947	19.60	0.04
A3571:SMC-51	13 46 01.40	−33 44 36.7	C95	21.81	0.16	0.22	1.9	1.110	19.63	0.04

(Continued)

Identification	R.A. (J2000)	Dec. (J2000)	run	R_{20}	A_B^{BH}	A_B^{SFD}	psf	$\log A_e$	SB_e	rms
A3571:SMC-60	13 45 02.81	−32 53 24.6	C95	21.79	0.18	0.21	1.7	0.911	20.14	0.02
A3578:SMC-115	13 57 17.44	−24 48 37.0	C95	21.77	0.29	0.28	2.1	1.096	19.93	0.03
A3578:SMC-29	13 58 36.22	−24 28 08.0	C95	21.51	0.20	0.27	2.2	1.349	20.55	0.06
E325-004	13 43 33.36	−38 10 30.5	C95	21.73	0.18	0.24	1.7	1.397	19.55	0.04
E325-013	13 45 17.41	−38 10 23.2	C95	21.95	0.19	0.28	1.8	1.017	19.25	0.00
E325-016	13 46 24.16	−37 58 14.8	C95	21.88	0.21	0.32	1.7	1.211	19.54	0.02
E382-002	13 03 01.12	−32 50 06.2	C95	22.01	0.28	0.31	1.5	1.193	18.87	0.01
E443-024	13 01 00.80	−32 26 29.2	C95	21.66	0.34	0.38	1.5	1.678	19.72	0.02
E509-008	13 26 44.11	−27 26 23.7	C95	21.82	0.20	0.22	1.9	1.286	19.22	0.03
E510-033	13 59 36.17	−24 22 02.9	C95	21.61	0.20	0.26	2.0	1.428	20.04	0.02
E510-034	13 59 41.98	−25 22 41.7	C95	21.89	0.32	0.29	1.8	1.156	19.61	0.01
I3986	13 01 32.63	−32 17 07.9	C95	21.88	0.36	0.39	1.7	1.517	19.29	0.01
I4289	13 34 48.22	−27 07 38.2	C95	21.63	0.22	0.27	1.6	1.470	20.14	0.01
I4296	13 36 39.37	−33 57 59.5	C95	21.65	0.12	0.25	2.2	1.792	19.50	0.02
N5193	13 31 53.33	−33 14 04.4	C95	21.87	0.15	0.23	2.0	1.621	19.58	0.01
A3581:SMC-75	14 07 44.13	−27 04 58.8	C95	22.02	0.16	0.24	1.9	1.176	19.25	0.01
A3581:SMC-75	14 07 44.13	−27 04 58.8	C95	22.03	0.16	0.24	2.1	1.169	19.22	0.01
A3581:SMC-76	14 07 35.17	−27 02 07.2	C95	22.23	0.16	0.25	1.9	0.814	18.80	0.03
A3581:SMC-76	14 07 35.17	−27 02 07.2	C95	22.26	0.16	0.25	2.1	0.794	18.73	0.03
A3581:SMC-76	14 07 35.17	−27 02 07.2	C95	22.29	0.16	0.25	1.9	0.808	18.79	0.03
A3581:SMC-76	14 07 35.17	−27 02 07.2	C95	22.33	0.16	0.25	2.2	0.808	18.76	0.03
A3581:SMC-77	14 07 20.92	−27 00 38.8	C95	22.17	0.16	0.25	1.9	0.906	18.94	0.02
A3581:SMC-77	14 07 20.92	−27 00 38.8	C95	22.21	0.16	0.25	2.2	0.887	18.85	0.02
A3581:SMC-78	14 07 16.96	−26 32 59.9	C95	21.90	0.16	0.26	2.1	1.180	19.36	0.02
A3581:SMC-78	14 07 16.96	−26 32 59.9	C95	21.94	0.16	0.26	2.3	1.158	19.27	0.02
E510-044	14 01 37.77	−26 25 54.5	C95	22.06	0.20	0.29	2.0	1.100	19.01	0.01
E510-044	14 01 37.77	−26 25 54.5	C95	22.06	0.20	0.29	2.1	1.083	19.00	0.01
E510-054	14 04 03.31	−26 12 57.2	C95	21.94	0.22	0.27	2.0	1.389	19.59	0.03
E510-054	14 04 03.31	−26 12 57.2	C95	21.96	0.22	0.27	2.2	1.382	19.56	0.03
E510-060	14 05 22.86	−26 36 01.2	C95	21.63	0.22	0.28	1.7	1.232	19.43	0.09
E510-063	14 06 16.07	−25 47 57.2	C95	22.09	0.26	0.31	2.0	1.050	18.57	0.03
E510-063	14 06 16.07	−25 47 57.2	C95	22.10	0.26	0.31	2.4	1.054	18.59	0.03
E510-066	14 07 15.62	−27 09 30.9	C95	21.63	0.17	0.24	2.0	1.423	19.89	0.03
E510-066	14 07 15.62	−27 09 30.9	C95	21.65	0.17	0.24	2.1	1.392	19.76	0.03
I4374	14 07 29.76	−27 01 04.2	C95	21.39	0.16	0.25	1.9	1.707	20.77	0.03
I4374	14 07 29.76	−27 01 04.2	C95	21.41	0.16	0.25	1.9	1.701	20.68	0.03
I4374	14 07 29.76	−27 01 04.2	C95	21.42	0.16	0.25	2.1	1.684	20.63	0.03
I4374	14 07 29.76	−27 01 04.2	C95	21.44	0.16	0.25	2.2	1.665	20.60	0.02
A2052:EFR-B	15 16 45.87	+07 00 14.6	C95	21.24	0.04	0.15	2.5	1.483	21.20	0.05
A2052:EFR-B	15 16 45.87	+07 00 14.6	C95	21.26	0.04	0.15	1.7	1.563	21.41	0.04
A2052:EFR-B	15 16 45.87	+07 00 14.6	C95	21.27	0.04	0.15	1.7	1.468	21.12	0.04
A2052:EFR-C	15 16 53.94	+06 56 21.7	C95	21.86	0.04	0.15	2.3	1.157	19.53	0.02
A2052:EFR-C	15 16 53.94	+06 56 21.7	C95	21.88	0.04	0.15	1.8	1.140	19.46	0.02
A2052:MKV-13	15 15 51.37	+07 01 00.9	C95	21.54	0.04	0.16	2.2	1.166	20.73	0.03
A2052:MKV-30	15 16 32.76	+06 53 38.2	C95	22.22	0.04	0.15	1.9	0.702	18.59	0.01
A2052:MKV-34	15 16 36.80	+06 58 01.4	C95	22.33	0.04	0.15	1.7	0.647	18.35	0.01
A2052:MKV-34	15 16 36.80	+06 58 01.4	C95	22.33	0.04	0.15	1.8	0.643	18.33	0.01
A2052:MKV-39	15 16 43.98	+07 05 34.8	C95	22.36	0.04	0.14	1.7	0.639	18.44	0.02
A2052:MKV-39	15 16 43.98	+07 05 34.8	C95	22.37	0.04	0.14	2.0	0.632	18.43	0.01
A2052:MKV-46	15 16 51.26	+07 06 32.2	C95	21.83	0.04	0.14	2.0	0.770	19.57	0.01
A2052:MKV-60	15 17 10.91	+06 56 29.3	C95	22.07	0.04	0.15	1.8	0.889	19.00	0.03

(*Continued*)

Identification	R.A. (J2000)	Dec. (J2000)	run	R_{20}	A_B^{BH}	A_B^{SFD}	psf	log A_e	SB_e	rms
A2052:MKV-64	15 17 15.76	+07 05 57.6	C95	21.79	0.04	0.15	1.6	0.875	19.52	0.02
U09799	15 16 44.49	+07 01 16.6	C95	20.99	0.04	0.15	1.7	2.106	22.37	0.02
U09799	15 16 44.49	+07 01 16.6	C95	20.99	0.04	0.15	1.7	2.135	22.44	0.02
U09799	15 16 44.49	+07 01 16.6	C95	20.99	0.04	0.15	2.5	2.143	22.45	0.02
I4913	19 56 47.49	−37 19 45.4	C94B	21.64	0.36	0.41	1.5	1.394	19.37	0.06
A3656:SMC-A	20 00 00.33	−38 30 17.9	C94B	21.83	0.33	0.32	1.3	1.293	19.16	0.03
A3656:SMC-A	20 00 00.33	−38 30 17.9	C94B	21.92	0.33	0.32	1.7	1.271	19.07	0.02
A3656:SMC-I	20 00 55.65	−38 41 48.6	C94B	21.98	0.32	0.28	1.4	1.109	18.88	0.03
A3656:SMC-I	20 00 55.65	−38 41 48.6	C94B	22.00	0.32	0.28	1.7	1.105	18.84	0.02
A3656:SMC-I	20 00 55.65	−38 41 48.6	C94B	22.00	0.32	0.28	1.8	1.098	18.83	0.03
A3656:SMC-P	20 03 26.80	−38 24 18.1	C94B	21.91	0.34	0.31	1.4	1.340	19.56	0.01
A3656:SMC-P	20 03 26.80	−38 24 18.1	C95	21.86	0.34	0.31	1.7	1.358	19.67	0.01
A3656:SMC-R	20 00 34.68	−38 47 27.0	C94B	21.89	0.33	0.28	1.6	1.067	19.43	0.02
A3656:SMC-R	20 00 34.68	−38 47 27.0	C94B	21.90	0.33	0.28	1.5	1.059	19.40	0.03
A3656:SMC-S	20 01 30.63	−39 03 47.5	C94B	22.07	0.31	0.29	1.3	0.858	18.72	0.03
A3656:SMC-T	20 00 47.89	−38 23 40.2	C94B	21.38	0.33	0.32	1.7	0.947	20.30	0.05
A3656:SMC-W	20 04 31.37	−39 04 03.1	C94B	21.83	0.28	0.55	1.8	1.333	19.81	0.03
A3656:SMC-X	20 01 08.76	−37 47 05.8	C94B	22.31	0.34	0.37	1.7	0.936	18.41	0.03
A3698:SMC-C	20 38 39.17	−25 07 30.3	C94B	21.75	0.17	0.18	1.6	1.368	19.81	0.01
A3698:SMC-D	20 37 12.90	−25 12 57.2	C94B	21.89	0.17	0.19	1.5	1.274	19.56	0.02
A3698:SMC-E	20 38 27.11	−25 25 04.0	C94B	21.77	0.22	0.19	1.5	1.090	19.48	0.02
A3698:SMC-F	20 35 12.84	−25 11 30.0	C94B	22.26	0.23	0.20	1.7	0.887	18.38	0.02
A3733:SMC-N	20 58 06.41	−27 48 05.1	C95	21.82	0.40	0.34	1.3	0.974	19.35	0.02
E339-019	20 00 29.57	−37 41 20.3	C94B	22.67	0.34	0.40	1.7	0.591	17.37	0.03
I4926	20 00 12.13	−38 34 42.3	C94B	21.94	0.33	0.30	1.3	1.371	19.21	0.01
I4931	20 00 49.97	−38 34 35.9	C94B	21.55	0.33	0.29	1.4	1.593	19.58	0.04
N6924	20 33 18.92	−25 28 25.6	C94B	21.48	0.21	0.19	1.5	1.696	20.50	0.02
A3733:SMC-A	21 02 03.66	−27 52 16.8	C94B	21.73	0.37	0.42	1.6	1.239	19.87	0.01
A3733:SMC-A	21 02 03.66	−27 52 16.8	C94B	21.74	0.37	0.42	1.4	1.243	19.88	0.01
A3733:SMC-A	21 02 03.66	−27 52 16.8	C94B	21.74	0.37	0.42	1.6	1.248	19.88	0.01
A3733:SMC-B	21 02 03.02	−28 23 54.2	C94B	21.72	0.43	0.44	1.6	1.278	19.77	0.01
A3733:SMC-B	21 02 03.02	−28 23 54.2	C94B	21.72	0.43	0.44	2.0	1.286	19.80	0.01
A3733:SMC-C	21 01 59.42	−28 15 36.3	C94B	21.68	0.42	0.43	1.5	1.187	19.77	0.02
A3733:SMC-C	21 01 59.42	−28 15 36.3	C94B	21.68	0.42	0.43	1.9	1.199	19.82	0.02
A3733:SMC-G	21 01 55.62	−27 45 56.6	C94B	21.35	0.36	0.39	1.5	1.301	20.78	0.08
A3733:SMC-H	21 01 38.48	−27 53 58.0	C94B	21.80	0.38	0.47	1.3	1.025	19.66	0.01
A3733:SMC-H	21 01 38.48	−27 53 58.0	C94B	21.80	0.38	0.47	1.4	1.034	19.67	0.01
A3733:SMC-H	21 01 38.48	−27 53 58.0	C94B	21.81	0.38	0.47	1.6	1.028	19.64	0.01
A3733:SMC-I	21 01 38.78	−28 18 09.3	C94B	21.76	0.42	0.43	1.4	1.052	19.79	0.01
A3733:SMC-I	21 01 38.78	−28 18 09.3	C94B	21.76	0.42	0.43	2.0	1.061	19.83	0.01
A3733:SMC-J	21 01 36.72	−28 03 24.1	C94B	21.94	0.40	0.46	1.4	1.013	19.40	0.01
A3733:SMC-J	21 01 36.72	−28 03 24.1	C94B	21.94	0.40	0.46	1.4	1.016	19.41	0.01
A3733:SMC-K	21 03 45.74	−28 02 06.4	C94B	21.73	0.37	0.47	1.3	1.037	19.98	0.01
A3733:SMC-L	21 05 50.20	−28 43 46.1	C94B	21.78	0.38	0.39	2.0	1.176	19.70	0.01
A3733:SMC-L	21 05 50.20	−28 43 46.1	C94B	21.81	0.38	0.39	1.8	1.151	19.59	0.01
A3733:SMC-M	21 00 36.09	−28 52 59.7	C95	21.84	0.46	0.46	1.2	1.184	19.64	0.03
A3742:SMC-E	21 06 08.86	−47 09 05.1	C94B	20.34	0.06	0.13	1.6	1.396	22.49	0.14
A3742:SMC-E	21 06 08.86	−47 09 05.1	C94B	20.36	0.06	0.13	1.4	1.410	22.53	0.15
A3742:SMC-F	21 04 29.71	−47 49 43.1	C94B	22.15	0.07	0.16	1.3	0.810	18.79	0.04
A3742:SMC-K	21 11 14.80	−48 30 15.9	C94B	21.68	0.06	0.14	1.3	1.344	20.13	0.03
A3744:SMC-E	21 07 22.08	−25 27 20.2	C94B	22.11	0.23	0.26	1.5	0.845	19.14	0.01

(Continued)

Identification	R.A. (J2000)	Dec. (J2000)	run	R_{20}	A_B^{BH}	A_B^{SFD}	psf	$\log A_e$	SB_e	rms
A3744:SMC-E	21 07 22.08	−25 27 20.2	C94B	22.11	0.23	0.26	1.6	0.835	19.11	0.01
A3744:SMC-E	21 07 22.08	−25 27 20.2	C95	22.12	0.23	0.26	1.3	0.844	19.13	0.02
A3744:SMC-G	21 07 25.63	−25 25 42.4	C94B	21.43	0.23	0.26	1.5	1.535	20.58	0.04
A3744:SMC-G	21 07 25.63	−25 25 42.4	C94B	21.46	0.23	0.26	1.6	1.541	20.58	0.04
A3744:SMC-G	21 07 25.63	−25 25 42.4	C95	21.37	0.23	0.26	1.3	1.614	20.77	0.04
A3744:SMC-I	21 07 32.35	−25 38 34.7	C94B	22.03	0.24	0.27	1.6	0.965	19.01	0.02
A3744:SMC-M	21 06 56.18	−25 24 46.5	C94B	21.85	0.23	0.27	1.5	0.866	19.41	0.01
A3744:SMC-M	21 06 56.18	−25 24 46.5	C94B	21.86	0.23	0.27	1.5	0.869	19.42	0.01
A3744:SMC-N	21 06 54.52	−25 21 12.6	C94B	21.54	0.23	0.26	1.5	0.980	20.30	0.01
A3744:SMC-N	21 06 54.52	−25 21 12.6	C94B	21.56	0.23	0.26	1.5	0.980	20.29	0.01
A3744:SMC-O	21 08 32.09	−25 25 47.8	C94B	21.38	0.23	0.25	1.6	0.781	20.11	0.04
A3744:SMC-O	21 08 32.09	−25 25 47.8	C95	21.40	0.23	0.25	2.1	0.945	20.72	0.02
A3744:SMC-P	21 05 53.19	−26 07 18.7	C94B	21.87	0.28	0.34	1.4	1.044	19.61	0.01
A3744:SMC-P	21 05 53.19	−26 07 18.7	C95	21.90	0.28	0.34	1.4	1.033	19.56	0.02
A3744:SMC-Q	21 06 03.73	−26 10 29.1	C94B	21.52	0.27	0.33	1.5	1.215	20.25	0.02
A3744:SMC-Q	21 06 03.73	−26 10 29.1	C95	21.52	0.27	0.33	1.4	1.210	20.21	0.02
A3744:SMC-R	21 05 13.99	−25 33 03.7	C94B	21.53	0.24	0.30	1.3	1.156	20.50	0.01
A3744:SMC-T	21 06 00.66	−26 06 16.3	C94B	21.78	0.28	0.34	1.4	0.985	19.71	0.02
A3744:SMC-T	21 06 00.66	−26 06 16.3	C95	21.78	0.28	0.34	1.3	1.005	19.78	0.02
A3744:SMC-V	21 08 09.95	−26 24 13.8	C94B	21.76	0.24	0.25	1.6	1.187	19.66	0.03
A3744:SMC-W	21 03 18.22	−25 41 29.6	C95	21.74	0.27	0.29	1.3	1.075	20.12	0.04
A3747:SMC-C	21 07 54.55	−43 15 43.7	C94B	21.82	0.06	0.10	1.5	1.081	19.85	0.02
A3747:SMC-F	21 08 23.45	−42 41 14.7	C94B	21.53	0.05	0.13	1.4	0.937	19.88	0.05
A3747:SMC-G	21 06 47.08	−44 23 55.1	C94B	21.72	0.07	0.14	1.8	1.228	19.98	0.01
A3747:SMC-G	21 06 47.08	−44 23 55.1	C95	21.73	0.07	0.14	1.9	1.226	19.97	0.01
A3747:SMC-H	21 11 32.47	−42 38 53.3	C95	21.93	0.07	0.15	2.3	0.883	19.43	0.01
E235-039	21 02 43.48	−48 21 25.9	C94B	21.92	0.06	0.14	1.5	1.189	19.33	0.03
E235-039	21 02 43.48	−48 21 25.9	C94B	21.93	0.06	0.14	1.8	1.179	19.28	0.03
E235-049	21 04 40.95	−48 11 24.2	C94B	22.07	0.06	0.18	1.5	1.281	18.82	0.02
E286-029	21 03 04.23	−47 08 45.3	C94B	21.88	0.06	0.13	1.3	1.118	19.26	0.06
E286-042	21 05 31.10	−47 02 45.4	C94B	21.77	0.06	0.13	1.5	1.261	19.74	0.01
E286-042	21 05 31.10	−47 02 45.4	C94B	21.77	0.06	0.13	1.5	1.269	19.77	0.01
E286-042	21 05 31.10	−47 02 45.4	C94B	21.77	0.06	0.13	1.7	1.265	19.75	0.01
E286-049	21 06 47.51	−47 11 16.8	C94B	22.02	0.06	0.14	1.5	1.354	19.41	0.01
E286-059	21 08 39.33	−43 29 08.9	C94B	21.69	0.05	0.12	1.3	1.380	19.87	0.02
E286-060	21 08 56.98	−43 41 10.0	C94B	21.78	0.05	0.13	1.4	1.271	19.58	0.02
E464-018	21 03 01.43	−28 20 19.6	C94B	21.63	0.41	0.42	1.4	1.458	20.11	0.02
N6998	21 01 37.68	−28 01 54.9	C94B	21.58	0.40	0.47	1.4	1.451	20.53	0.04
N6998	21 01 37.68	−28 01 54.9	C94B	21.59	0.40	0.47	1.4	1.450	20.52	0.04
N6999	21 01 59.54	−28 03 32.1	C94B	21.47	0.40	0.48	1.5	1.531	20.86	0.03
N6999	21 01 59.54	−28 03 32.1	C94B	21.47	0.40	0.48	1.5	1.542	20.90	0.03
N7014	21 07 52.25	−47 10 46.6	C94B	21.80	0.07	0.13	1.6	1.346	18.95	0.04
N7014	21 07 52.25	−47 10 46.6	C94B	21.82	0.07	0.13	1.4	1.343	18.94	0.04
N7014	21 07 52.25	−47 10 46.6	C95	21.79	0.07	0.13	2.0	1.364	19.05	0.03
N7016	21 07 16.19	−25 28 08.4	C94B	21.71	0.23	0.26	1.5	1.379	19.95	0.01
N7016	21 07 16.19	−25 28 08.4	C94B	21.71	0.23	0.26	1.6	1.376	19.92	0.01
N7016	21 07 16.19	−25 28 08.4	C95	21.73	0.23	0.26	1.3	1.353	19.84	0.01
A2657:D-015	23 43 42.27	+08 59 31.2	J97	21.62	0.24	0.90	1.1	0.987	20.21	0.00
A2657:D-031	23 44 16.10	+09 02 56.3	J97	21.54	0.23	0.53	1.2	1.311	20.50	0.02
A2657:D-043	23 44 56.41	+09 07 53.6	J97	21.87	0.22	0.50	1.2	0.906	19.81	0.03
A2657:D-043	23 44 56.41	+09 07 53.6	J97	21.90	0.22	0.50	1.7	0.830	19.55	0.01

(Continued)

Identification	R.A. (J2000)	Dec. (J2000)	run	R_{20}	A_B^{BH}	A_B^{SFD}	psf	$\log A_e$	SB_e	rms
A2657:D-064	23 45 17.21	+09 16 15.8	J97	21.75	0.21	0.46	1.2	1.112	19.84	0.03
A2657:D-071	23 44 30.50	+09 15 48.2	J97	21.56	0.22	0.51	1.2	1.334	20.49	0.05
A2657:D-072	23 44 27.78	+09 16 00.2	J97	22.20	0.22	0.51	1.2	0.698	18.92	0.02
A4049:D-011	23 52 43.44	−28 29 35.0	C94B	21.83	0.01	0.07	1.4	1.035	19.99	0.03
A4049:D-015	23 52 59.58	−28 25 37.2	C94B	21.77	0.01	0.07	1.4	0.754	19.63	0.02
A4049:D-033	23 51 35.39	−28 17 05.5	C94B	22.48	0.01	0.08	1.7	0.463	18.13	0.02
A4049:D-047	23 51 34.80	−28 04 28.6	C94B	22.10	0.01	0.08	1.5	0.984	18.93	0.01
A4049:D-047	23 51 34.80	−28 04 28.6	C94B	22.11	0.01	0.08	1.6	0.987	18.94	0.01
A4049:D-055	23 51 54.37	−27 55 48.0	C94B	21.86	0.00	0.08	1.4	1.195	19.53	0.01
A4049:D-055	23 51 54.37	−27 55 48.0	C94B	21.86	0.00	0.08	1.7	1.199	19.54	0.01
A4049:D-062	23 53 44.89	−27 54 10.4	C94B	21.22	0.01	0.09	2.1	1.366	21.34	0.02
A4049:D-066	23 50 35.26	−27 47 35.9	C94B	22.17	0.02	0.09	1.3	0.903	19.00	0.02
A4049:D-066	23 50 35.26	−27 47 35.9	C94B	22.18	0.02	0.09	2.1	0.892	18.94	0.02
A4049:SMC-B	23 51 01.22	−27 56 22.8	C94B	21.14	0.01	0.09	1.4	1.291	21.31	0.04
A4049:SMC-B	23 51 01.22	−27 56 22.8	C94B	21.16	0.01	0.09	2.0	1.277	21.25	0.04
A4049:SMC-D	23 52 24.15	−29 01 22.3	C94B	22.05	0.00	0.07	1.6	1.019	18.91	0.01
A4049:SMC-E	23 52 10.10	−29 04 41.5	C94B	21.99	0.00	0.07	1.7	1.215	19.27	0.01
A4049:SMC-G	23 54 45.76	−28 03 33.4	C94B	21.84	0.00	0.08	2.1	1.036	19.59	0.01
A4049:SMC-H	23 50 12.60	−29 00 24.7	C94B	21.46	0.00	0.08	1.8	1.478	20.74	0.02
A4049:SMC-M	23 51 03.51	−27 47 52.7	C94B	20.98	0.02	0.09	1.4	1.211	21.68	0.05
A4049:SMC-M	23 51 03.51	−27 47 52.7	C94B	21.02	0.02	0.09	2.0	1.197	21.62	0.04
I5362	23 51 36.62	−28 21 52.9	C94B	21.65	0.01	0.08	1.7	1.464	19.90	0.03
N7626	23 20 42.29	+08 13 02.5	C94B	21.43	0.00	0.29	1.8	1.780	20.53	0.04

Table A.3: Merged dataset for FP sample. See text of Appendix A for details.

Cluster	Galaxy	R.A. (J2000)	Dec. (J2000)	$cz_\odot$	$\log\sigma$	Mg_2	$\log R_e$	$\langle\mu\rangle_e$	T
A0076	A0076:D-016	00 39 36.63	+06 39 54.2	11638	2.141	0.296	0.877	20.51	E
	A0076:D-018	00 39 15.62	+06 41 21.5	11582	2.234	0.310	0.854	19.92	E
	I1565	00 39 26.27	+06 44 03.3	11323	2.494	0.340	1.231	20.33	E
	I1566	00 39 33.35	+06 48 54.5	11946	2.403	0.309	0.985	19.82	L
	I1568	00 39 55.96	+06 50 54.9	11986	2.481	0.342	1.091	20.38	E
	I1569	00 40 28.02	+06 43 10.9	11334	2.356	0.309	0.924	20.07	E
A0189	A0189:SMC-A	01 23 26.33	+01 42 17.8	10273	2.363	0.299	0.873	19.51	L
	A0189:SMC-C	01 23 23.69	+01 46 03.6	9524	2.203	0.290	0.761	19.90	E
	A0189:SMC-I	01 24 58.92	+01 33 23.2	9191	2.081	0.198	1.058	21.19	E
	A0189:SMC-J	01 24 43.94	+01 22 01.6	8985	2.113	0.251	0.753	20.04	L
	I0103	01 24 36.44	+02 02 39.3	9594	2.402	0.322	0.799	18.98	E
A0194	A0194:D-012	01 23 40.72	-01 49 48.1	5579	2.038	0.300	0.630	19.04	L
	A0194:D-028	01 25 48.05	-01 29 31.5	5118	1.881	—	0.880	20.60	L
	A0194:D-045	01 25 47.68	-01 20 40.5	5543	2.103	0.247	0.750	19.32	L
	A0194:D-052	01 25 52.45	-01 15 59.7	6290	1.938	0.213	0.630	19.51	E
	A0194:D-071	01 28 02.12	-00 44 18.0	5699	1.961	0.204	0.950	20.31	L
	I0120	01 28 12.97	-01 54 52.0	4793	2.066	0.250	0.900	19.86	L
	I1696	01 24 52.53	-01 37 01.7	5814	2.216	0.297	0.840	19.18	E
	N0541	01 25 44.29	-01 22 46.0	5424	2.334	0.312	1.330	20.24	E
	N0543	01 25 50.00	-01 17 34.2	5275	2.362	0.317	0.650	18.44	L
	N0545	01 25 59.21	-01 20 25.3	5324	2.386	0.316	1.420	20.27	E
	N0547	01 26 00.68	-01 20 44.4	5539	2.406	0.319	1.100	19.33	E
	N0548	01 26 02.49	-01 13 31.7	5399	2.162	0.250	1.100	20.56	E
	N0560	01 27 25.48	-01 54 44.7	5495	2.280	0.285	1.010	19.18	L
	N0564	01 27 48.29	-01 52 43.3	5823	2.380	0.302	1.130	19.58	E
	U00996	01 25 32.02	-01 30 09.6	5801	2.160	0.257	0.700	18.62	L
	U01003	01 25 44.25	-01 27 24.1	5237	2.199	0.261	0.760	18.91	L
	U01030	01 27 16.15	-01 16 19.1	4747	2.243	0.272	0.800	19.15	L
	U01040	01 27 36.03	-01 06 18.0	4476	2.079	0.236	0.920	19.47	L
A0262	A0262:B-018	01 53 50.15	+36 20 59.0	4152	2.163	0.264	1.026	19.86	Q
	A0262:B-019	01 52 37.70	+36 07 37.2	4712	2.194	0.281	0.852	19.13	L
	A0262:B-038	01 52 32.57	+36 06 55.0	4278	2.094	0.270	0.853	19.93	E
	A0262:B-042	01 50 14.75	+36 13 43.5	5141	2.134	0.237	0.839	20.11	E
	A0262:PP-A05096	01 57 59.89	+36 55 04.4	5239	1.951	0.221	0.989	20.46	E
	I0171	01 55 10.27	+35 16 53.6	5366	2.277	0.255	1.477	20.42	Q
	N0679	01 49 43.79	+35 47 06.8	5051	2.387	0.302	1.083	18.98	E
	N0687	01 50 33.28	+36 22 14.1	5099	2.365	0.303	1.142	19.26	E
	N0703	01 52 39.68	+36 10 16.5	5574	2.369	0.312	1.017	19.48	E
	N0708	01 52 46.45	+36 09 06.8	4858	2.346	0.313	1.656	21.29	E
	N0712	01 53 08.53	+36 49 10.8	5359	2.407	—	1.013	19.10	E
	N0759	01 57 50.41	+36 20 34.3	4651	2.405	0.259	1.227	19.67	E
	U01269	01 49 05.81	+34 58 58.6	3841	2.065	0.186	1.178	20.98	L
	U01308	01 50 51.24	+36 16 33.0	5232	2.353	—	1.378	19.39	E
A0347	A0347:PP-B03C	02 23 12.87	+42 59 16.0	6643	2.472	0.308	0.287	17.50	Q

(Continued)

Cluster	Galaxy	R.A. (J2000)	Dec. (J2000)	$cz_\odot$	$\log\sigma$	Mg_2	$\log R_e$	$\langle\mu\rangle_e$	T
	A0347:PP-B07	02 24 53.14	+43 19 29.4	5295	2.306	0.312	0.899	19.21	L
	A0347:PP-B16	02 32 28.26	+41 56 39.4	4879	2.183	0.270	1.035	19.93	E
	N0909	02 25 22.79	+42 02 08.4	4972	2.271	0.274	0.983	19.35	E
	N0911	02 25 42.39	+41 57 21.3	5760	2.398	0.326	0.905	18.81	L
	N0912	02 25 42.73	+41 46 38.8	4412	2.233	0.293	0.918	19.51	E
	U01837	02 22 58.46	+43 00 43.3	6576	2.285	0.305	1.288	20.41	E
	U01841	02 23 11.47	+42 59 30.8	6367	2.361	0.307	1.511	20.75	E
	U01859	02 24 44.43	+42 37 23.7	5911	2.549	0.352	0.881	18.69	E
A0400	A0400:D-017	02 59 48.58	+05 44 33.1	6874	2.137	0.268	0.600	19.14	E
	A0400:D-041	02 57 47.41	+06 01 39.6	7334	2.334	0.268	0.490	18.19	E
	A0400:D-044	02 57 33.67	+05 58 36.9	6849	2.442	0.341	0.720	18.42	L
	A0400:D-052	02 57 37.45	+06 02 50.1	7439	2.150	0.292	0.508	18.62	E
	A0400:D-057	02 58 54.22	+06 06 59.6	7229	2.090	0.264	0.779	19.69	L
	A0400:D-058	02 58 21.02	+06 05 42.5	6784	2.361	0.324	0.981	19.66	E
	A0400:D-070	02 55 14.85	+06 10 39.3	7552	2.258	0.282	0.888	19.43	L
	A0400:D-089	02 58 24.58	+06 35 30.5	6321	2.218	0.291	1.100	19.54	L
A0426	A0426:7S-PER163	03 20 28.65	+41 29 18.2	5463	2.200	0.282	0.527	18.37	E
	A0426:7S-PER199	03 19 09.80	+41 05 01.5	5092	2.318	0.286	0.731	18.80	L
	A0426:PP-P07	03 18 19.26	+41 28 07.3	3538	2.079	0.241	1.035	20.53	E
	A0426:PP-P08	03 18 22.52	+41 24 36.0	6456	2.271	0.268	1.181	20.07	E
	A0426:PP-P11	03 18 57.74	+41 42 11.2	4241	2.190	0.277	0.975	19.90	E
	A0426:PP-P15	03 19 17.75	+41 38 39.7	6207	2.315	0.290	0.796	19.00	E
	A0426:PP-P20	03 19 44.48	+41 26 50.5	3957	1.923	0.281	0.531	19.30	E
	A0426:PP-P21	03 19 43.99	+41 27 40.6	3934	2.146	0.311	0.560	19.00	E
	A0426:PP-P22	03 19 47.80	+41 35 46.8	7458	2.307	0.296	0.794	18.91	E
	A0426:PP-P26	03 20 00.69	+41 33 49.7	5309	2.305	0.285	0.522	17.98	E
	A0426:PP-P33	03 20 49.53	+41 22 17.0	4944	2.214	0.291	0.853	19.15	L
	I0293	03 10 56.15	+41 08 13.6	4702	2.172	0.270	1.296	20.74	E
	I0310	03 16 42.98	+41 19 30.4	5654	2.338	0.261	1.327	19.99	L
	I0312	03 18 08.38	+41 45 14.8	4976	2.343	0.306	1.098	19.59	L
	I0313	03 20 57.88	+41 53 36.4	4426	2.372	0.333	1.092	19.51	L
	I1907	03 19 34.23	+41 34 49.0	4477	2.338	0.301	1.159	19.99	L
	N1224	03 11 13.63	+41 21 49.3	5229	2.381	0.272	1.154	19.67	L
	N1270	03 18 58.02	+41 28 12.0	4978	2.534	0.362	0.848	18.13	E
	N1272	03 19 21.30	+41 29 26.7	3796	2.418	0.337	1.488	20.38	E
	N1273	03 19 26.79	+41 32 25.4	5385	2.321	0.280	0.974	18.87	E
	N1278	03 19 54.15	+41 33 47.9	6067	2.412	0.307	1.363	20.00	E
	N1281	03 20 06.08	+41 37 47.3	4294	2.429	0.326	0.868	18.79	E
	N1283	03 20 15.52	+41 23 54.7	6738	2.337	0.301	0.921	19.07	E
	N1293	03 21 36.46	+41 23 34.2	4160	2.337	0.325	0.978	19.08	E
	U02673	03 20 01.58	+41 15 04.5	4422	2.291	0.298	1.258	20.26	E
	U02698	03 22 02.85	+40 51 50.7	6454	2.556	0.337	1.005	18.93	E
	U02717	03 24 36.47	+40 41 27.0	3781	2.187	0.236	1.135	19.64	E
	U02725	03 25 29.54	+41 14 27.3	6209	2.331	0.295	0.898	19.00	L
A0539	A0539:D-016	05 17 17.86	+06 08 14.4	9673	2.323	0.296	0.890	19.28	L
	A0539:D-031	05 15 35.90	+06 15 51.7	8742	2.190	0.249	1.080	20.43	L
	A0539:D-039	05 15 47.86	+06 19 19.9	8631	2.243	0.271	0.930	19.97	L

(Continued)

Cluster	Galaxy	R.A. (J2000)	Dec. (J2000)	$cz_\odot$	$\log\sigma$	Mg_2	$\log R_e$	$\langle\mu\rangle_e$	T
	A0539:D-041	05 16 50.74	+06 22 47.4	8133	2.189	0.271	0.530	18.89	L
	A0539:D-042	05 16 49.45	+06 23 20.5	8685	2.206	0.274	0.811	19.82	L
	A0539:D-043	05 16 45.84	+06 22 43.7	8412	2.083	0.207	0.910	20.62	L
	A0539:D-044	05 16 28.86	+06 24 08.9	7442	2.311	0.279	0.719	18.99	L
	A0539:D-045	05 16 25.49	+06 20 33.2	8716	2.344	0.326	0.780	19.33	E
	A0539:D-047	05 16 37.33	+06 26 27.3	8170	2.284	0.321	1.473	21.53	E
	A0539:D-048	05 16 37.20	+06 26 13.3	7744	2.260	0.303	0.160	17.57	E
	A0539:D-049	05 16 37.15	+06 26 53.0	8721	2.339	0.295	0.607	18.66	E
	A0539:D-050	05 16 37.01	+06 27 06.4	8554	2.350	0.296	0.882	19.56	E
	A0539:D-051	05 16 38.94	+06 27 52.2	9364	2.219	0.274	0.700	19.24	L
	A0539:D-052	05 16 34.12	+06 26 57.6	8081	2.137	0.277	0.450	18.96	L
	A0539:D-054	05 15 59.88	+06 25 19.0	8840	2.130	0.263	0.790	20.25	L
	A0539:D-057	05 17 07.27	+06 29 39.2	10014	2.225	0.308	0.790	19.93	L
	A0539:D-059	05 16 46.98	+06 29 55.6	7214	2.222	0.287	1.030	20.29	L
	A0539:D-061	05 16 38.69	+06 30 42.2	7880	2.148	0.277	0.270	18.16	L
	A0539:D-062	05 16 36.26	+06 29 19.4	9308	2.230	0.288	0.811	19.45	L
	A0539:D-063	05 16 35.68	+06 30 13.4	7117	2.254	0.242	0.743	18.92	E
	A0539:D-064	05 16 33.58	+06 30 14.6	8666	2.100	0.235	0.980	20.53	L
	A0539:D-068	05 16 55.12	+06 33 09.5	9694	2.472	0.342	1.085	19.52	E
	A0539:D-069	05 16 44.52	+06 32 08.8	9933	2.364	0.310	0.150	17.29	L
	A0539:D-075	05 16 54.52	+06 37 14.1	9102	2.109	0.290	0.360	18.72	E
A0548SE	A0548:D-019	05 44 29.72	-26 03 32.6	11691	2.481	—	0.716	19.03	E
	A0548:D-020	05 44 25.94	-26 04 41.0	11354	2.276	—	0.435	18.59	E
	A0548:D-052	05 44 56.19	-25 55 16.8	12686	2.216	—	0.870	20.06	E
	A0548:D-068	05 45 27.20	-25 53 53.9	13770	2.299	—	0.580	19.41	L
	E488-009	05 45 29.67	-25 55 58.6	13337	2.219	—	0.484	19.01	L
A0569N	A0569:SMC-B	07 13 54.02	+50 23 54.4	5825	2.220	0.286	0.947	19.40	E
	A0569:SMC-G	07 08 24.18	+50 08 11.7	5763	2.268	0.296	0.649	18.77	E
	I0458	07 10 34.01	+50 07 06.3	6488	2.323	0.290	0.965	19.13	L
	I0464	07 11 04.79	+50 08 11.2	4834	2.240	0.254	0.904	19.32	E
	N2330	07 09 28.40	+50 09 09.1	4808	2.136	0.290	0.728	19.40	L
	N2332	07 09 34.20	+50 10 54.5	5832	2.420	0.302	1.115	19.34	E
	N2340	07 11 10.84	+50 10 27.7	5927	2.396	0.343	1.741	21.43	E
A0569S	A0569:SMC-L	07 09 44.85	+48 41 25.7	5737	2.135	0.273	0.842	19.59	L
	A0569:SMC-N	07 07 59.60	+48 39 58.7	5336	2.335	0.278	0.927	19.21	L
	A0569:SMC-Q	07 06 40.14	+48 29 24.5	5860	2.368	0.305	0.912	19.37	L
	A0569:SMC-R	07 08 52.74	+48 27 00.0	6151	2.214	0.286	1.081	20.10	L
	N2329	07 09 08.01	+48 36 55.5	5808	2.383	0.275	1.327	20.05	E
	U03696	07 09 23.05	+48 38 07.5	6138	2.431	0.301	0.880	18.63	E
A0576	A0576:SMC-A	07 21 36.44	+56 10 16.5	10913	2.111	0.245	0.683	19.62	L
	A0576:SMC-B	07 20 20.43	+55 53 11.3	11882	2.147	0.231	0.754	19.59	E
	A0576:SMC-C	07 21 19.42	+55 48 38.2	11158	2.413	0.308	1.068	20.38	E
	A0576:SMC-D	07 21 21.55	+55 47 52.1	12095	2.346	0.334	0.840	19.70	E
	A0576:SMC-I	07 19 28.53	+55 36 31.8	9862	2.294	0.290	0.853	19.82	E
	A0576:SMC-J	07 25 48.27	+55 29 40.7	10725	2.128	0.249	0.836	20.31	E

(Continued)

Cluster	Galaxy	R.A. (J2000)	Dec. (J2000)	$cz_\odot$	$\log\sigma$	Mg_2	$\log R_e$	$\langle\mu\rangle_e$	T
A0999	A0999:SMC-C	10 23 22.53	+13 05 34.9	9618	2.072	0.272	0.667	19.67	L
	A0999:SMC-D	10 23 23.85	+12 50 05.8	9752	2.418	0.321	1.041	19.73	E
	A0999:SMC-E	10 23 26.29	+12 48 54.8	9302	2.307	0.293	0.734	19.35	E
	A0999:SMC-F	10 23 43.10	+12 42 55.8	9167	2.385	0.305	0.687	18.88	E
	A0999:SMC-G	10 25 06.66	+12 24 52.8	9967	2.227	0.301	0.635	19.49	L
A1016	A1016:SMC-A	10 30 00.79	+11 08 18.2	9605	1.926	0.236	0.590	19.83	L
	A1016:SMC-B	10 27 05.83	+11 03 16.8	9714	2.341	0.295	0.792	19.45	L
	A1016:SMC-C	10 27 10.58	+11 01 15.8	9792	2.208	0.278	0.476	19.02	L
	A1016:SMC-E	10 26 36.48	+10 56 06.4	10087	2.190	0.218	0.754	19.84	L
	A1016:SMC-F	10 26 23.50	+10 55 06.2	9596	2.159	0.260	0.874	20.04	E
	A1016:SMC-G	10 27 42.58	+10 49 28.1	9440	2.042	0.231	0.724	20.48	E
	I0613	10 27 07.79	+11 00 38.5	9728	2.425	0.321	0.985	19.70	E
A1060	A1060:JFK-RMH26	10 36 04.23	-27 30 31.6	2289	2.019	—	0.890	19.84	E
	A1060:JFK-RMH28	10 36 23.01	-27 21 16.8	3001	2.116	0.274	0.790	19.32	L
	A1060:JFK-RMH29	10 36 27.65	-27 19 10.8	3431	2.211	—	0.610	17.99	L
	A1060:JFK-RMH35	10 36 41.18	-27 33 39.2	4753	2.079	—	0.800	19.19	L
	A1060:JFK-RMH50	10 37 41.45	-27 02 40.3	3077	1.938	—	0.820	20.22	L
	E436-044	10 34 47.46	-28 29 56.0	3146	2.196	0.259	0.980	18.97	L
	E436-045	10 34 50.46	-28 30 56.1	3383	2.261	0.268	0.460	17.77	E
	E437-011	10 36 50.47	-27 55 11.7	4940	2.259	—	0.920	18.90	L
	E437-013	10 36 53.89	-27 55 02.6	3501	2.214	—	0.800	18.57	L
	E437-021	10 38 10.81	-28 47 01.4	3912	2.231	0.284	1.060	19.44	L
	E437-045	10 41 59.38	-28 46 37.1	3738	2.085	0.280	1.090	19.80	L
	E501-003	10 31 48.11	-26 33 57.1	4180	2.305	0.285	1.140	19.65	E
	E501-013	10 33 30.16	-26 53 53.9	3501	2.334	0.306	0.950	18.84	L
	I2597	10 37 47.23	-27 04 49.8	2947	2.360	0.317	1.360	19.66	E
	N3305	10 36 11.75	-27 09 43.9	3981	2.368	—	0.970	18.76	E
	N3308	10 36 22.22	-27 26 20.0	3563	2.274	0.302	1.510	20.51	E
	N3309	10 36 35.72	-27 31 03.2	4086	2.394	0.325	1.340	19.57	E
	N3311	10 36 42.74	-27 31 41.3	3860	2.271	0.333	2.060	22.10	L
A1139	A1139:D-016	10 58 38.93	+01 22 55.0	12327	2.124	0.242	0.835	20.63	L
	A1139:D-029	10 57 43.29	+01 34 01.1	11784	2.397	0.285	0.800	19.82	L
	A1139:D-030	10 57 01.60	+01 33 59.9	11271	2.290	0.289	0.619	19.37	L
	A1139:D-036	10 58 15.23	+01 36 56.9	11834	2.447	0.322	0.536	18.65	E
	A1139:D-037	10 58 13.10	+01 36 24.5	11545	2.437	0.319	0.711	19.39	E
	A1139:D-039	10 58 11.02	+01 36 15.4	11541	2.415	0.335	1.096	20.30	L
	A1139:D-041	10 57 32.91	+01 37 16.3	10579	2.171	0.274	0.473	19.38	E
	I0660	10 58 26.67	+01 22 57.9	12277	2.413	0.304	0.909	19.94	L
	I0661	10 58 51.49	+01 39 02.2	11948	2.252	0.288	1.134	20.82	L
	I0662	10 59 20.55	+01 35 55.3	11736	2.418	0.298	0.813	19.54	E
A1177	A1177:SMC-B	11 10 25.84	+22 06 36.4	9434	2.049	0.264	0.922	20.79	E
	A1177:SMC-C	11 10 48.19	+22 03 33.0	9802	2.028	0.237	0.612	20.04	E
	A1177:SMC-F	11 09 41.02	+21 44 23.1	9670	2.393	0.340	0.508	18.51	L
	A1177:SMC-H	11 09 19.73	+21 38 53.4	9273	2.134	0.268	0.442	19.15	E
	N3551	11 09 44.44	+21 45 31.7	9577	2.428	0.333	1.434	21.01	E
	N3555	11 09 50.33	+21 48 36.7	9449	2.342	0.318	0.569	18.56	L

(Continued)

Cluster	Galaxy	R.A. (J2000)	Dec. (J2000)	$cz_\odot$	$\log\sigma$	Mg_2	$\log R_e$	$\langle\mu\rangle_e$	T
A1228	A1228:SMC-G	11 21 26.94	+34 27 09.1	10602	2.327	0.303	0.670	19.09	L
	A1228:SMC-H	11 22 07.30	+34 21 57.6	10254	2.399	0.310	0.716	19.25	E
	A1228:SMC-M	11 23 24.52	+33 49 44.6	10319	2.384	0.298	0.861	19.57	E
	I2738	11 21 23.06	+34 21 24.0	10499	2.424	0.332	0.917	19.55	E
	I2744	11 21 42.48	+34 21 45.9	10642	2.309	0.307	1.104	20.55	E
A1257	A1257:SMC-B	11 25 30.88	+35 30 16.2	10131	2.467	0.340	0.701	18.88	E
	A1257:SMC-C	11 23 47.02	+35 26 32.1	10206	2.120	0.174	0.395	18.91	E
	A1257:SMC-E	11 26 18.38	+35 20 57.4	10190	2.250	0.277	0.679	19.44	L
	A1257:SMC-G	11 26 17.26	+35 20 24.2	10279	2.252	0.278	0.966	20.08	E
	A1257:SMC-GC	11 26 15.69	+35 19 42.5	10903	2.163	0.237	0.636	20.03	L
A1314	A1314:SMC-A	11 36 30.55	+49 07 52.8	11117	2.413	0.297	1.026	20.07	E
	A1314:SMC-B	11 32 34.81	+49 06 34.7	10188	2.247	0.254	0.717	19.38	E
	A1314:SMC-D	11 35 26.29	+49 05 13.4	9649	2.230	0.256	0.500	19.15	E
	A1314:SMC-E	11 34 59.83	+49 04 53.6	9478	2.189	0.280	0.382	18.70	E
	A1314:SMC-G	11 36 36.65	+49 03 46.8	9707	2.412	0.305	0.878	19.69	E
	I0708	11 33 59.22	+49 03 43.4	9492	2.426	0.326	1.082	19.79	E
	I0709	11 34 14.54	+49 02 35.3	9508	2.389	0.287	0.858	19.34	E
A1367	A1367:B-020	11 48 03.36	+20 00 22.6	7243	2.192	0.262	0.793	18.98	L
	A1367:B-021	11 45 14.95	+19 50 42.3	7731	2.218	0.242	1.052	20.13	L
	A1367:B-041	11 44 07.69	+19 44 15.5	7753	2.140	0.253	0.865	20.09	E
	I2955	11 45 03.88	+19 37 14.0	6490	2.271	0.273	0.796	19.27	E
	N3837	11 43 56.42	+19 53 40.4	6318	2.410	0.305	0.953	19.15	E
	N3841	11 44 02.19	+19 58 18.7	6339	2.255	0.293	0.957	19.69	E
	N3842	11 44 02.17	+19 56 58.7	6275	2.483	0.332	1.439	20.38	E
	N3851	11 44 20.41	+19 58 50.3	6394	2.363	0.301	0.701	18.93	L
	N3862	11 45 05.00	+19 36 22.7	6503	2.404	0.297	1.134	19.60	E
	N3873	11 45 46.06	+19 46 24.9	5410	2.384	0.291	1.124	19.69	E
A1656	A1656:D-024	12 57 09.40	+27 27 58.8	7477	2.297	0.294	0.615	18.66	E
	A1656:D-027	13 00 26.80	+27 30 55.8	7820	1.986	0.262	0.667	19.84	E
	A1656:D-057	12 59 46.90	+27 42 38.0	8342	2.195	0.254	0.940	19.73	L
	A1656:D-065	13 00 06.10	+27 46 30.8	6092	2.049	0.240	0.809	20.24	L
	A1656:D-067	12 59 24.92	+27 44 19.3	6033	2.157	0.265	0.408	18.65	L
	A1656:D-081	13 01 09.22	+27 49 05.5	5966	2.112	0.257	0.815	20.34	E
	A1656:D-087	12 59 30.84	+27 47 35.1	6476	1.854	0.219	0.422	19.22	E
	A1656:D-096	13 01 50.23	+27 53 36.9	7584	2.263	0.270	0.651	19.20	E
	A1656:D-098	13 00 59.10	+27 53 59.6	6828	2.154	0.254	0.720	19.46	L
	A1656:D-101	12 59 46.09	+27 51 25.0	8062	2.088	0.257	0.528	18.99	L
	A1656:D-106	12 59 22.82	+27 53 49.0	5114	2.189	0.229	0.365	18.58	E
	A1656:D-107	12 59 20.83	+27 53 15.0	6518	1.838	0.231	0.790	20.41	E
	A1656:D-108	12 59 04.50	+27 54 39.4	6396	2.052	0.260	0.512	19.35	L
	A1656:D-116	13 00 42.70	+27 57 47.5	8366	2.102	0.235	0.663	19.58	L
	A1656:D-119	13 00 27.80	+27 57 21.4	6984	2.174	0.268	0.462	18.90	L
	A1656:D-120	13 00 18.46	+27 57 32.1	6349	2.147	0.257	0.770	18.90	E
	A1656:D-121	13 00 17.60	+27 57 19.5	6848	2.304	0.268	0.300	18.07	E
	A1656:D-125	12 59 42.76	+27 55 37.4	6929	2.233	0.253	0.175	17.70	E

(Continued)

Cluster	Galaxy	R.A. (J2000)	Dec. (J2000)	$cz_\odot$	$\log\sigma$	Mg_2	$\log R_e$	$\langle\mu\rangle_e$	T
	A1656:D-128	12 59 39.86	+27 57 22.3	8001	2.007	0.238	0.379	18.98	L
	A1656:D-132	12 59 25.31	+27 58 03.9	7683	2.092	0.251	0.578	19.75	L
	A1656:D-135	12 58 59.86	+27 58 02.6	8322	2.002	0.237	0.510	19.71	E
	A1656:D-136	12 58 55.87	+27 58 01.5	5697	2.238	0.267	0.184	17.77	E
	A1656:D-140	12 56 29.80	+27 56 23.6	6675	2.250	0.295	0.786	19.76	E
	A1656:D-146	13 00 38.70	+28 00 51.7	7537	2.009	0.234	0.905	20.57	L
	A1656:D-153	12 59 43.73	+27 59 47.4	6686	2.125	0.275	0.506	19.02	E
	A1656:D-156	12 59 26.40	+27 59 54.3	6706	1.990	0.213	0.497	19.65	E
	A1656:D-157	12 59 25.41	+27 58 22.9	6082	2.088	0.239	0.509	19.23	L
	A1656:D-161	12 58 30.19	+28 00 52.8	7169	2.268	0.300	0.864	19.60	E
	A1656:D-173	13 00 12.70	+28 04 31.6	7493	2.126	0.275	0.484	18.91	L
	A1656:D-176	12 59 31.10	+28 02 48.2	6832	2.195	0.270	0.539	18.91	L
	A1656:D-177	12 59 28.80	+28 02 25.0	5569	1.986	0.244	0.566	19.71	L
	A1656:D-181	12 58 50.60	+28 05 02.3	6018	2.140	0.236	0.419	18.81	L
	A1656:D-191	13 00 44.94	+28 05 59.5	6582	1.935	0.235	0.503	19.33	L
	A1656:D-192	13 00 35.50	+28 08 46.4	5441	1.945	0.210	0.846	20.38	L
	A1656:D-193	12 59 54.90	+28 07 41.8	7575	2.076	0.266	0.547	19.32	E
	A1656:D-204	13 01 22.80	+28 11 45.9	7643	2.155	0.249	0.773	20.04	E
	A1656:D-206	13 00 17.90	+28 12 07.7	8490	2.322	0.279	1.000	19.53	L
	A1656:D-207	13 00 08.90	+28 10 13.2	6779	2.173	0.259	0.579	19.18	E
	A1656:D-210	12 57 48.70	+28 10 48.6	7243	2.169	0.247	0.515	18.70	E
	A1656:D-230	13 00 52.09	+28 21 57.3	7667	2.321	—	0.890	19.40	L
	A1656:D-238	12 57 53.90	+28 29 58.6	7330	2.089	0.255	0.415	18.66	E
	A1656:D-239	12 57 33.88	+28 28 54.0	6276	2.258	0.290	0.971	19.58	E
	A1656:D-240	12 57 31.89	+28 28 16.0	6805	2.401	0.314	1.226	19.94	E
	I3947	12 58 52.10	+27 47 05.6	5676	2.176	0.265	0.546	18.80	E
	I3955	12 59 05.90	+27 59 48.2	7676	2.221	0.280	0.812	19.73	E
	I3957	12 59 07.91	+27 46 10.7	6389	2.191	0.285	0.567	18.95	E
	I3959	12 59 08.00	+27 47 02.7	7079	2.304	0.302	0.746	19.15	E
	I3960	12 59 07.94	+27 51 16.7	6599	2.231	0.324	0.653	19.18	L
	I3963	12 59 13.51	+27 46 27.4	6812	2.099	0.257	0.849	20.10	L
	I3976	12 59 29.20	+27 51 00.4	6817	2.388	0.306	0.478	18.36	L
	I4011	13 00 06.20	+28 00 14.7	7263	2.031	0.270	0.665	19.59	E
	I4012	13 00 07.80	+28 04 42.7	7266	2.257	0.285	0.412	18.07	E
	I4021	13 00 14.60	+28 02 28.6	5735	2.200	0.286	0.496	18.65	E
	I4026	13 00 22.00	+28 02 50.1	8220	2.134	0.277	0.803	19.85	L
	I4041	13 00 40.70	+27 59 47.9	7110	2.107	0.273	0.800	19.99	L
	I4042	13 00 42.73	+27 58 16.2	6363	2.198	0.262	0.732	19.13	L
	I4045	13 00 48.50	+28 05 26.8	6938	2.326	0.296	0.662	18.65	E
	I4051	13 00 52.56	+28 00 21.7	5026	2.379	0.332	1.223	20.62	E
	I4133	13 03 50.76	+27 59 18.1	6367	2.213	0.282	0.701	19.16	E
	N4816	12 56 12.16	+27 44 42.4	6922	2.360	0.305	1.236	20.40	E
	N4824	12 56 34.20	+27 32 20.3	7122	2.204	0.279	0.678	19.38	E
	N4839	12 57 24.27	+27 29 47.9	7364	2.433	0.316	1.582	21.26	E
	N4840	12 57 32.70	+27 36 37.0	6089	2.374	0.319	0.802	19.01	E
	N4850	12 58 21.82	+27 58 03.7	6033	2.237	0.259	0.706	19.03	E
	N4854	12 58 47.20	+27 40 29.0	8406	2.303	0.310	1.126	20.71	L
	N4860	12 59 03.79	+28 07 25.6	7951	2.419	0.338	0.893	19.27	E
	N4864	12 59 13.00	+27 58 37.2	6839	2.277	0.288	0.883	19.48	E
	N4869	12 59 22.82	+27 54 44.0	6856	2.303	0.311	0.898	19.46	E

(Continued)

Cluster	Galaxy	R.A. (J2000)	Dec. (J2000)	$cz_\odot$	$\log\sigma$	Mg_2	$\log R_e$	$\langle\mu\rangle_e$	T
	N4871	12 59 29.80	+27 57 21.2	6717	2.213	0.269	0.856	19.70	L
	N4872	12 59 33.90	+27 56 47.3	7222	2.318	0.290	0.543	18.46	E
	N4873	12 59 32.50	+27 59 00.2	5848	2.163	0.271	0.823	19.67	L
	N4874	12 59 34.77	+27 57 38.2	7213	2.412	0.317	1.804	21.66	E
	N4875	12 59 37.80	+27 54 26.5	8041	2.251	0.283	0.520	18.64	E
	N4876	12 59 44.30	+27 54 44.6	6727	2.269	0.244	0.673	19.03	E
	N4881	12 59 57.60	+28 14 50.6	6730	2.297	0.295	1.026	19.91	E
	N4882	13 00 04.20	+27 59 14.8	6400	2.211	0.254	0.915	19.88	E
	N4883	12 59 55.90	+28 02 04.9	8071	2.222	0.285	0.834	19.61	L
	N4889	13 00 07.68	+27 58 32.8	6519	2.597	0.344	1.561	20.51	E
	N4906	13 00 39.50	+27 55 26.5	7519	2.225	0.279	0.777	19.40	E
	N4908	13 00 51.48	+28 02 35.4	8749	2.296	0.285	0.837	19.24	L
	N4919	13 01 17.50	+27 48 33.0	7327	2.272	0.290	0.789	19.12	L
	N4923	13 01 31.70	+27 50 50.2	5507	2.321	0.300	0.909	19.52	E
	N4926	13 01 54.45	+27 37 28.8	7881	2.434	0.322	1.031	19.49	E
	N4927	13 01 57.50	+28 00 21.1	7754	2.447	0.334	1.047	19.98	E
	N4929	13 02 44.35	+28 02 43.1	6230	2.266	—	1.019	20.25	L
A1736	A1736:D-039	13 27 02.69	-27 26 07.8	10167	2.150	0.273	0.532	19.15	L
	A1736:D-137	13 26 11.01	-26 49 35.6	10016	2.328	0.290	0.959	19.79	E
	A1736:D-144	13 25 51.13	-26 45 03.1	10100	2.027	0.187	0.469	19.23	E
	E509-008	13 26 44.11	-27 26 23.7	10545	2.500	0.305	0.985	19.20	L
A2052	A2052:EFR-B	15 16 45.87	+07 00 14.6	9321	2.199	0.282	1.118	20.87	E
	A2052:EFR-C	15 16 53.94	+06 56 21.7	10026	2.395	0.301	0.860	19.48	E
	A2052:MKV-13	15 15 51.37	+07 01 00.9	10189	2.187	0.230	0.865	20.65	E
	A2052:MKV-60	15 17 10.91	+06 56 29.3	10953	2.368	0.282	0.631	19.09	E
	U09799	15 16 44.49	+07 01 16.6	10336	2.316	0.284	1.748	22.09	E
A2063	A2063:D-033	15 23 20.89	+08 23 38.8	9121	2.131	0.280	0.802	20.30	L
	A2063:D-034	15 23 20.47	+08 24 16.9	9756	2.020	0.198	0.672	20.09	L
	A2063:D-035	15 22 55.17	+08 24 01.8	9521	2.050	—	0.682	20.34	L
	A2063:D-046	15 23 10.45	+08 30 18.7	10755	2.197	—	0.535	18.91	L
	A2063:D-050	15 23 07.52	+08 31 41.0	9881	2.313	—	0.793	19.90	L
	A2063:D-059	15 23 15.06	+08 34 24.4	10389	2.289	—	0.730	19.60	L
	A2063:D-060	15 23 05.35	+08 36 31.9	10227	2.325	—	1.258	20.67	E
	A2063:D-065	15 22 17.97	+08 34 47.7	10821	2.138	0.246	0.797	20.24	L
	A2063:D-071	15 23 15.20	+08 39 47.8	9202	2.370	—	0.387	18.79	E
	A2063:D-072	15 23 14.06	+08 38 42.3	10542	2.330	0.300	0.744	19.60	E
	A2063:D-073	15 23 10.92	+08 38 02.1	10505	2.235	0.279	0.728	19.62	L
	A2063:D-074	15 23 06.92	+08 40 35.8	10139	2.268	—	0.423	18.81	L
	A2063:D-077	15 22 56.46	+08 39 01.9	10032	2.392	—	0.316	18.01	L
	A2063:D-089	15 23 15.98	+08 44 54.4	10094	2.337	—	0.622	19.41	L
	A2063:D-090	15 22 52.81	+08 44 41.6	11269	2.351	—	0.707	19.58	L
	I1116	15 21 55.39	+08 25 24.5	11758	2.410	0.289	1.099	20.02	E
A2199	A2199:B-004	16 28 44.42	+39 28 26.1	8151	2.177	0.310	1.315	21.42	L
	A2199:B-005	16 27 55.33	+39 15 30.1	8710	2.311	0.284	0.948	19.94	E
	A2199:B-008	16 27 03.69	+39 31 37.5	10157	2.192	0.263	0.944	20.01	E
	A2199:B-015	16 28 23.29	+39 34 12.8	8773	2.241	0.286	0.890	20.09	E

(Continued)

Cluster	Galaxy	R.A. (J2000)	Dec. (J2000)	$cz_{\odot}$	$\log\sigma$	Mg_2	$\log R_e$	$\langle\mu\rangle_e$	T
	A2199:B-019	16 29 20.80	+39 49 13.0	7905	2.383	0.264	0.537	18.67	L
	A2199:B-020	16 27 55.99	+39 16 52.7	9625	2.272	0.298	0.641	19.10	E
	A2199:B-021	16 30 20.30	+39 48 15.0	8825	2.209	0.295	0.631	19.22	E
	A2199:B-024	16 28 31.10	+39 31 15.0	10261	2.462	0.323	0.644	18.84	L
	A2199:B-026	16 29 45.10	+39 48 37.0	9131	2.313	0.273	0.526	18.74	E
	A2199:B-028	16 26 59.80	+39 19 11.0	8924	2.209	0.246	0.631	19.21	L
	A2199:B-029	16 28 46.18	+39 27 46.2	7850	2.102	0.272	0.800	20.16	L
	A2199:B-030	16 28 45.03	+39 26 13.2	10616	2.342	0.303	0.524	18.86	L
	A2199:B-033	16 28 24.70	+39 44 27.0	9304	2.198	0.250	0.560	19.06	L
	A2199:B-034	16 29 07.22	+39 29 44.2	8712	1.998	0.220	0.809	20.35	E
	A2199:B-035	16 27 17.90	+39 08 35.0	8694	2.274	0.315	0.441	18.62	E
	A2199:B-038	16 28 59.80	+39 41 02.0	8400	2.242	0.299	0.510	19.03	E
	A2199:B-044	16 27 32.40	+39 34 14.0	8035	2.061	0.285	0.589	19.48	L
	A2199:B-045	16 28 57.30	+39 42 30.0	9392	2.253	0.296	0.395	18.50	E
	A2199:B-047	16 29 07.60	+39 08 54.0	8132	2.156	0.240	0.496	19.13	L
	A2199:B-048	16 27 11.10	+39 18 18.0	7835	2.223	0.246	0.468	18.91	E
	A2199:B-050	16 28 31.20	+39 43 40.0	9380	2.282	0.296	0.531	19.22	L
	A2199:B-054	16 28 19.80	+39 57 32.0	9513	2.150	0.273	0.439	18.83	E
	A2199:B-061	16 28 44.50	+39 30 55.0	8237	2.437	0.305	0.318	18.08	E
	A2199:B-066	16 28 49.50	+39 36 57.0	9174	2.279	0.301	0.266	18.12	L
	A2199:B-069	16 27 57.52	+39 15 09.9	8954	2.353	0.326	0.474	18.53	L
	A2199:B-073	16 28 45.86	+39 36 34.8	8046	2.219	0.268	0.316	18.71	E
	A2199:B-074	16 28 36.10	+39 32 02.0	8527	2.390	0.267	0.299	17.92	E
	A2199:B-084	16 28 33.91	+39 32 56.0	9688	2.140	0.263	0.303	18.73	E
	A2199:B-087	16 28 14.24	+39 32 44.2	7858	1.932	0.239	0.717	20.82	E
	A2199:B-095	16 28 45.63	+39 31 39.7	8267	2.195	0.272	0.403	18.93	E
	A2199:EFR-H	16 31 19.19	+39 09 02.6	8886	2.381	0.286	0.709	19.21	E
	A2199:EFR-O	16 24 17.61	+39 12 39.6	9048	2.295	0.309	0.997	20.23	E
	A2199:L-0163	16 28 35.85	+39 33 13.0	8895	2.169	0.283	-0.150	17.36	L
	A2199:RS-008	16 25 41.82	+39 36 00.0	9035	2.398	0.295	0.856	19.38	E
	A2199:RS-163	16 31 22.60	+39 10 04.0	8906	2.328	0.298	0.601	18.98	L
	N6146	16 25 10.36	+40 53 34.3	8738	2.430	0.285	1.004	18.94	E
	N6158	16 27 40.96	+39 22 57.5	8944	2.287	0.277	0.929	19.60	E
	N6160	16 27 41.20	+40 55 36.1	9408	2.365	0.291	1.367	20.85	E
	N6166	16 28 38.31	+39 33 03.3	9374	2.474	0.321	1.862	22.04	E
	N6173	16 29 44.89	+40 48 41.8	8824	2.448	0.309	1.292	20.00	E
A2634	A2634:B-013	23 38 28.61	+26 49 06.8	9480	2.204	0.247	0.737	19.08	L
	A2634:B-016	23 39 13.44	+27 32 54.9	9302	2.341	0.323	0.788	19.35	L
	A2634:B-021	23 40 33.61	+27 14 32.4	10849	2.363	0.277	0.824	19.66	E
	A2634:B-030	23 38 12.54	+26 29 39.3	9216	2.251	0.288	0.465	18.52	E
	A2634:D-031	23 39 58.59	+26 50 02.8	8705	2.366	0.281	0.974	20.10	E
	A2634:D-036	23 38 44.18	+26 51 02.6	9032	2.293	0.302	0.655	19.27	L
	A2634:D-038	23 38 18.63	+26 53 11.2	9320	2.381	0.274	0.715	19.22	E
	A2634:D-043	23 37 20.11	+26 52 40.8	8521	2.383	0.285	0.689	19.17	L
	A2634:D-056	23 38 34.47	+26 58 46.0	8512	2.379	0.312	0.276	17.72	E
	A2634:D-057	23 38 29.34	+26 58 42.1	9554	2.339	0.322	0.912	19.73	E
	A2634:D-061	23 37 46.65	+26 58 50.6	11051	2.089	0.261	0.476	18.75	L
	A2634:D-068	23 39 02.69	+27 06 08.9	9962	2.364	0.294	0.626	19.34	E
	A2634:D-069	23 38 53.93	+27 02 45.6	9649	2.147	0.256	-0.040	17.06	L

(Continued)

Cluster	Galaxy	R.A. (J2000)	Dec. (J2000)	$cz_\odot$	$\log\sigma$	Mg_2	$\log R_e$	$\langle\mu\rangle_e$	T
	A2634:D-071	23 38 49.26	+27 07 22.2	8899	2.237	0.262	0.288	18.26	L
	A2634:D-073	23 38 42.07	+27 07 06.8	9498	2.224	0.277	0.311	18.30	L
	A2634:D-074	23 38 36.28	+27 01 46.5	8424	2.318	0.299	0.734	19.46	L
	A2634:D-075	23 38 33.26	+27 02 05.2	9863	2.276	0.295	0.458	18.90	E
	A2634:D-076	23 38 29.58	+27 02 03.6	8118	2.311	0.293	0.469	18.43	E
	A2634:D-077	23 38 29.53	+27 01 53.0	9090	2.515	0.331	1.313	20.25	E
	A2634:D-079	23 38 20.68	+27 03 02.8	10164	2.213	0.295	0.496	19.05	L
	A2634:D-080	23 38 18.62	+27 02 06.8	9576	2.265	0.283	0.367	18.60	E
	A2634:D-082	23 37 55.38	+27 06 01.7	10168	2.038	0.214	0.735	20.33	L
	A2634:D-087	23 37 26.01	+27 04 17.3	10004	2.096	—	1.022	20.75	L
	A2634:D-093	23 40 03.22	+27 10 00.6	8985	2.234	0.264	0.660	19.45	L
	A2634:D-102	23 38 56.24	+27 09 41.4	9189	2.196	0.283	0.397	18.35	L
	A2634:D-104	23 38 46.26	+27 10 20.1	9785	2.169	0.275	0.526	19.20	L
	A2634:D-107	23 38 22.88	+27 09 27.8	9264	2.291	0.262	0.667	18.95	E
	A2634:D-119	23 38 50.61	+27 16 03.8	9289	2.445	0.314	0.831	18.92	E
	A2634:D-130	23 38 13.66	+27 24 50.4	9349	2.357	0.282	0.645	18.91	L
	A2634:L-BO3C	23 40 50.54	+26 49 51.2	8733	2.224	0.265	0.797	19.80	E
	A2634:L-BU5	23 40 19.10	+26 33 39.0	8701	2.427	0.309	1.247	20.69	L
	I5341	23 38 26.82	+26 59 06.4	10835	2.342	0.308	0.874	19.72	E
	I5342	23 38 38.80	+27 00 40.9	9282	2.345	0.299	0.787	19.34	E
	N7728	23 40 00.95	+27 07 58.6	9409	2.530	0.331	1.103	19.37	E
	N7735	23 42 17.30	+26 13 53.0	9606	2.443	0.294	1.210	20.14	E
A2657	A2657:D-031	23 44 16.10	+09 02 56.3	11877	2.370	0.353	0.915	19.98	E
	A2657:D-043	23 44 56.41	+09 07 53.6	11938	2.348	0.299	0.567	19.49	L
	A2657:D-064	23 45 17.21	+09 16 15.8	12276	2.364	0.342	0.870	19.95	E
	A2657:D-070	23 44 43.91	+09 12 55.2	12387	2.314	0.282	0.498	18.76	E
	A2657:D-071	23 44 30.50	+09 15 48.2	12347	2.404	0.299	0.938	19.93	L
	A2657:D-072	23 44 27.78	+09 16 00.2	12596	2.235	0.300	0.349	18.56	E
A2806	A2806:SMC-C	00 40 04.23	-56 10 50.2	8502	2.344	0.296	0.907	19.54	E
	A2806:SMC-D	00 40 24.59	-56 13 22.9	8714	2.124	0.290	0.714	19.57	L
	A2806:SMC-E	00 40 43.21	-55 55 46.9	7712	2.177	0.300	0.666	19.24	E
	A2806:SMC-F	00 37 56.94	-56 03 43.4	8645	2.060	0.256	0.677	19.48	L
	N0212	00 40 13.31	-56 09 10.8	8260	2.344	0.340	1.395	21.15	E
	N0215	00 40 48.93	-56 12 51.1	8239	2.464	0.300	1.015	19.34	E
A2877	A2877:D-011	01 09 49.81	-46 12 24.9	7299	2.105	—	0.704	19.92	L
	A2877:D-021	01 09 35.48	-46 03 18.5	8411	2.088	—	0.489	18.86	L
	A2877:D-025	01 10 06.59	-45 55 54.9	7342	2.098	—	0.620	19.63	L
	A2877:D-028	01 09 37.79	-45 53 52.3	6735	2.312	—	0.749	19.29	L
	A2877:D-033	01 10 19.84	-45 51 18.8	6951	2.077	—	1.125	21.12	L
	A2877:D-035	01 09 47.27	-45 52 40.9	6921	2.051	—	0.327	18.57	E
	A2877:D-037	01 08 05.01	-45 51 18.5	7275	2.159	—	0.618	19.16	L
	A2877:D-040	01 10 47.72	-45 47 01.9	7444	2.051	—	0.917	20.66	L
	A2877:D-042	01 10 33.47	-45 47 40.8	8303	2.247	—	0.835	19.54	L
	A2877:D-045	01 10 47.21	-45 45 24.3	6974	2.339	—	0.686	19.27	L
	A2877:D-048	01 09 20.47	-45 40 56.0	7149	2.150	—	0.506	18.83	L
	A2877:FCP-24	01 10 01.48	-45 58 08.0	8043	1.908	—	0.412	19.29	E
	A2877:FCP-30	01 09 44.50	-45 58 35.0	7374	1.702	—	0.995	22.03	E

(Continued)

Cluster	Galaxy	R.A. (J2000)	Dec. (J2000)	$cz_\odot$	$\log\sigma$	Mg_2	$\log R_e$	$\langle\mu\rangle_e$	T
	A2877:FCP-31	01 09 45.00	-45 59 23.4	6357	1.913	—	0.466	19.87	E
	A2877:FCP-32	01 09 39.65	-45 59 31.0	7123	2.230	—	0.207	17.91	E
	A2877:FCP-48	01 09 00.95	-45 48 05.0	7447	1.919	—	0.829	20.62	E
	E243-041	01 08 51.88	-45 49 58.5	7288	2.378	—	0.766	18.74	L
	E243-045	01 09 04.58	-45 46 23.8	7758	2.343	—	1.164	19.92	E
	E243-049	01 10 27.72	-46 04 28.0	6730	2.362	—	0.801	19.19	L
	E243-052	01 11 27.70	-45 56 16.6	8212	2.173	—	1.046	20.01	L
	I1633	01 09 55.35	-45 55 52.8	7263	2.595	0.337	1.219	19.25	E
A3193	A3193:SMC-B	03 58 12.49	-52 27 09.5	10114	2.151	0.280	0.677	19.47	L
	A3193:SMC-F	03 56 40.80	-51 33 28.0	10938	2.321	0.317	0.947	20.09	E
	N1500	03 58 13.96	-52 19 43.8	10122	2.451	0.334	1.097	19.99	E
	N1506	04 00 21.28	-52 34 26.6	10259	2.405	0.324	1.132	20.16	E
A3381	A3381:D-021	06 09 32.97	-33 50 30.7	11313	2.285	0.311	0.651	19.65	L
	A3381:D-025	06 06 47.50	-33 48 54.6	11476	2.290	0.290	1.102	20.22	E
	A3381:D-033	06 10 55.36	-33 44 13.7	11679	2.248	0.243	0.490	18.18	L
	A3381:D-034	06 10 49.27	-33 43 49.2	11357	2.368	0.252	0.820	19.95	L
	A3381:D-037	06 09 52.73	-33 41 23.1	11156	1.973	0.219	0.570	20.19	L
	A3381:D-055	06 09 54.49	-33 35 33.2	11557	2.326	0.328	1.193	20.86	E
	A3381:D-056	06 09 49.29	-33 35 47.8	11308	2.334	0.317	0.819	19.94	L
	A3381:D-064	06 10 34.31	-33 31 37.1	11489	2.129	0.196	0.500	19.38	L
	A3381:D-067	06 09 59.07	-33 32 58.5	11257	2.054	0.260	0.230	18.44	E
	A3381:D-068	06 09 58.36	-33 33 08.5	11316	2.178	0.286	0.680	19.75	E
	A3381:D-073	06 10 17.62	-33 27 28.9	11215	2.116	0.252	0.670	19.90	L
	A3381:D-075	06 10 10.78	-33 28 49.4	11465	2.331	0.277	0.770	19.64	E
	A3381:D-100	06 11 07.28	-33 18 23.5	11469	2.294	0.286	0.800	19.53	L
	A3381:D-112	06 11 40.49	-33 07 26.9	11040	2.331	0.290	1.070	20.28	E
A3389	A3389:D-043	06 21 13.85	-65 00 59.4	7844	2.147	0.287	0.807	19.58	L
	A3389:D-048	06 23 48.97	-64 57 17.1	7243	2.209	0.262	0.671	19.30	E
	A3389:D-049	06 23 07.44	-64 55 52.0	8477	2.296	0.281	0.516	18.57	E
	A3389:D-053	06 22 04.85	-64 57 37.9	8355	2.084	0.260	0.638	19.48	E
	A3389:D-060	06 22 19.57	-64 14 08.8	7836	2.296	0.273	0.829	18.88	E
	N2230	06 21 27.47	-64 59 37.2	8074	2.450	0.312	1.240	20.02	E
	N2235	06 22 22.04	-64 56 05.5	8335	2.403	0.267	1.438	20.57	E
A3526	A3526:D-009	12 51 00.30	-41 43 25.0	2459	2.221	0.217	0.869	19.19	E
	A3526:D-015	12 51 56.40	-41 32 21.0	3722	2.096	—	0.865	19.44	L
	A3526:D-026	12 50 57.48	-41 23 48.0	4496	1.797	—	1.159	20.93	L
	A3526:D-027	12 50 07.74	-41 23 52.8	4969	2.042	0.264	0.872	19.22	E
	A3526:D-033	12 51 37.25	-41 18 13.2	3450	2.120	—	0.762	18.83	L
	A3526:D-035	12 50 11.80	-41 17 58.2	4193	1.836	—	0.724	20.03	E
	A3526:D-036	12 49 18.54	-41 20 08.6	3142	1.908	—	0.374	18.43	E
	A3526:D-038	12 48 53.86	-41 19 07.4	2334	1.999	—	0.216	17.89	E
	A3526:D-040	12 48 31.03	-41 18 24.1	3012	1.896	—	0.629	19.46	E
	A3526:D-041	12 52 22.56	-41 16 54.5	4678	2.309	—	0.826	18.78	L
	A3526:D-046	12 52 40.89	-41 13 47.2	4839	2.155	—	0.466	18.15	L
	A3526:D-047	12 51 50.75	-41 11 11.1	4745	1.721	—	0.919	20.69	E
	A3526:D-049	12 50 11.48	-41 13 17.1	2968	2.080	0.305	0.745	18.96	E

(Continued)

Cluster	Galaxy	R.A. (J2000)	Dec. (J2000)	$cz_\odot$	$\log\sigma$	Mg_2	$\log R_e$	$\langle\mu\rangle_e$	T
	A3526:D-050	12 49 51.57	-41 13 34.2	2182	2.067	0.261	1.025	19.83	E
	A3526:D-052	12 47 59.76	-41 13 11.0	4108	1.794	—	1.308	21.87	L
	A3526:D-059	12 51 48.00	-40 59 37.6	2676	1.885	—	0.834	19.93	L
	A3526:FCP-E44	12 49 42.01	-41 13 46.4	3709	1.539	—	0.812	21.13	Q
	A3526:FCP-JF6	12 47 59.05	-41 11 21.7	3131	1.685	—	1.385	22.45	L
	E322-075	12 46 25.96	-40 45 04.1	4520	2.171	0.264	1.069	19.19	L
	E322-081	12 47 21.68	-41 14 16.7	3097	2.388	0.289	1.126	19.07	L
	E322-089	12 48 22.83	-41 07 24.7	3700	2.122	—	0.785	18.99	E
	E322-099	12 49 26.19	-41 29 23.5	4288	2.068	—	0.951	19.15	L
	E322-100	12 49 26.68	-41 27 47.8	4841	1.986	—	1.392	20.96	L
	E322-101	12 49 34.41	-41 03 19.4	2089	2.206	0.305	0.993	19.33	L
	E322-102	12 49 37.84	-41 23 17.4	3691	2.023	—	1.041	19.54	L
	E323-005	12 50 12.26	-41 30 54.4	2513	2.332	—	0.835	18.11	L
	E323-008	12 50 34.39	-41 28 15.9	5315	2.133	0.223	1.035	19.59	L
	E323-009	12 50 42.96	-41 25 49.7	2394	2.121	—	0.887	19.07	L
	E323-034	12 53 26.01	-41 12 11.8	4338	2.374	0.293	1.258	18.99	E
	N4616	12 42 16.40	-40 38 29.5	4585	2.242	0.267	1.373	20.50	E
	N4645	12 44 10.18	-41 44 58.0	2638	2.284	0.279	1.136	18.47	E
	N4661	12 45 14.69	-40 49 24.1	2566	2.178	0.262	1.001	20.10	E
	N4683	12 47 42.27	-41 31 42.4	3566	2.210	—	1.228	19.78	L
	N4696	12 48 49.12	-41 18 41.4	2970	2.399	0.277	2.226	21.74	E
	N4706	12 49 54.15	-41 16 46.4	3856	2.328	0.298	0.987	18.69	L
	N4709	12 50 03.88	-41 22 56.0	4682	2.389	0.328	1.499	19.91	E
	N4729	12 51 46.29	-41 07 56.4	3341	2.155	0.277	1.276	19.61	E
	N4730	12 52 00.47	-41 08 50.3	2092	2.323	0.305	1.023	18.96	L
	N4743	12 52 15.98	-41 23 26.4	3041	2.108	0.262	1.148	19.43	L
	N4767	12 53 52.70	-39 42 52.3	3001	2.319	0.291	1.340	19.21	E
	N4946	13 05 29.23	-43 35 27.5	3033	2.308	0.303	1.339	19.83	E
A3537	A3537:SMC-156	12 58 41.86	-32 07 17.1	5215	2.233	0.282	0.914	19.37	L
	E382-002	13 03 01.12	-32 50 06.2	4846	2.331	0.300	0.892	18.84	E
	E443-024	13 01 00.80	-32 26 29.2	5116	2.459	0.310	1.377	19.68	E
	I3986	13 01 32.63	-32 17 07.9	4606	2.442	0.313	1.216	19.25	E
A3558	A3558:FCP-02	13 27 29.62	-31 23 24.9	14415	2.562	—	1.112	20.18	E
	A3558:FCP-03	13 27 54.95	-31 32 18.9	15542	2.525	—	1.021	20.00	E
	A3558:FCP-04	13 27 50.68	-31 34 06.8	12344	2.345	—	0.664	19.66	L
	A3558:FCP-05	13 27 39.08	-31 32 23.3	14298	2.257	—	1.134	20.93	E
	A3558:FCP-06	13 27 34.90	-31 32 58.2	12909	2.368	—	0.619	19.10	E
	A3558:FCP-08	13 27 45.56	-31 47 51.5	13263	2.433	—	0.987	19.86	E
	A3558:FCP-09	13 28 02.62	-31 45 21.0	12864	2.418	—	0.746	19.29	E
	A3558:FCP-13	13 28 49.49	-31 34 34.8	15711	2.383	—	0.875	19.91	E
	A3558:FCP-14	13 28 54.21	-31 29 17.6	15799	2.483	—	0.649	19.23	E
	A3558:FCP-15	13 29 09.98	-31 32 49.1	14773	2.137	—	0.578	19.56	E
	A3558:FCP-16	13 29 20.70	-31 32 25.2	15238	2.324	—	0.800	19.67	E
	A3558:FCP-17	13 29 28.10	-31 33 05.4	15415	2.409	—	1.097	20.37	E
	A3558:FCP-18	13 28 38.62	-31 20 49.0	15672	2.482	—	0.775	19.51	E
	A3558:FCP-21	13 28 10.44	-31 23 10.2	13211	2.305	—	0.722	19.77	E
	A3558:FCP-24	13 27 46.62	-31 27 15.7	13602	2.434	—	0.542	18.89	L
	A3558:FCP-25	13 27 44.57	-31 28 42.9	13973	2.322	—	0.330	18.47	E

(Continued)

Cluster	Galaxy	R.A. (J2000)	Dec. (J2000)	$cz_\odot$	$\log\sigma$	Mg_2	$\log R_e$	$\langle\mu\rangle_e$	T
	A3558:FCP-26	13 27 48.51	-31 28 45.9	15663	2.392	—	0.506	19.00	L
	A3558:FCP-29	13 28 02.22	-31 31 44.5	13123	2.202	—	0.579	19.38	E
	A3558:FCP-31	13 28 47.23	-31 41 35.1	14136	2.110	—	0.846	20.65	L
	A3558:FCP-33	13 27 04.28	-31 20 07.9	14058	2.247	—	0.563	19.64	L
	A3558:FCP-34	13 26 55.90	-31 24 46.4	14197	2.414	—	0.382	18.59	L
	A3558:FCP-35	13 26 55.96	-31 25 26.7	13106	2.055	—	0.689	20.11	L
	A3558:FCP-50	13 28 02.29	-31 34 44.5	15047	2.351	—	0.410	18.72	E
	A3558:FCP-56	13 27 24.67	-31 40 43.0	14967	2.071	—	0.600	19.98	L
	A3558:FCP-57	13 27 27.02	-31 41 07.0	13576	2.283	—	0.614	19.99	E
	E444-046	13 27 56.85	-31 29 43.9	14065	2.467	—	1.897	22.35	E
A3570	A3570:SMC-50	13 45 46.12	-37 56 46.2	12220	2.289	0.260	0.866	19.80	L
	A3570:SMC-64	13 44 00.44	-38 17 11.6	9652	2.116	0.266	0.719	19.88	E
	E325-004	13 43 33.36	-38 10 30.5	10177	2.533	0.333	1.096	19.50	E
	E325-013	13 45 17.41	-38 10 23.2	11225	2.348	0.289	0.716	19.18	E
	E325-016	13 46 24.16	-37 58 14.8	11318	2.447	0.304	0.910	19.46	E
A3571	A3571:SMC-10	13 49 25.59	-33 36 50.1	11610	2.292	0.224	0.898	19.78	E
	A3571:SMC-112	13 52 38.36	-32 53 17.3	11161	2.412	0.306	0.701	19.30	E
	A3571:SMC-13	13 48 58.08	-32 51 26.1	11652	2.397	0.304	0.661	19.00	E
	A3571:SMC-164	13 49 45.42	-32 22 52.4	11017	2.456	0.282	0.837	19.23	E
	A3571:SMC-171	13 48 06.14	-32 30 31.7	11723	2.360	0.296	0.967	20.10	E
	A3571:SMC-21	13 48 14.26	-33 22 57.8	12213	2.369	0.285	0.843	19.24	E
	A3571:SMC-29	13 47 48.91	-33 17 25.4	12303	2.242	0.265	0.607	19.19	L
	A3571:SMC-32	13 47 37.28	-32 45 04.7	11595	2.385	0.312	0.516	18.41	E
	A3571:SMC-38	13 47 30.94	-33 35 18.8	11275	2.529	0.317	0.641	18.64	L
	A3571:SMC-40	13 47 16.47	-32 49 00.4	10799	2.128	0.264	0.554	19.45	E
	A3571:SMC-44	13 47 00.73	-33 16 48.8	10586	2.206	0.280	0.678	19.66	L
A3574	A3574:W-024	13 47 23.34	-30 25 01.0	4310	2.318	0.257	1.230	19.62	L
	A3574:W-074	13 50 45.39	-29 59 54.5	4238	2.345	0.299	0.720	18.54	L
	E445-028	13 47 17.74	-29 48 33.3	4557	2.349	0.305	0.890	18.73	E
	E445-040	13 48 38.64	-30 48 37.7	5072	2.152	0.258	1.560	21.37	L
	E445-054	13 50 32.39	-30 02 53.9	5392	1.960	0.171	0.950	19.72	L
	E445-059	13 51 39.47	-30 29 21.7	4555	2.294	0.285	1.090	19.60	L
	I4329	13 49 05.17	-30 17 43.7	4562	2.448	0.329	1.490	20.18	E
	N5304	13 50 01.41	-30 34 42.0	3730	2.338	0.279	1.289	20.09	E
A3581	A3581:SMC-75	14 07 44.13	-27 04 58.8	6495	2.314	0.282	0.871	19.18	E
	A3581:SMC-76	14 07 35.17	-27 02 07.2	5903	2.128	0.272	0.505	18.70	E
	A3581:SMC-77	14 07 20.92	-27 00 38.8	5972	2.262	0.305	0.595	18.83	L
	A3581:SMC-78	14 07 16.96	-26 32 59.9	6005	2.331	0.287	0.868	19.23	E
	E510-054	14 04 03.31	-26 12 57.2	6037	2.269	0.254	1.085	19.52	E
	E510-063	14 06 16.07	-25 47 57.2	6966	2.424	0.323	0.751	18.53	L
	E510-066	14 07 15.62	-27 09 30.9	7302	2.360	0.296	1.107	19.77	E
	I4374	14 07 29.76	-27 01 04.2	6543	2.428	0.328	1.389	20.60	E
A3656	A3656:SMC-I	20 00 55.65	-38 41 48.6	6303	2.318	0.289	0.803	18.86	L
	A3656:SMC-P	20 03 26.80	-38 24 18.1	6359	2.269	0.291	1.048	19.62	E
	A3656:SMC-S	20 01 30.63	-39 03 47.5	5689	2.211	0.270	0.557	18.71	L

(Continued)

Cluster	Galaxy	R.A. (J2000)	Dec. (J2000)	$cz_\odot$	$\log\sigma$	Mg_2	$\log R_e$	$\langle\mu\rangle_e$	T
	I4926	20 00 12.13	-38 34 42.3	5624	2.393	0.305	1.070	19.21	E
	I4931	20 00 49.97	-38 34 35.9	6000	2.457	0.318	1.292	19.59	E
A3716	A3716:D-051	20 50 30.29	-52 54 02.1	12878	2.252	—	0.510	18.88	L
	A3716:D-061	20 52 34.23	-52 50 44.2	13054	2.085	—	0.439	19.54	L
	A3716:D-065	20 51 52.40	-52 49 49.5	13604	2.431	—	0.883	19.16	L
	A3716:D-067	20 51 35.13	-52 51 41.4	12335	2.261	—	0.625	19.68	E
	A3716:D-078	20 52 09.95	-52 47 45.4	13951	2.446	—	0.865	19.40	E
	A3716:D-080	20 51 57.46	-52 48 06.0	13443	2.398	—	0.917	19.68	E
	A3716:D-081	20 51 51.16	-52 47 41.3	14592	2.273	—	0.501	19.31	L
	A3716:D-084	20 51 46.84	-52 47 01.1	12547	2.403	—	0.558	18.76	E
	A3716:D-090	20 50 03.32	-52 47 42.3	12790	2.281	—	0.773	19.85	E
	A3716:D-098	20 52 00.23	-52 45 17.0	13007	2.390	—	1.184	20.69	E
	A3716:D-099	20 51 56.83	-52 45 10.3	13742	2.434	—	0.760	19.02	E
	A3716:D-116	20 51 19.14	-52 40 40.3	13342	2.507	—	0.541	18.60	E
	A3716:D-117	20 51 16.06	-52 41 25.5	13146	2.332	—	0.747	19.57	E
	A3716:D-135	20 53 04.05	-52 35 15.1	14932	2.323	—	0.732	19.38	E
	A3716:D-141	20 51 59.11	-52 35 04.8	14586	2.279	—	0.260	18.34	L
	E187-020	20 51 19.98	-52 38 09.4	13105	2.504	—	0.898	19.38	L
A3733	A3733:SMC-A	21 02 03.66	-27 52 16.8	12621	2.341	0.308	0.942	19.82	E
	A3733:SMC-B	21 02 03.02	-28 23 54.2	10056	2.265	0.288	0.981	19.75	E
	A3733:SMC-C	21 01 59.42	-28 15 36.3	9957	2.347	0.307	0.892	19.77	E
	A3733:SMC-G	21 01 55.62	-27 45 56.6	11993	2.073	0.240	1.000	20.74	L
	A3733:SMC-H	21 01 38.48	-27 53 58.0	11629	2.325	0.292	0.728	19.58	E
	A3733:SMC-I	21 01 38.78	-28 18 09.3	11909	2.198	0.274	0.756	19.78	E
	A3733:SMC-K	21 03 45.74	-28 02 06.4	9840	2.140	0.208	0.736	19.89	L
	E464-018	21 03 01.43	-28 20 19.6	11896	2.421	0.325	1.157	20.08	E
	N6998	21 01 37.68	-28 01 54.9	11884	2.453	0.338	1.149	20.45	E
	N6999	21 01 59.54	-28 03 32.1	10994	2.463	0.337	1.236	20.80	E
A3742	E235-039	21 02 43.48	-48 21 25.9	4865	2.210	0.301	0.883	19.26	E
	E235-049	21 04 40.95	-48 11 24.2	5195	2.366	0.290	0.980	18.74	E
	E286-029	21 03 04.23	-47 08 45.3	4988	2.346	0.244	0.817	19.21	E
	E286-049	21 06 47.51	-47 11 16.8	5289	2.322	0.309	1.053	19.36	L
	N7014	21 07 52.25	-47 10 46.6	4851	2.470	0.332	1.050	18.93	L
A3744	A3744:SMC-E	21 07 22.08	-25 27 20.2	11382	2.425	0.301	0.540	19.10	L
	A3744:SMC-I	21 07 32.35	-25 38 34.7	12270	2.302	0.272	0.664	18.98	E
	A3744:SMC-Q	21 06 03.73	-26 10 29.1	11980	2.265	0.298	0.911	20.18	E
	A3744:SMC-T	21 06 00.66	-26 06 16.3	11967	2.263	0.283	0.694	19.68	E
	N7016	21 07 16.19	-25 28 08.4	11041	2.478	0.342	1.068	19.87	E
A4038	A4038:D-032	23 48 20.43	-28 13 54.5	8101	2.485	0.325	0.850	19.27	E
	A4038:D-038	23 48 25.73	-28 11 21.8	9012	2.146	0.293	0.510	18.77	L
	A4038:D-043	23 47 43.17	-28 08 38.1	8114	2.286	0.276	0.960	20.11	L
	A4038:D-044	23 47 45.23	-28 09 49.1	9541	2.222	0.293	-0.040	17.02	E
	A4038:D-045	23 47 43.35	-28 10 21.3	8292	2.108	0.223	0.670	19.85	E
	A4038:D-051	23 47 47.16	-28 08 05.9	8221	2.189	—	0.260	18.57	L
	A4038:D-053	23 47 45.78	-28 06 27.3	8166	1.803	—	0.270	19.33	L

(Continued)

Cluster	Galaxy	R.A. (J2000)	Dec. (J2000)	$cz_\odot$	$\log\sigma$	Mg_2	$\log R_e$	$\langle\mu\rangle_e$	T
	A4038:D-055	23 47 31.76	-28 06 25.5	8459	2.248	0.301	0.520	18.70	E
	A4038:D-060	23 47 16.84	-28 07 27.2	8932	2.113	0.245	0.600	19.28	E
	A4038:D-066	23 47 30.62	-28 02 34.9	8234	2.029	—	0.510	19.76	L
	A4038:D-067	23 47 20.11	-28 03 46.4	8353	2.011	—	0.800	20.95	L
	A4038:D-068	23 47 14.15	-28 01 48.4	8374	2.096	—	0.230	18.90	E
	A4038:D-070	23 46 58.16	-28 02 55.2	8034	2.133	0.280	0.090	18.12	E
	A4038:D-076	23 47 22.37	-27 58 32.6	7469	2.147	—	0.620	19.66	L
	A4038:D-083	23 47 11.01	-27 55 43.8	8798	2.106	—	0.830	20.15	L
	I5350	23 47 14.62	-27 57 27.8	8574	2.338	0.284	0.880	19.34	L
	I5353	23 47 28.59	-28 06 34.1	8238	2.425	0.321	1.200	20.19	E
	I5354	23 47 28.43	-28 08 07.4	8345	2.416	0.286	0.830	19.16	E
	I5358	23 47 45.03	-28 08 26.7	8637	2.347	0.334	1.320	20.90	E
A4049	A4038:D-033	23 47 49.50	-28 12 13.2	9573	1.941	—	0.670	20.48	L
	A4038:D-037	23 48 26.96	-28 08 59.1	9288	1.946	—	0.690	20.31	L
	A4038:D-039	23 48 19.05	-28 10 44.3	10568	2.109	—	0.730	20.07	L
	A4038:D-049	23 48 26.75	-28 06 36.9	9842	2.100	—	0.440	19.26	L
	A4038:D-052	23 47 49.50	-28 05 11.5	9690	1.837	0.231	0.650	20.57	E
	A4038:D-059	23 47 23.24	-28 07 08.6	9766	2.233	—	0.730	19.85	L
	A4038:D-065	23 48 23.22	-28 04 29.6	10244	2.338	—	1.030	20.12	L
	A4049:D-047	23 51 34.80	-28 04 28.6	9687	2.441	0.360	0.685	18.89	L
	A4049:D-055	23 51 54.37	-27 55 48.0	8766	2.387	0.312	0.896	19.48	L
	A4049:SMC-D	23 52 24.15	-29 01 22.3	8661	2.365	0.296	0.718	18.86	E
	A4049:SMC-E	23 52 10.10	-29 04 41.5	8682	2.338	0.300	0.914	19.23	E
	I5362	23 51 36.62	-28 21 52.9	8266	2.432	0.311	1.163	19.85	E
H0122	H0122:PP-H01051	01 21 05.63	+33 22 44.1	5228	2.099	0.267	0.799	19.31	E
	I1673	01 20 46.35	+33 02 41.8	5083	2.260	0.276	0.555	18.06	E
	N0499	01 23 11.51	+33 27 37.3	4384	2.404	0.332	1.244	19.36	E
	N0501	01 23 22.40	+33 25 58.7	5004	2.208	0.304	0.728	19.08	E
	N0507	01 23 39.77	+33 15 23.2	4929	2.463	0.298	1.367	19.63	L
	N0508	01 23 40.59	+33 16 51.5	5509	2.336	0.311	1.144	19.89	E
	N0528	01 25 33.63	+33 40 17.3	4791	2.402	—	1.029	19.14	E
	N0529	01 25 40.22	+34 42 47.1	4803	2.365	0.294	1.123	19.10	E
J8	I1803	02 29 13.98	+23 04 57.7	9577	2.563	0.350	1.094	19.43	E
	I1806	02 29 34.95	+22 56 35.6	10210	2.333	0.313	1.065	20.24	E
	I1807	02 30 31.00	+22 56 59.0	9034	2.308	0.277	0.756	19.00	E
	J8:EFR-A	02 30 16.49	+23 09 11.7	8553	2.494	0.320	0.832	19.04	E
	J8:EFR-C	02 29 54.42	+23 05 49.5	9540	2.371	0.331	1.347	20.88	E
	J8:EFR-D	02 29 49.91	+23 06 29.6	9610	2.182	0.292	1.578	21.98	E
	J8:EFR-H	02 28 39.84	+23 00 43.3	9097	2.123	0.166	0.555	18.77	L
	J8:EFR-I	02 29 13.98	+22 57 57.7	9229	2.300	0.313	0.879	19.84	E
	J8:EFR-K	02 27 33.13	+23 03 35.7	9792	2.289	0.295	0.892	19.86	E
	J8:PP-J01080	02 30 36.64	+22 43 09.8	9725	2.214	0.253	0.568	19.02	L
	J8:PP-J03049	02 29 43.83	+23 57 21.6	9925	2.399	0.273	1.137	20.34	E
	J8:PP-J07038	02 26 54.41	+23 37 32.5	10130	2.260	0.282	0.692	19.59	L
MKW12	MKW12:FCP-09	14 03 47.32	+09 31 25.6	7040	2.279	—	1.023	20.11	L
	N5423	14 02 48.62	+09 20 28.7	5966	2.418	—	0.926	18.85	E

(Continued)

Cluster	Galaxy	R.A. (J2000)	Dec. (J2000)	$cz_\odot$	$\log\sigma$	Mg_2	$\log R_e$	$\langle\mu\rangle_e$	T
	N5424	14 02 55.71	+09 25 14.6	6002	2.311	0.300	1.133	19.83	E
	N5438	14 03 48.00	+09 36 38.0	6704	2.292	—	1.118	20.03	E
PISC	I1618	01 05 55.98	+32 24 43.8	4718	1.950	0.224	0.946	20.12	L
	I1648	01 13 42.11	+33 13 05.6	5535	2.082	0.267	0.815	19.40	L
	N0375	01 07 05.92	+32 20 53.4	5913	2.250	0.275	0.539	18.44	L
	N0379	01 07 15.60	+32 31 12.0	5496	2.362	0.302	1.241	19.79	L
	N0380	01 07 17.60	+32 28 58.0	4432	2.473	0.338	1.018	18.84	E
	N0382	01 07 23.87	+32 24 12.8	5239	2.286	0.272	0.785	18.82	E
	N0383	01 07 24.98	+32 24 44.8	5095	2.440	0.308	1.489	20.18	E
	N0384	01 07 25.00	+32 17 33.0	4261	2.411	0.312	0.889	18.82	E
	N0385	01 07 27.20	+32 19 11.0	5005	2.289	0.288	1.095	19.61	E
	N0386	01 07 31.29	+32 21 43.2	5550	2.097	0.245	0.774	19.32	E
	N0388	01 07 47.14	+32 18 35.9	5450	2.133	0.255	0.580	18.62	E
	N0392	01 08 23.46	+33 07 59.5	4676	2.372	0.297	1.073	19.24	E
	N0394	01 08 25.98	+33 08 52.5	4382	2.258	0.268	0.751	18.72	L
	N0397	01 08 31.10	+33 06 33.1	4984	2.109	0.259	0.715	19.23	E
	N0398	01 08 53.67	+32 30 52.3	4906	2.005	0.262	0.854	19.57	L
	N0410	01 10 58.87	+33 09 08.3	5305	2.471	0.347	1.433	19.89	E
	N0420	01 12 10.04	+32 07 22.7	5017	2.254	0.247	1.230	19.80	E
	PISC:PP-Z01032	01 08 12.90	+32 27 12.0	4751	2.013	0.272	0.799	20.03	L
	PISC:PP-Z01034	01 05 34.20	+32 25 47.1	5148	2.080	0.268	0.891	19.72	E
	PISC:PP-Z01047	01 06 58.20	+32 18 30.0	5487	2.109	0.286	0.538	18.60	E
	PISC:PP-Z01073	01 09 13.48	+31 58 46.0	5169	2.185	0.279	0.760	19.12	E
	PISC:PP-Z10020	01 11 51.21	+31 33 32.9	4846	1.918	0.228	0.833	20.06	L
S0301	I1858	02 49 08.41	-31 17 21.2	6088	2.280	—	1.061	19.90	L
	I1860	02 49 33.71	-31 11 20.8	6868	2.419	—	1.389	20.48	E
	S0301:D-017	02 49 55.84	-31 17 15.4	6458	2.232	—	0.512	18.57	L
	S0301:D-020	02 49 39.29	-31 12 17.0	7910	2.098	—	0.689	19.80	E
	S0301:D-022	02 49 43.79	-31 09 28.6	7023	2.121	—	0.955	20.25	L
	S0301:D-024	02 49 32.82	-31 11 57.2	7530	2.019	—	0.854	20.63	L
	S0301:D-026	02 49 31.93	-31 10 22.8	6870	2.047	—	0.641	20.01	E
	S0301:D-027	02 49 29.84	-31 09 24.3	7854	1.981	—	0.424	19.54	E
	S0301:D-031	02 49 56.18	-31 08 00.5	7217	2.198	—	0.706	19.73	L
	S0301:D-034	02 49 33.38	-31 07 16.0	7126	2.062	—	0.847	20.31	L
	S0301:FCP-20	02 49 35.60	-31 01 25.4	7011	1.833	—	0.609	20.88	E
S0753	E384-023	13 58 29.89	-34 14 32.5	3953	2.079	0.236	1.560	21.24	Q
	E384-029	14 00 46.27	-34 13 27.6	3436	2.178	0.247	1.110	19.77	E
	E384-036	14 03 12.95	-33 21 27.3	4684	2.273	0.261	1.060	19.54	E
	E384-049	14 06 06.92	-33 55 22.8	4485	2.300	0.285	0.860	18.67	L
	N5397	14 01 10.10	-33 56 44.8	4148	2.423	0.302	1.070	19.21	L
	N5419	14 03 38.29	-33 58 49.5	4182	2.526	0.335	1.610	19.99	E
	S0753:W-010	13 58 40.29	-33 28 06.1	3949	2.125	0.228	0.620	18.38	L
	S0753:W-012	13 58 51.33	-33 29 25.7	4156	2.226	0.283	0.800	18.93	L
	S0753:W-017	13 59 51.19	-34 19 02.6	4162	2.018	0.199	0.740	19.14	E
	S0753:W-037	14 02 10.14	-33 47 25.6	3911	2.247	0.300	0.690	18.49	L
	S0753:W-047	14 02 54.66	-34 15 20.9	4253	2.092	0.251	0.770	18.96	L
	S0753:W-049	14 03 06.50	-34 01 54.5	5122	2.411	0.302	0.460	17.19	L

(Continued)

Cluster	Galaxy	R.A. (J2000)	Dec. (J2000)	$cz_\odot$	$\log\sigma$	Mg_2	$\log R_e$	$\langle\mu\rangle_e$	T
	S0753:W-051	14 03 07.56	-34 05 54.5	4013	2.196	0.248	0.910	19.59	E
	S0753:W-073	14 04 33.69	-33 57 38.3	3836	2.285	0.302	1.050	19.40	L
	S0753:W-095	14 06 50.54	-34 29 29.2	4646	2.133	0.261	0.910	19.54	E
S0761	E511-021	14 18 14.45	-27 24 54.1	7704	2.416	—	0.884	18.78	E
	E511-023	14 18 26.58	-27 22 43.1	6788	2.405	0.298	1.105	19.44	E
	E511-026	14 18 50.78	-27 24 36.8	7125	2.418	—	0.994	19.37	E
	E511-032	14 19 30.45	-27 22 33.2	6459	2.369	—	1.151	19.95	L
	S0761:FCP-04	14 19 02.03	-27 23 23.3	6662	2.340	—	0.778	18.87	E
	S0761:FCP-05	14 19 02.24	-27 27 34.3	6531	2.176	—	0.627	19.00	L
	S0761:FCP-11	14 18 48.67	-27 23 37.6	6838	2.205	—	0.391	18.01	E
	S0761:FCP-14	14 19 56.04	-27 28 17.9	7904	2.195	—	0.973	20.62	E
	S0761:FCP-26	14 18 23.98	-27 22 57.1	6801	1.921	—	0.220	18.69	E
S0805	E103-046	18 41 24.18	-64 00 49.6	4578	2.340	—	0.893	18.82	L
	E104-002	18 46 53.64	-63 21 40.4	4222	2.078	—	0.837	19.45	L
	E104-007	18 47 17.95	-63 21 33.8	4066	2.337	—	1.138	19.31	E
	I4748	18 42 45.85	-64 04 20.8	4226	2.179	—	0.903	18.99	E
	I4765	18 47 17.93	-63 19 52.8	4503	2.452	0.338	1.572	20.46	E
	I4767	18 47 41.58	-63 24 20.0	3502	2.143	0.253	1.215	20.48	L
	S0805:D-021	18 46 24.94	-63 19 30.6	3635	2.064	—	0.725	18.99	L
	S0805:D-023	18 44 11.29	-63 18 29.3	4394	1.928	—	0.861	20.57	E
	S0805:D-029	18 45 50.71	-63 14 08.7	4694	1.981	—	0.495	18.95	E
	S0805:FCP-09	18 42 15.94	-63 36 59.0	4740	2.061	—	1.002	19.72	E
S21	I1548	00 21 55.16	+22 00 22.7	5769	2.164	0.201	0.691	18.80	L
	N0079	00 21 02.85	+22 33 59.7	5473	2.279	0.311	1.053	19.85	E
	N0080	00 21 11.22	+22 21 29.3	5735	2.407	0.310	1.390	20.17	E
	N0083	00 21 22.76	+22 26 08.3	6256	2.396	0.324	1.358	20.30	E
	N0085A	00 21 25.52	+22 30 42.4	6183	2.025	0.243	1.201	20.83	L
	S21:PP-S06	00 21 20.90	+21 59 00.0	5640	2.102	0.210	0.827	20.22	L
	S21:PP-S07	00 20 51.75	+21 32 11.4	5920	2.052	0.258	0.827	19.41	L

Appendix B

Cluster charts

The charts in this appendix display the redshift-space distribution of galaxies in each SMAC sample cluster.

For each cluster, the upper panel shows the galaxy distribution on the sky, relative to the adopted cluster center, which is indicated by the large cross. The charts have North at the top and East at the left, and the axis units are h^{-1}Mpc at the distance of the cluster. The solid circle indicates the projected radius, $R_{\rm cl}$, used in defining cluster membership. In some plots, dotted circles indicate the same quantity for neighbouring clusters. Several samples of galaxies are plotted: squares denote galaxies used to determine the mean redshift, $cz_{\rm cl}$, and velocity dispersion, $\sigma_{\rm cl}$, of the cluster. Filled squares indicate the with full FP data, used in the distance estimates. Open squares are from the extended sample of early-type galaxies with redshifts. These galaxies are used in determining $cz_{\rm cl}$ and $\sigma_{\rm cl}$, but do not have full FP data. Galaxies indidated by small crosses lie outside the selection criteria for the cluster (or have been assigned to a neighbouring cluster). The recession velocities for these galaxies are indicated at the lower right of the crosses. The large open square, where present, indicates the position of the BCG defined by Lauer & Postman (1994). Small dots show the positions of galaxies from the NED database within the projected radius $R_{\rm cl}$.

The lower panel shows the distribution, in redshift, of the galaxy redshifts. Two samples are plotted: The solid histogram (left hand axis) shows the distribution of redshifts in the early-type galaxy sample, within $R_{\rm cl}$. The dotted histogram (right hand axis) shows the sme for galaxies within $R_{\rm cl}$ from the NED database. The horizontal axis gives the heliocentric cz in km s^{-1}. The solid crosses indicate the mean redshift, $cz_{\rm cl}$, and its error, for galaxies in the early-type sample. The tick marks give the $2.6\sigma_{\rm cl}$ range used to define cluster membership, also for the early-type sample. The dashed cross indicates the mean reshift and its error, determined from the NED galaxies.

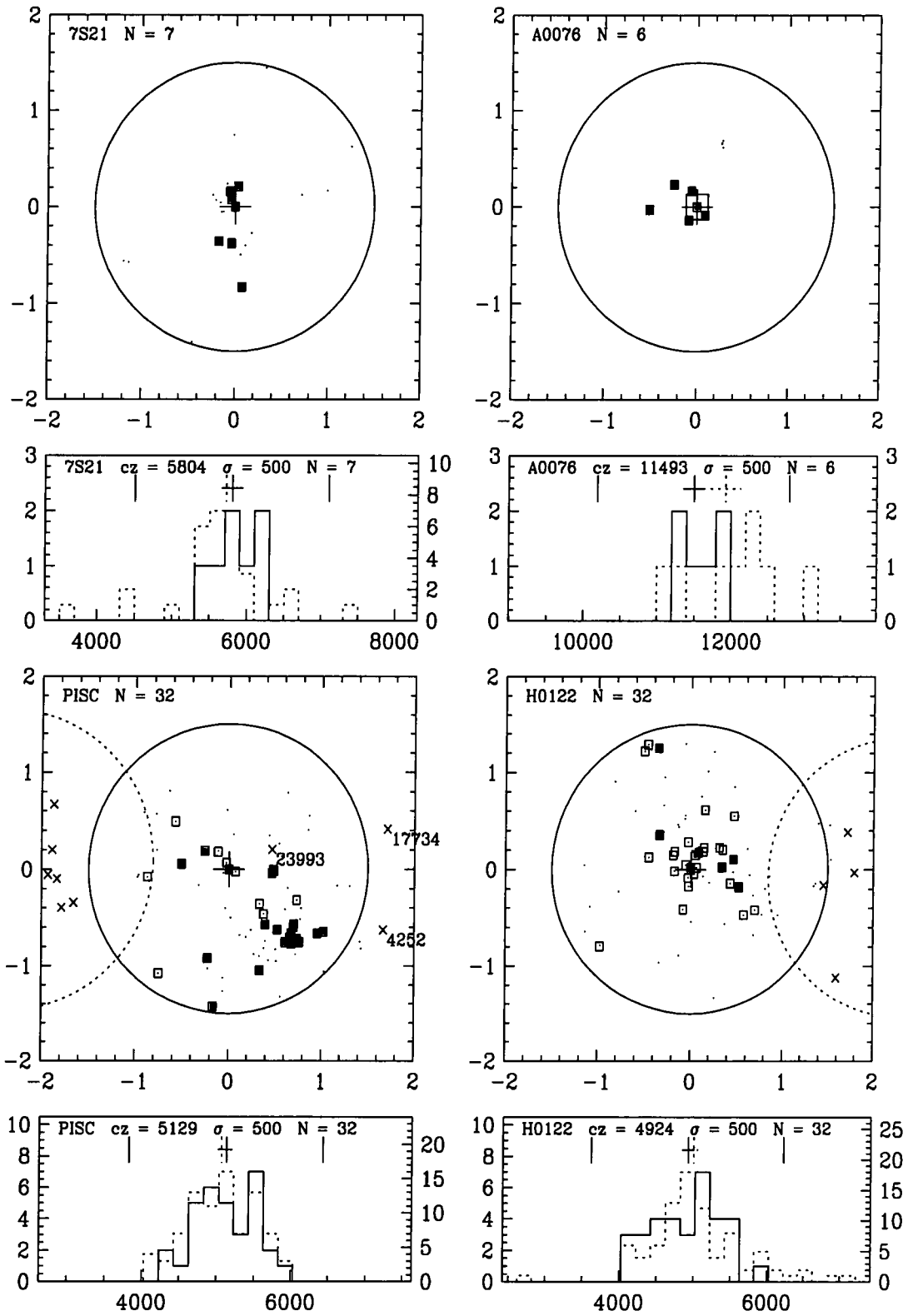

Figure B.1: Cluster sample plots., See text for a full details..

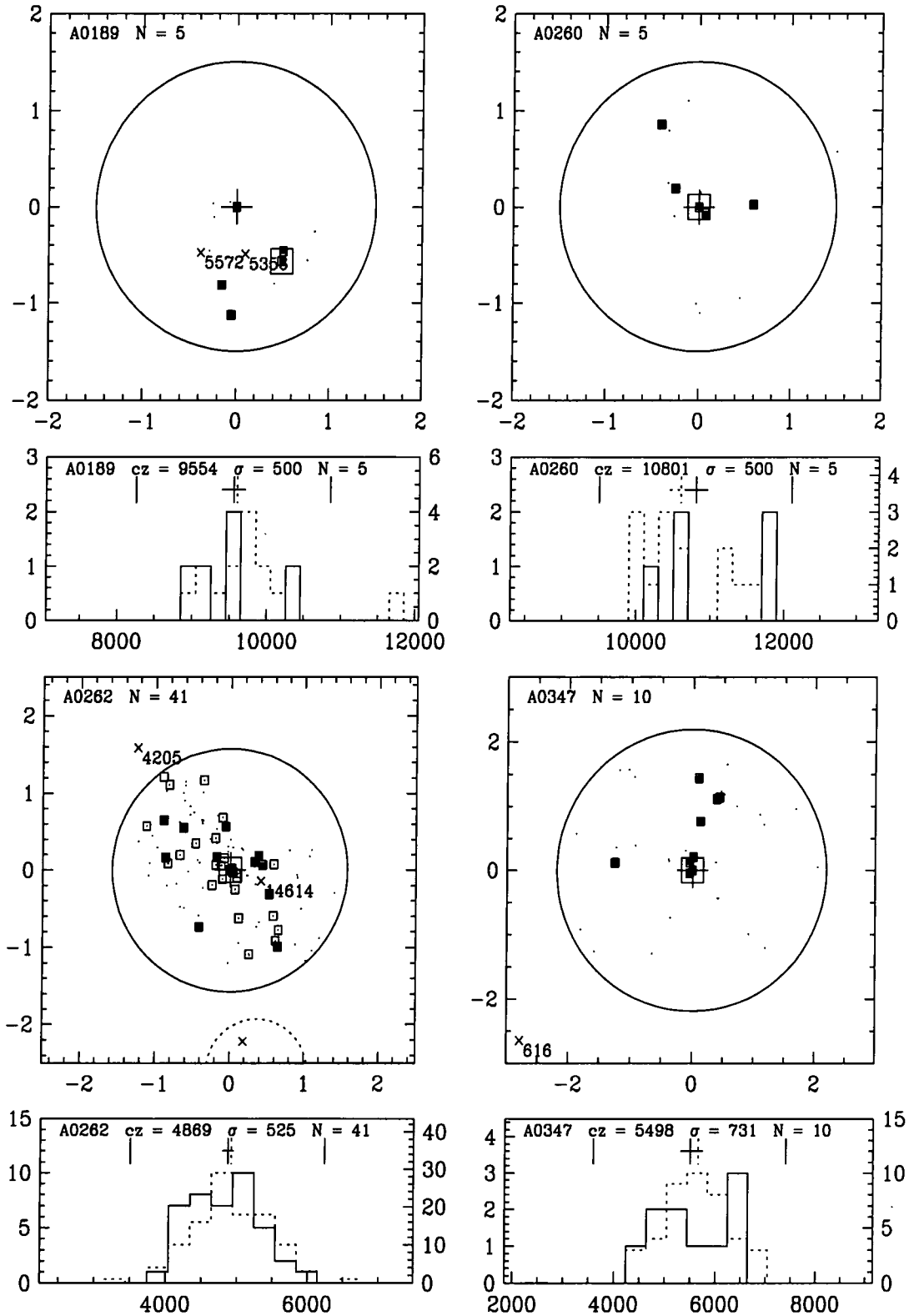
A0189 N = 5
5572
5358
A0260 N = 5
A0189 cz = 9554 σ = 500 N = 5
A0260 cz = 10801 σ = 500 N = 5
A0262 N = 41
4205
4614
A0347 N = 10
616
A0262 cz = 4869 σ = 525 N = 41
A0347 cz = 5498 σ = 731 N = 10

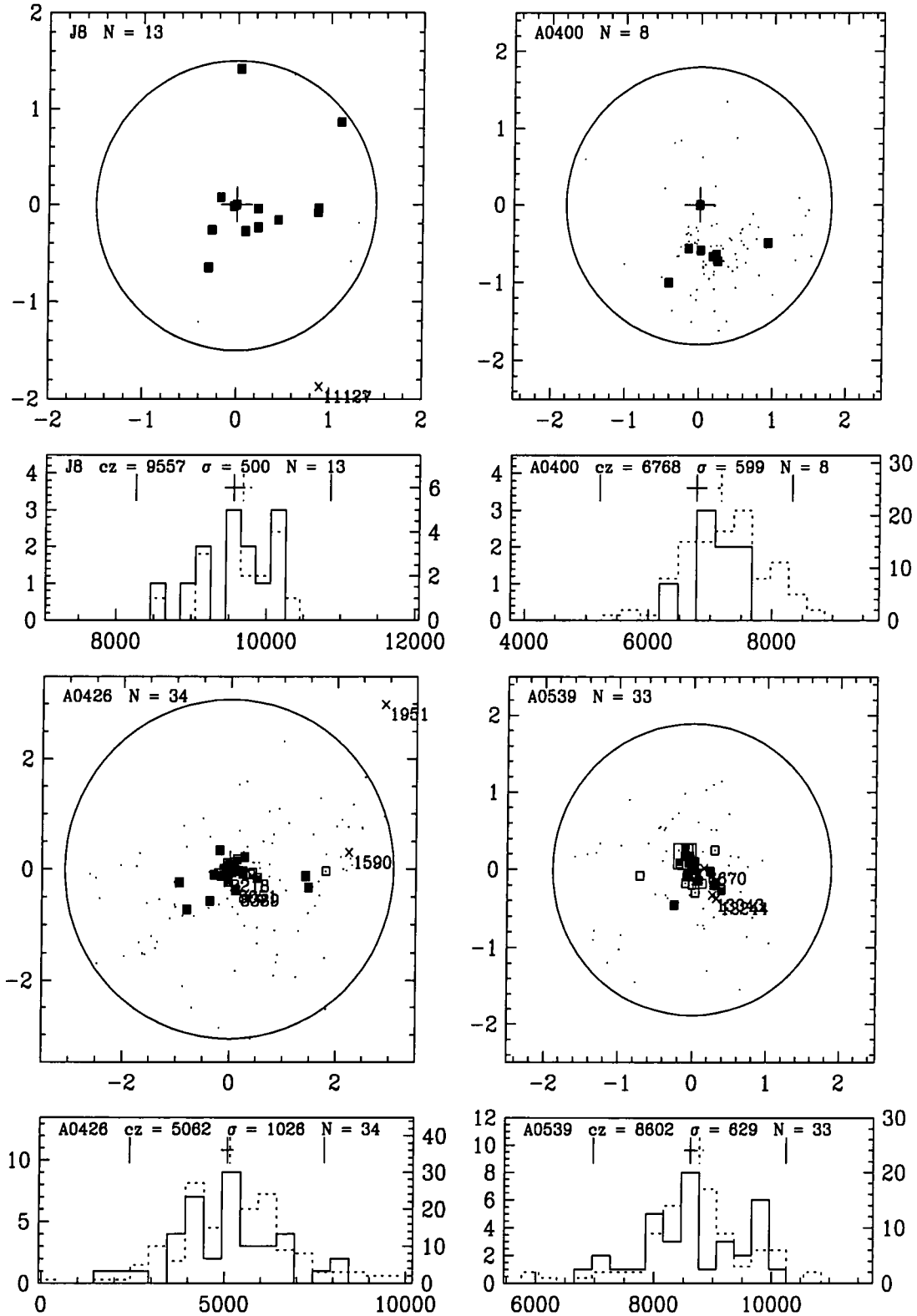
J8 N = 13
11127
A0400 N = 8
J8 cz = 9557 σ = 500 N = 13
A0400 cz = 6768 σ = 599 N = 8
A0426 N = 34
1951
1590
A0539 N = 33
A0426 cz = 5062 σ = 1026 N = 34
A0539 cz = 8602 σ = 629 N = 33

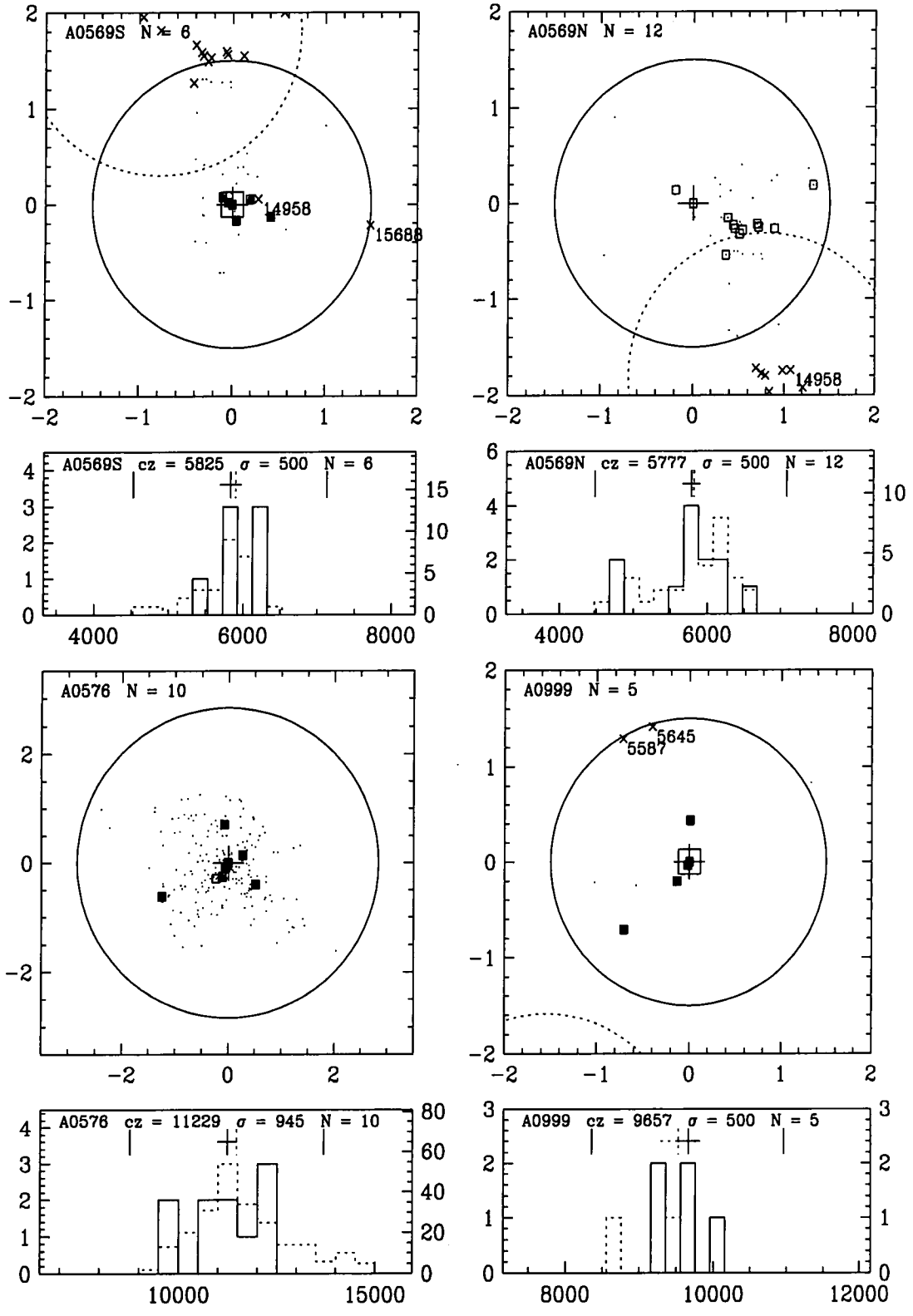
A0569S N = 6
14958
15688
A0569N N = 12
14958
A0569S cz = 5825 σ = 500 N = 6
A0569N cz = 5777 σ = 500 N = 12
A0576 N = 10
A0999 N = 5
5645
5587
A0576 cz = 11229 σ = 945 N = 10
A0999 cz = 9657 σ = 500 N = 5

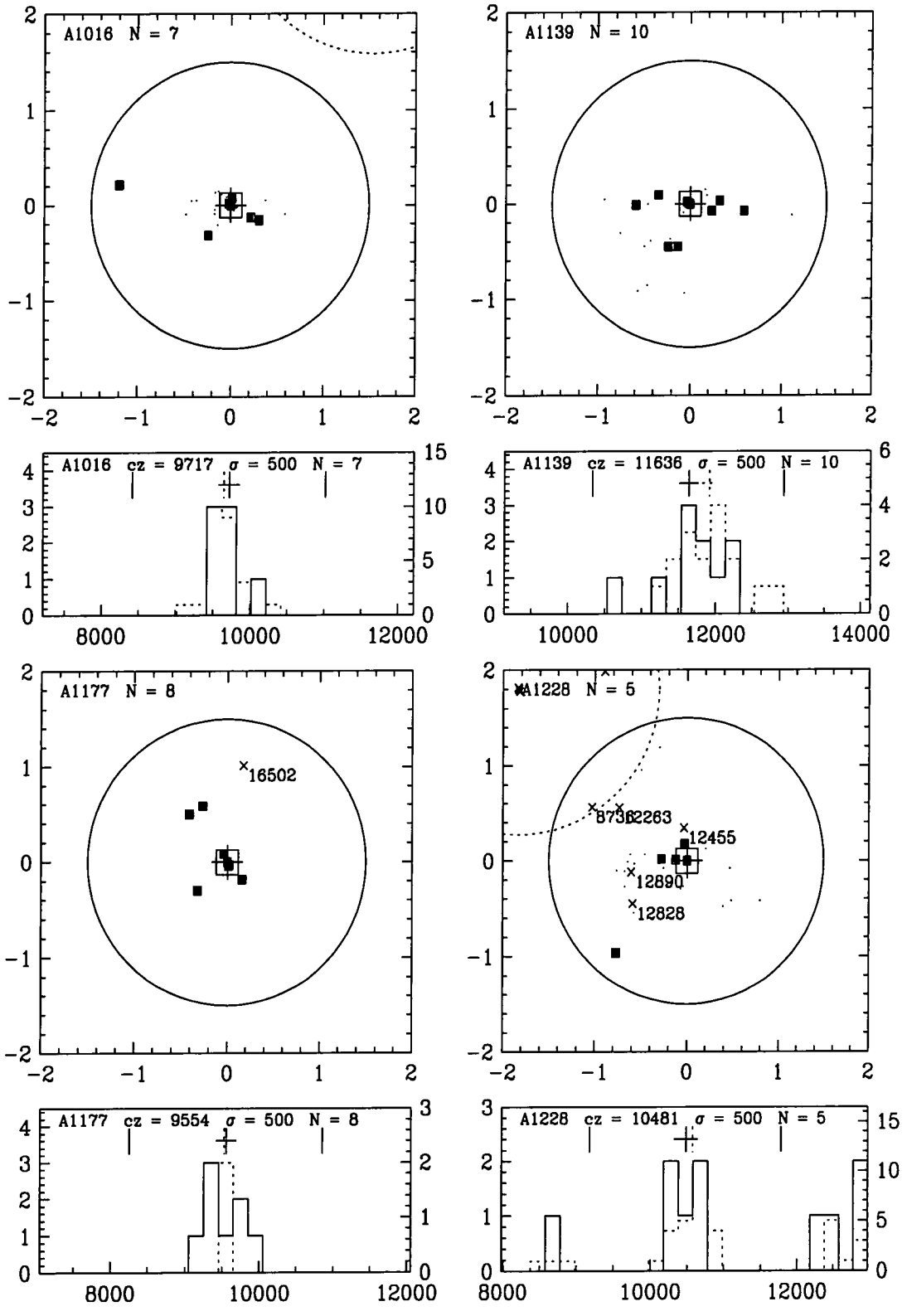
A1016 N = 7
A1016 cz = 9717 σ = 500 N = 7
A1139 N = 10
A1139 cz = 11636 σ = 500 N = 10
A1177 N = 8
16502
A1177 cz = 9554 σ = 500 N = 8
A1228 N = 5
12455
12890
12828
A1228 cz = 10481 σ = 500 N = 5

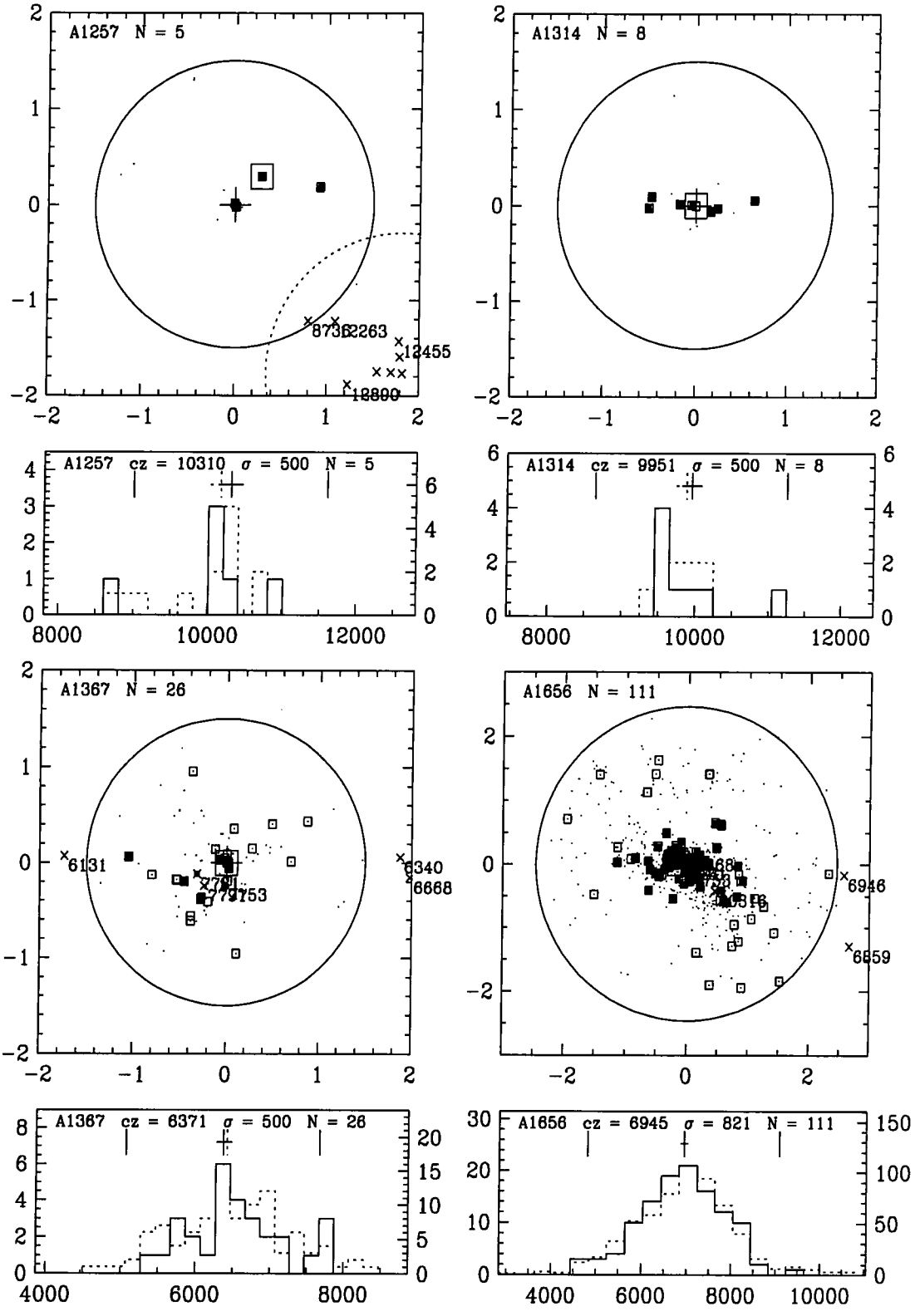
A1257 N = 5
A1314 N = 8
A1257 cz = 10310 σ = 500 N = 5
A1314 cz = 9951 σ = 500 N = 8
A1367 N = 26
A1656 N = 111
A1367 cz = 6371 σ = 500 N = 26
A1656 cz = 6945 σ = 821 N = 111

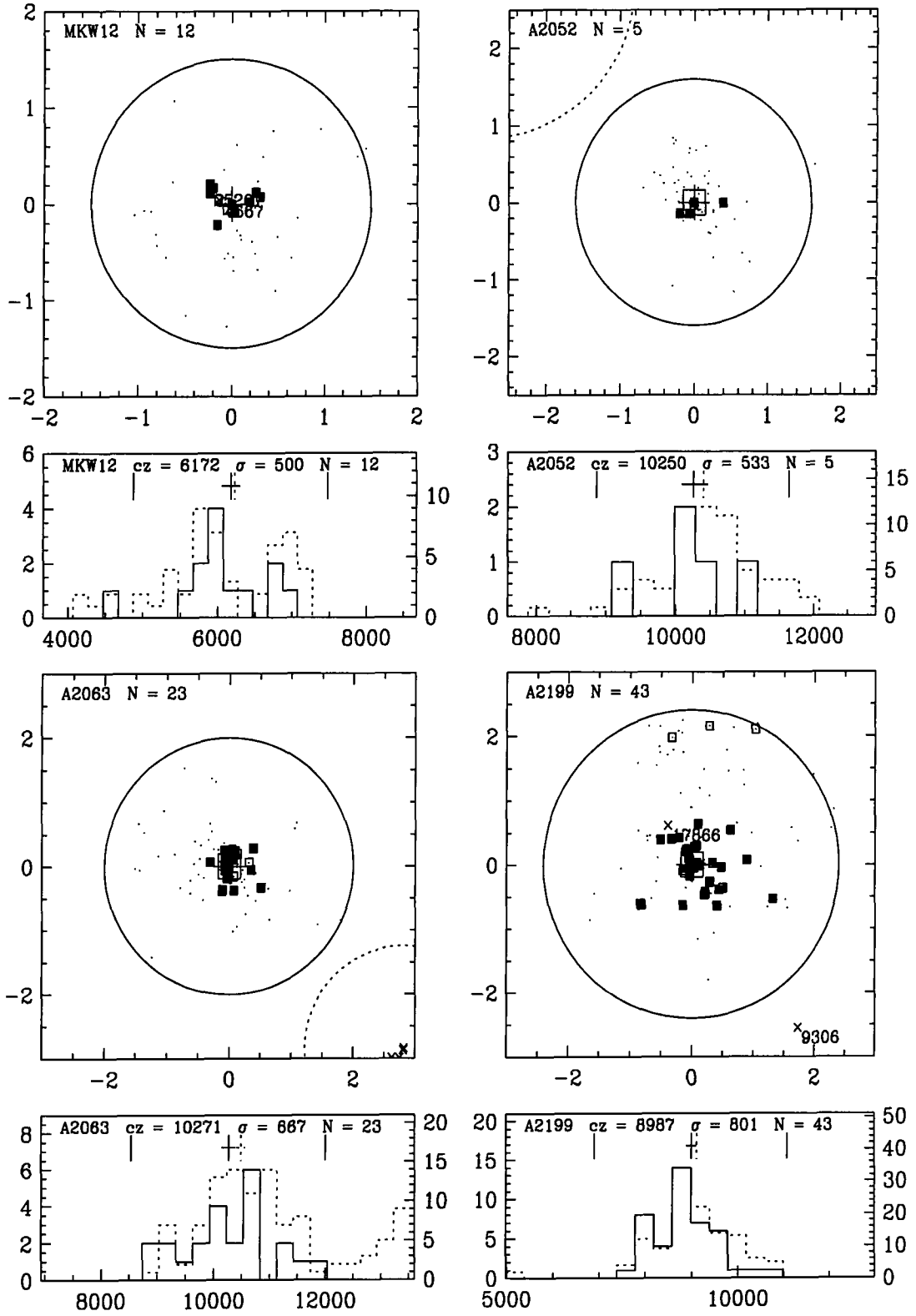
MKW12 N = 12
A2052 N = 5
MKW12 cz = 6172 σ = 500 N = 12
A2052 cz = 10250 σ = 533 N = 5
A2063 N = 23
A2199 N = 43
9306
A2063 cz = 10271 σ = 667 N = 23
A2199 cz = 8987 σ = 801 N = 43

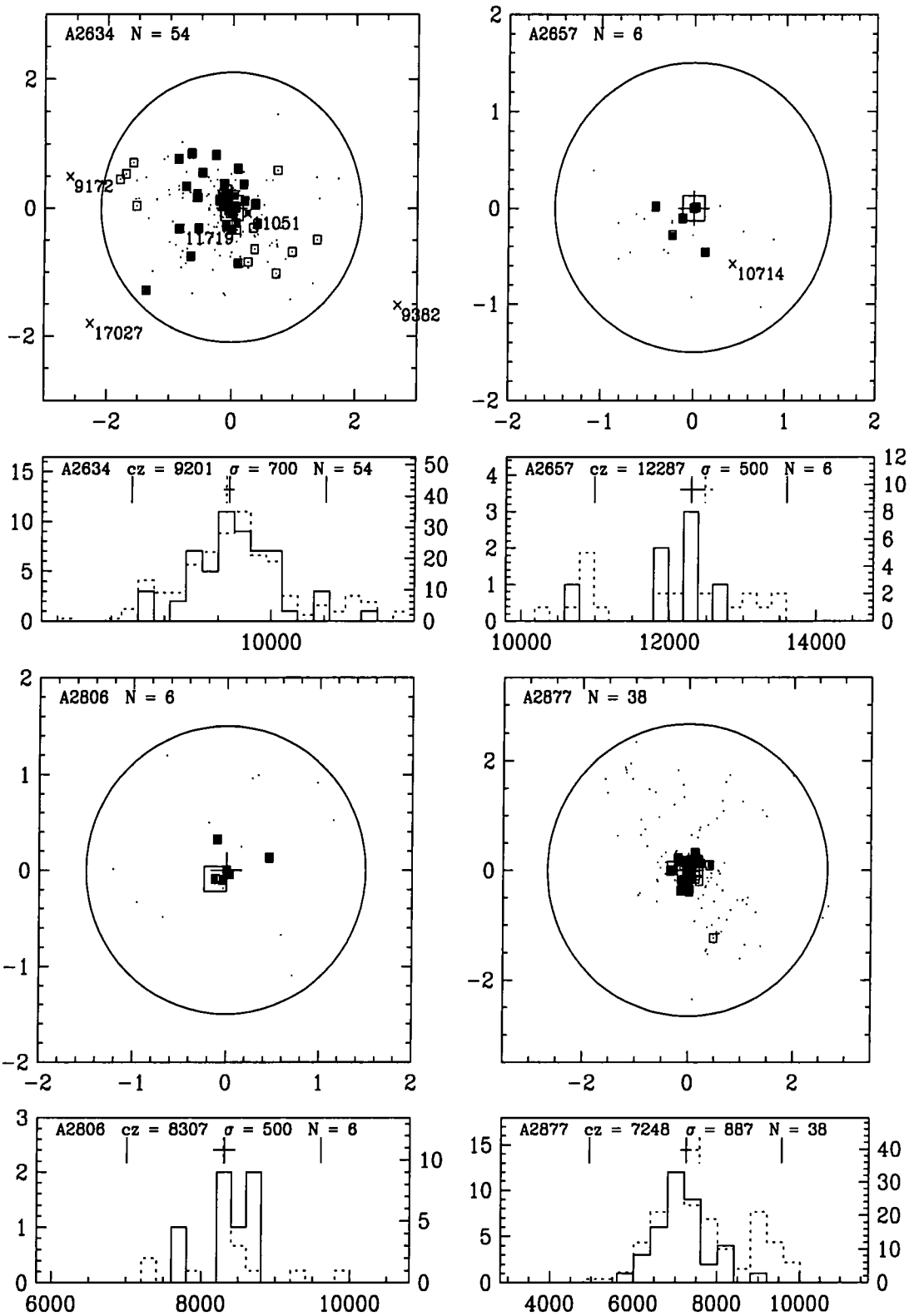
A2634 N = 54
9172
11051
11719
17027
9382
A2657 N = 6
10714
A2634 cz = 9201 σ = 700 N = 54
A2657 cz = 12287 σ = 500 N = 6
A2806 N = 6
A2877 N = 38
A2806 cz = 8307 σ = 500 N = 6
A2877 cz = 7248 σ = 887 N = 38

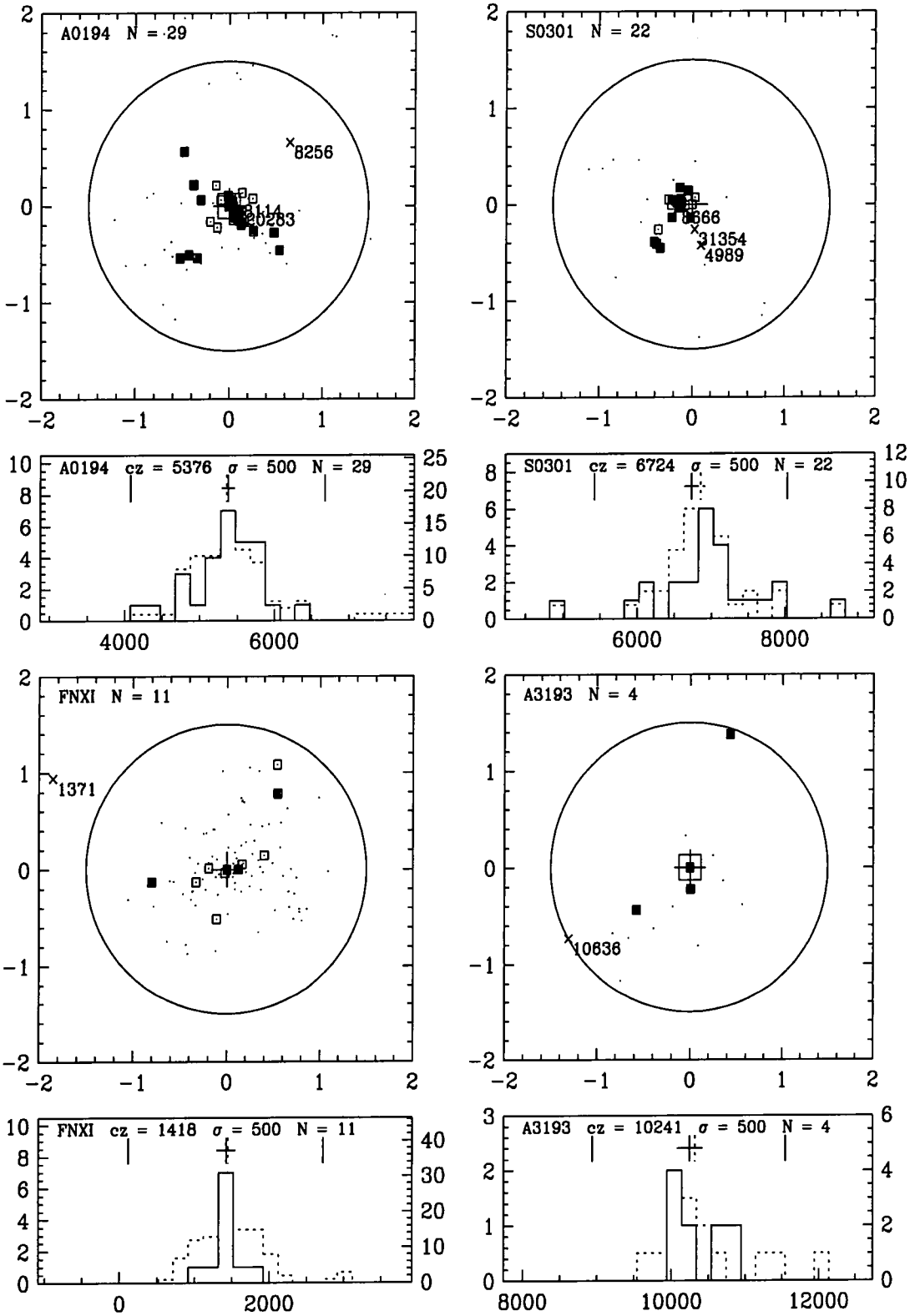
A0194 N = 29
8256
20283
A0194 cz = 5376 σ = 500 N = 29
S0301 N = 22
8666
31354
4989
S0301 cz = 6724 σ = 500 N = 22
FNXI N = 11
1371
FNXI cz = 1418 σ = 500 N = 11
A3193 N = 4
10636
A3193 cz = 10241 σ = 500 N = 4

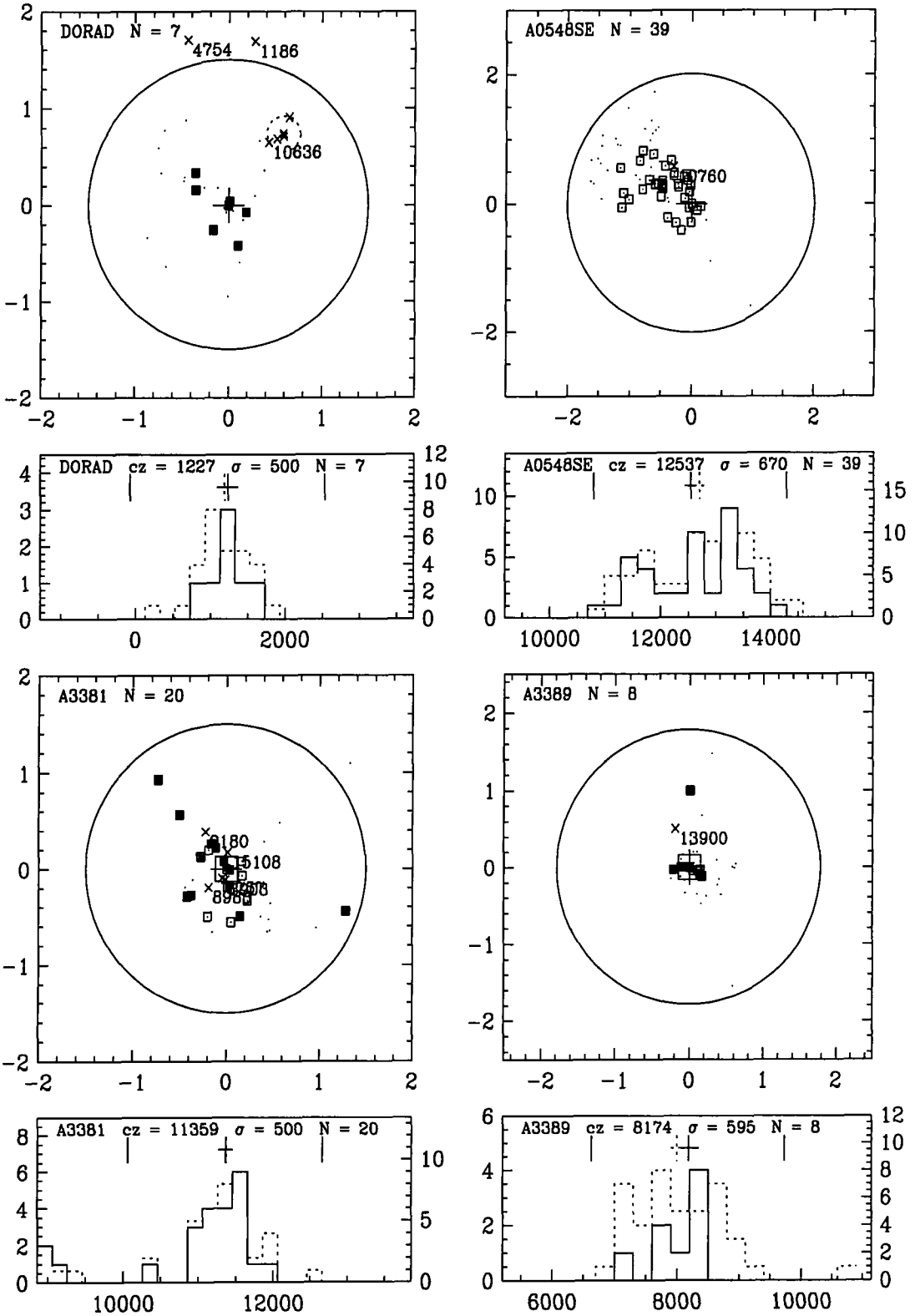
DORAD N = 7
4754
1186
10636
A0548SE N = 39
DORAD cz = 1227 σ = 500 N = 7
A0548SE cz = 12537 σ = 670 N = 39
A3381 N = 20
A3389 N = 8
13900
A3381 cz = 11359 σ = 500 N = 20
A3389 cz = 8174 σ = 595 N = 8

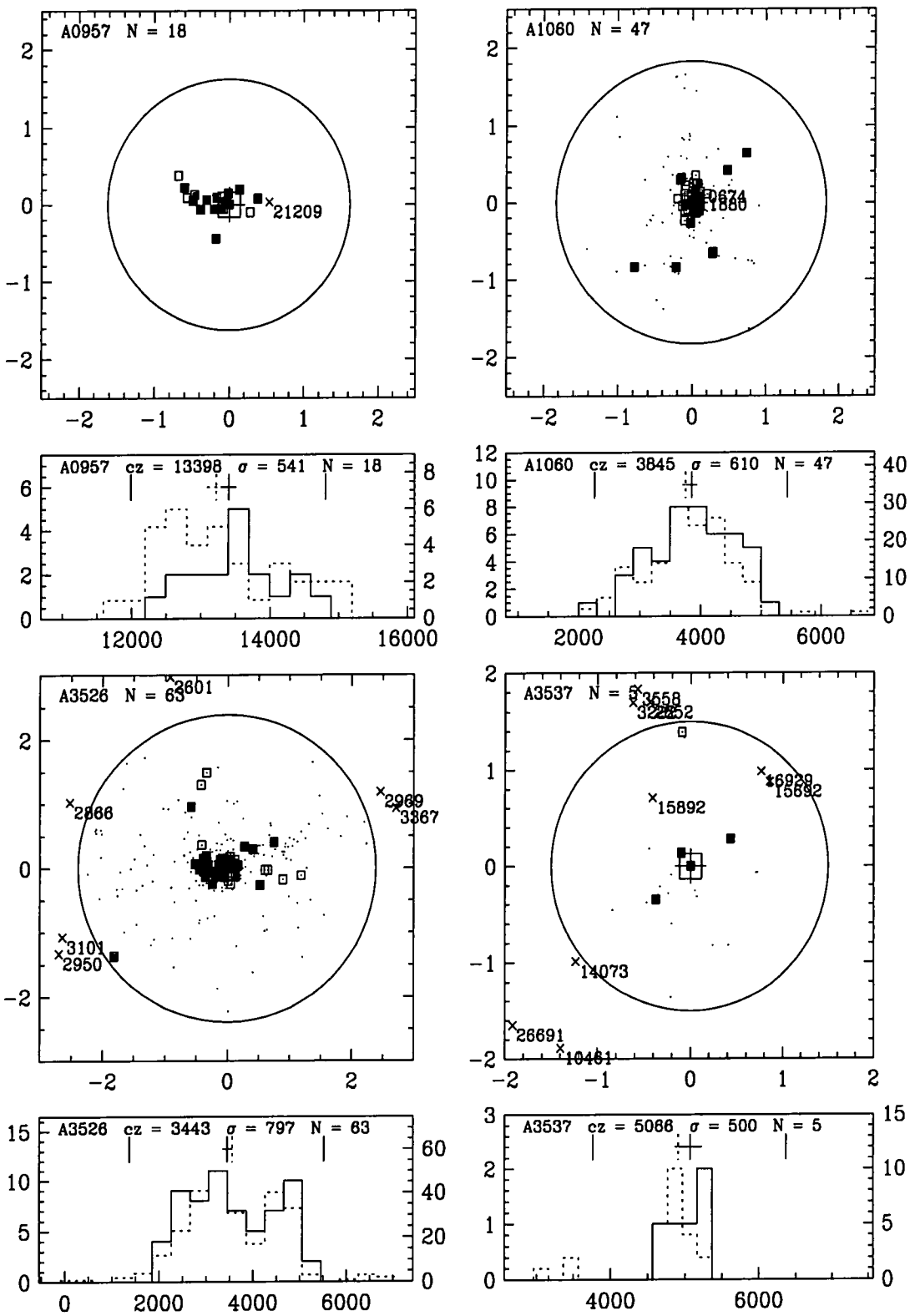
A0957 N = 18
21209
A1060 N = 47
A0957 cz = 13398 σ = 541 N = 18
A1060 cz = 3845 σ = 610 N = 47
A3526 N = 63
2601
2866
2989
3367
3101
2950
A3537 N = 5
15892
14073
26691
10481
A3526 cz = 3443 σ = 797 N = 63
A3537 cz = 5066 σ = 500 N = 5

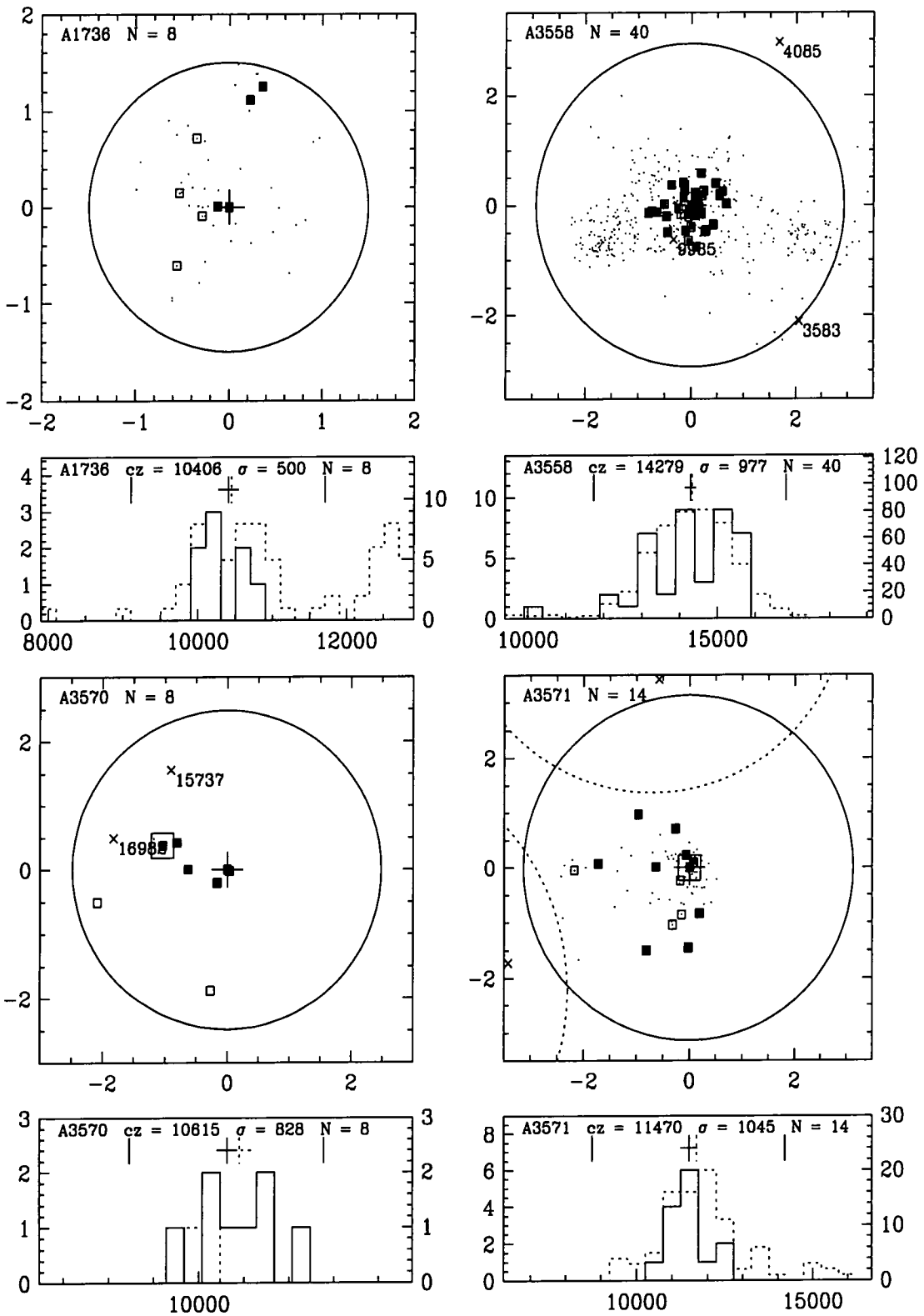
A1736 N = 8
A3558 N = 40
4085
3583
A1736 cz = 10406 σ = 500 N = 8
A3558 cz = 14279 σ = 977 N = 40
A3570 N = 8
15737
A3571 N = 14
A3570 cz = 10615 σ = 828 N = 8
A3571 cz = 11470 σ = 1045 N = 14

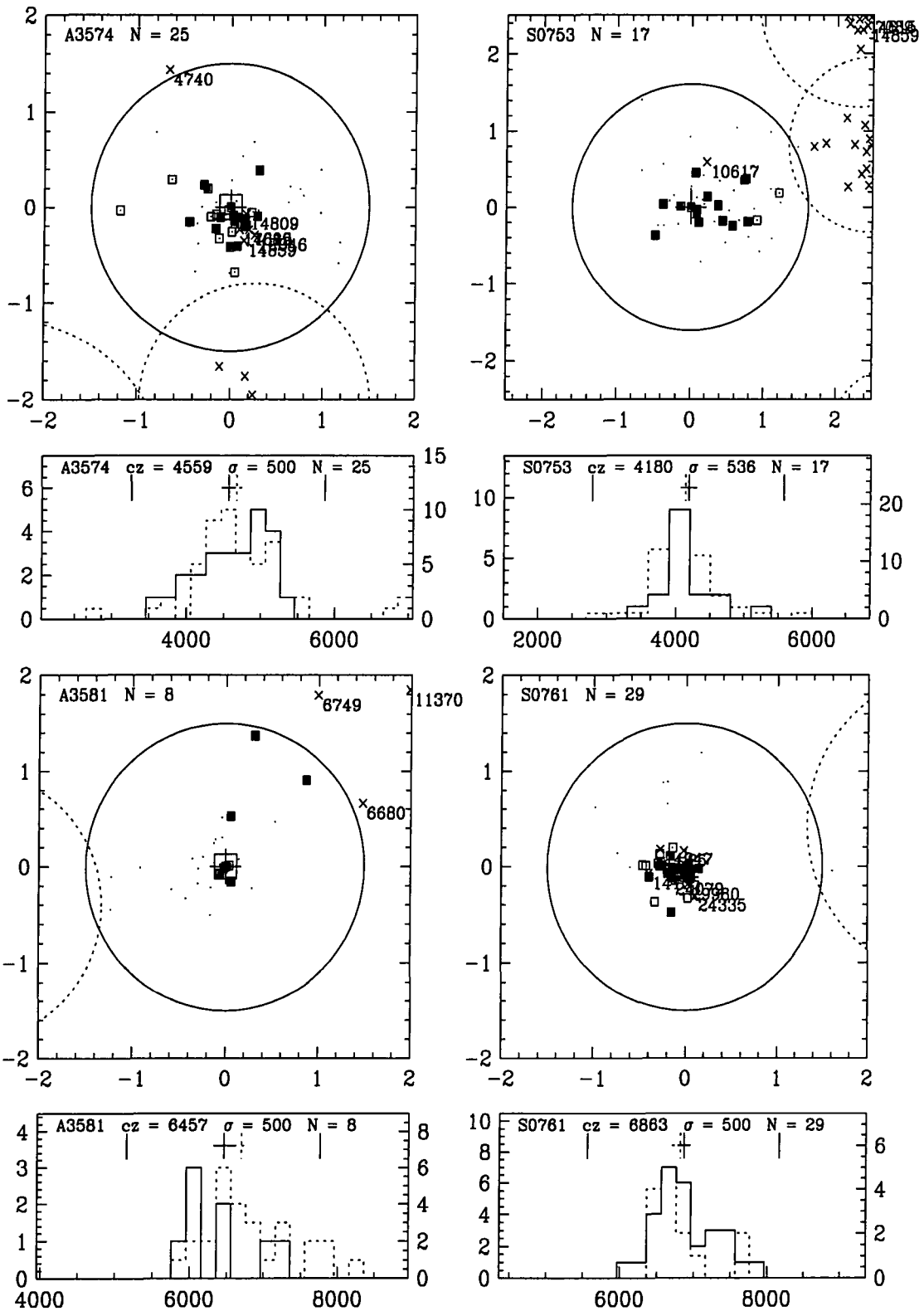
A3574 N = 25
4740
14809
14659
A3574 cz = 4559 σ = 500 N = 25
S0753 N = 17
10617
S0753 cz = 4180 σ = 536 N = 17
A3581 N = 8
6749
11370
6680
A3581 cz = 6457 σ = 500 N = 8
S0761 N = 29
24335
S0761 cz = 6863 σ = 500 N = 29

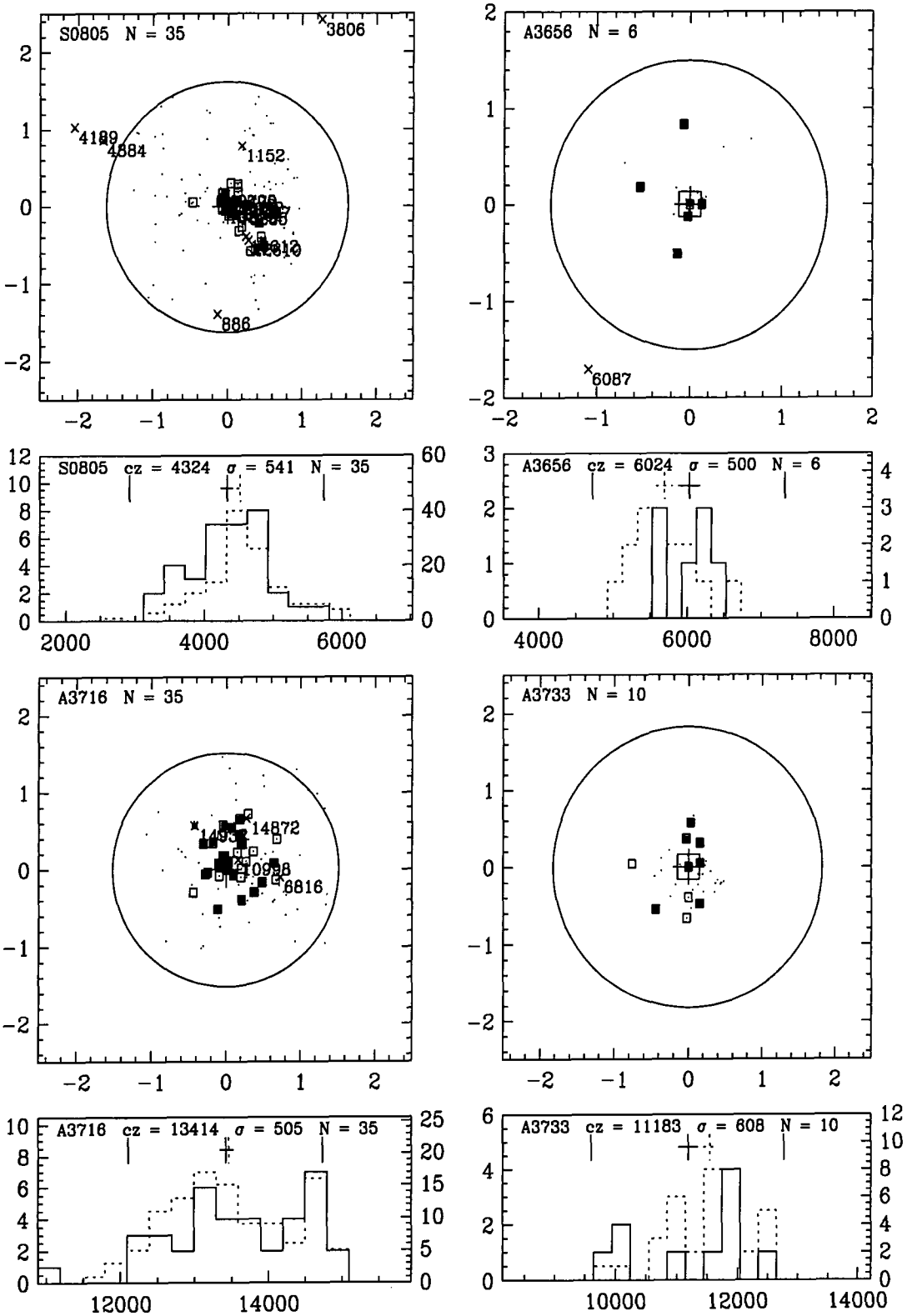
S0805 N = 35
3806
4189
4884
1152
886
S0805 cz = 4324 σ = 541 N = 35
A3656 N = 6
6087
A3656 cz = 6024 σ = 500 N = 6
A3716 N = 35
14872
8816
A3716 cz = 13414 σ = 505 N = 35
A3733 N = 10
A3733 cz = 11183 σ = 608 N = 10

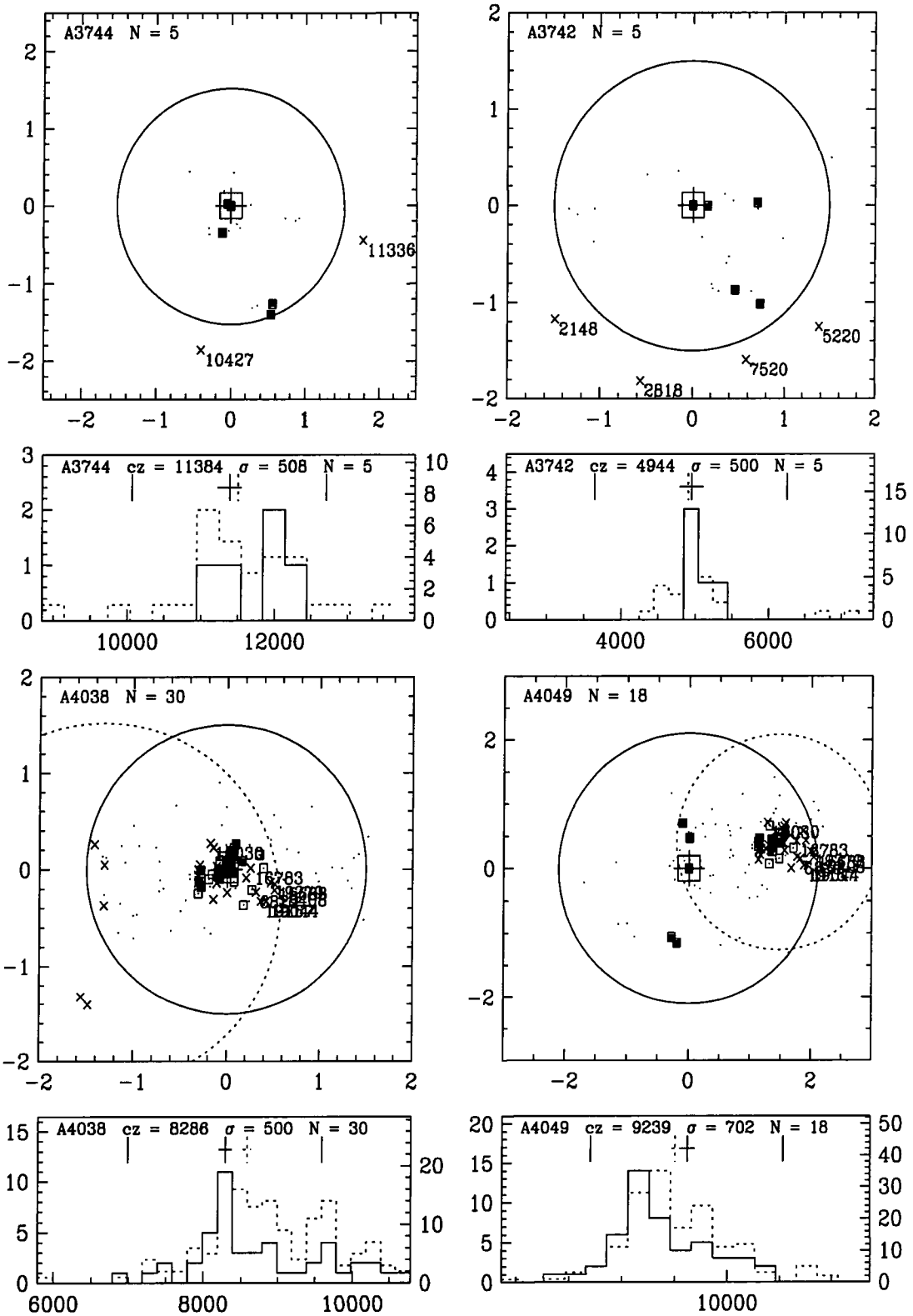
A3744 N = 5
11336
10427
A3742 N = 5
2148
5220
7520
2818
A3744 cz = 11384 σ = 508 N = 5
A3742 cz = 4944 σ = 500 N = 5
A4038 N = 30
A4049 N = 18
A4038 cz = 8286 σ = 500 N = 30
A4049 cz = 9239 σ = 702 N = 18